# MODELLING OF THE SETTLEMENT INTERACTION OF NEIGHBOURING BUILDINGS ON SOFT GROUND

RUSTAM EFFENDI
(Ir., M.A.Sc.)

A THESIS SUBMITTED FOR THE DEGREE OF DOCTOR OF PHILOSOPHY
DEPARTEMENT OF CIVIL AND STRUCTURAL ENGINEERING
UNIVERSITY OF SHEFFIELD

NOVEMBER 2007

*O mankind! if ye have a doubt about the Resurrection, (consider) that We created you out of dust, then out of sperm, then out of a leech-like clot, then out of a morsel of flesh, partly formed and partly unformed, in order that We may manifest (our power) to you; and We cause whom We will to rest in the wombs for an appointed term, then do We bring you out as babes, then (foster you) that ye may reach your age of full strength; and some of you are called to die, and some are sent back to the feeblest old age, so that they know nothing after having known (much), and (further), thou seest the earth barren and lifeless, but when We pour down rain on it, it is stirred (to life), it swells, and it puts forth every kind of beautiful growth (in pairs).*

*[Qur'an 22:5]*

# ACKNOWLEDGEMENTS

# ABSTRACT

The research described in this thesis investigated the soil deformation due to the interaction of two neighbouring buildings founded on soft clay. The study involved small-scale 1g physical modelling in which mitigation of the interaction was studied by inserting a model sheet pile wall between two footings. The results were used to validate finite element analyses that were then extended to simulate a prototype of two buildings with raft foundations constructed on Singapore clay.

In the physical models, two 100 mm wide strip footings were placed on a 200 mm thick bed of preconsolidated kaolin in a rigid chamber with a transparent front wall. Tests were conducted without a wall between the footings, with a 100mm long floating wall, and with a vertically restrained (fixed) 100 mm long wall. The footings were loaded in turn and the second footing was only loaded after the consolidation, due to loading on the first footing or subsequent wall insertion, was completed. The soil and footing displacements were photographed through the transparent chamber wall and measured using a combination of Particle Image Velocimetry (PIV) and close range photogrammetry. A stiffer soil response was observed beneath the second footing than beneath the first. Some additional settlement of the first footing was induced by the loading on the second footing and this was not significantly mitigated by a floating wall. In contrast, with a fixed wall, the settlement of the footing was substantially reduced. Overall, the tilting in the tests with a floating wall was comparable to that in the tests without a wall. The tilting of the first footing, though not the second, was effectively mitigated when a fixed wall was used.

Plane strain finite element analyses with the BRICK constitutive soil model were performed to simulate the physical models. In general, the observed behaviour patterns were well reproduced, although the finite element analyses tended to exaggerate the stiffness of the soil response under the second footing relative to that under the first when a wall was present.

The simulated prototype comprised two 10 m wide, 800 mm thick concrete rafts separated by 2 m resting on 40m of clay. The analyses were similar to those conducted for the physical model simulations. In addition to modelling the effects of installing a float-

ing or a fixed wall, parametric studies were undertaken to examine the influence of wall length and stiffness. A longer floating wall reduced the settlement of both footings due to loading on the second footing but even greater settlement mitigation was obtained with a fixed wall. The stiffness of the wall did not have a significant effect on the settlement mitigation except in the case of an unrealistically stiff fixed sheet pile. Without any wall, both footings tilted towards each other. The presence of a wall generally reduced tilting and the reduction increased with wall stiffness

**Keyword**: closely-spaced footings, settlement, tilting, physical modelling, numerical modelling, finite element analysis, particle image velocimetry

# CONTENTS

# LIST OF SYMBOLS

| | |
|---|---|
| $A$ | Area, 28, 71 |
| $\alpha$ | Angle defined in Figure 3.5, 36 |
| $\alpha$ | Material coefficient, 18 |
| | |
| $B$ | Width of footing/foundation, 4, 6, 8, 10, 11, 102, 180, 182, 183, 206 |
| $B$ | Width, 38 |
| $\beta$ | Angle defined in Figure 3.5, 36 |
| $\beta$ | Overconsolidation parameter, 30 |
| $\beta$ | Angular distortion (see $\delta/l$), 16 |
| $\beta_G$ | Overconsolidation parameter of stiffness, 30, 141 |
| $\beta_\phi$ | Overconsolidation parameter of strength, 30, 141 |
| | |
| $(C_x, C_y)$ | Coordinate of centroid with respect to an x-y axis, 71 |
| | |
| $\delta$ | Deflection, 38, 39, 137, 138 |
| $\delta$ | Differential settlement between two points, 14 |
| $\Delta$ | Relative deflection, 15 |
| $\Delta$ | Spacing between centres of two footings, 10, 11 |
| $\Delta/L$ | Deflection ratio, 15, 16 |
| DF | Test on two closely-spaced footings, 56, 59, 83 |
| $D_f$ | Embedment depth of footing, 8 |
| DF1 | First test on two closely-spaced footings, 83, 90, 92–94, 99, 100, 105, 108, 117 |
| DF2 | Second test on two closely-spaced footings, 83, 90–94, 99, 100, 105, 108, 117 |
| $\delta/l$ | Angular distortion, 14–16, 108, 112, 121, 132, 155, 161, 180, 192, 197, 206 |
| | |
| $E$ | Modulus of elasticity (Young's modulus), 16, 38, 39, 137, 138, 143, 174, 175, 197 |
| $e$ | Void ratio, 34, 35 |
| $e_0$ | Initial void ratio, 83, 84, 139 |
| $EI$ | Bending stiffness, 39, 137, 197 |

| | |
|---|---|
| $\varepsilon_{crit}$ | Critical tensile strain, 15, 16 |
| $\varepsilon_x, \varepsilon_y, \varepsilon_z$ | Normal strains, 29 |
| $E_s$ | Young's modulus of soil, 13 |
| $\eta^2$ | Coefficient of determination for non-linear correlation (statistics), 44 |
| $f$ | Focal length of a lens, 68, 77 |
| f/number | Indicator of camera aperture (related to focal length $f$ of a lens of a camera), 49, 50 |
| FX | Test on two closely-spaced footings with a fixed (vertically restrained) sheet wall, 56, 59, 83 |
| FX1 | First test on two closely-spaced footings with a fixed (vertically restrained) sheet wall, 83, 90–92, 94, 99, 114, 123, 125, 126, 130, 132 |
| FX2 | Second test on two closely-spaced footings with a fixed (vertically restrained) sheet wall, 83, 90, 91, 94, 99, 114, 123, 125, 126, 130, 132 |
| $G$ | Shear modulus, 16, 30 |
| $g$ | Acceleration due to gravity, 18, 19, 32 |
| $\gamma$ | Shear strain, 28, 140 |
| $\gamma_{xy}, \gamma_{yz}, \gamma_{zx}$ | Shear strains, 29 |
| $G_{max}$ | Maximum shear modulus, 30, 140 |
| $G_s$ | Specific gravity, 35, 84 |
| $G_t$ | Tangent shear modulus, 28, 30, 140 |
| $H$ | Height, 15, 34 |
| $H$ | Thickness of ground, 183, 206 |
| $I$ | Intensity of image brightness, 21 |
| $I$ | Second moment of inertia, 39, 137, 197 |
| $\iota$ | Proportionality constant, 30, 141 |
| $k$ | Coefficient of radial distortion of a lens, 68 |
| $K_0$ | Coefficient of earth pressure at rest, 29, 38, 141 |
| $K_{0nc}$ | $K_0$ for normal consolidation, 29, 141 |
| $\kappa$ | Slope of unloading–reloading line, 30, 140 |
| $\kappa^*$ | Slope of unloading–reloading line in $\log_e(v) - \log_e(p')$ space, 30, 140, 141, 174 |
| $k_h$ | Coefficient of horizontal permeability, 140 |
| $k_v$ | Coefficient of vertical permeability, 140 |
| $L$ | Length/span, 15, 38, 39 |
| $\lambda$ | Ratio of loads on footings, 8 |

$\lambda$      Scaling factor of transformation, 77

$\lambda$      Slope of normal consolidation line, 30, 140

$\lambda^*$      Slope of normal consolidation line in $\log_e(v) - \log_e(p')$ space, 30, 140, 141, 174

$M(\mathbf{U})$      Mask test patch, 22

$n$      Geometry scale factor, 18, 32, 39

$n$      Refraction index, 78, 81

$N_\gamma, N_q$      Bearing capacity coefficients, 6

$\nu$      Poisson's ratio, 30, 38, 141, 143

$P$      Point load, 39, 137, 138

$p$      Mean stress, 90

$\phi$      Angle of incidence of a ray, 78

$\phi'$      Angle of refraction of a ray, 78

$\phi'$      Angle of internal shearing resistance, 28, 29, 141

$\phi'_{mob}$      Mobilised angle of friction, 28

$\varphi, \omega, \kappa$      Eulerian angles, 22

$q$      Deviator stress, 90

$q$      Surcharge pressure beside a footing, 6

$q$      Uniform load, 36, 38

$q_u$      Ultimate bearing capacity, 4, 6

$\mathbf{R}$      Orthonormal rotation matrix, 77

$r$      Coefficient of correlation (statistics), 44

$r^2$      Coefficient of determination (statistics), 44, 46, 48

$\rho_{F1}(\sigma_{vF1})$      Settlement at the centre of Footing I due to the loading applied on Footing I, 83

$\rho_{F1}(\sigma_{vF2})$      Settlement at the centre of Footing I due to the loading applied on Footing II, 83

$\rho_{F2}(\sigma_{vF1})$      Settlement at the centre of Footing II due to the loading applied on Footing I, 83

$\rho_{F2}(\sigma_{vF2})$      Settlement at the centre of Footing II due to the loading applied on Footing II, 83

$\rho$      Vertical displacement, 83, 94, 99, 105, 112, 116, 117, 125, 126

$R(\mathbf{s})$      Correlation estimator, 21

$S$      Spacing between centres of two footings, 8

$\sigma$      Standard deviation, 44, 73, 74

$s$      Mean stress in plane strain, 28

$s$      Ratio of image pixel dimension, 68, 77

$S_0$      Settlement of a single footing, 10

$S_e$      Settlement of footing, 8

| | |
|---|---|
| $S_i$ | Settlement due to footing interaction, 10 |
| $\sigma_{\bar{w}_i}$ | Standard deviation of averaged initial water content, 83 |
| SP | Test on two closely-spaced footings with a floating sheet wall, 56, 59, 83 |
| SP1 | First test on two closely-spaced footings with a floating sheet wall, 83, 90, 91, 94, 99, 110, 112, 114, 116, 117, 121 |
| SP2 | Second test on two closely-spaced footings with a floating sheet wall, 83, 90, 91, 94, 99, 110, 112, 114, 116, 117, 121 |
| $S/B$ | Ratio of spacing $S$ between footings, 8 |
| $S_r$ | Degree of saturation of pores, 84 |
| $s_u$ | Undrained shear strength, 18, 87 |
| $\Delta\sigma_v$ | Increment of effective vertical stress, 54 |
| $\sigma_v'$ | Effective vertical stress/pressure, 35, 54 |
| $\sigma_x$ | Horizontal stress, 36 |
| $\sigma_{x0}'$ | Initial lateral stress, 186, 187 |
| $\sigma_y$ | Vertical stress, 36 |
| $\sigma_{y0}'$ | Initial vertical stress, 186, 187 |
| | |
| $t$ | Coefficient of tangential distortion of a lens, 68 |
| $t$ | Shear stress in plane strain, 28 |
| $\mathbf{t}$ | Translation in image transformation, 77 |
| $\theta$ | Rotation angle of footing due to tilting, 11 |
| $\tau_{xy}$ | Shear stress, 161, 165, 187, 192 |
| | |
| $u$ | Local axis for horizontal direction, 61, 65, 74 |
| $(u_0, v_0)$ | Principal point (optical centre), 68 |
| | |
| $V$ | Volume, 35 |
| $v$ | Local axis for vertical direction, 61, 65, 74 |
| $v$ | Specific volume, 140 |
| $v$ | Volumetric strain, 28–30 |
| | |
| $w$ | Water content, 35, 87 |
| $w_i$ | Initial water content, 35, 84 |
| $\bar{w}_i$ | Averaged initial water content, 83 |
| $w_L$ | Liquid limit, 33, 35 |
| $w_P$ | Plastic limit, 33 |
| | |
| $\xi_\gamma, \xi_q$ | Ratios of the interference of closely-spaced footings/foundations related respectively to the bearing capacity coefficients $N_\gamma$ and $N_q$, 6, 8 |

# LIST OF ABBREVIATIONS

# LIST OF TABLES

# LIST OF FIGURES

Chapter 1

# INTRODUCTION

## 1.1 BACKGROUND

The lack of land in urban areas forces buildings to be located very close to each other. Interaction of the buildings in the underlying ground is therefore inevitable. The interaction can have a major impact on the settlement of the buildings. Figure 1.1, for example, shows differential settlement due the interaction of buildings in Banjarmasin City in Indonesia. The buildings are supported



**Figure 1.1:** Tilting buildings in Banjarmasin City (Indonesia)

by raft foundations with slender timber piles of 7 metres length in very soft clay extending to a depth of approximately 20 metres (Suzuki and Yasuhara, 2004). The ground profile in that region is quite typical for an alluvial soil, as also found in Singapore Marine Clay (see Hanzawa and Adachi, 1983; Cao et al., 2001; Tan et al., 2002). This uneven settlement can be observed when two buildings are constructed at the same time or after a new building is constructed adjacent to existing buildings.

1

So far, no research has been found directly related to this problem. Even if closely-spaced footings are considered as down-scaled models of neighbouring building foundations, the available studies are still very limited. Most existing research used sand as the model ground (e.g. Stuart, 1962; Das and Larbi-Cherif, 1983b; Graham et al., 1984; Khing et al., 1992). Recent attempts at using the finite element method to study the interaction of closely-spaced footings on cohesive soils have been conducted by Jao et al. (2002) and Maharaj et al. (2004). However, the underlying soils in the numerical modelling were very stiff.

The demand for new buildings on alluvial ground (e.g. in the region mentioned above) seems irresistible and tends to neglect this problem. Predictive capability and economic mitigation measures for neighbouring building interaction are therefore urgently required.

## 1.2 OBJECTIVES

The research described in this thesis aimed at achieving a deep understanding of the soil deformation due to interaction of two neighbouring buildings. The study involved a small-scale model in the laboratory and finite element modelling. The mitigation of the interaction was studied by the insertion of a sheet pile wall between two model building foundations. To reach these goals the following research objectives were set:

1. To design reliable small-scale $1g$ experiments for simulating soil deformation due to the interaction of two neighbouring buildings constructed on soft ground.

2. To accurately determine soil deformation through non-intrusive measurement: Particle Image Velocimetry coupled with photogrammetry.

3. To obtain soil deformation patterns over fields of interest.

4. To select a relevant soil constitutive model to be used in finite element analyses.

5. To use the data resulting from the physical modelling, to validate the finite element analyses.

6. To extend and implement finite element analyses to field problems.

7. To determine whether a sheet pile wall inserted between two footings mitigates the effects of interaction.

## 1.3  THESIS STRUCTURE

This thesis comprises seven chapters. The following paragraphs outline the contents of each chapter, excluding Chapter 1.

**Chapter 2**  reviews the literature relevant to this research. It covers the physical and numerical modelling of two closely-spaced footings on sand and clay. The possible damage of buildings related to the deformation of the structures is addressed. The chapter continues by reviewing previous work on Particle Image Velocimetry and photogrammetry. The chapter ends with a review of finite element methods emphasising the soil constitutive model BRICK.

**Chapter 3**  describes the equipment used in the physical modelling, commencing with the design of a consolidation chamber, footings, and a sheet wall. Besides the measurement techniques, the performance and the accuracy of the measuring instruments are also discussed. All the procedures adopted in the testing programmes are elaborated.

**Chapter 4**  describes the implementation of Particle Image Velocimetry and its accuracy and precision specific to this research. The photogrammetry is also outlined, including the camera calibration, image–object space transformations, and refraction corrections.

**Chapter 5**  discusses the results from the physical modelling. It reports three types of test: plain double footings as a benchmark, double footings with a floating sheet wall between, and double footings with a vertically restrained sheet wall between.

**Chapter 6**  presents the results from the numerical modelling using the finite element method. The discussions are divided into two parts. The first part deals with the validation of this method using the outcomes obtained from the physical modelling. The second part discusses the implementation of the finite element method in simulating field conditions. Here the analyses are extended to include varying lengths and stiffnesses of sheet pile.

**Chapter 7**  summarises the important findings discussed in the previous chapters and proposes recommendations for future research.

# LITERATURE REVIEW

## 2.1 INTRODUCTION

In this chapter previous studies on the interaction of closely-spaced footings are reviewed. Although not all of these were designed to simulate the behaviour of whole buildings, as is the purpose of the present research, they can be considered representative if a scaling law is applied. Only very limited studies of this problem have been found in published literature, especially for footings on clay. The impact of the interaction, especially the damage to buildings is also reviewed. To simulate the prototype behaviour, such as the interaction of neighbouring buildings, in small-scale laboratory work, sufficient accuracy and precision in displacement measurement is required. As stated by White (2002) and Take (2003), the use of Particle Image Velocimetry (PIV) in their laboratory observations delivered high accuracy and precision.

The Finite Element Method used as the analysing tool in the present research, will not be explained in this chapter since it is widely described in many textbooks (e.g. Desai and Abel, 1972; Zienkiewicz, 1977; Britto and Gunn, 1987; Potts and Zdravković, 2001a). Explanations of the great variety of soil constitutive models can also be found in several established publications (Wood, 1990; Potts and Zdravković, 2001a; Wood, 2004) and are not duplicated here. However, it is necessary to discuss BRICK, the constitutive model introduced by Simpson (1992), since it is the one employed in this thesis.

## 2.2 RESEARCH ON CLOSELY-SPACED FOOTINGS

### 2.2.1 Closely-Spaced Footings on Sand

Attempts to investigate the behaviour of soil subjected to pressures from two closely-spaced foot-ings can be traced back to Stuart (1962), four decades ago. He carried out physical modelling in a laboratory, using pairs of model footings made of wood and polished steel. The footings of two different dimensions were tested in two different boxes filled with compacted fine dry sand. One pair were 13 inches long and 1 inch wide. These were tested on sand 8 inches deep in a box 20 inches long and 15 inches wide. The other pair were 9 inches long and $1/2$ inch wide, tested on sand 25 inches deep in a box 40 inches long and 30 inches wide. The loadings were applied simultaneously on a pair of footings, using a lever system and a hydraulic jack, and were measured with a proving ring. The soil movements were observed through a glass window in the front wall of each box. From one of the results shown in Figure 2.1 he postulated that interference would occur when two loaded footings were close enough so that Prandtl's failure mechanisms for the footings overlapped. Using Hill's mechanism (Hill, 1950) as a modification of the Prandtl mecha-
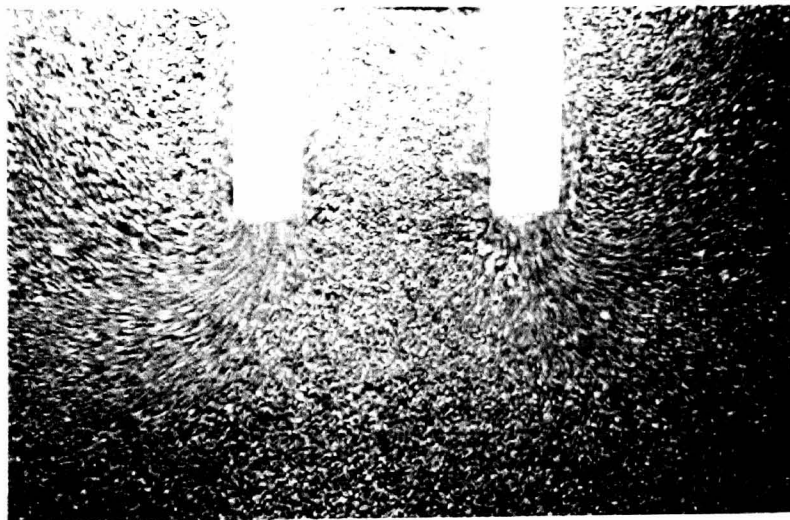


**Figure 2.1:** Pattern of sand movement during loading on two adjacent footings
(Stuart, 1962)

nism, Stuart arrived at a theoretical solution describing the effect of distance on the interference of two adjacent footings. This is presented in Figure 2.2. The footings act as isolated footings with no interference if the distance between them is large (see Figure 2.2.a). As the distance becomes very small as shown in Figure 2.2.d, the footings act as a single footing with combined width $2B$. He introduced interference into Terzaghi's bearing capacity equation (Terzaghi, 1943; Meyerhof,
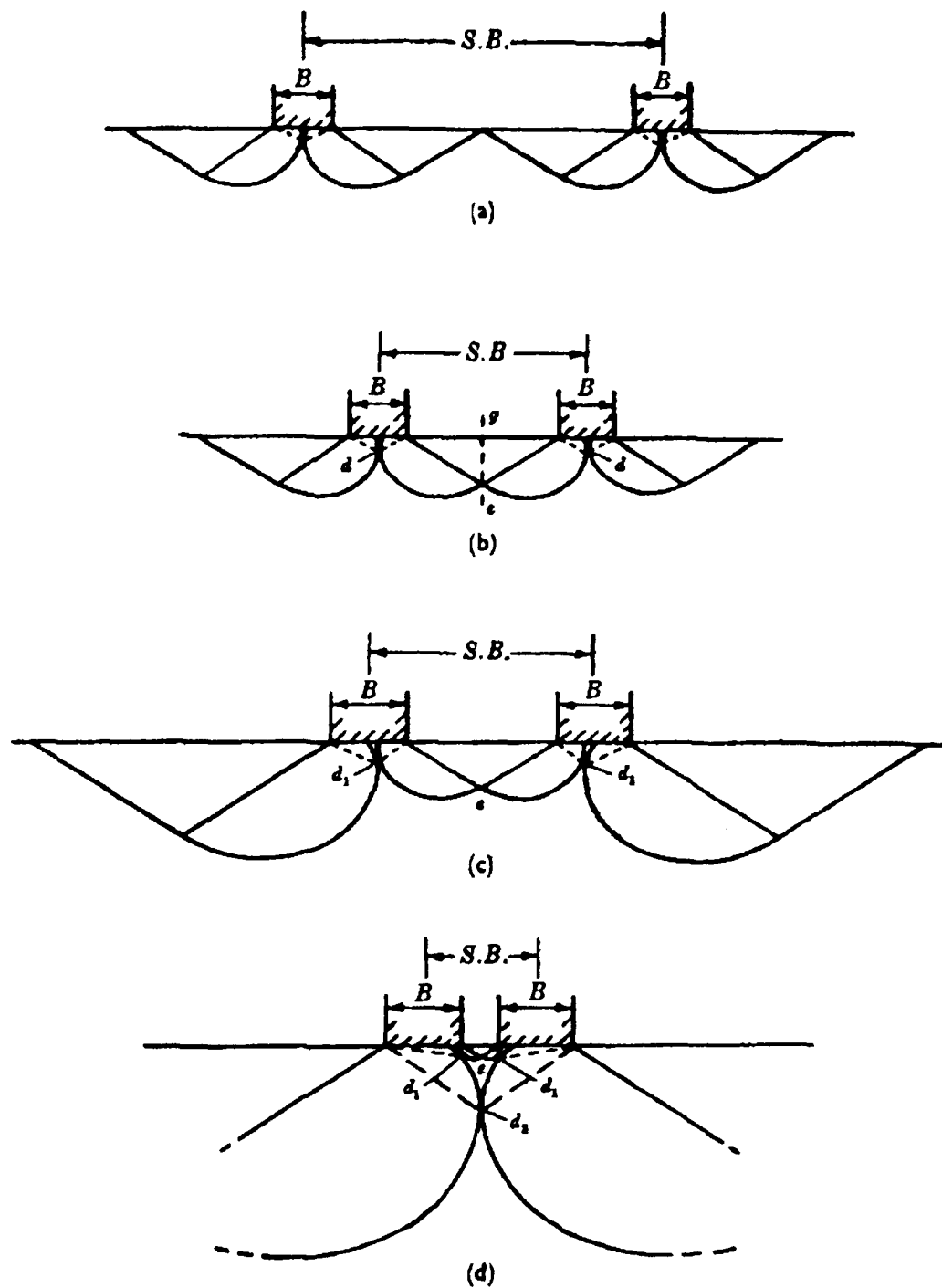
**Figure 2.2:** Failure pattern of two rough-based foundations on a cohesionless soil (Stuart, 1962)

1951; Vesić, 1973) to allow for the effect of interference on the ultimate bearing capacity $q_u$. The modified bearing capacity for an individual footing is shown in Equation 2.1,

$$q_u = q\xi_q N_q + \tfrac{1}{2}\gamma B \xi_\gamma N_\gamma \qquad (2.1)$$

where $\xi_\gamma$ and $\xi_q$ are ratios of the interfering to isolated values of the bearing capacity coefficients ($N_\gamma$ and $N_q$); $B$ is the footing width; $q$ is the surcharge pressure; and $\gamma$ is the unit weight of the soil. In the case of large spacings, the ratios $\xi_\gamma$ and $\xi_q$ would be equal to unity. The ratios increased with decreasing spacing which, in turn, increases the ultimate bearing capacity of the footings.

Das and Larbi-Cherif (1983a,b) also investigated the interference of two closely-spaced footings on sand. The arrangement of the model footings is shown in Figure 2.3. Both of the model foundations were fixed with two steel shafts that were connected by a steel bar. The loads and vertical displacements were measured using a proving ring and a dial gauge respectively.
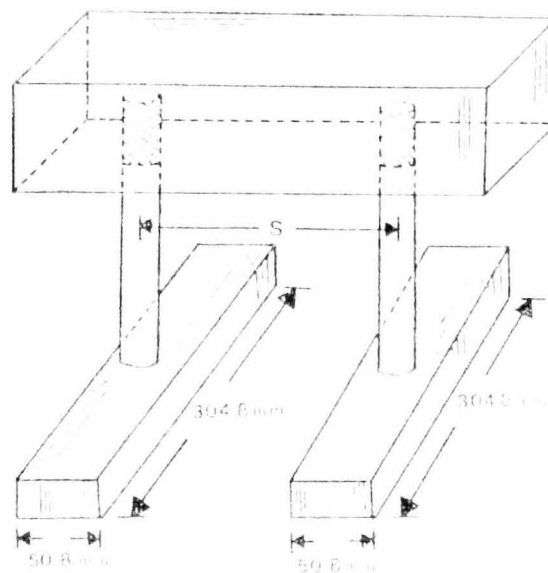


**Figure 2.3:** Two closely-spaced footings model (Das and Larbi-Cherif, 1983b)

Das and Larbi-Cherif (1983a) considered that the failure mechanism observed in their tests followed the local shear mode as defined by Vesić (1973). According to Vesić, there were three principal modes of shear failure under foundations, i.e., general shear failure, local shear failure, and punching shear failure. General shear failure could be identified from an obvious slip of the ground beneath and around a foundation. This was usually followed by significant settlement and tilting of the foundation. If the foundation was loaded in strain-controlled conditions, the failure would be indicated by a decrease of load while the foundation experienced continuous, excessive settlement (see Figure 2.4.a). Punching shear failure was defined for failure in which the slip pattern was unclear. Only the area directly beneath the foundation seemed to be affected under continued loading (Figure 2.4.c). A failure was called local shear failure when the slip beneath

a foundation was clearly defined (see Figure 2.4.b). The slip surface would appear at the ground only if the foundation experienced significant settlement of up to 50% of the foundation width.

Das and Larbi-Cherif (1983a) concluded that the general trend of the interference ratios $\xi_\gamma$ and $\xi_q$ were consistent with those postulated by Stuart (1962). In magnitude, however, the ratios were considerably lower. They also found that the settlement of the foundation generally decreased with increasing distance between the two foundations. This finding is illustrated in Figure 2.5 in which $S_e$, $S$, $B$, and $D_f$ are respectively the settlement, spacing, width, and embedment depth of the foundation. The settlements were constant after the spacing ratios $S/B$ were larger than 4.5. In a
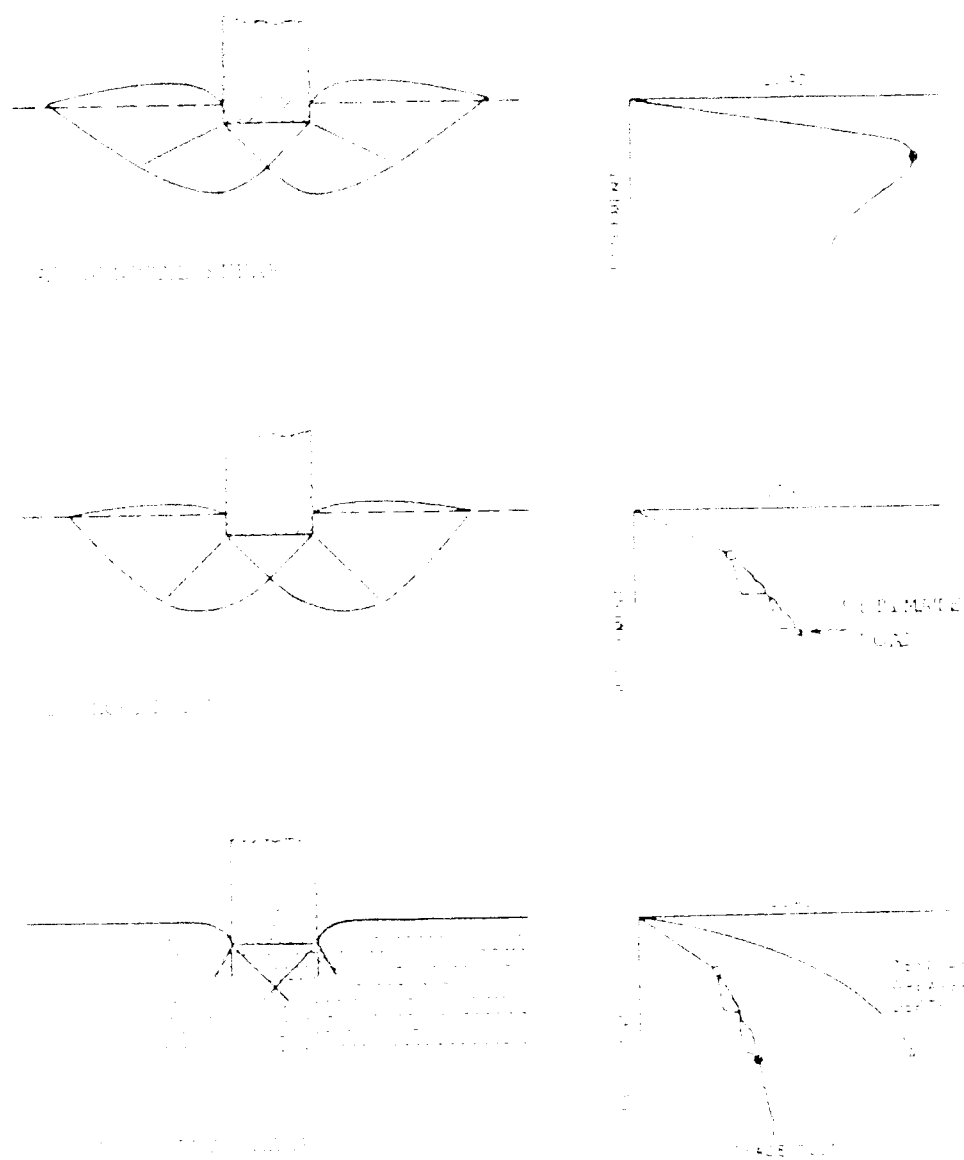


**Figure 2.4:** Modes of shear failure (Vesić, 1973)
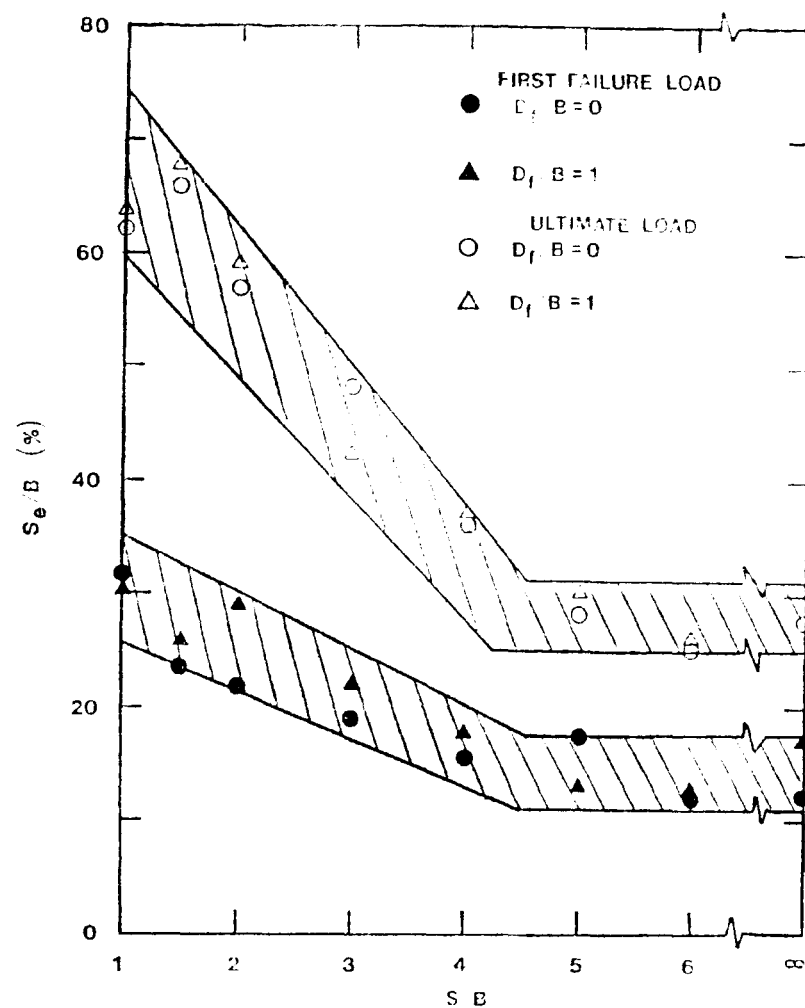
**Figure 2.5:** Effect of distance on settlement of two closely-spaced footings (Das and Larbi-Cherif, 1983b)

glass-sided chamber 900 mm wide and 300 mm deep, Graham et al. (1984) investigated the bearing capacity of three closely-spaced footings on three types of sand, simulating grillage foundations. The footing width $B$ and the distance between the centrelines of the footings ($S$) were varied. The two outer footings were rigidly connected and loaded independently of the central footing. A term $\lambda$ was then introduced as the ratio of loads on the outer footings to that on the central footing. In order to examine the effect of the roughness of the footing bases, steel and aluminium with different roughness were used. They found that the roughness had little effect on the bearing capacity (Figure 2.6(a)) and the interaction of the footings. As in previously mentioned work (Stuart, 1962; Das and Larbi-Cherif, 1983b), the bearing capacity of the footings increased with decreasing spacing. Graham et al. (1984) observed the interaction by performing tests on 38 mm wide footings. As shown in Figure 2.6(b), the interaction among the three footings provides a much stiffer soil response compared to that in the tests using a single footing. The pre-failure settlement
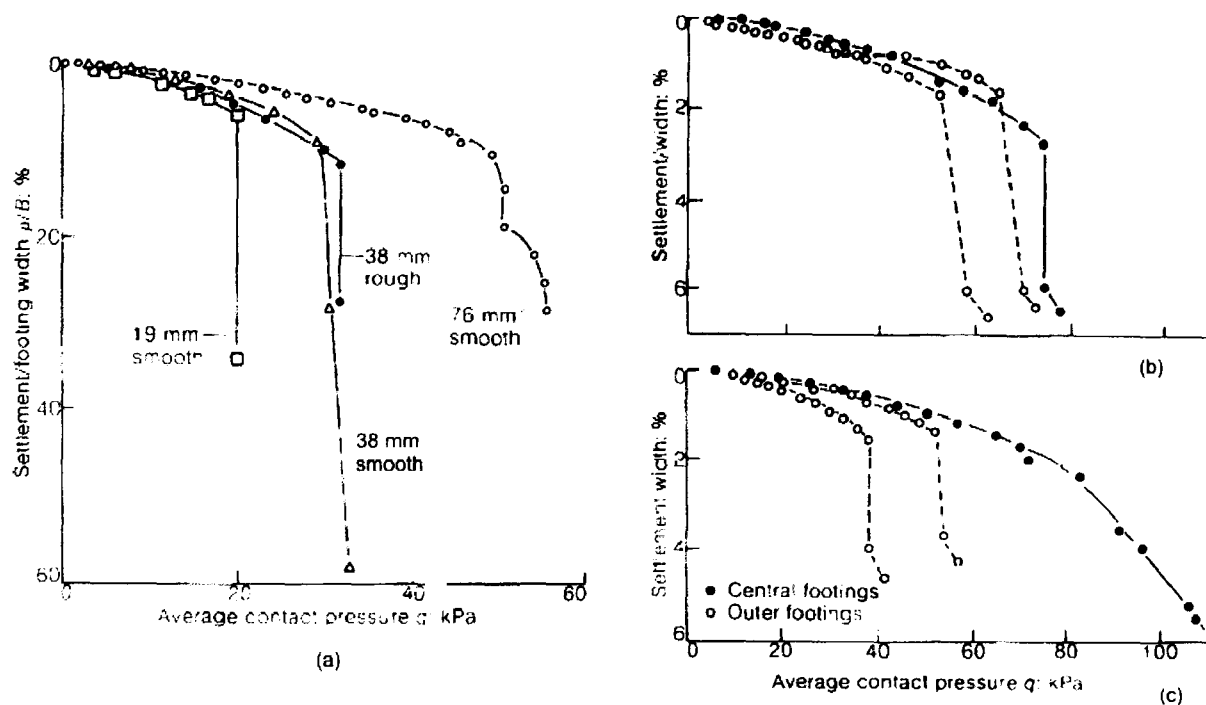
**Figure 2.6:** Load–settlement curves of tests on smooth footings: (a) Single footing, (b) $\lambda = 100\%$ ($S/B = 1.7$), and (c) $\lambda = 50\%$ ($S/B = 1.7$) (Graham et al., 1984)

of the footings loaded with the same magnitude ($\lambda = 100\%$ ) was only about 10% of that of the single footing. The settlement of the central footing was further decreased (Figure 2.6(c)) once the load applied on the outer footings was only half of that on the central footing ($\lambda = 50\%$ ).

### 2.2.2 Closely-Spaced Footings on Clay

The previously mentioned studies involved sands which are cohesionless. Recently several attempts have been made to investigate the behaviour of neighbouring foundations resting on cohesive soils. For instance, Jao et al. (2002) used the finite element method to study plastic yielding of clayey soil underlying two closely-spaced strip footings as well as the settlement and tilting of the footings. In this numerical modelling, the soil was modelled to represent compacted kaolin and the footings were assumed to be made of reinforced concrete. The soil was modelled as a nonlinear elastic perfectly plastic material and the footings were of a linear elastic material. The elastic portion of the soil behaviour was modelled with the hyperbolic stress-strain law. The plastic behaviour of the soil was simulated using the Drucker-Prager yield criterion.

With various spacings, the footings were incrementally loaded. The footings were located either on the ground surface or embedded at a depth $D_f$ equal to the footing width $B$. Figure 2.7

shows the relationship between the spacing $\Delta$ normalised by the width of the footing $B$ and the

settlement ratio $S_i/S_o$. The spacing $\Delta$ was measured from centre to centre of the footings. $S_i$
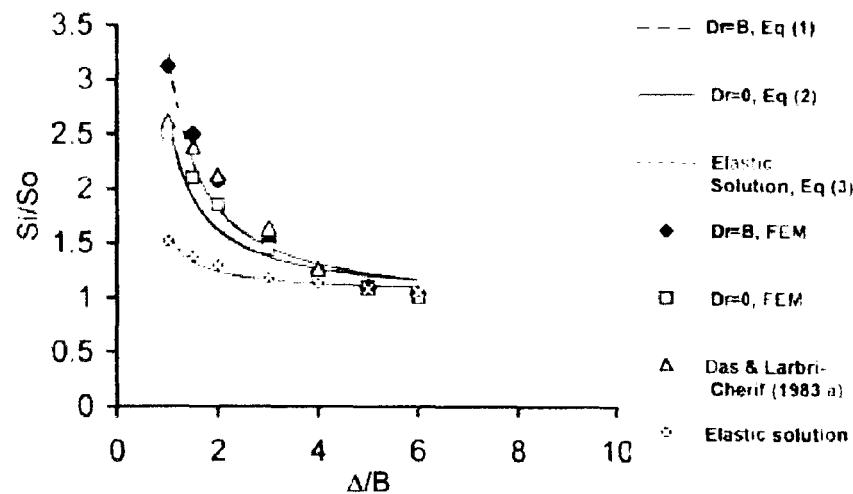


Eq(1): $S_i/S_o = 1.390e^{B/\Delta} - 0.471$

Eq(2): $S_i/S_o = 0.972e^{B/\Delta} - 0.022$

Eq(3): $S_i/S_o = 0.296e^{B/\Delta} + 0.756$

**Figure 2.7:** Effect of spacing on footing settlement (Jao et al., 2002)

is the settlement due to interference while $S_o$ is the settlement of a single footing. The results were compared with those obtained from an elastic solution for the surface footing. In general, the settlements decreased with increasing spacing. The effect of the interference became insignificant when the spacing reached six times the footing width. The embedment did not seem to have a substantial influence. These results were in good agreement with those observed by Das and Larbi-Cherif (1983b) for the two closely-space footings on sand. However, the results from the elastic solution fell below the others.

The plastic yielding at the footing spacing $\Delta/B = 4$ is shown in Figure 2.8. It was symmetrical to the centre of the two footings but asymmetrical relative to each footing. The plastic yielding was more extensive beneath the outer sides of the footings. This resulted in an inward tilting of the footings as illustrated in Figure 2.9. The tilting, represented with rotation angle $\theta$, increased with increasing footing pressure. The tilting was larger when the footing spacing was decreased, Figure 2.10.

Similar to Jao et al. (2002), Maharaj et al. (2004) used nonlinear finite element analysis (Maharaj, 2003) to study the interaction between two adjacent strip shell footings. The soil was as-
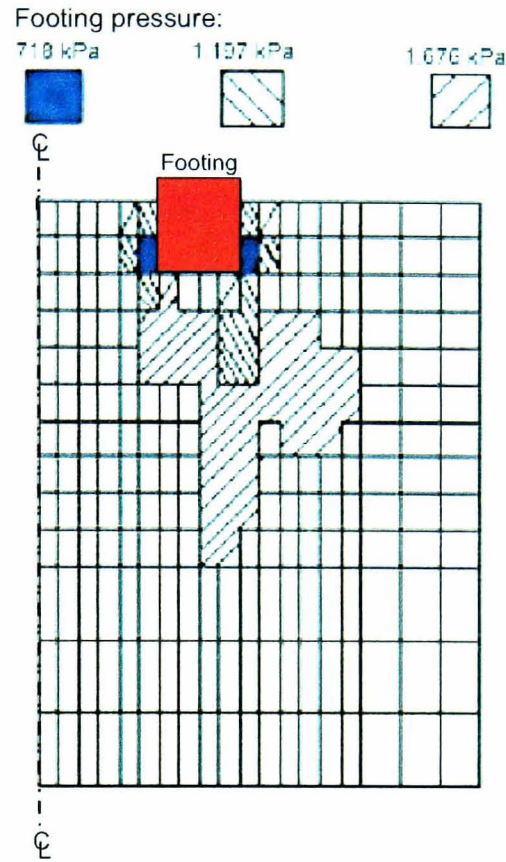
**Figure 2.8:** Plastic yielding zones under different pressures of a pair of footings (after Jao et al., 2002)
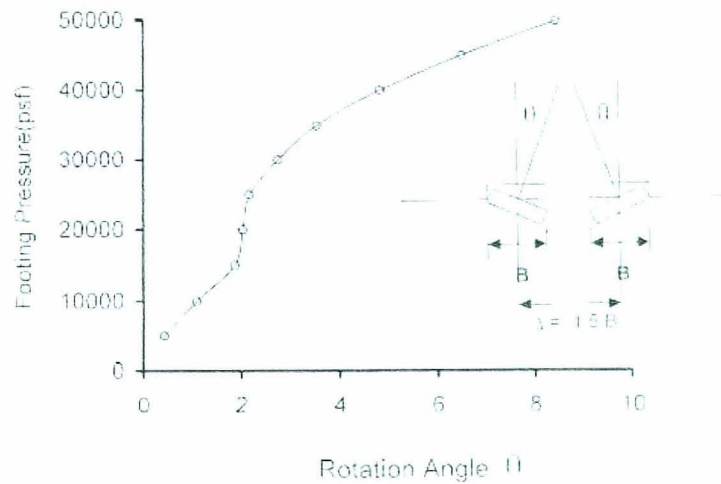


**Figure 2.9:** Effect of footing pressures on tilting (Jao et al., 2002)

sumed to be an elastoplastic material, following a constitutive model with a Drucker-Prager yield criterion. The shell was a linear elastic material representing concrete. The analysis included the effect of various soil moduli on load–settlement characteristics. The discretisation of the problem is shown in Figure 2.11. Both the soil and the shell foundation were discretised into four-noded
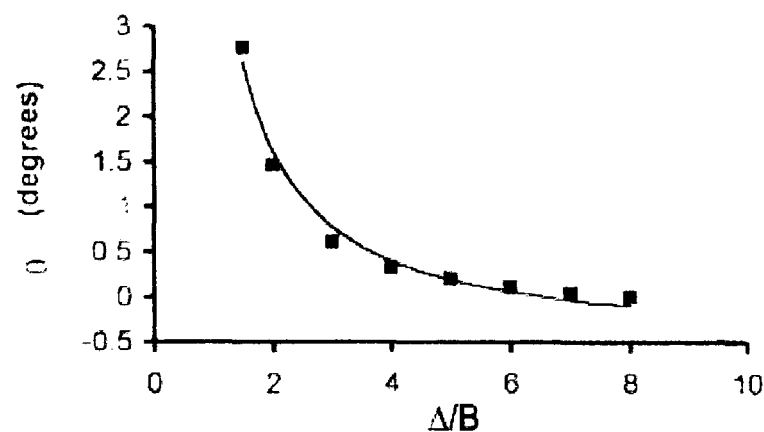
**Figure 2.10:** Effect of spacing on footing tilting (Jao et al., 2002)
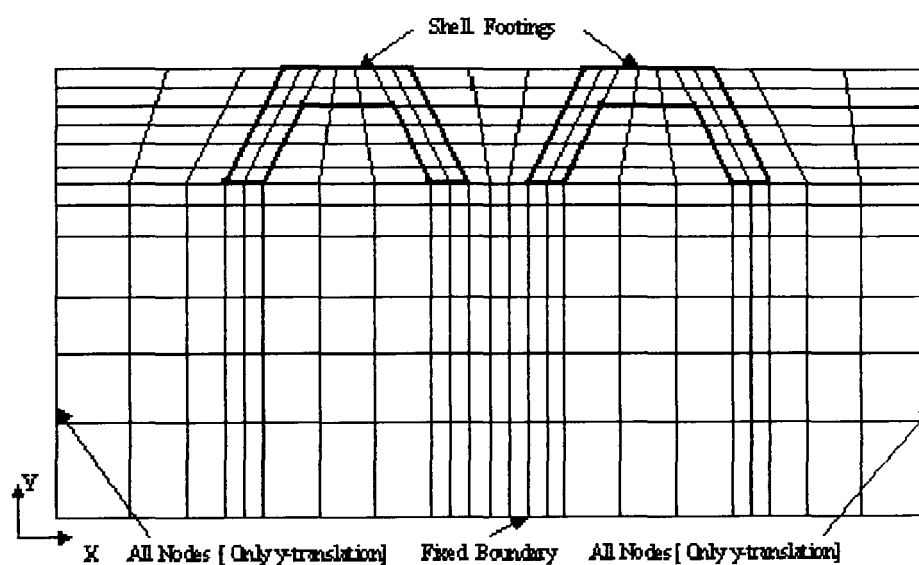


**Figure 2.11:** Finite element mesh (Maharaj et al., 2004)

isoparametric elements. The soil domain from the centre of either foundation to the nearest side boundary was 10 m and the soil depth was 20 m. The bottom boundary was modelled as fixed, while side boundaries were only permitted to move vertically.

Six analyses were carried out whereby a single footing, a double footing at 0.10 m spacing, and a double footing with 1.0 m spacing were loaded on soil with different moduli of $E_s = 32$ MPa and $E_s = 76$ MPa. The results are plotted in Figure 2.12. It was obvious that soil modulus had a major effect on the settlements in all cases. The settlements were reduced in proportion to the increase of the soil modulus. With either soil modulus, a decrease in spacing resulted in a larger settlement. Greater interference was observed from the overlap of the pressure bulb induced by each footing
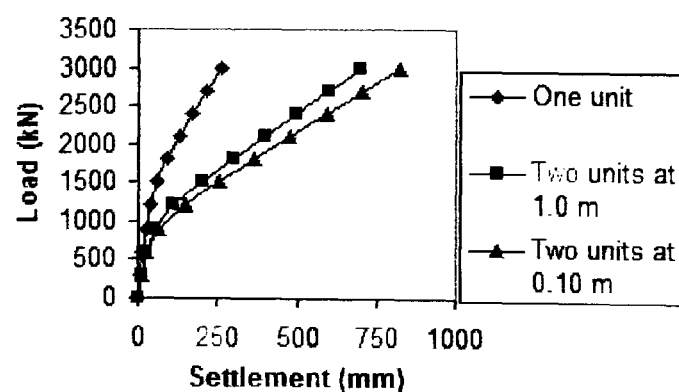
(a) $E_s = 32$ MPa
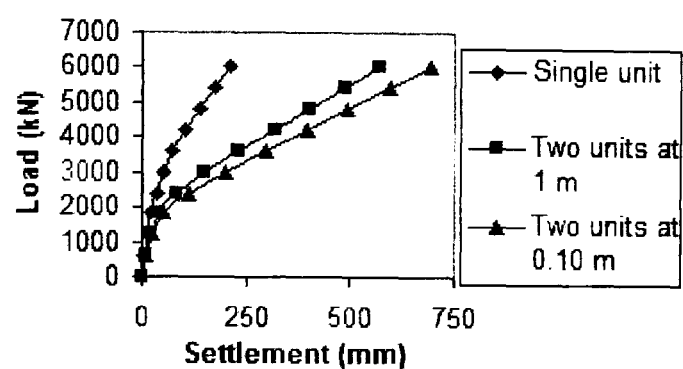


(b) $E_s = 76$ MPa

**Figure 2.12:** Effect of various elastic modulus of soil $E_s$ and footing spacing (Maharaj et al., 2004)

as it was subjected to higher loading. This could be also interpreted from the overlap of the curves at lower load, suggesting that in this range of loading the interference was insignificant.

## 2.3 SETTLEMENT AND BUILDING DAMAGE

As discussed in the previous section, one of the impacts of the interaction of closely-spaced foundations was tilting. The same phenomenon would be expected to apply to neighbouring buildings. In this case, interaction produces an asymmetrical stress distribution beneath each building. This gives rise to differential settlement and tilting that can cause damage. In order to define criteria of how settlement could damage buildings, Skempton and MacDonald (1956) conducted a survey of 98 buildings that were mostly constructed with load-bearing walls. They found the walls were cracked when angular distortion exceeded 1/300. The angular distortion was defined as the ratio of the differential settlement $\delta$ and the horizontal distance $l$ between two points (see Fig-

ure 2.13). Damage of frames, formed from beams and stanchions, was encountered when $\delta/l$
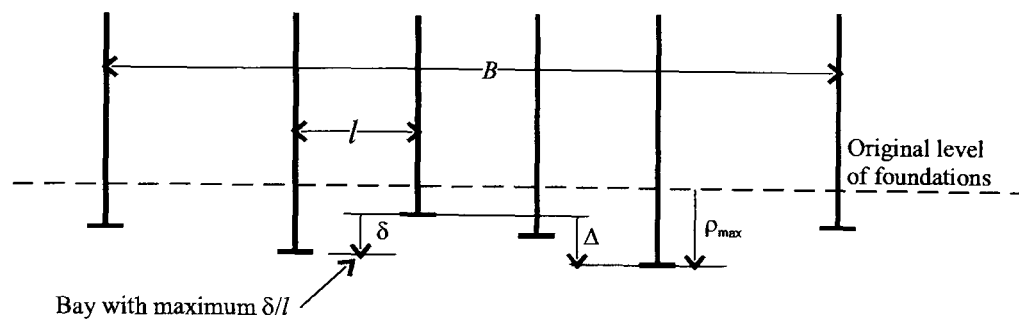


**Figure 2.13:** Definition angular distortion $\delta/l$, maximum settlement $\rho_{max}$, and greatest differential settlement $\Delta$ (after Skempton and MacDonald, 1956)

exceeded 1/150. To prevent a building from damage Skempton and MacDonald (1956) suggested that $\delta/l$ less than 1/500 should be achieved, preferably 1/1000. From data of more than 100 sites, collected over 25 years, Polshin and Tokar (1957) observed similar values which were $\delta/l \sim 1/150$ and $\delta/l \sim 1/500$ respectively for structural damage and cracking in walls of framed buildings and reinforced load bearing walls.

A similar investigation was carried out by Grant et al. (1974). The data of Skempton and MacDonald (1956) were enriched with additional data surveyed from 95 buildings. They used the maximum net slope $\delta/l$ of the deflection curve, as shown in Figure 2.14, to determine the damage criteria. The buildings were found to suffer from damage when the maximum deflection $(\delta/l)_{max}$ exceeded 1/300.

Burland and Wroth (1974) and Burland et al. (2001) used a criterion of critical tensile strain $\varepsilon_{crit}$ for building damage assessment, as also suggested by Polshin and Tokar (1957). They postulated that cracking appeared once the critical tensile strain was reached. To formulate the criteria of initial cracking from the tensile strain, a building was assumed to be a simple beam as depicted in Figure 2.15(a) where $L$ and $H$ are the length and the height of the beam. The maximum deformation of the beam soffit is denoted by $\Delta$, i.e. the maximum displacement relative to the straight line between two points separated by a distance $L$. Later, Burland and Wroth (1974) defined $\Delta/L$ as the deflection ratio. The deformation of the beam comprised two modes, bending and shearing. The bending deformation shown in Figure 2.15, with upward concavity, is termed "sagging". The term "hogging" is used when the deformation forms downward concavity. Cracking in the bending mode occurs when tensile strain is developed (below and above the neutral axis for sagging and
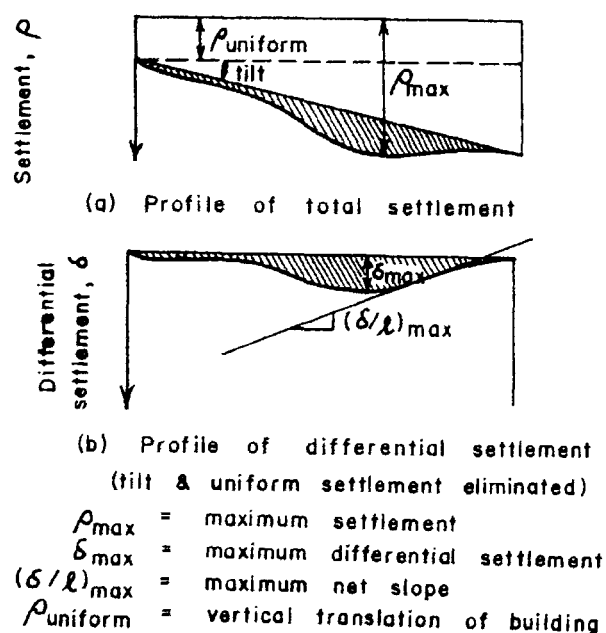
**Figure 2.14:** Terms used by Grant et al. (1974) for building damage criteria

hogging respectively), while in the shearing mode, cracking is ascribed to diagonal tensile strain. In practice both deformation modes occur simultaneously, although the type of building structure governs which mode dominates.

Setting the criteria for the cracking, Burland and Wroth (1974) also involved the influence of the ratio $E/G$, where the moduli of elasticity, $E$ and $G$, represent the longitudinal and shear stiffness of a beam. Buildings with frames or reinforced load-bearing walls are very good at restraining tensile bending strain but are relatively low in shear stiffness. Thus, the limiting factor for cracking is diagonal tensile strain. Due to their insignificant resistance to direct tensile strain, the limiting factor for traditional brick or masonry buildings mostly depends on the bending. Cracking can take place at a very low value of $\Delta/L$.

In practice the deformation of a building can be highly restrained by its foundation, such as a reinforced concrete raft. In this case, tensile strains might be caused only by hogging. In general, the limiting values of $\Delta/L$ depend on $L/H$ as well as $\beta$ (defined as $\delta/l$ by Skempton and MacDonald (1956)). In the estimation of the limiting values of $\Delta/L$, Burland and Wroth (1974) used a moderate value of 0.075% for critical tensile strain $\varepsilon_{crit}$, averaged from those ranging from 0.05% to 0.10% found by Mainstone and Weeks (1970) and Mainstone (1971). Guidelines, as summarised by Tomlinson (2001), are given in Table 2.1 for the limiting values of angular distor-

tion $\delta/l$ and in Table 2.2 for deflection ratio $\Delta/L$. In the tables, recommendations of Meyerhof (1956) are included.

Actual Building

L

H

Beam: simple idealisation of building

Δ

Deflected shape of soffit of beam

(a)

Bending deformation with cracking due to direct tensile strain

(b)

Shear deformation with cracking due to diagonal tensile strain

(c)
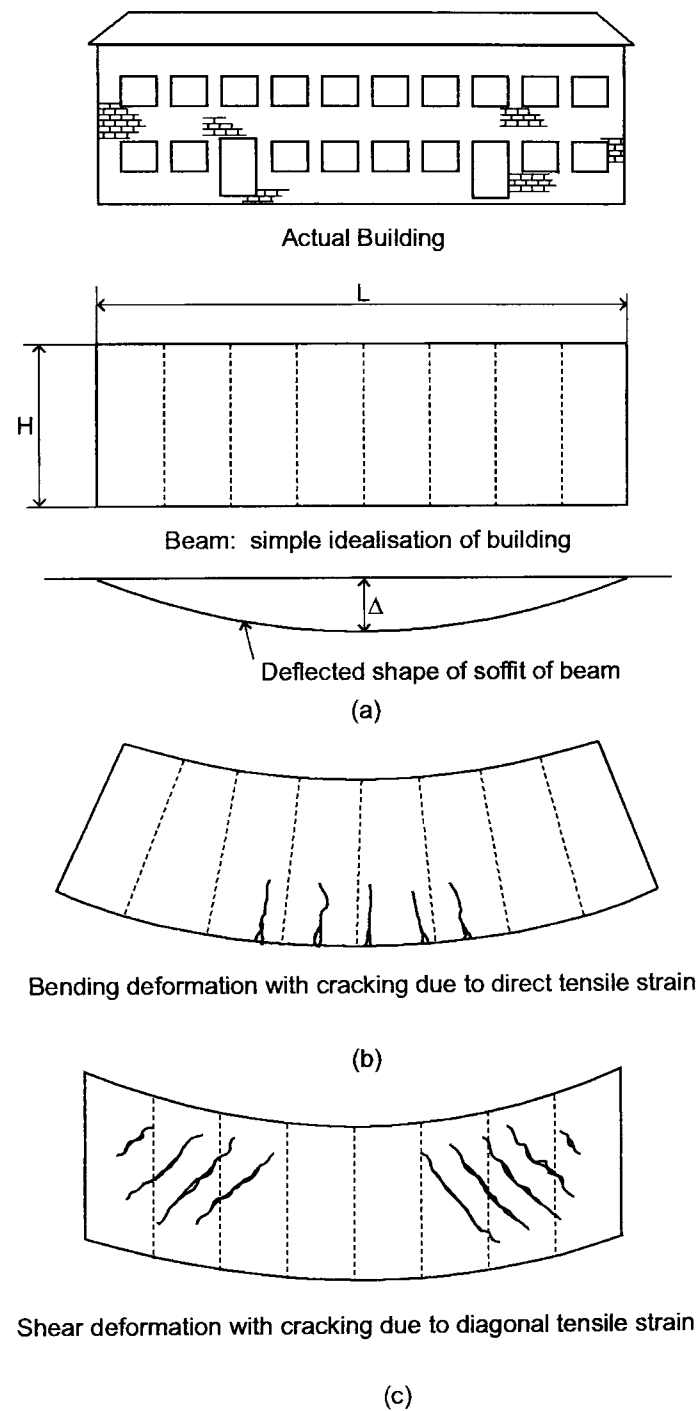
**Figure 2.15:** Cracking due to bending and shear deformation of an idealised simple beam (after Burland and Wroth, 1974)

**Table 2.1:** Criteria for limiting values of angular distortion $\delta/l$ (after Tomlinson, 2001)

| *Type of damage* | *Limiting values for relative rotation (angular distortion)* | |
| --- | --- | --- |
| | *Skempton and MacDonald (1956)* | *Meyerhof (1956)* |
| Structural damage | 1/150 | 1/250 |
| Cracking in walls and partitions | 1/300 (but 1/500 recommended) | 1/500 |

*Note*: The limiting values for framed buildings are for structural members of average dimensions. Values may be much less for exceptionally large and stiff beams or columns for which the limiting values of relative rotation should be obtained from structural analysis.

**Table 2.2:** Criteria for limiting values of deflection ratio $\Delta/L$ (after Tomlinson, 2001)

| *Type of damage* | *Limiting values of deflection ratio ($\Delta$/L)* | |
| --- | --- | --- |
| | *Meyerhof (1956)* | *Burland and Worth (1974)* |
| Cracking by sagging | $0.4 \times 10^{-3}$ | At $L/H = 1$: $0.4 \times 10^{-3}$<br>At $L/H = 5$: $0.8 \times 10^{-3}$ |
| Cracking by hogging | – | At $L/H = 1$: $0.2 \times 10^{-3}$<br>At $L/H = 5$: $0.4 \times 10^{-3}$ |

## 2.4 PHYSICAL MODELLING

### 2.4.1 Scaling Laws

In laboratory observations small-scale models are often used to represent their prototypes. A model is considered representative of its prototype if it is geometrically, kinematically, and dynamically similar. For this purpose, Wood (2004) listed the scaling laws necessary for a model to have similitude, as shown in Table 2.3 where $n$ is the geometry scale factor. The parameter $\alpha$ depends on material type; typically $\alpha = 0.5$ for sand and $\alpha = 1$ for clay.

In homogenous ground, the soil strength and stiffness increase with depth. The strength or stiffness profile of a prototype in a "conventional" $1g$ test of a small-scale model cannot be correctly simulated since the strength and stiffness are stress dependent. In downscaling the ground thickness

**Table 2.3:** Scale factors (Wood, 2004)

| Quantity | Scale factors | | |
|---|---|---|---|
| | **General** | **$1g$** (laboratory) | **$ng$** (centrifuge) |
| length | $n_l$ | $1/n$ | $1/n$ |
| mass density | $n_\rho$ | 1 | 1 |
| acceleration | $n_g$ | 1 | $n$ |
| stiffness | $n_G$ | $1/n^\alpha$ | 1 |
| stress | $n_p n_g n_l$ | $1/n$ | 1 |
| force | $n_p n_g n_l^3$ | $1/n^3$ | $1/n^2$ |
| force/unit length | $n_p n_g n_l^2$ | $1/n^2$ | $1/n$ |
| strain | $n_p n_g n_l / n_G$ | $1/n^{1-\alpha}$ | 1 |
| displacement | $n_p n_g n_l^2 / n_G$ | $1/n^{2-\alpha}$ | $1/n$ |
| time (diffusion) | $n_\mu n_l^2 / n_G$ | $1/n^{2-\alpha}$ | $1/n^2$ |
| time (creep) | 1 | 1 | 1 |
| time (dynamic) | $n_l (n_\rho / n_G)^{1/2}$ | $1/n^{2-\alpha/2}$ | $1/n$ |

by a factor of $n$ in a model, the vertical stresses at corresponding points are also scaled down by $n$. The prototype stress at any depth in the ground can be achieved in a centrifuge model by adjusting the acceleration of the machine to $ng$. However, the undrained strength profile of a prototype is still possible to approach in $1g$ laboratory tests on clay. This is usually achieved by preconsolidation of the model soil. The undrained strength $s_u$ is also dependent on the overconsolidation ratio OCR, as shown in Equation 2.2 (Springman, 2004),

$$\frac{s_u}{\sigma_v'} = a.\text{OCR}^b \tag{2.2}$$

where the coefficients $a$ and $b$ from different researchers are listed in Table 2.4. However, while the

**Table 2.4:** The coefficients $a$ and $b$ for Equation 2.2 from different researchers (after Springman, 2004)

| Researcher | a | b |
|---|---|---|
| Phillips and Valsangkar (1987) | 0.19 | 0.67 |
| Nunez (1989) | 0.22 | 0.62 |
| Springman (1989) | 0.22 | 0.71 |

typical shape of the OCR and the undrained strength profiles with depth can be very well simulated in a centrifuge model (see Figure 2.16), in a $1g$ model the profile is almost constant with depth.
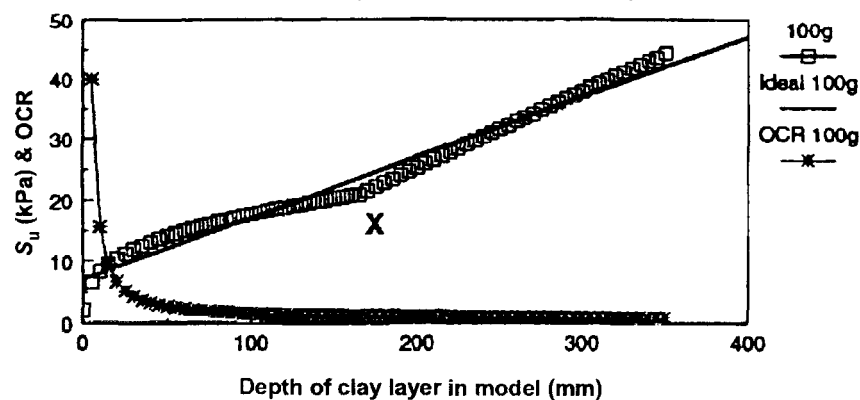
**Figure 2.16:** Profiles of undrained strength $s_{u\text{-vane}}$ and OCR with depth from centrifuge modelling at $100g$ (after Springman, 2004)

## 2.4.2 Displacement Measurement: Particle Image Velocimetry

Particle Image Velocimetry, or PIV, was pioneered by Adrian (1991). This particle-imaging technique was developed to determine the velocity of a fluid flow seeded with small particles. The particles were illuminated with a sheet of light and images captured by a photographic camera with double flash or a video recorder with its optical axis perpendicular to the sheet. The velocity was derived from the mean displacement over the time during which a pair of images was captured. Discussions of PIV analysis, including enhancements, can be found in many publications (e.g. Willert and Gharib, 1991; Grant and Wang, 1995; Westerweel, 1997; Westerweel et al., 1997; Hart, 2000; Okamoto et al., 2000; Forliti et al., 2000). Besides its original purpose of application, the technique has been extended to a variety of industrial applications (Santiago et al., 1998; Hill et al., 2000; Wernet, 2000; Elavarasan et al., 2000; Lecuona et al., 2004; Tonddast-Navaei and Sharp, 2005).

PIV has also gained popularity in geotechnical engineering. It was used under a different name, the block-matching method, by Guler et al. (1999). White (2002) implemented PIV to make observations of the behaviour of soil displacements during pile installation. He also developed the GeoPIV software (White and Take, 2002) for use in geotechnical engineering. His PIV-related contributions are described in, for example, White et al. (2003) and White and Bolton (2004). Take (2003) deployed PIV to study the characteristics of clay slope subject to seasonal moisture cycles. Another PIV application to geotechnical engineering was established by Iskander et al. (2002) who

observed deformations of transparent soil due to loading on square and circular footings. Liu and Iskander (2004) used the term digital image correlation (DIC) instead of PIV.

The following paragraphs will briefly explain the PIV method suggested by White (2002) (see also White et al., 2003), since it is the most relevant to the research in this thesis. While PIV was mostly applied by White to sand with natural texture, he also obtained a good result from textured clay.

The method of image interrogation was based on the equation of the cross-correlation estimator $R(\mathbf{s})$ (see Keane and Adrian, 1990, 1992), expressed in Equation 2.3.

$$R(\mathbf{s}) = \sum_{\mathbf{U}} I_{\text{test}}(\mathbf{U}) \cdot I_{\text{search}}(\mathbf{U+s}) \qquad (2.3)$$

Figure 2.17 shows a pair of digital images captured at different times between which some displacement occurs. One or several patches can be located in the first image, depending on the
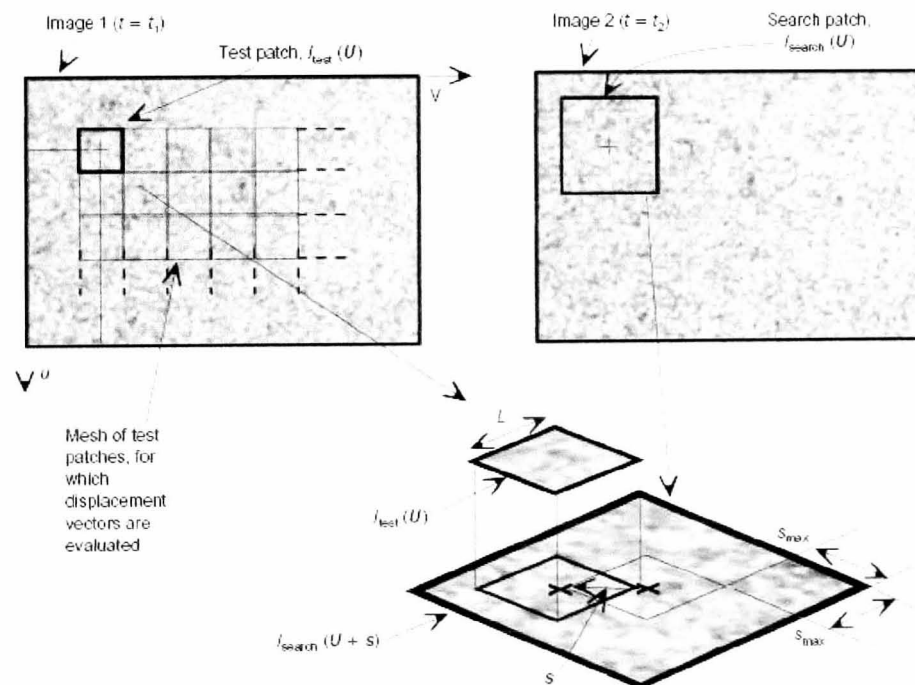


**Figure 2.17:** Image interrogations in a PIV analysis (White et al., 2003)

location $\mathbf{U}(u-v)$, where the displacements are to be examined. Each individual patch of the image contains its own matrix of brightness intensity $I$. This test patch intensity $I_{\text{test}}(\mathbf{U})$ is compared with the intensity of an area of the search patch $I_{\text{search}}(\mathbf{U+s})$ in the second image. The variable $\mathbf{s}$ here represents the distance of the the test patch centre from its initial position.

However, White (2002) thought that Equation 2.3 could not guarantee to identify the location of the best match when dealing with illumination variation over the patch and the size discrepancy between the test patch $I_{test}$ in Image 1 and the search patch $I_{search}$ in Image 2. He accordingly enhanced the equation by normalising the estimator $R(s)$. The normalised estimator $R_n(s)$ is expressed in Equation 2.4,

$$R_n(s) = \frac{R(s)}{\sum_U [I_{search}(U+s) \cdot I_{search}(U+s)] M(U)} \tag{2.4}$$

where $M(U)$ is a mask test patch of uniform intensity.

The displacement vector $s_{peak}$ resulting from the above convolution is indicated by the projection of the highest peak of the correlation in the $s_u$-$s_v$ plane (see Figure 2.18). The correlation is determined with a discrete interval, i.e. a single pixel. A spatial coordinate can be established using a bicubic interpolation over the values around the peak. A typical smoothed surface is shown in Figure 2.18.c. A higher resolution could be attained by using smaller interval. However White et al. (2003) indicated that increasing the resolution to a sub-pixel level of less than 0.005 pixel was not necessary.

The displacements obtained from a PIV analysis are still in an image space and are usually stated in units of pixels. Conversion to "real" units, i.e. object scale, was accomplished by White (2002) through a transformation from image coordinates to object space, following the procedures suggested by Abdel-Aziz and Karara (1971) and Heikkilä and Silvén (1997) (see also Heikkilä, 2000b; White et al., 2003). Using a Matlab tool provided by Heikkilä (2000a), the internal and external camera parameters could be identified. The internal camera parameters included the imperfection of the lens (radial and tangential distortion (Slama, 1980)), focal length, and aspect ratio of the CCD (charge-couple device) pixel. The external parameters consisted of the rotation and the translation of the camera. The latter parameters can be explained by considering a pure perspective projection with the pinhole camera model shown in Figure 2.19. In this camera, the object points are projected to an image plane through a "perfect lens" at a common origin $O$ in the camera frame. The camera rotation with respect to $x$, $y$, and $z$ axes is respectively described with Eulerian angles $\omega$, $\varphi$, and $\kappa$. The translation is defined as the spatial position discrepancies between the object ($X$-$Y$-$Z$) and the camera ($x$-$y$-$z$) frames. The determination of both internal and external parameters is known as the camera calibration. In the calibration some points in the object space
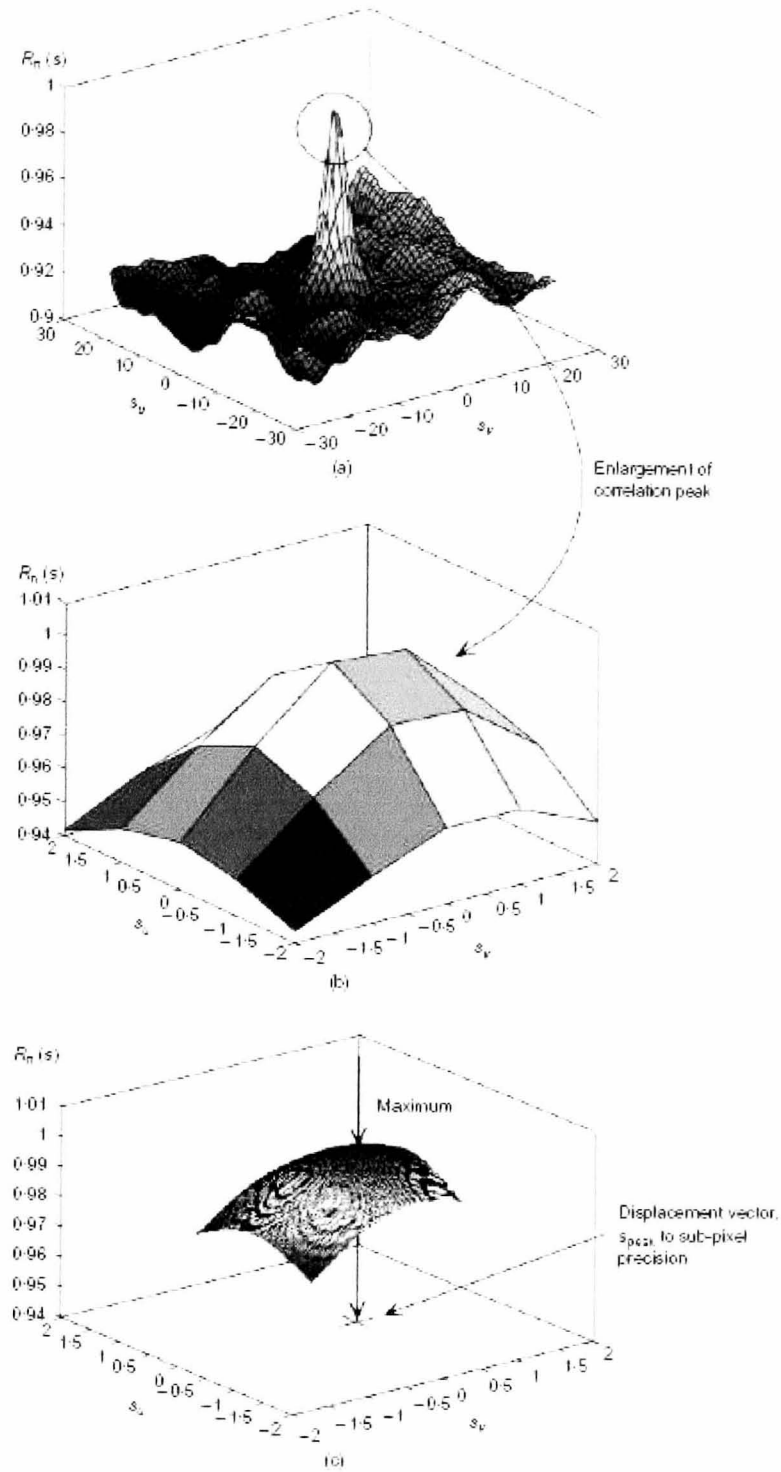
**Figure 2.18:** (a,b) Cross-correlation surface showing peak of the best match image interrogation (c) Surface of the peak smoothed with bicubic interpolation (White et al., 2003)

are usually distributed over an areas of interest and their coordinates should be first known. For this purpose, White (2002) and Take (2003) used some target markers on the Perspex window in the front of their models. The coordinates of the markers in image space were determined by using
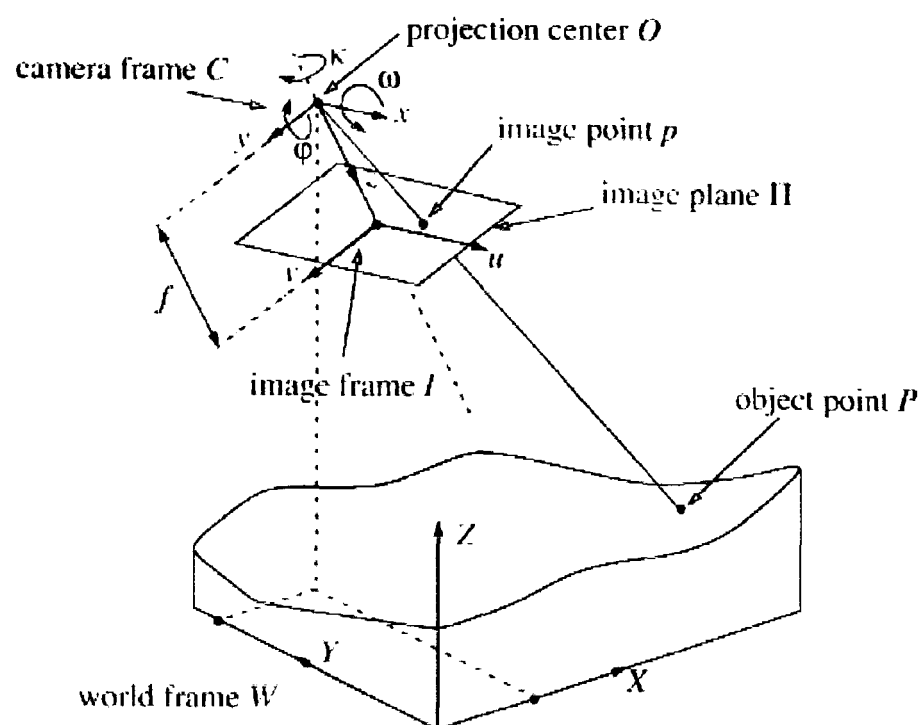
**Figure 2.19:** Pinhole camera model, after (Heikkilä, 2000b)

multiple-threshold centroiding. Since the observed object existed behind a Perspex window, White et al. (2003) then incorporated the effect of refraction into the transformation.

Compared with various other methods of displacement measurement, such as X-ray techniques and video photography, the PIV method used by White (2002) is superior. White (2002) found the precision of his PIV analysis using patches of $50 \times 50$ pixels over an area of interest and $25 \times 25$ pixels for control points was 4.6 $\mu$m. Using an X-ray technique, (Andrawes and Butterfield, 1973) found that the precision in their measurements was 5 $\mu$m. The same technique was implemented by Potts (1976) and Mair (1979). The quoted precision ranged from about 85 $\mu$m to 100 $\mu$m. From images captured on video tape, Taylor et al. (1998) observed the precision of their centroiding-based measurement in tracking the movement of target markers was 60 $\mu$m. By manually digitising video images, Saada et al. (1999) found a precision of 130 $\mu$m. Other researchers implementing the video capture method, e.g. Allersma et al. (1994) and Obaidat and Attom (1996) reported that their measurement resolutions were approximately 200 $\mu$m.

## 2.5 NUMERICAL MODELLING

In order to solve geotechnical analysis problems, a complete theoretical solution should fulfil four conditions, i.e. equilibrium, compatibility, material constitutive behaviour, and boundary conditions. At least one of these requirements cannot be satisfied, limit equilibrium, stress field, or limit analysis solutions (Potts, 2003; Potts and Zdravković, 2001a). As shown in Table 2.5, only closed form and full numerical analyses, such as finite difference or finite element methods, meet these four conditions. Closed form solutions are restricted to linear elastic soils.

**Table 2.5:** Capability of various methods of analysis in satisfying basic solution requirements (Potts, 2003)

| Method of analysis | | Solution requirements | | | Boundary conditions | |
|---|---|---|---|---|---|---|
| | | Equilibrium | Compatibility | Constitutive behaviour | Force | Displacement |
| Closed form | | S* | S | Linear elastic | S | S |
| Limit equilibrium | | S | NS** | Rigid with a failure criterion | S | NS |
| Stress field | | S | NS | Rigid with a failure criterion | S | NS |
| Limit Analysis | Lower bound | S | NS | Ideal plasticity with associated flow rule | S | NS |
| | Upper bound | NS | S | | NS | S |
| Full Numerical analysis | | S | S | Any | S | S |

*S = satisfied
**NS = not satisfied

Wood (2004) stated that numerical modelling was able to deal with all the problems that could be solved with any conventional analysis. Numerical modelling accommodates realistic behaviour of soil and irregular or three-dimensional geometries, which generally is difficult or impossible with simpler theoretical models. However, Potts (2003) warned that numerical modelling could result in unreasonable predictions if an inappropriate constitutive model was chosen.

### 2.5.1 Constitutive Soil Models

In finite element analysis, the stress–strain behaviour of soil can be simulated with constitutive models, which should be carefully selected. A great variety of models is available. Akai et al. (1978) described soils as geomechanical materials that possess strain-hardening-softening, elasto-plastic, rate-sensitive, and dilatant behaviours. A constitutive model cannot necessarily be expected to cover all of these.

The Cam-clay model was the first hardening plasticity model (Wood, 2004). The model allows a soil to isotropically harden. Britto and Gunn (1987) explained that yield surfaces could undergo

translation in stress space which was called kinematic hardening. The assumption of isotropic hardening is less realistic for many materials.

For triaxial stress space Al-Tabbaa (1987) and Al-Tabbaa and Wood (1989) developed a model in which a small kinematic yield surface, a bubble-like elastic region, moves inside a bounding surface (Figure 2.20). Its movements develop plastic strains while the plastic stiffness is controlled
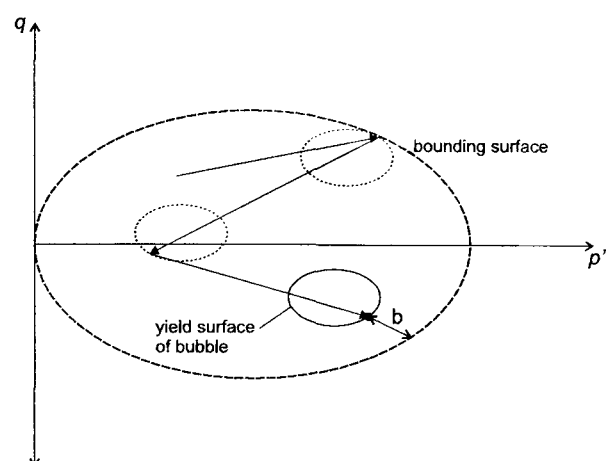


**Figure 2.20:** Bubble model (after Wood, 2004)

by the separation $b$. Later, similar models for different purposes were also introduced. For instance, Stallebrass and Taylor (1997) formulated the three-surface kinematic hardening (3-SKH) model in order to simulate the behaviour of overconsolidated clays. Similarly, Puzrin and Burland (1998) develop a model for predicting the generalised small-strain behaviour of soils. Other "bubble" models were also introduced by Rouainia and Wood (2000) and Kavvadas and Amorosi (2000). These models seem to adequately to describe complex soil behaviour in geotechnical problems. However, due to their complexity, their practical application remains very limited Potts et al. (2001).

Another kinematic hardening model is BRICK, first introduced by Simpson (1992). The model uses multiple kinematic hardening yield surfaces in a strain space. Uses and explanations of this model can be found in Simpson (1992), Lehane and Simpson (2000), Puzrin and Houlsby (2001), Osman et al. (2004), and Jovičić et al. (2006). This model is available and incorporated in the finite element software SAFE of the Oasys GEO Suite.

### 2.5.2 BRICK Model

Simpson (1992) compared the strain behaviour of a soil element to a system in which a man is dragging several bricks with separate strings around a room. The room is analogous to strain space whereas positions of the man and each brick respectively represent the strain in the element and in a proportion of the element. The movements of the bricks represent plastic strain.

Figure 2.21 illustrates a man dragging his bricks, each connected with a string. The bricks
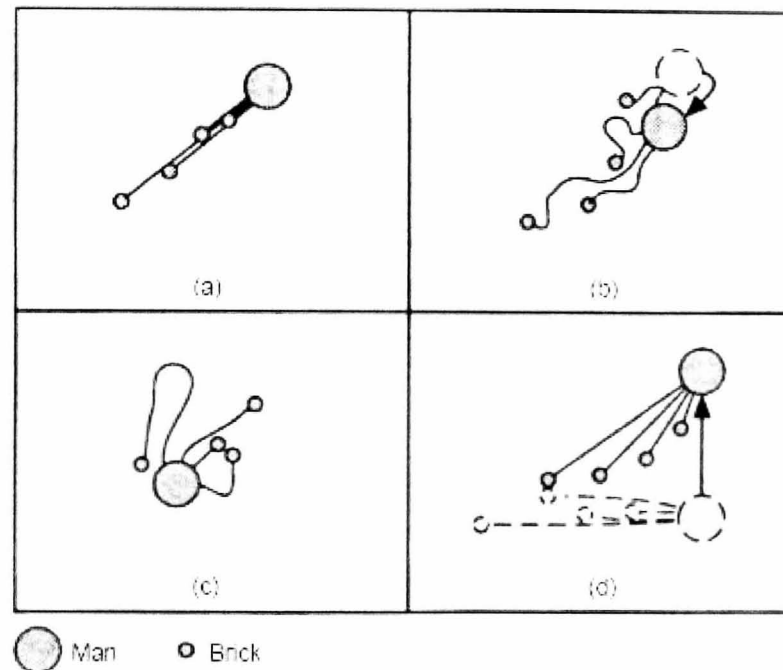


**Figure 2.21:** Analogy for the BRICK model (Simpson, 1992)

follow the man if they are dragged only in one direction (Figure 2.21.a). When the man changes direction, for instance turning around to the opposite direction (Figure 2.21.b), initially the bricks do not move. As soon as the distances between the man and any bricks are equal to their respective strings, the bricks move in the pulling direction (Figure 2.21.c). At this moment, some of the bricks might still have slack strings and not be moved. A similar explanation can be also addressed to the case depicted in Figure 2.21.d, in which the direction of movement is suddenly changed by 90° from the previous direction. In this case, there is, however, no chance for any of the strings to slacken. To some extent the movement of bricks initially continues in the previous direction before it eventually coincides with the pulling direction.

The opportunity for the soil to behave purely elastically is very limited since it only occurs when bricks are unmoved. Figure 2.22 shows the S–shaped relationship between strain and soil
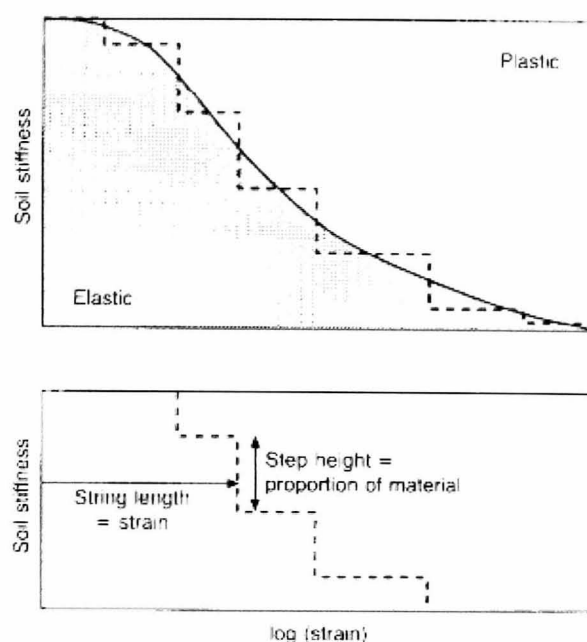
**Figure 2.22:** Strings development for BRICK model (Simpson, 1992)

stiffness. Simpson (1992) divided the strain into elastic and plastic components and purely elastic behaviour only exists at very small strain. Changes in stress are only caused by the elastic component. The proportions of a soil element (represented by the bricks) are expressed by the step heights along the curve. The distance to each step on the strain axis is analogous to the length of a string connecting a brick to the man. With progressive straining, the soil experiences progressive drops in stiffness and behaves more plastically.

The above-mentioned S-curve also governs the angle of shearing resistance of the soil. Figure 2.23 depicts the S-curve with normalised tangent shear modulus $G_t$ for the stiffness axis and shear strain $\gamma$ for the strain axis. Given that the stiffness is assumed to be proportional to mean stress $s$, the area $A$ under the curve can be used to predict the stress ratio at failure. With reference to Equation 2.5, if $s$ is constant and $G_t$ is equal to $\mathrm{d}t/\mathrm{d}\gamma$, the area $A$ is equal to $t/s$, which is equivalent to $\sin\phi'$ at failure.

$$A = \int (G_t/s)\mathrm{d}\gamma \qquad (2.5)$$

The mobilised angle of friction $\sin\phi'_{\mathrm{mob}}$ during one-dimensional normal consolidation can be inferred from the positions of the strain points and bricks that lie on a line at $45°$ with volumetric strain $v$ and shear strain $\gamma$ axes. This coefficient is therefore given by $\sin\phi'_{\mathrm{mob}} = \sin\phi'/\sqrt{2}$. Simpson (1992) suggested that the coefficient of lateral earth pressure $K_0$ can be predicted by
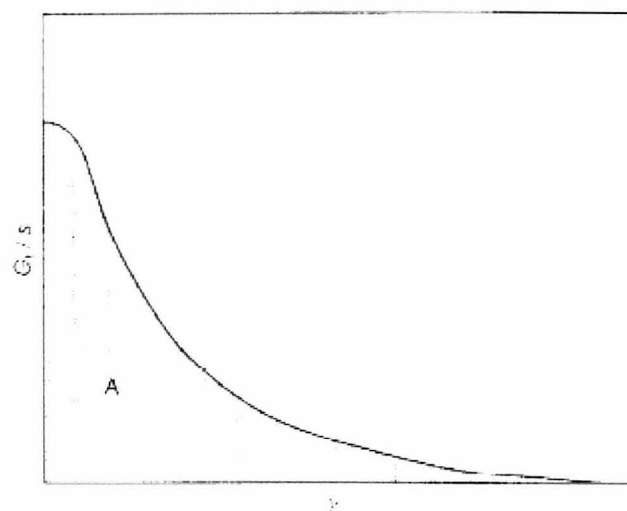
**Figure 2.23:** The area $A$ covered by the curve of normalised tangent shear modulus and shear strain relationship (Simpson, 1992)

using Equation 2.6.

$$K_0 = \frac{(1 - \sin \phi'/\sqrt{2}}{(1 + \sin \phi'/\sqrt{2}} = \frac{(\sqrt{2} - \sin \phi')}{(\sqrt{2} + \sin \phi')} \qquad (2.6)$$

As shown in Figure 2.24, this prediction agrees very well with those proposed by Jaky (1944), Brooker and Ireland (1965), and Bolton (1991).
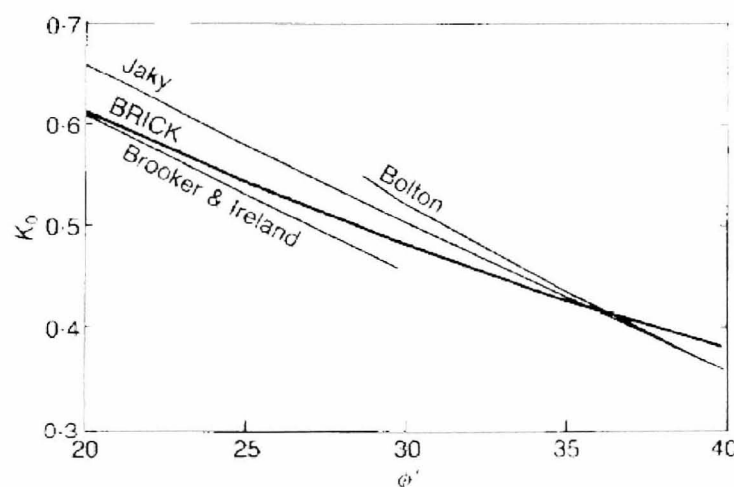


**Figure 2.24:** Coefficient of lateral pressure at rest $K_0$ by BRICK, compared to those from other theories (Simpson, 1992)

For heavily overconsolidated soils, Simpson (1992) found that $K_0$ predicted by BRICK was close to that obtained by using $K_0 = K_{0nc}\text{OCR}^{\sin \phi'}$ (Mayne and Kulhawy, 1982) in which $K_{0nc}$ is the value of $K_0$ during virgin compression of the normal consolidation line. The compression and swelling characteristics of the BRICK model in one-dimensional conditions are depicted in

Figure 2.25. The curve is linear during compression, slightly arching at the beginning of swelling,
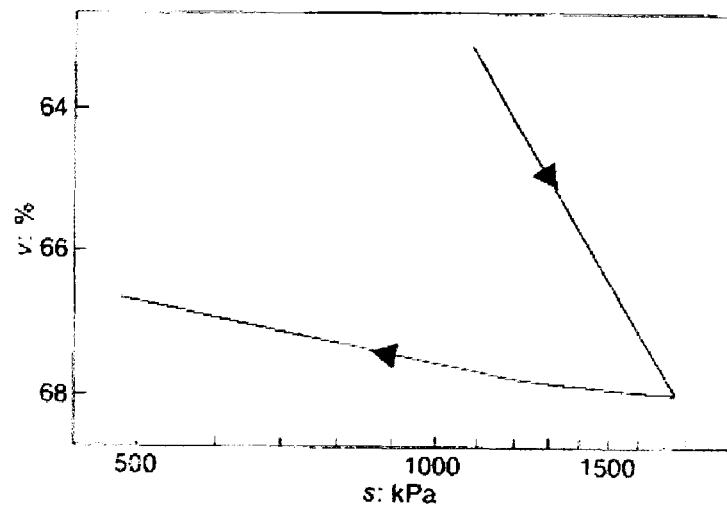


**Figure 2.25:** Typical one-consolidation behaviour in the stress $s$ and volumetric
strain $v$ space, predicted by BRICK (Simpson, 1992)

and gradually flattening at higher overconsolidation ratios. This was not considered typical for
isotropic swelling and was corrected in later versions of BRICK. Originally designed as a plane
strain model, BRICK was also modified to become a generalised three-dimensional model. The
shear strain $\gamma$ in the original model was replaced with five shear strain components ($\varepsilon_z - \varepsilon_x$, ($2\varepsilon_y -$
$\varepsilon_x - \varepsilon_z)/\sqrt{3}$, $\gamma_{xy}$, $\gamma_{yz}$, and $\gamma_{zx}$). A similar modification was also applied for the shear stresses.
This generalised version can be readily used in the finite element analysis software SAFE. Other
enhancements to the original BRICK model are explained by Lehane and Simpson (2000).

In its application, the BRICK model requires some input parameters such as string lengths
(Figure 2.22), stress history, compression and swelling line gradients ($\lambda$ and $\kappa$ respectively), a
Poisson's ratio $\nu$, a proportionality constant $\iota$, and a soil constant $\beta$. The stiffness of the soil is
determined from ratios of tangent to maximum elastic shear modulus ($G_t/G_{max}$). The elastic shear
modulus $G$ (at very small strain, less than 0.005% for many soils) can be obtained from shear
wave velocity measurements or from the initial stages of laboratory tests with high-resolution local
strain instrumentation (Lehane and Simpson, 2000). As a kinematic hardening model, BRICK can
memorise previous stress path histories (Jovičić et al., 2006). In SAFE an overconsolidated stress
history is achieved by building and removing a certain height of soil (Ove Arup and Partners,
2006). The gradients, $\lambda$ and $\kappa$, are identical to $\lambda^*$ and $\kappa^*$ proposed by Houlsby and Wroth (1991).
A Poisson's ratio $\nu = 0.2$ was suggested by Simpson (1992) since many soils have Poisson's ratios

around this value. The proportionality constant $\iota$ governs the ratio of stiffness to mean effective stress at very small strain. Simpson (1992) expressed this relationship as $\delta s = s\delta v_e/\iota$ where $\delta s$, $s$, and $\delta v_e$ are mean normal stress increment, mean stress, and elastic volumetric strain increment respectively. The soil constant $\beta$ is a multiplier that determines the effect of overconsolidation on stiffness and strength. It is incorporated in $(1 + \beta(v - v_0 - \lambda \ln s/s_0))$, where $v$ is volumetric strain and the subscript 0 represents the initial state of the respective parameters. Previously a single $\beta = 4$ was used for London Clay to consider the effects of overconsolidation on both stiffness and strength (Simpson, 1992). This parameter was later separated into two parameters with different magnitudes, i.e. $\beta_G = 4$ and $\beta_\phi = 3$ resulting in better modelling of stiffness and strength respectively (Jovičić et al., 2006).

## 2.6 GAPS IN PREVIOUS RESEARCH

From the reviews above, some gaps in previous research concerning settlement due the interaction of neighbouring footings or buildings can be identified. These are that:

- neither physical nor numerical modelling has been carried out regarding the interaction of neighbouring footings on soft ground.

- although there has been some research observing the interaction between closely-spaced footings on stiff clays and sands, successive loading (i.e. loading applied to a model footing after being previously applied to an adjacent model footing) has not been investigated.

- no accurate measurement using a technique such as PIV has been conducted to observe the displacement field on a cross-section beneath interacting footings.

- no research has been carried out to mitigate the interaction with a sheet wall inserted between two closely-spaced footings.

The present research aims to remove or, at least, reduce these gaps.

# Chapter 3

# LABORATORY SCHEMES

## 3.1 INTRODUCTION

The rigid consolidation chamber specially designed for this research was used to accommodate Speswhite kaolin and two small-scale footings during several series of tests. The footings and the soil were intended to simulate a prototype of two neighbouring buildings founded on soft ground. The loads of the buildings were imitated with a pressure system integrated into the equipment. The resulting displacements were measured using two methods. The settlements at the centres of the footings were obtained from electrical displacement transducers, whereas the displacements of the soil were obtained using Particle Image Velocimetry (PIV) from a series of images captured with a digital camera. The application of the PIV is described in Chapter 4. The camera was mounted in front of the chamber, the front wall of which was a transparent window of Perspex.

Three series of tests were conducted with two closely-spaced footings after a preliminary test with a single footing. Each series of tests was performed twice to examine the repeatability of the experiments. In the first series of tests the second footing was loaded immediately after 100% consolidation under the final loading on the first footing. This imitated a situation where the second building is built after the first. In the second series of tests, before the second footing was loaded, an aluminium sheet, 100 mm long, was inserted between the footings. The test simulated the effect of inserting a sheet pile wall between the two buildings. A similar test configuration was adopted for the third series. The only difference was that the tip of the aluminium sheet was vertically restrained with two small stainless steel rods resting on the base of the consolidation chamber. The test was intended to model a sheet pile wall vertically fixed at a hard stratum.

## 3.2 EQUIPMENT

### 3.2.1 Consolidation Chamber

#### 3.2.1.1 Design

Due to limited space in a laboratory, the almost infinite length of the soil mass in the field must be inevitably restricted. In this research, the soft ground underlying two neighbouring buildings was represented with kaolin and bounded with a rigid chamber. Since the results obtained from the laboratory tests were to be used in conjunction with numerical modelling, parameters used in this $1g$ laboratory test were not necessarily rigorously scaled from a prototype. The model could, however, still be regarded to approximate a prototype with a geometric scaling ratio $n$ of $1/100$. The chamber parameters such as the height, length, width, and rigidity will be discussed in this section, in addition to the design of the model footings and the sheet wall.

**3.2.1.1.1 Height**   The height was designed by considering the thickness of the soft ground in the field. The simulated ground was based on the alluvial clays widely found in Southeast Asia such as Banjarmasin clay (Suzuki and Yasuhara, 2004) and Singapore clay (Hanzawa and Adachi, 1983). The profiles of both clays are shown in Figure 3.1 and Figure 3.2, revealing similar characteristics.
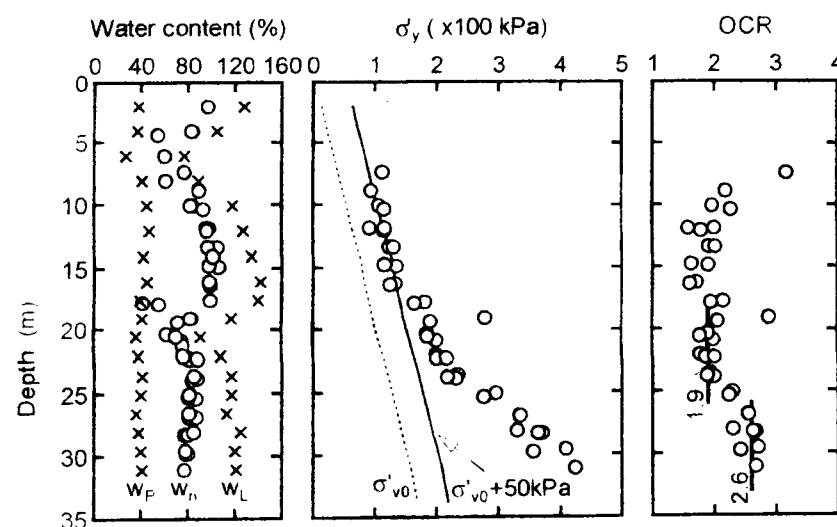


**Figure 3.1:** Profile of Banjarmasin clay (Suzuki and Yasuhara, 2004)

The values of the plastic limit $w_P$ and the liquid limit $w_L$ of the clays are comparable to those found in kaolinite clay such as Spestone or Speswhite kaolin (Parry and Nadarajah, 1973; Bhaskaran, 1974; Al-Tabbaa and Wood, 1987; Rossato et al., 1992). In this research Speswhite kaolin was
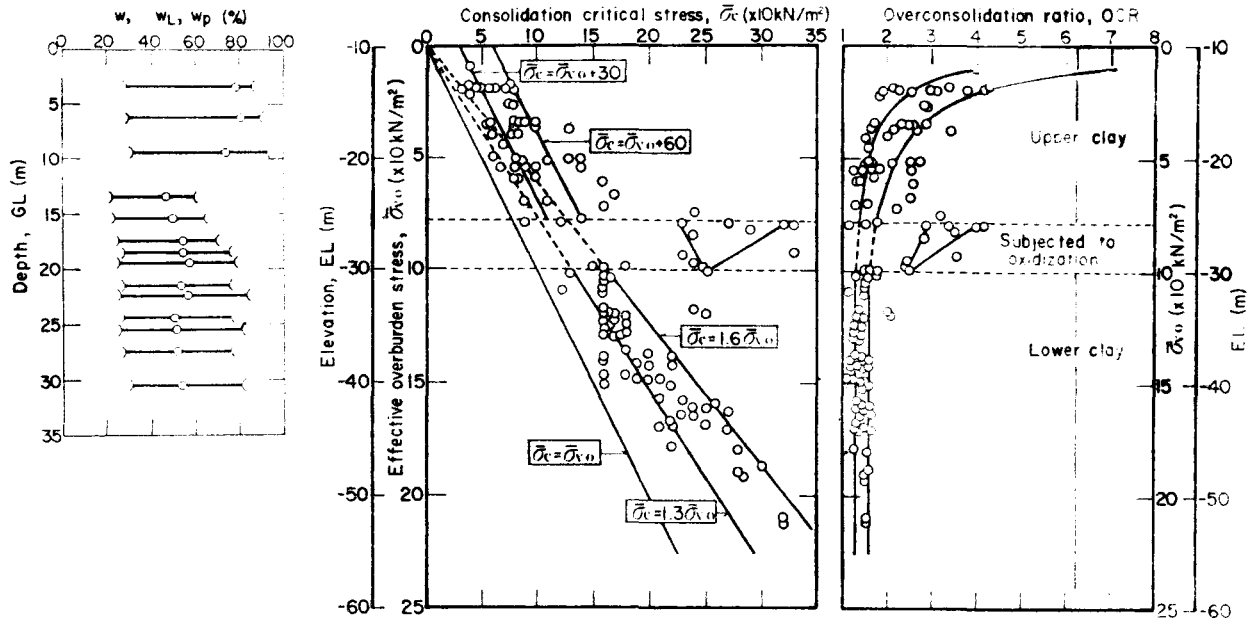
**Figure 3.2:** Profile of Singapore clay (Hanzawa and Adachi, 1983)

selected to model the ground. Given the strength profile of Singapore clay in Figure 3.3, the clay can be considered soft to a depth of about 40 metres. However, for practical reasons only half of the depth (=20 metres) was adopted in this small-scale $1g$ physical modelling, i.e. 200 mm after it was scaled down by 1/100.



(a) Simpson (1992)

(b) Tan et al (1992)
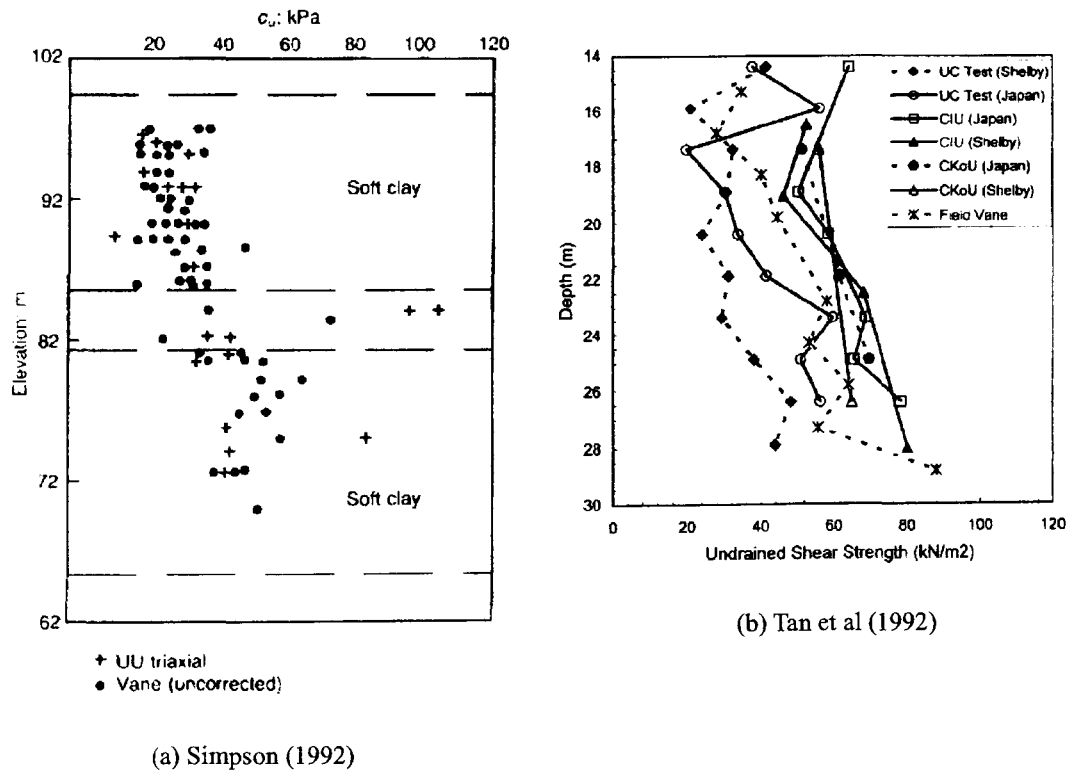
**Figure 3.3:** Undrained strength of Singapore clay (Simpson, 1992; Tan et al., 2002)

The model soil was to be initially created from a slurry of Speswhite kaolin by preconsolidation. The height of slurry to produce the model thickness of 200 mm was calculated from the void ratios of the slurry ($e_{slurry}$) and of the model ($e_{model}$). The following expression was used to estimate this height $H_{slurry}$.

$$\frac{H_{slurry}}{H_{model}} = \frac{V_{slurry}}{V_{model}} = \frac{1 + e_{slurry}}{1 + e_{model}} \tag{3.1}$$

where $V$ is the volume at the related soil state. By assuming that the slurry was fully saturated and knowing its specific gravity $G_s$ of 2.60 (Eid, 1978; Yong, 1979), the void ratio was simply calculated with the expression of $e_{slurry} = G_s.w$. The initial water content $w_i$ of 138% was twice the liquid limit of the kaolin observed by Al-Tabbaa and Wood (1987) ($w_L = 69\%$) and slightly above twice that of the kaolin in this research ($w_L = 61.8\%$), resulting in $e_{slurry} = 3.6$. The void ratio of the model $e_{model}$ was calculated from the stress history applied to the soil. Equation 2.2 suggests that the undrained strength of a soil is a function of its stress history and the applied vertical stress. After consideration of the implications of the equation, in preconsolidation, a maximum effective vertical pressure of 50 kPa was applied and then the pressure was reduced to 5 kPa. This created overconsolidated soil with an OCR of 10. The undrained strength of the model soil from using the coefficients $a$ and $b$ (see Table 2.4 in Section 2.4.1) was expected to range from 4.4 kPa to 5.6 kPa. Figure 3.4 shows the data obtained from preconsolidations of Speswhite kaolin by Hird and Moseley (2000) and Srisakthivel (2003). It indicated that the void ratio at 50 kPa ranged from 1.5 to 1.7. The value $e_{model}$ was assumed to be 1.6. From Equation 3.1, the height of the slurry
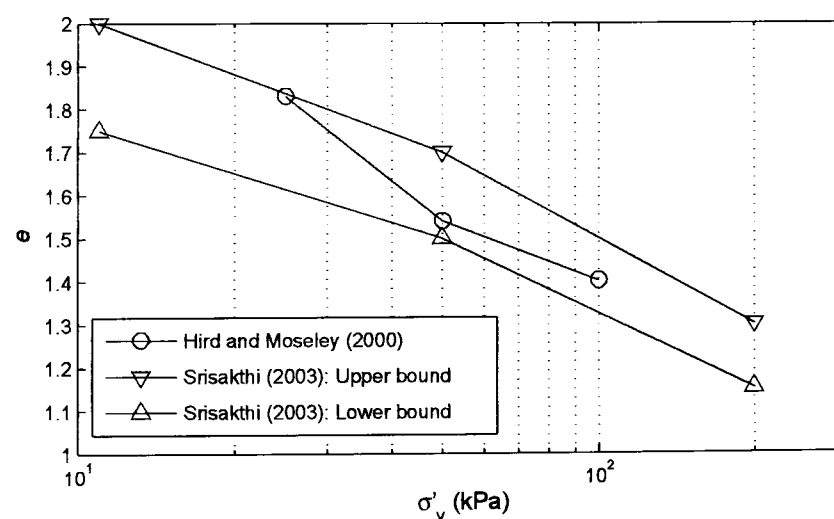


**Figure 3.4:** Variation of void ratio $e$ of kaolin under effective vertical stress $\sigma_v'$

was predicted to be about 352.9 mm. Allowing for the consolidation piston height of 40 mm, the height of the box was conservatively designed to be 450 mm.

**3.2.1.1.2  Length**  The mode of the deformation in this study was idealised to be in plane strain and the length of the box was limited to 150 mm. This selection was based on practical considerations such as the preparation of the model system.

**3.2.1.1.3  Width**  The width of the chamber was determined from a consideration of the stress distribution that might occur in the model soil. Equation 3.2, as found in many textbooks (Scott, 1980; Atkinson, 1981; Craig, 1987; Azizi, 2000), was used to determine the stresses at a point in an elastic medium under a uniform strip load $q$.

$$\sigma_y = \frac{q}{\pi}(\alpha + \sin\alpha\cos(\alpha + 2\beta))$$

$$\sigma_x = \frac{q}{\pi}(\alpha - \sin\alpha\cos(\alpha + 2\beta)) \qquad (3.2)$$

$$\tau_{xy} = \frac{q}{\pi}(\sin\alpha\sin(\alpha + 2\beta))$$

where $\sigma_y$, $\sigma_x$, and $\tau_{xy}$ are the vertical, horizontal and shear stresses at a point at a depth z below the surface, Figure 3.5, and $\alpha$ and $\beta$ are defined in the same figure.
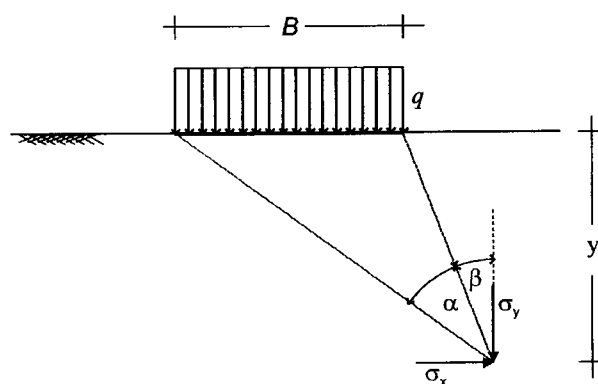


**Figure 3.5:** Stress due to a uniformly-loaded strip

Figure 3.6 shows the profile of vertical stress $\sigma_y$, calculated with Equation 3.2, in the soil due to a pressure $q$ of 80 kPa from two footings. The 100 mm wide footings were scaled down to 1/100th of their prototype size (10 m). The distance between the footings was 20 mm or 2 metres in the prototype. Each curve represents the vertical stress at a certain depth y. The profile of horizontal stress $\sigma_x$ is depicted in Figure 3.7. It was clear from the figures that the width of the
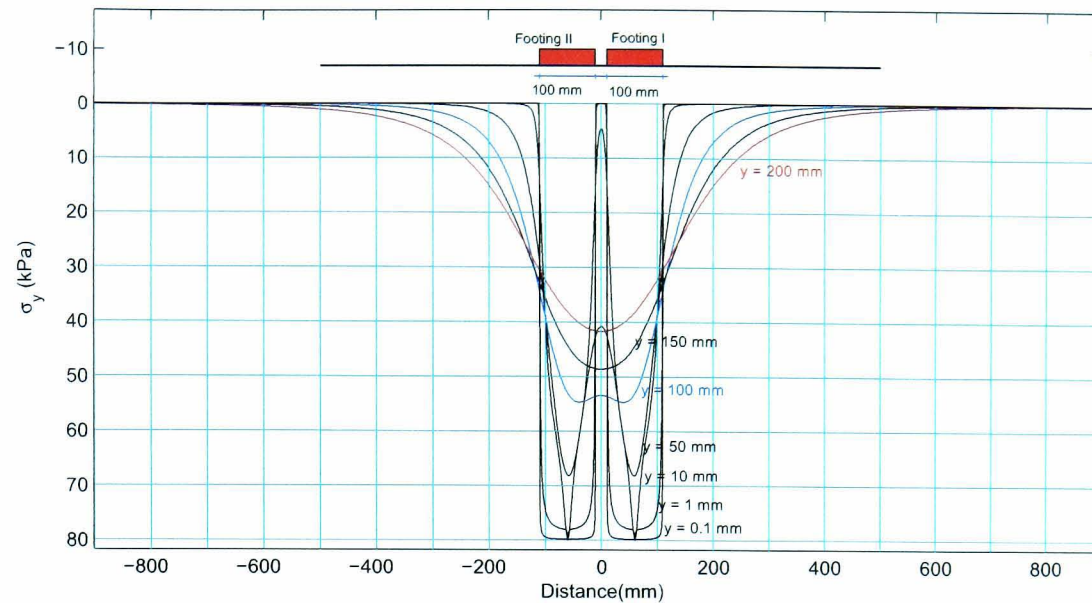
**Figure 3.6:** Profile of vertical stress $\sigma_y$ subjected to double footing pressure of 80 kPa

chamber should be ideally at least 2000 mm if the boundary was not to affect the soil deformation. However, this was considered impractical. The chamber was planned to be rotated for the purpose of texturing the model soil (see Section 3.4.3). With a width of 2000 mm, the chamber and the model soil would have weighed more than 150 kg. A width of 400 mm was decided, resulting in a total weight of only about 35 kg. Boundary effects would be addressed in the analysis of data using the finite element method.
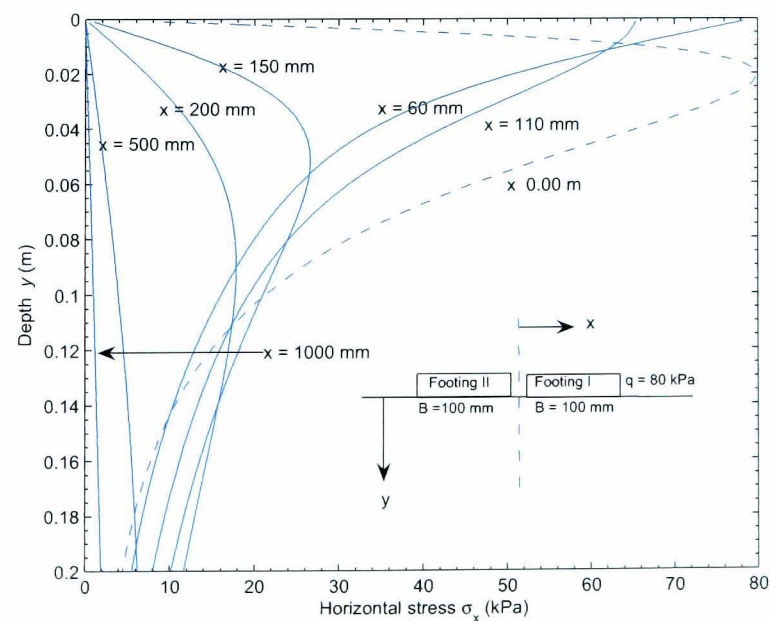


**Figure 3.7:** Profile of horizontal stress $\sigma_x$ subjected to double footing pressure of 80 kPa

**3.2.1.1.4 Thickness of Chamber Walls** The walls bounding the model soil were intended to provide rigid boundaries. The chamber consisted of two side walls, a base, a back wall, and a front wall. To allow visual documentation for PIV data acquisition, the front wall was made of Perspex and the others were made of aluminium. The most critical loading condition of the walls was during preconsolidation with the maximum pressure of 50 kPa. The height of soil at this pressure was about 200 mm. Although the design pressure on the model footings was higher at 80 kPa, the horizontal stresses acting on the walls would only be concentrated locally (Figure 3.7).

During preconsolidation the horizontal stress normal to the walls was assumed uniform since the thickness of the soil was small. Neglecting the soil particle resistance (i.e. $K_0 = 1$), the normal stress acting on the walls was taken to be the same as the piston pressure. The walls were assumed to be plates fixed at all edges. The calculation of deflection $\delta$ was based on Equation 3.3 suggested by Timoshenko and Woinowsky-Krieger (1959),

$$\delta = \frac{cqB^4}{D}, \quad \text{where} \quad D = \frac{Et^3}{12(1 - \nu^2)} \tag{3.3}$$

The coefficient $c$ depended on the ratio of the length $L$ to the width $B$ of the given plate. The resulting deflections of the walls subjected to a uniform load $q$ of 50 kPa (= the maximum preconsolidation pressure) are shown in Table 3.1. The thickness of each wall was taken as 20 mm.

**Table 3.1:** Deflection of chamber walls during preconsolidation pressure of 50 kPa

| Wall location | $B$ (m) | $L$ (m) | $\frac{L}{B}$ | $c^*$ | $\nu$ | $D$ (kN.m) | $\delta$ (mm) |
|---|---|---|---|---|---|---|---|
| Front (Perspex) | 0.20 | 0.40 | 2.00 | 0.00254 | 0.38 | 2.198 | 0.087 |
| Back (Aluminium) | 0.20 | 0.40 | 2.00 | 0.00254 | 0.33 | 51.622 | 0.004 |
| Sides (Aluminium) | 0.15 | 0.20 | 1.33 | 0.00207 | 0.33 | 51.622 | 0.001 |

*Taken from Timoshenko and Woinowsky-Krieger (1959) page 202.

The elastic moduli $E$ of the Perspex and the aluminium wall were successively $3 \times 10^6$ kPa (Ineos Acrylics UK Ltd., 2001) and $6.9 \times 10^7$ kPa (Dwight, 1999; Engineers Edge, 2004). The Poisson's ratios $\nu$ were 0.38 for the Perspex and 0.33 for the aluminium. The deflections were less than 0.10 mm for all the walls. The rigid boundary assumption was deemed to be satisfied.

**3.2.1.1.5 Footings** The design dimensions of one of the model footings are shown in Figure 3.8. The model was intended to simulate the raft foundation of a building. Based on the scaling
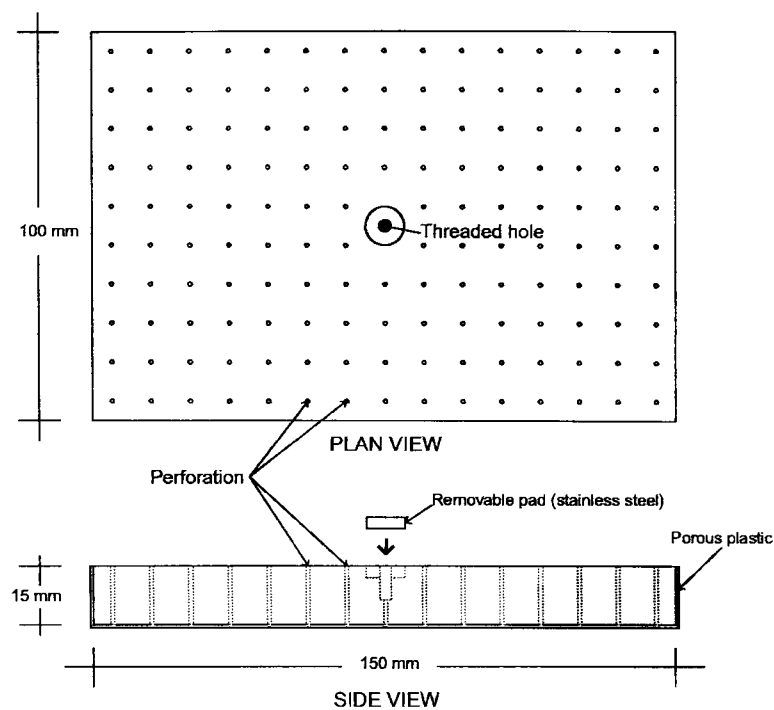
**Figure 3.8:** Model footing made of Perspex

law for flexural stiffness, the following equation could be applied,

$$E_{\text{model}}I_{\text{model}} = \frac{1}{n^3}E_{\text{prototype}}I_{\text{prototype}}$$  (3.4)

where $E$, $I$, and $n$ are respectively the modulus of elasticity, the second moment of inertia, and the scaling factor. In plane strain, the thickness of the model footing of 15 mm corresponded approximately to a 800 mm thick concrete raft with $E = 2 \times 10^7$ kPa. The deflection of the model footing was conservatively examined using

$$\delta = \frac{PL^3}{48EI}$$  (3.5)

for a simple beam with a point load $P$ at the midst of its span $L$ (Richard Liew and Shanmugam, 2003; British Steel, 1997). In order to produce a footing pressure of 80 kPa, a point load $P$ of 1.2 kN was required. The maximum deflection at the centre of the beam was only 0.198 mm with $L = 100$ mm or 1 mm if $L$ was 150 mm. This calculation neglected the footing perforation which removed less than 0.1% of the footing.

**3.2.1.1.6 Sheet Wall** The interaction of neighbouring buildings in the soil would possibly be mitigated with the insertion of a wall. In the physical modelling the wall was represented with an aluminium sheet. The selection of the thickness of the model wall was based on a practical consideration at field scale, i.e. the maximum driving lengths. Table 3.2 lists various types of steel sheet pile with respective dimensions, properties, and recommended driving lengths. Section GSP2

**Table 3.2:** Dimensions and properties of sheet pile (British Steel, 1997)
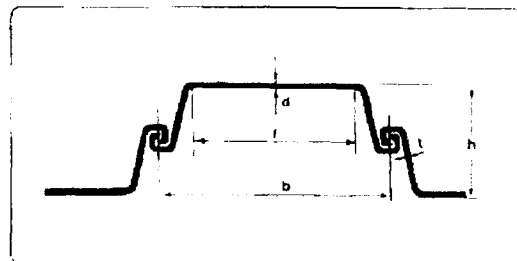


| Section | b mm (nominal) | h mm (nominal) | d mm | t mm (nominal) | f Flat of Pan mm | Sectional Area cm²/m of wall | Mass kg per linear metre | Mass kg/m² of wall | Combined Moment of Inertia cm⁴/m | Section Modulus cm³/m | Driving Lengths Approximate Maximum Lengths Depending Upon Steel Grade and Ground Strata (m) |
|---|---|---|---|---|---|---|---|---|---|---|---|
| LX8 | 600 | 310 | 8.2 | 8.0 | 250 | 116 | 54.6 | 91.0 | 12861 | 830 | 14 |
| LX12 | 600 | 310 | 9.7 | 8.2 | 386 | 136 | 63.9 | 106.4 | 18723 | 1208 | 17 |
| LX16 | 600 | 380 | 10.5 | 9.0 | 365 | 157 | 74.1 | 123.5 | 31175 | 1641 | 20 |
| LX20 | 600 | 430 | 12.5 | 9.0 | 330 | 177 | 83.2 | 138.6 | 43478 | 2022 | 23 |
| LX25 | 600 | 450 | 15.6 | 9.2 | 330 | 200 | 94.0 | 156.7 | 56824 | 2525 | 25 |
| LX32 | 600 | 450 | 21.5 | 9.8 | 328 | 242 | 113.9 | 189.8 | 72028 | 3201 | 28 |
| 6W | 525 | 212 | 7.8 | 6.4 | 331 | 108 | 44.7 | 85.1 | 6459 | 610 | 9 |
| GSP2 | 400 | 200 | 10.5 | 8.6 | 265 | 153 | 48.0 | 120.0 | 8740 | 874 | 19 |
| GSP3 | 400 | 250 | 13.0 | 8.6 | 271 | 191 | 60.0 | 150.0 | 16759 | 1340 | 23 |
| GSP4 | 400 | 340 | 15.5 | 9.7 | 259 | 242 | 76.0 | 190.0 | 38737 | 2270 | 27 |
| 6 (122kg) | 420 | 440 | 22.0 | 14.0 | 248 | 370 | 122.0 | 290.5 | 92452 | 4200 | 30 |
| 6 (131kg) | 420 | 440 | 25.4 | 14.0 | 251 | 397 | 131.0 | 311.8 | 102861 | 4675 | 30+ |
| 6 (138.7kg) | 420 | 440 | 28.6 | 14.0 | 251 | 421 | 138.7 | 330.2 | 111450 | 5066 | 30+ |

was selected to allow the prototype sheet pile to be driven to a depth of 20 metres in soft ground. The thickness of the sheet pile used in the model was designed using the scaling law expressed in Equation 3.4. Given that the moduli of elasticity of steel and aluminium were respectively $2.1 \times 10^8$ kPa and $6.9 \times 10^7$ kPa, the thickness of the model wall was calculated as 1.5 mm.

*3.2.1.2 Equipment Setup*

Figure 3.9(a) shows the typical setup of the equipment prior to the laboratory tests, comprising the main components that are schematically depicted in Figure 3.9(b). The equipment consists functionally of three elements: a model boundary (rigid chamber), a pressure system, and a drainage system. The effective dimensions of the chamber were 400 mm wide, 450 mm high, and 150 mm long. The chamber comprises 20 mm thick aluminium walls except for a detachable front window of transparent Perspex with the same thickness (see Section 3.2.1.1.4). The inner aluminium walls
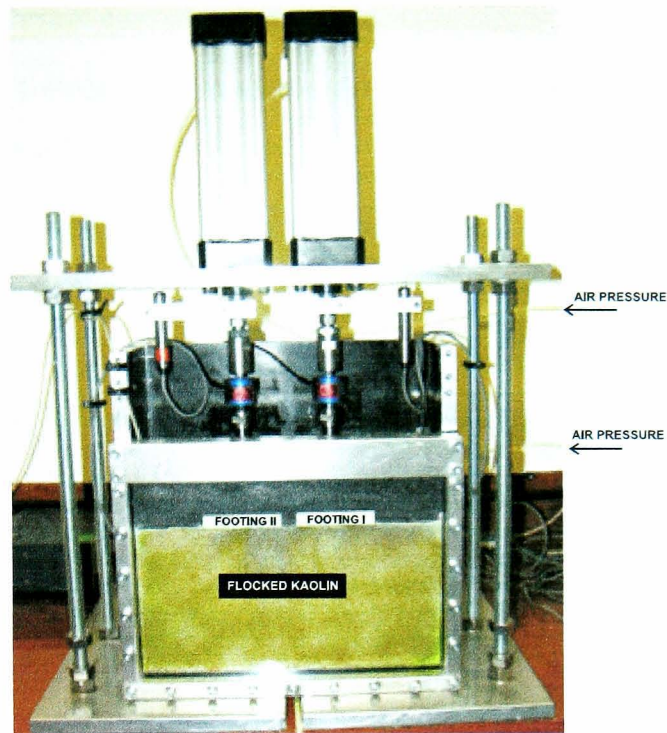
(a) Equipment and test setup
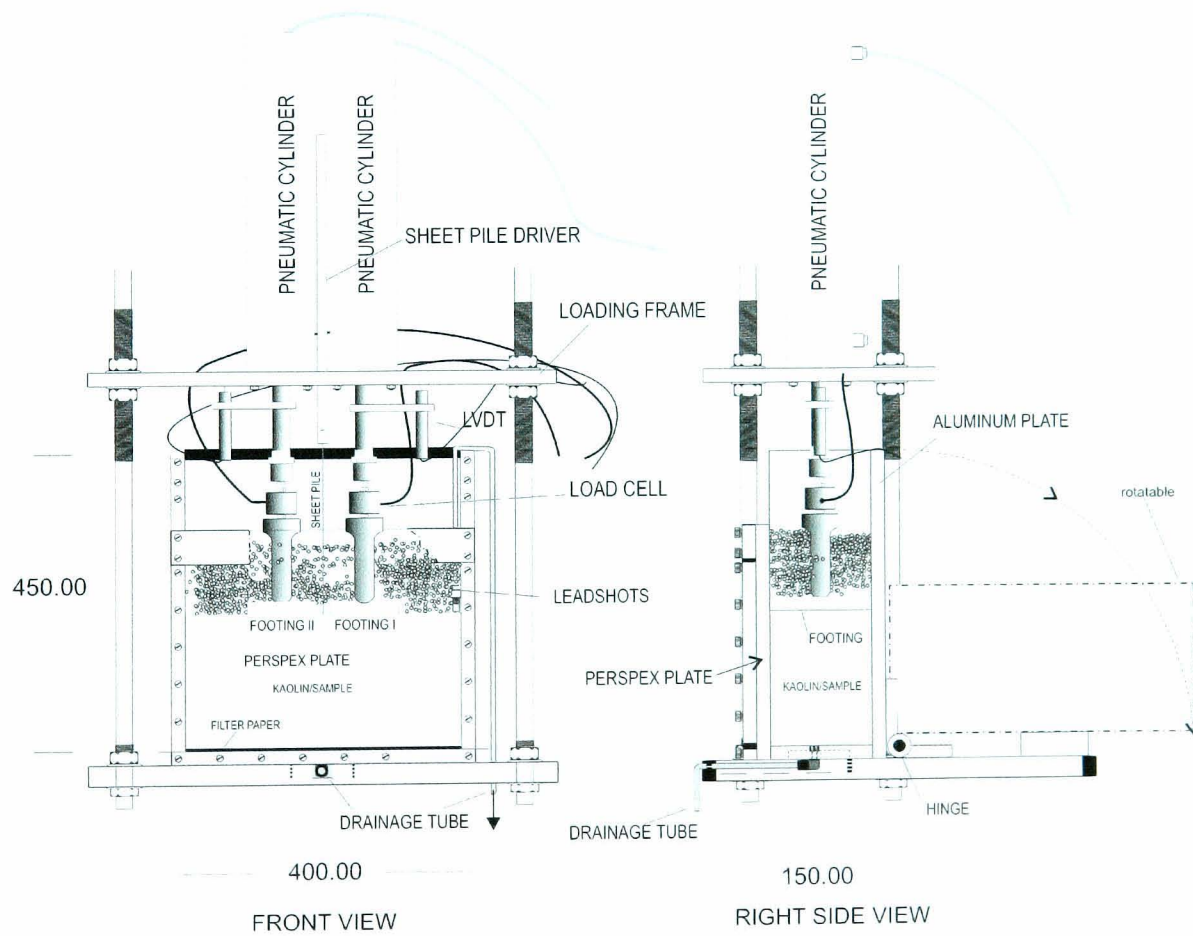


(b) Equipment details with a typical test setup

**Figure 3.9:** The equipment used for physical modelling in the present research

were painted black to prevent corrosion due to the lengthy duration of the tests. The whole chamber was rotatable using a hinge at the back edge of the base to enable texturing of the soil sample with flock (see Section 3.4.3).

Two different interchangeable Perspex plates were always used during each test. The first plate covered the whole front face of the chamber. This plate was used during preconsolidation of the soil (Figure 3.18) since it had to accommodate the initial thickness of the slurry sample (350 mm), the drainage system (two porous plastic sheets of about 3 mm thickness) and a consolidation piston (40 mm thick). The top of the plate was reinforced with an aluminium beam and the other three edges of the plate were bolted to the aluminium chamber. The smaller Perspex plate (see Figure 3.9) was used during the main tests where the thickness of the soil was already reduced to approximately 200 mm by preconsolidation. The first plate was removed after the final stage of the preconsolidation was completed. It was unbolted, slid slowly away from the soil face and replaced with the second Perspex plate as soon as texturing of the sample (see Section 3.4.3) was completed.

### 3.2.2 Pressure System

As shown in Figure 3.9 the compressive forces transferred onto the footings, or the consolidation piston, were established by pressurising pneumatic cylinders, P1E-S080MS-0200 type, manufactured by the Parker Hannifin Corporation. Each of the cylinders was capable of sustaining a maximum air pressure of 10 bars, theoretically equivalent to approximately 5 kN force at the tip of the cylinder shaft. The air pressures were regulated and maintained using a pressure system, into which an air pressure of 7 bars, less than the cylinder capacity, was constantly supplied. The pressure in each cylinder was controlled with a valve regulator and determined with an 8-bar Budenburg type dial gauge. The accuracy of the readings is described in Section 3.3.1.1.

Each pneumatic cylinder was equipped with a double-acting piston with which its shaft could be pushed out or pulled in. Two two-way valves were provided to control the operation of the cylinders. The cylinders were mounted on the loading frame that was supported by four threaded rods. During the preconsolidation stages only one cylinder was used and bolted in the middle of the loading frame.

The magnitude of forces applied by the cylinders depended on the the pressures to be imposed on the soil surface. A force of 3 kN was required to be applied on the middle of the aluminium con-

solidation piston with plan dimensions of 400 mm × 150 mm to give the maximum preconsolidation pressure of 50 kPa. On the other hand, only 1.125 kN was applied on each 100-mm × 150-mm Perspex footing at the maximum contact pressure.

### 3.2.3   Drainage System

Two-way 1-D drainage was implemented to allow the dissipation of excess porewater pressure during preconsolidation of the soil. Two porous plastic sheets were laid over the top and bottom of the soil sample. A drainage hole with a tube connection was provided in the centre of the chamber base and two holes were drilled through the consolidation piston to collect the water from the upper porous plastic. To assist the water flow to the two holes, small channels were machined in the lower face of the piston.

It was desired that the footings should also behave as permeable boundaries. This condition was achieved by drilling small holes through the footings and placing a porous plastic sheet beneath (Figure 3.8). The porewater was able to drain through the holes as the footings were loaded.

### 3.3   MEASUREMENT METHODS

Figure 3.10 shows the measurement systems employed during the experiment. In general, there were two types of measurement: the applied pressures or forces and the associated soil displacements. The magnitudes of pressures or forces were determined using two dial gauges and two load
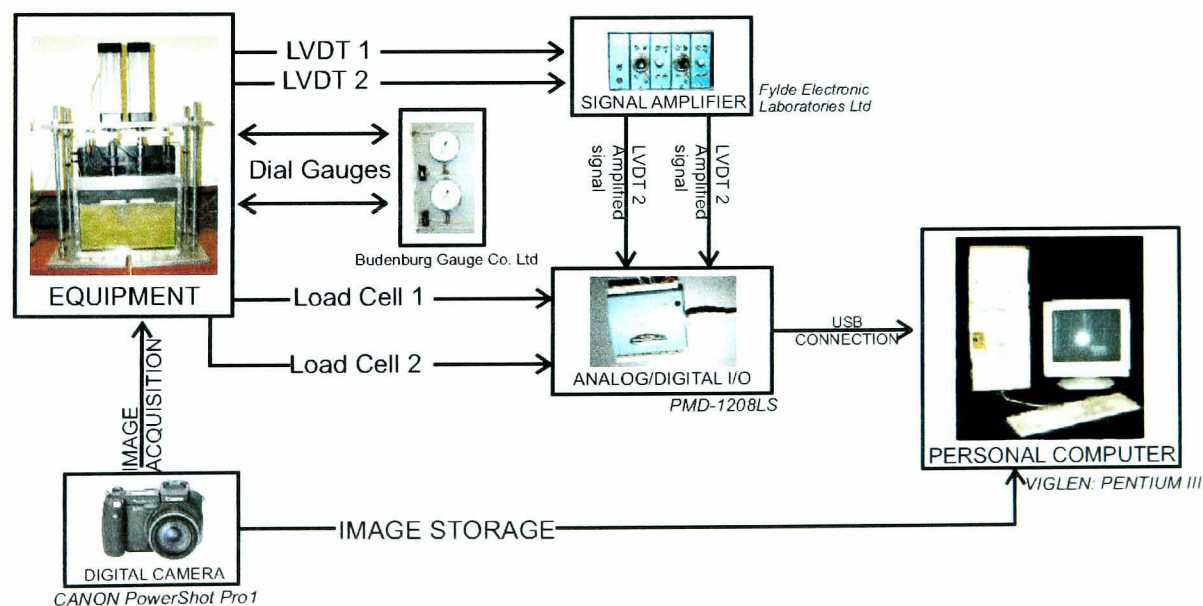


**Figure 3.10:** Diagram of data acquisition

cells, whereas the displacements were acquired with a digital camera and two LVDTs. All data were continuously recorded by a personal computer using logging and image capturing software.

### 3.3.1  Pressure and Force Measurement

#### 3.3.1.1  Dial Gauges and Pneumatic Cylinders

During the preconsolidation stages the magnitude of the force produced by the cylinders was determined solely from dial (Budenburg) gauges since the maximum force applied was 3 kN which exceeded the capacity of the load cells. However, the dial gauges were also used simultaneously with the load cells in the footing load tests, where they provided a cross-check for the load cell readings. Calibrations were required to find the correlation between the input pressures read from the dials and the output forces transmitted by the cylinder shafts. These calibrations were established using a 5-kN proving ring.

The dial gauge mounted in the ring was capable of measuring the deflection as small as its division intervals of 0.002 mm. With the calibration coefficient of 7.981 N/division, the proving ring was used to calibrate a pressure dial gauge of 0–800 kPa range. The pressure dial showed 20 divisions for 100 kPa, i.e. 5 kPa per-division, and, disregarding the pressure loss and friction in the cylinder, one division represented a force of 25.1 N. Assuming that the losses were different for each of the cylinders, calibrations were performed separately for each paired cylinder and dial gauge. Each cylinder was incrementally loaded to 600 kPa, mainly with 50 kPa increments, and then unloaded with the same increments. This was conducted in three cycles.

The correlations between the input pressures read from the dials and the output forces derived from the dial readings of the proving ring for Cylinder I are shown, for example, in Figure 3.11. Three best fit curves in the figure represent one linear and two non-linear correlations for the same data. The regression curves were established using a polynomial function of Matlab Release 13. To examine the strength of the linear association between the air pressure ($AP$) and the resulting force ($F$), the *coefficient of determination* $r^2$, i.e. the square of the *correlation coefficient* $r$, was used. On the other hand, the strength of the non-linear correlations were estimated with the *eta square coefficient* $\eta^2$ which is the squared ratio of the standard deviation of the predicted values $\sigma_{\hat{A}P}$ to that of the actual data $\sigma_{AP}$. Very strong correlations are reflected in all three cases. The precision was further examined through a residual plot as shown in Figure 3.12.
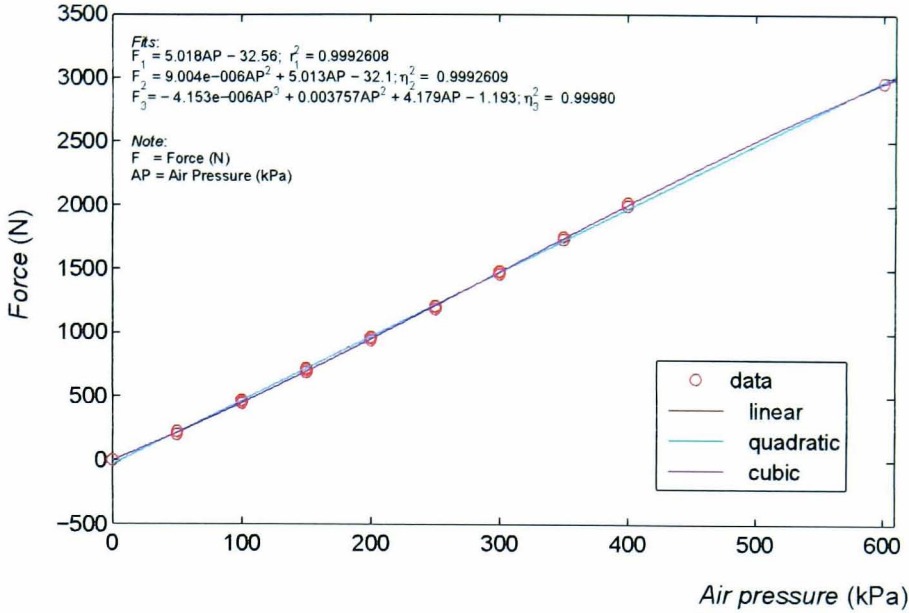
**Figure 3.11:** Calibration data of Cylinder I

As inferred from the variation of the residual data with respect to zero residual values, the precision of pressure measurement over the range 0–600 kPa, with the cylinder, was in general less than 0.5 kPa. The linear best fit was implemented in measurements since further enhancement implementing a higher order polynomial formula did not seem to achieve much improvement. Similar results were observed in the calibration of the cylinder when the pressures were decreased from 600 kPa to 0 kPa, i.e. tracing back the previous pressures. Almost identical results were also found from the calibration of Cylinder II.
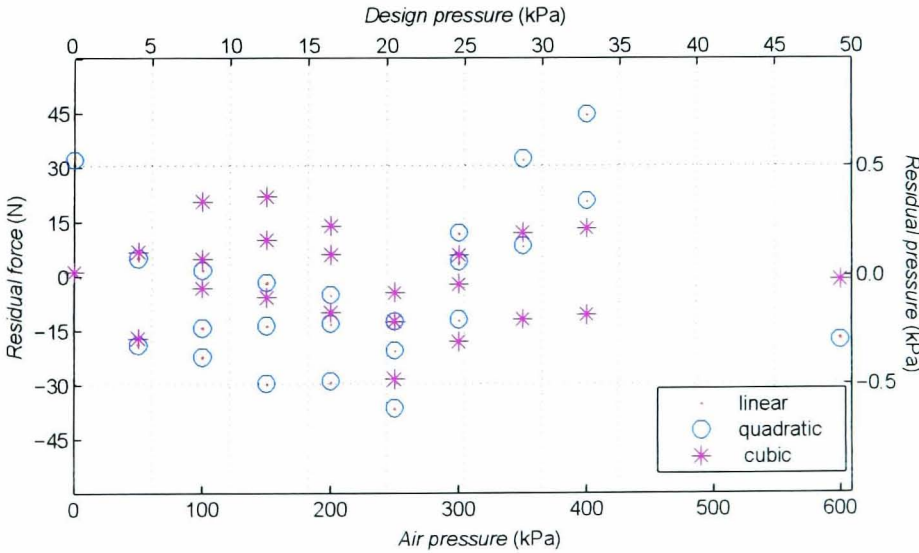


**Figure 3.12:** Residual plot from the calibration data of Cylinder I

### 3.3.1.2  Load Cells

To provide more accurate force measurements than available from the pneumatic cylinder cal-ibration and allow continuous logging of force data, two 2-kN load cell transducers made by RDP Electronics Ltd. were mounted at the tips of both shafts of the pneumatic cylin-ders. Data acquisition was carried out using a logging device, PMD-1208LS, manufactured by the Measurement Computing Corporation. The device was capable of measuring a differ-ential analog output of 0.1 mV and a maximum output of 10 V. Two 12-bit channels were used for the input connections from the load cells. The output signals were recorded on the hard disk of a Pentium-III personal computer through a USB connection that also supplied power from the com-puter to the logging device. The rate of sampling of the data was configured with *InstalCal*™ Version 5.54 for Windows, the software that was shipped together with the device. The analog outputs from the logger were displayed by means of a simple strip chart provided by the software. This enabled direct inspections during the tests.

To avoid submerging the load cells below water lying above the surface of the soil, two exten-sion rods were used to transfer the applied forces from the load cells to the footings. The load cells were supplied with ±15 Volts from an additional power supply.

Load cell calibrations were performed using a load cell calibrator (a dead weight tester made by Budenburg Ltd.), by loading each load cell with 200-N increments from zero to the full scale of 2000 N. After reaching the maximum capacity of the load cells, the force was successively unloaded to the previous magnitudes. The reading for each force was averaged from the logging at rate of 4 samples per second for a 1-minute period. This procedure was repeated three times for each load cell. Although the resolution of measurement was 0.1 mV, the noise content of 20 mV in the output signal limited the precision.

The correlation for one of the load cells is presented in Figure 3.13. In this regression analysis, the data from the loading are treated separately from those from the unloading. The combination of the coefficient $r^2$ of approximately unity and randomly distributed residuals, shown in Figure 3.14, suggests that the linear relationship was sufficient for predicting the force from the output of the load cell. Considerable variations from the prediction line occurred at low forces, especially at zero loading. It diminished once the force was increased to 200 N, equivalent to 14 kPa if the force

is converted to the pressure of the footing on the surface of the soil sample. Further increments tended to result in residuals of less than 0.5 kPa.
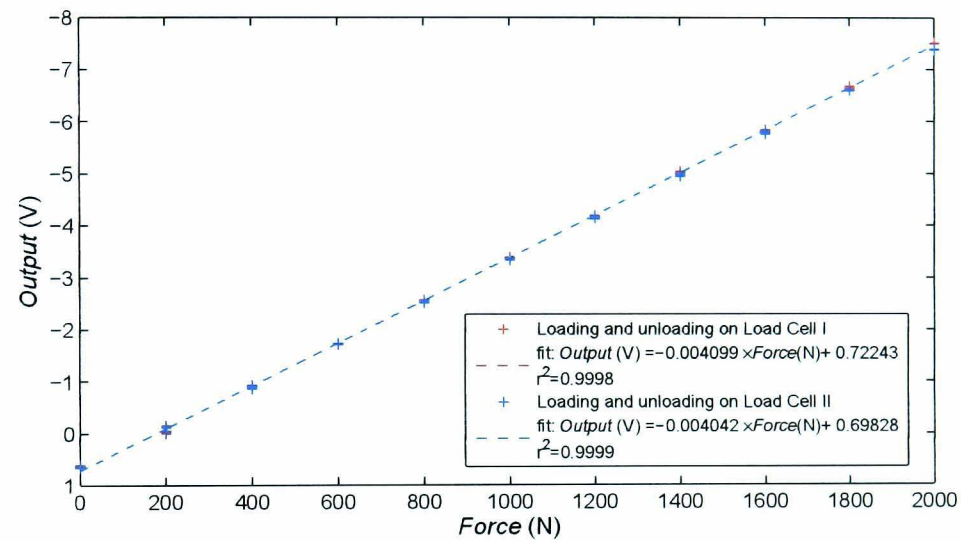


**Figure 3.13:** Calibration results of Load Cell I
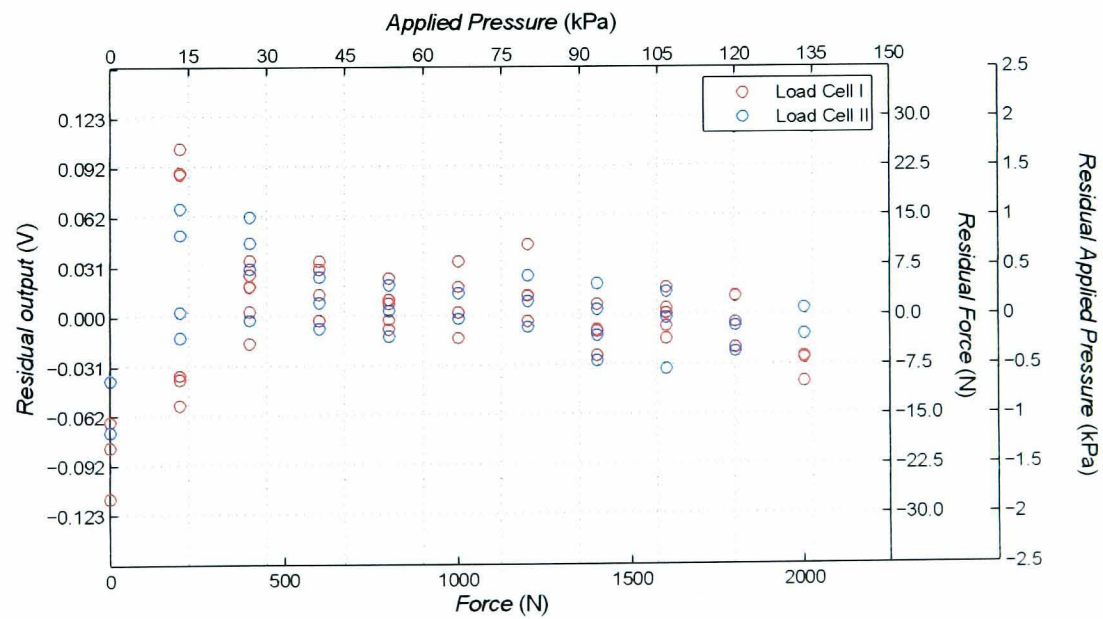


**Figure 3.14:** Residual plot from the calibration of Load Cell I

### 3.3.2 Displacement Measurement

#### *3.3.2.1 Linear Variable Differential Transformers (LVDTs)*

Two 25-mm LVDTs supplied by `MPE Electronics Ltd.` were used for measuring the displacements at the centre of each of the footings during the main tests or the displacements of the consolidation piston during the preconsolidation stages. The transducers were mounted on the shafts of the pneumatic cylinders (see Figure 3.9). The tips of their armatures touched the loading frame as an initial reference for the measurements. The LVDTs were connected to a signal amplifier supplied by `Fylde Electronic Laboratories Ltd.` Besides magnifying the signals 200 times, the amplifier also supplied 10 Volts DC energisation to the transducers. The same logging device and data acquisition system used by the load cells were also applied for all displacement measurements.

The LVDT calibrations were conducted using a digital micrometer calibrator supplied by `Mitutoyo Corporation.` The LVDTs were fixed to the calibrator frame. The calibration points were selected by cranking the calibrator to push in and out the armature slider of the LVDT in 4 cycles. The maximum span that could be measured by the calibrator was 50 mm with a resolution of 0.001 mm. The readings were displayed on an LCD panel.The resulting output data for each distance contained noise of around 5 mV peak-to-peak fluctuation, equivalent to ±0.007 mm when the linear correlation formulae were implemented.

Figure 3.16 shows a residual plot derived from a very strong linear correlation ($r^2 \approx 1$) of the calibration data as indicated in Figure 3.15. The randomly distributed data in the residual plots suggest no further enhancement of prediction curves was required. On average, the measurement error using either of the LVDTs could reach up to 0.025 mm.
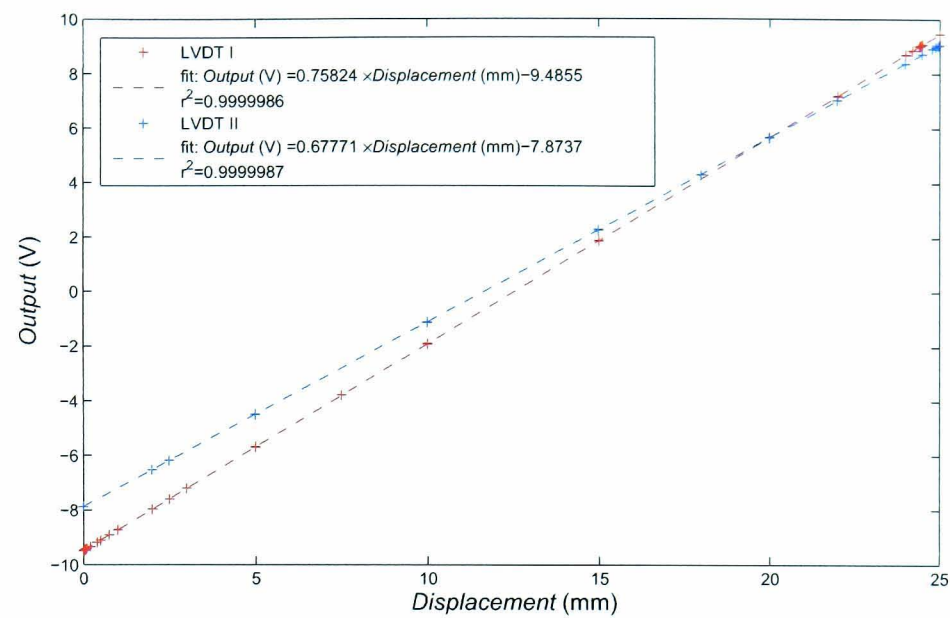
**Figure 3.15:** Linear regression of LVDT1 calibration data
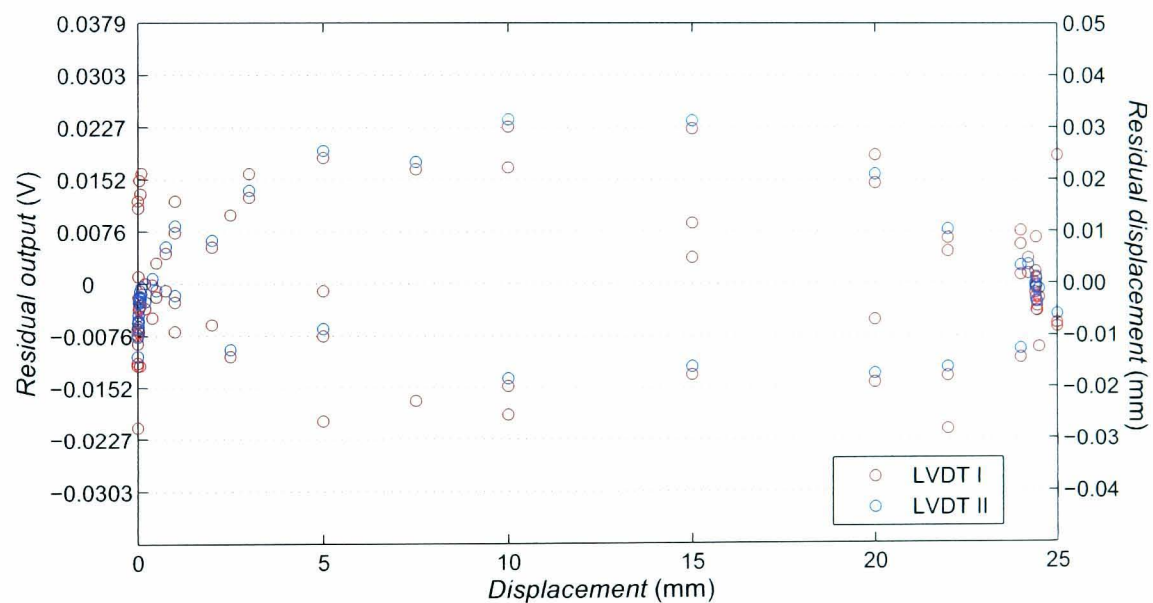


**Figure 3.16:** Residual plot of LVDT1 calibration data

### 3.3.2.2 Digital Camera

A Canon Powershot Pro1 digital camera was devoted to capturing images of soil deformation through the Perspex window of the consolidation chamber. Table 3.3 lists the camera specifications. The camera deploys a CCD (charged-couple device) as a light-sensing device, instead of film and was able to produce an image of $3264 \times 2448$ pixels.

**Table 3.3:** Selected specifications of Canon PowerShot Pro1 digital camera[a]

| IMAGE SENSOR | |
| --- | --- |
| Type | CCD |
| Effective pixels | Approx. 8.0M |
| Size | 8.8 mm×6.6 mm |
| LENS | |
| Focal length | 7.2 - 50.8 mm |
| Maximum f/number | f/2.4 - f/3.5 |
| SHUTTER | |
| Speed | $15 - \frac{1}{4000}$ sec |
| RECORDING PIXELS | |
| Image size | 3264×2448 (Large) |
| | to |
| | 640×480 (Small) |
| EXPOSURE CONTROL | |
| ISO Speed Equivalent | AUTO, 50, 100, 200, 400 |
| WHITE BALANCE | |
| Settings | Auto, Daylight, Cloudy, |
| | Tungsten, Fluorescent, |
| | Fluorescent H, Flash, |
| | Custom |

[a]Product Specification of Canon PowerShot Pro1 (Canon Inc., 2004)

Throughout the tests the camera was mounted on an aluminium frame that was slotted and bolted to the front rods of the loading frame as shown in Figure 3.17. The distance of the camera to the perspex was approximately 620 mm. By adjusting the optical zoom facility, only the chamber was included in the field of view of the camera. The focal length selected from the optical zoom adjustment was 13.1 mm equivalent to approximately 52.1 mm of a conventional 35-mm film camera system.

To get a clear image under the lighting in the laboratory, a suitable selection of the shutter speed and the diaphragm aperture of the lens was required. Throughout the tests the camera was set to its manual mode with locked autofocus. The shutter speed was adjusted to 0.5 second while the aperture, which is represented with the f/number, was maintained at 3.2. It was impossible to use the built-in flash due to the intense reflection from the perspex. The apparent white illumination on the sample from the fluorescent tube lamps used in the laboratory was compensated by setting the *White Balance* facility of the camera to *fluorescent* mode. The ISO speed was set to 50. The setup remained constant throughout the tests.
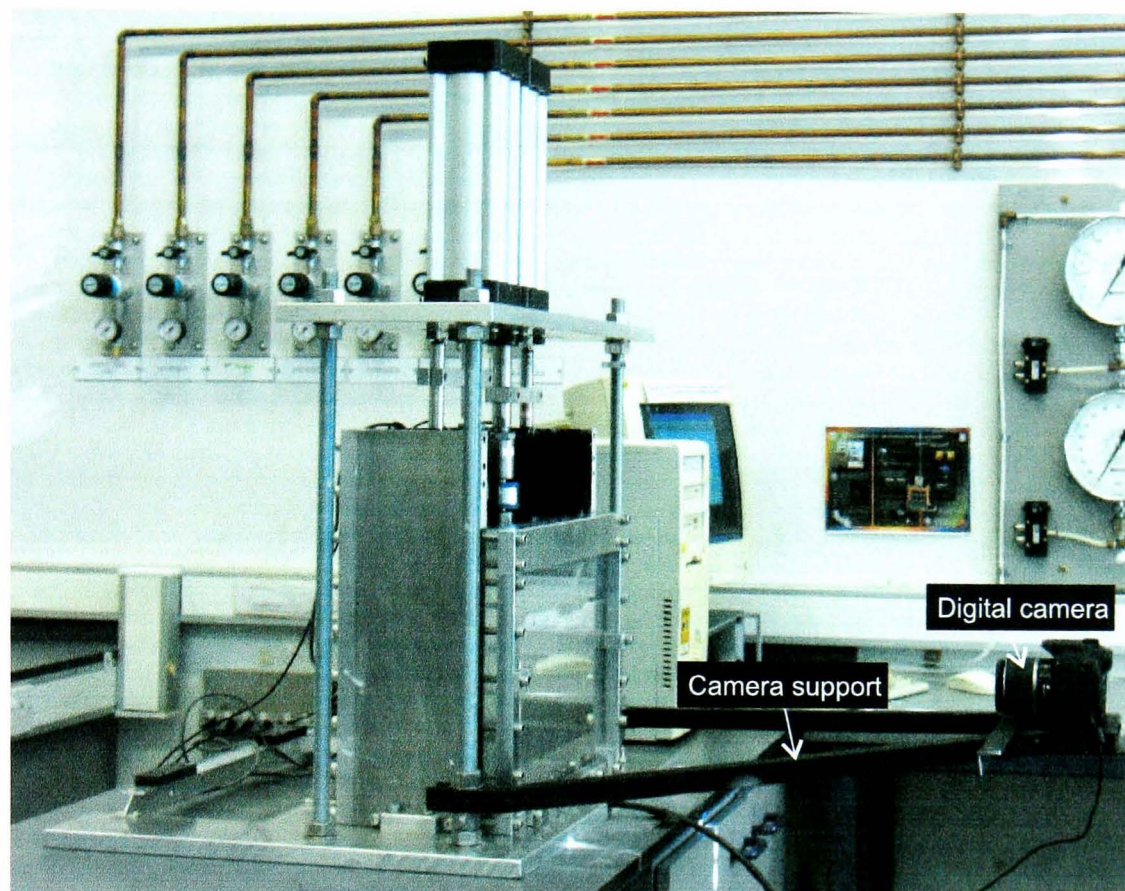
**Figure 3.17:** Digital camera support during testing

Since high accuracy was demanded in the measurement of field displacement, some other parameters regarding imperfection of the camera lens were also required. From these parameters, discussed in Section 4.3, distorted images taken with the camera were corrected.

As indicated in Figure 3.10, the images captured by the camera were immediately stored on a hard disk through a USB cable connection. The acquisitions were assisted by remote shooting software, `RemoteCapture Task Version 1.0`, developed by the Canon Inc. The software provided an option of capturing the images at desired intervals of time. The images were saved using the `JPEG` type of compression with `.JPG` extensions to the filenames.

### 3.4   MODEL PREPARATION

#### 3.4.1   Slurry

Soil samples were initially prepared from slurry by mixing Speswhite kaolin powder with distilled water at a water content of 138% which is slightly above twice its liquid limit (see Section 3.2.1.1.1). The selection of the water content aimed at achieving a homogeneous sample and was based on the workability during the mixing, as suggested by Sheeran and Krizek (1971). This

method has been widely followed by many researchers (e.g. Parry and Nadarajah, 1973; Bai and Smart, 1997; Hird and Moseley, 2000; Anadarajah, 2000; Srisakthivel, 2003). To produce a 35-cm thickness of slurry in the consolidation chamber, 15 kg of kaolin powder was prepared and kept in an oven at 105° C for 4 days to prevent biological activity (Moseley, 1998) during prolonged tests. While waiting for the powder to be air-cooled, 20.7 kg of distilled water was poured into a mixer drum. The kaolin was then slowly and carefully spread onto the water to avoid clouds of the powder. The powder was left to sink under gravity for some time before more powder was added. A spatula was occasionally used to help floating powder fully descend beneath the surface of the water. After 15 minutes the submerged kaolin was blended by turning the drum against a static propeller. The slurry was finally ready for preconsolidation after 1-hour of mixing.

### 3.4.2 Preconsolidation

The slurry was placed in buckets and brought to the consolidation chamber. With the larger perspex plate in place(see Section 3.2.1) and the loading frame unmounted, the slurry was poured into the chamber via a funnel. This was gradually raised as the slurry depth increased to 35 cm. The sample was then smoothed with a specially made template. During this preparation three samples were taken for determining the actual initial water content of each test by oven-drying. The first sample was scooped from the first pour of the slurry when the thickness reached about 10 cm. The second one was sampled at the surface of 20 cm thick slurry and subsequently the last sample was taken from the excess at the time of levelling the slurry.

In order to achieve the overconsolidation ratio (OCR) of 10 (see Section 3.2.1.1) a one-dimensional preconsolidation was required for each of the tests. The experimental setup for the tests is shown photographically in Figure 3.18(a) and schematically in Figure 3.18(b).

Initially, a small pressure of around 2 kPa was needed to avoid squeezing the colloidal slurry through the gap between the edges of the consolidation piston and the inner wall of the chamber. A jar of leadshot together with the self-weight of the piston, was used to produce the pressure. The pressure was maintained until the soil was stiff enough to sustain higher pressures. This was determined from real time logging of the vertical displacement of the sample. For this purpose the two LVDT transducers were mounted on the edges of the piston and attached to the rods of the loading frame. Close observation of the consolidation piston during the first loading was made
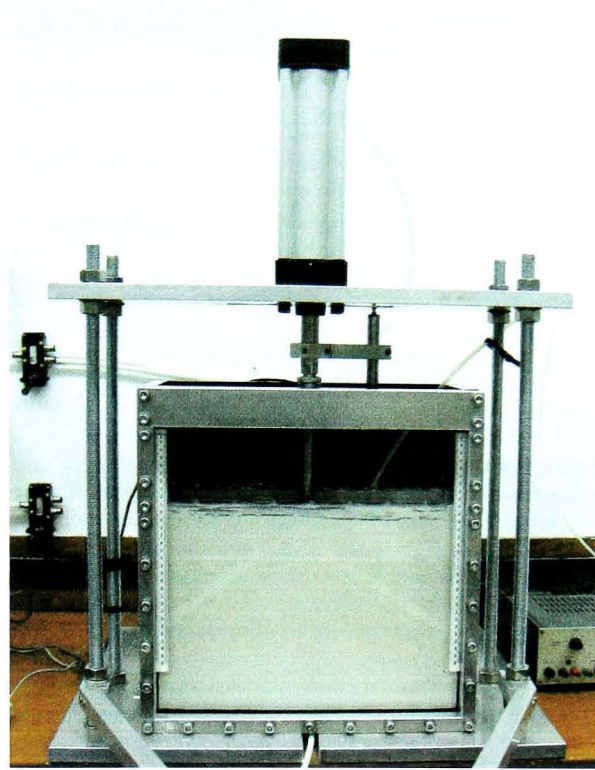
(a) Photograph of test
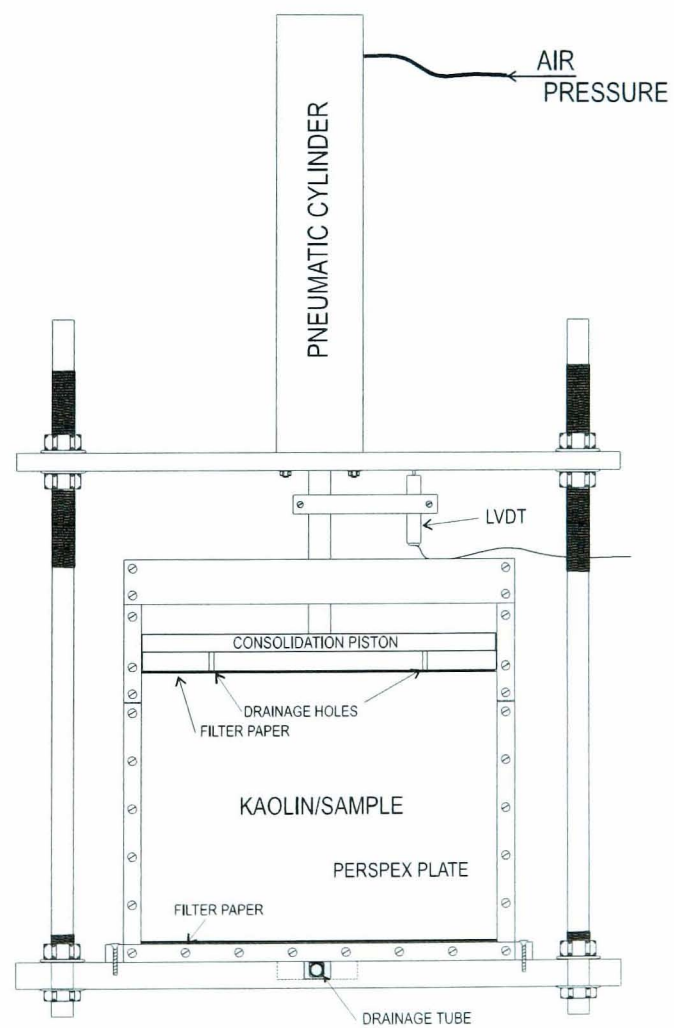


(b) Schematic of main components

**Figure 3.18:** Preconsolidation test

3.4 Model Preparation

in case a small eccentricity of loading caused the piston to tilt. To check that the piston did not tilt longitudinally, two ruler tapes were glued on the left and right sides of the Perspex window to directly inspect the gradient of the piston. The overall inclination of the piston was also observed with a levelling bubble. Several adjustments were made to keep the piston level.

The next series of loadings, beginning with 12.5 kPa, were conducted using a pneumatic cylinder, implementing a load increment ratio (LIR) of unity, i.e. the magnitude of the next vertical stress increment ($\Delta\sigma_v$) was equal to the current vertical effective stress ($\sigma_v'$). The cylinder was positioned and bolted in the centre of the loading frame. Before applying the first load the shaft of the cylinder was lowered to touch the centre of the consolidation piston. An LVDT mounted on the cylinder shaft was used to record the vertical displacements with increase of the preconsolidation pressure. Pressure increments were applied after 100% consolidation had been achieved under the previous increment. The completion of the consolidation was determined using Casagrande's method and displacement-log $t$ relationship. The consolidation data were retrieved from a text file logged by the data acquisition system. After the consolidation under the intended maximum pressure of 50 kPa was complete, the pressure was reduced to 5 kPa to produce an overconsolidated sample with OCR = 10.

During the preconsolidation stages, the consolidation piston was occasionally adjusted to a level position following a slight tilt. The tilts were attributed to a difference in the clearances between the right and left edges of the piston and the chamber walls. The adjustment needed the applied consolidation pressures to be temporarily reduced to zero and it was initially assumed that this did not significantly alter the properties of the soil in its final state. However, this assumption was revised in view of inconsistent magnitudes of settlement from one test to another when the soil was subjected to the footing loadings. The effect of unloading and reloading during preconsolidation on footing settlement behaviour is specifically addressed in Chapter 5 and Chapter 6, beginning in Section 5.3.1.1 and Section 6.2.3.1.4 respectively.

### 3.4.3 Texturing of Sample

To obtain the displacement field beneath the loaded footings, PIV analyses were carried out. The analyses were mainly influenced by the texture of the material as explained in Section 4.2.1. Since the kaolin sample was merely white and did not have any texture, it required an additive placed

on the surface behind the Perspex window. Flock was used for this purpose since White (2002) had successfully applied a PIV analysis to flocked kaolin. The flock was commercially available in model shops. The greenish material was first washed and dried to avoid staining the soil and the perspex window.

Prior to the texturing, the final consolidation pressure (5 kPa) was released. After the cylinder shaft was pulled in, the cylinder was taken off to allow rotation of the chamber (see Figure 3.9(b)). The chamber was fully rotated once the excess water from the preconsolidation was drained out. Immediately after it had been unbolted, the perspex window was slid off the chamber. At this stage, the consolidation piston was not removed, for it provided support to retain the sample. To minimise evaporation, the texturing was performed as quickly as possible (in less than 10 minutes). The flock was spread with a tea filter. This enabled observation of the uniformity of the texture while spreading the flock on the soil face. A light blow on the flocked sample was mandatory to remove unnecessary particles that thickened the flock layer. Finally, the smaller Perspex window (see Section 3.2.1) was bolted onto the chamber. The chamber was then rotated back to its initial position. A layer of 3-mm diameter leadshot, which will be described in Section 3.5, was placed on the model surface to provide a surcharge of about 5 kPa.

## 3.5 TESTING PROGRAMME

### 3.5.1 Test Notation

Table 3.4 lists the notations of the test categories that will be used throughout the thesis. SF,

Table 3.4: Symbols of Test Category

| No | Test Name | Description |
|----|-----------|-------------|
| 1 | SF | Single footing (preliminary test) |
| 2 | DF$n$ | Double footing without sheet wall |
| 3 | SP$n$ | Double footing with floating sheet wall |
| 4 | FX$n$ | Double footing with fixed sheet wall |

standing for Single Footing, denotes a test observing soil deformations due to loading on a single footing. Such a test was performed only once as a preliminary, trial test. The main tests were always carried out with two closely-space footings and are referred to as *double footing* tests. DF is abbreviated from Double Footing. SP represents a test performed with a double footing and the insertion of an aluminium sheet pile. In this test, a "floating" sheet pile 100 mm long was driven

between the two footings. Lastly, FX symbolises the presence of a "fixed" sheet pile in the tests with a double footing. Two small rods resting on the chamber base were used to restrain the tip of a 100-mm sheet pile from vertical movement. The letter $n$ in Table 3.4 identifies the $n^{th}$ test of each category. For instance, DF2 means the second test with a double footing.

### 3.5.2   Model Tests

As described at the end of Section 3.4.3, leadshot was used to provide a small surcharge pressure after texturing the model. However, before pouring the leadshot, the two footings were positioned. Figure 3.9 illustrates the model test setup. After the texturing was complete and the chamber was rotated back to the normal position, the consolidation piston and the porous plastic sheets were taken off. Immediately, two cylinders were mounted on the loading frame where their positions were fixed for the designed separation (20 mm) of the two footings. Each footing was placed on the surface of the sample by connecting it to the cylinder shaft and by slowly lowering until the footing base lightly touched the surface of the sample. To facilitate this purpose, threaded holes were provided in the centre of each footing. The connection was done by screwing a cut bolt into the footing and also into an adaptor that was attached at the tip of the shaft. Once the footing was perfectly placed on the sample, the connection was unbolted and the shaft was fully pushed into the cylinder. The procedures were repeated for the placement of the second footing. At this stage, the cylinders were still unconnected to the pressure system, preventing accidental application of pressure on the footings. A mini bubble level was laid on the footings to make sure that they were properly levelled.

Thin filter paper was laid out to cover the soil surface outside the footings to avoid penetration of the leadshot. The load cells and the round tipped adaptors were then mounted at the tips of the cylinder shafts and carefully lowered until the adaptor tips lightly touched the centres of the footings. For the displacement measurements at the centres of the footings, an LVDT was mounted on each shaft and positioned to provide an initial reference for the measurements. To replace the final consolidation pressure of 5 kPa, 30.6 kg of leadshot was then poured onto the sample.

There were three different procedures for placing the leadshot onto the sample, depending on the type of test. In the DF tests, the leadshot was dropped with a small cup to cover all the footings. In the SP tests, the aluminium sheet (Figure 3.19, but without the restraining rods), as described

in Section 3.2.1.1.6, with a length of 100 mm was first placed in the middle of the gap between the two footings before gradually placing the leadshot. As illustrated in Figure 3.20, the tip of the
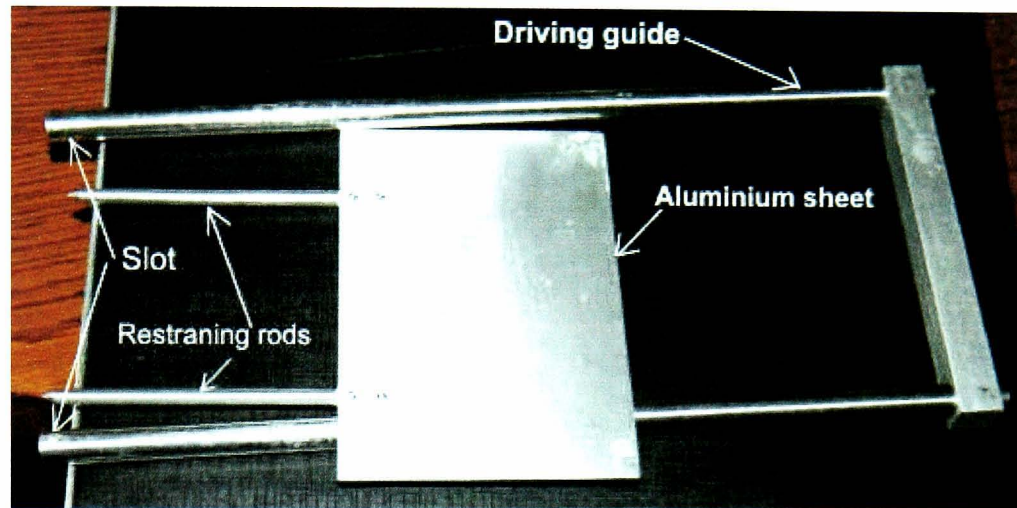


**Figure 3.19:** The aluminium sheet and the driving guide used in the FX tests (no restraining rods in SP tests)

sheet stood on the soil surface, while the other end was held inside the slots at the tips of a driving guide. In order not to load the sheet, the driving rods were slotted through holes in the loading frame and supported by clips. In the FX tests, an aluminium sheet with the same length was used. However, its tip was connected to two small rods (Figure 3.19) with which the sheet was restrained vertically with respect to the base of the chamber. Before the placement of the leadshot, the tips of the rods were positioned on the soil surface in the centre of the gap between the footings.

After placement, the surface of the leadshot was levelled with a spatula. To keep the soil fully saturated, distilled water was poured in until its level was approximately 5 mm above the soil surface. The setup was left for at least 12 hours. At the commencement of each test, some of the surface water was drained out to leave a water depth of about 2 mm. Since every test could take more than a month, some water had to be occasionally added to compensate for evaporation.

For the purpose of determining the transformation from image to object space, a target marker sheet (Figure 3.21) was attached in front of the Perspex window of the chamber. The marker sheet is discussed in detail in Section 4.4.1. At this stage, the camera frame was attached to the rods of the loading frame. Levelling of the frame on which the camera was supported was checked with a mini bubble level. The digital camera was mounted and connected to the personal computer for
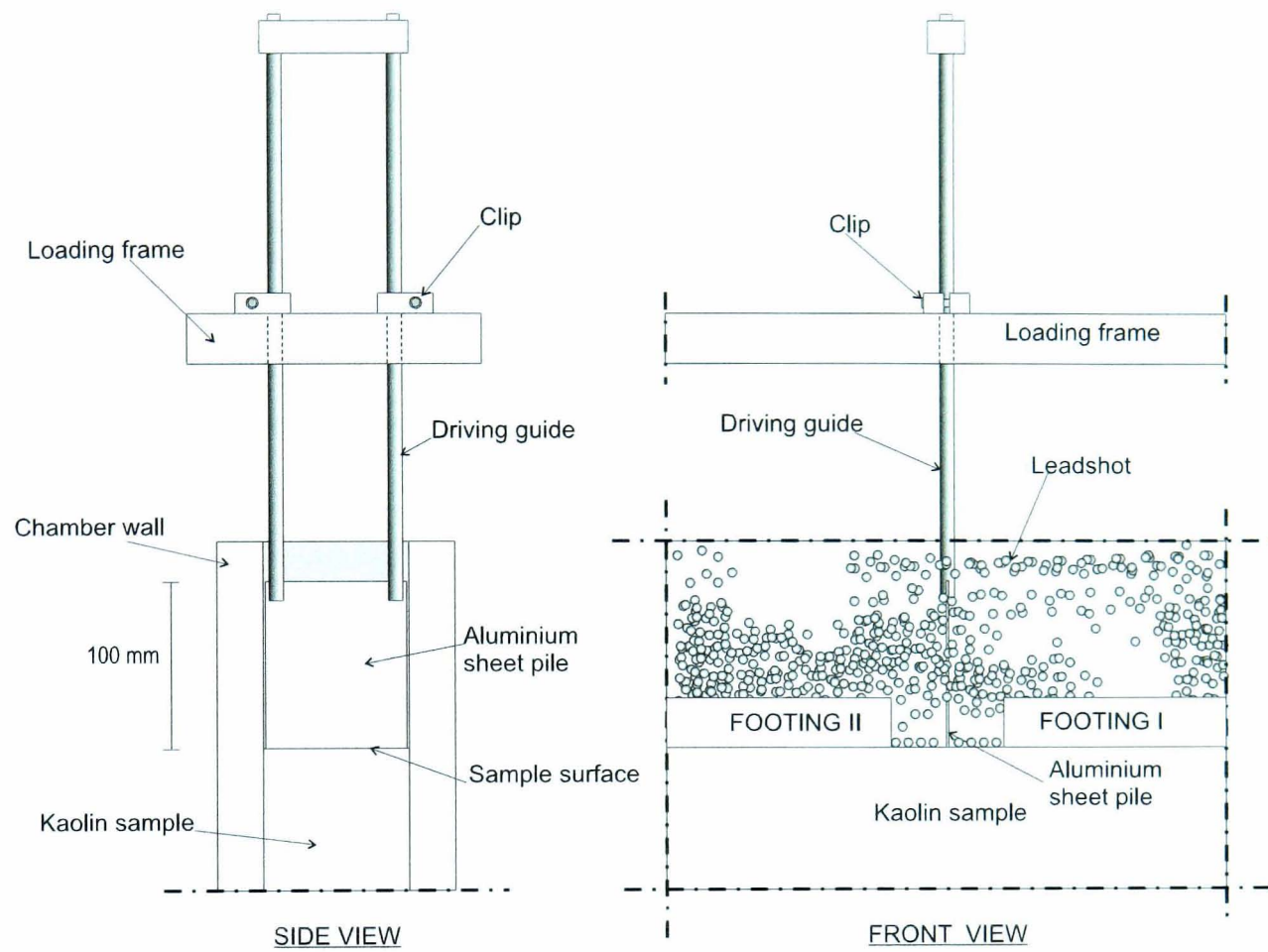
**Figure 3.20:** The aluminium sheet and the driving guide setup in SP tests (some components are not displayed)
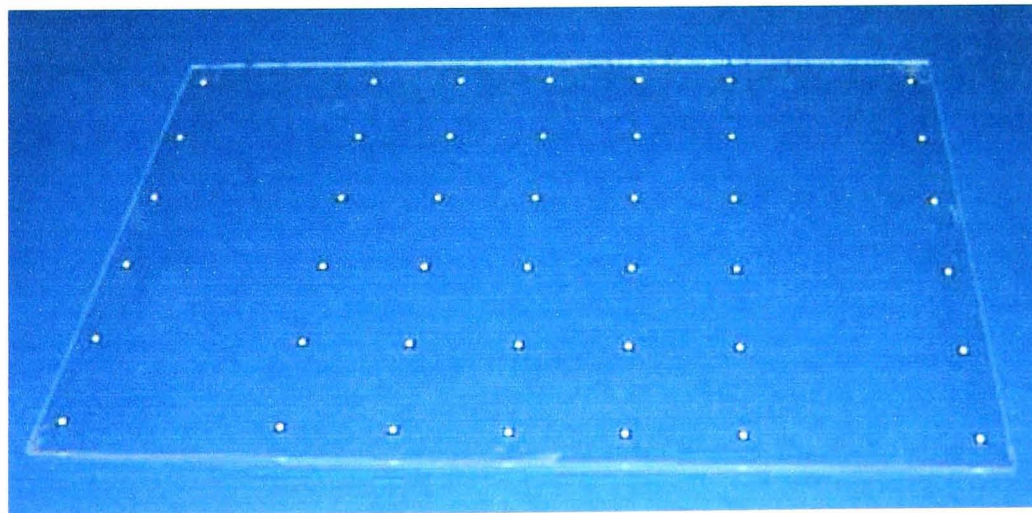


**Figure 3.21:** Target markers for camera calibration

image storage. The position of the camera was adjusted to be as coplanar as possible with the Perspex window.

All the main tests commenced with loading of Footing I (see Figure 3.9). The maximum pressure of 80 kPa, including the leadshot surcharge, was applied on each footing. The loading was divided into 15 increments. Further pressure increments were applied once the consolidation under each increment was completed. In the DF tests, the first loading on Footing II was applied immediately after 100% consolidation under the final pressure of 80 kPa on Footing I. The pressures were increased in the same manner as those applied on the Footing I. Dissimilarly, in the SP and the FX tests the loading on Footing II was commenced only after 100% consolidation under stresses due to the insertion of the aluminium sheet. This time was based on the consolidation monitored at the centre of Footing I.

In the SP tests, the full pile length of 100 mm was pushed down with the driving guide. The rate of penetration was about 10 mm/s but penetration was halted for 1 minute at intervals of 10 mm to allow image acquisition to investigate the effect of the insertion on the first footing. The intervals were inscribed on both rods of the driving guide with a permanent marker pen. Including the image acquisition, the total time of the penetration was about 11 to 15 minutes. In the FX tests, the full lengths of the rods supporting the sheet pile were first inserted in one push. After a pause for image acquisition, the insertion of the sheet was continued in the same manner as for the SP tests.

All the tests were completed with sampling of the water content and testing of the undrained strength of the soil. The locations of the sampling and the strength testing are detailed in Figure 3.22. For each numbered box an average value of the corresponding water content was obtained from three samples perpendicular to the perspex window. One undrained strength test was carried out at each location shown in the figure. A 33-mm diameter hand shear vane (Pilcon-Edeco supplied by English Drilling Equipment Co. Ltd.) was utilised for these tests.
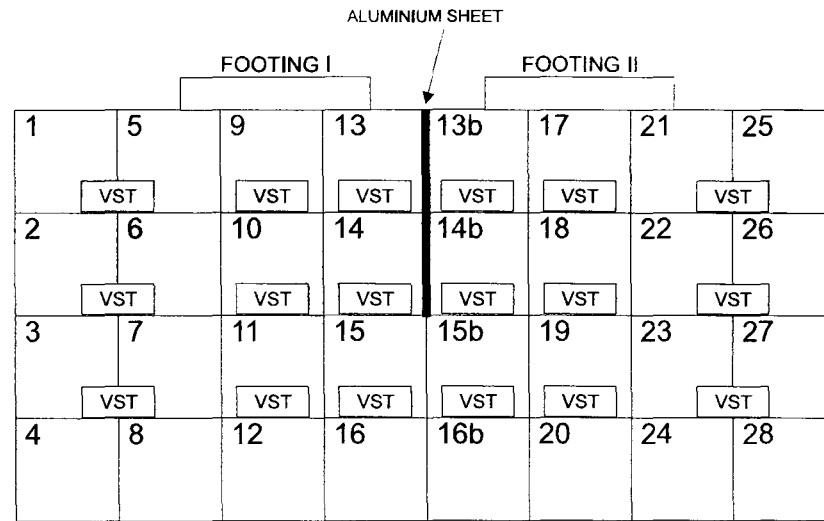
**Figure 3.22:** Locations of water content sampling and vane shear tests

# Chapter 4

# MEASUREMENT OF SOIL DISPLACEMENT: PIV AND PHOTOGRAMMETRY

## 4.1 INTRODUCTION

Particle Image Velocimetry (PIV) was used as a main tool for measurement of the displacement field. In addition, several photogrammetric procedures were performed in order to convert the results in image space to actual displacements in world coordinates. The analysis consisted of four main steps: PIV analysis, distortion correction, image-to-object transformation, and refraction correction. In the PIV analysis the displacement was represented in pixels of which the coordinates were still distorted by the camera system. The correction of the pixel locations was performed after the intrinsic camera parameters were known from a camera calibration. The amount of actual displacement was still unknown until a transformation from image to object space was established. Since the images were captured from the objects existing behind the Perspex window, the apparent positions of the objects were then corrected to obtain their actual positions. All of the analyses were carried out using algorithms written with `Matlab`™.

## 4.2 PARTICLE IMAGE VELOCIMETRY (PIV) ANALYSIS

As described in Section 3.3.2.2, digital images were captured during each test for tracing the soil displacement with PIV analyses. The analyses were conducted using the `GeoPIV` software, a `Matlab`™ module developed for geotechnical engineering purposes by White and Take (2002). The applications of `GeoPIV` had been validated by its developers in their research (White, 2002;

61

Take, 2003; White et al., 2003; White and Bolton, 2004). Figure 4.1 schematically illustrates the principles of the PIV analysis. The displacement was determined by comparing patches taken from
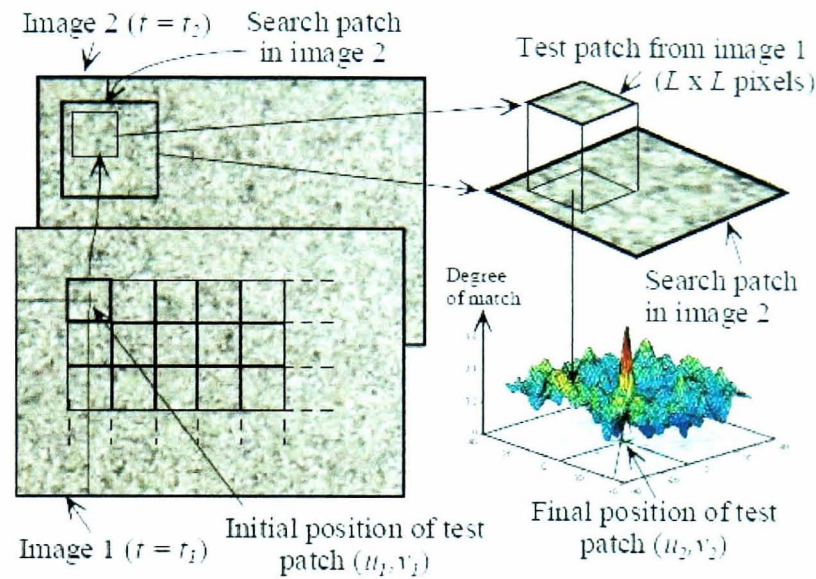


**Figure 4.1:** PIV analysis (after White and Take (2002))

the areas of interest of the first image to the search zones in the second image. The displaced points were indicated by the highest degree of match of the patch in the search zone. PIV analysis was unsuccessful in searching matched areas in an image if the areas did not have enough surface texture. In hydraulics research, to study flow characteristics with PIV, particulate materials are seeded in water to create texture over the area of interest in the images captured. The first consideration before conducting the physical modelling was therefore the selection of a suitable texture. An error could be also introduced from inappropriate selections of patch size and search zone in the analysis. Prior to the tests both issues, the texturing and the patch size, were therefore carefully addressed.

### 4.2.1  Effect of Texture

The flocking of the kaolin surface (see Section 3.4.3) was used to enhance its texture. In image processing, the texture of the flocked kaolin surface could be easily recognised from the brightness intensity of the pixels comprising the image. Figure 4.2(d) illustrates the brightness intensity of a cropped image of the Speswhite kaolin after a preconsolidation test. Compared with that of sand (Figure 4.2(b)), the brightness of the kaolin image is more uniform and has a much narrower

bandwidth. The bandwidth was extended after the addition of the flock on the surface of the kaolin (Figure 4.2(d)).

To show that the PIV analysis was successful, several images were taken on graded flock glued on a piece of white paper and a Perspex plate which were horizontally displaced with a micrometer(see Figure 4.3(a)). The effect of the flock distribution covered by the mesh on the PIV analysis was examined. Figure 4.3(b) illustrates the displacement vectors of the points in the



(a)  Sand



(b)  Intensity



(c)  Image of pure kaolin



(d)  Intensity of pure kaolin image



(e)  Image of flocked kaolin



(f)  Intensity of flocked kaolin image
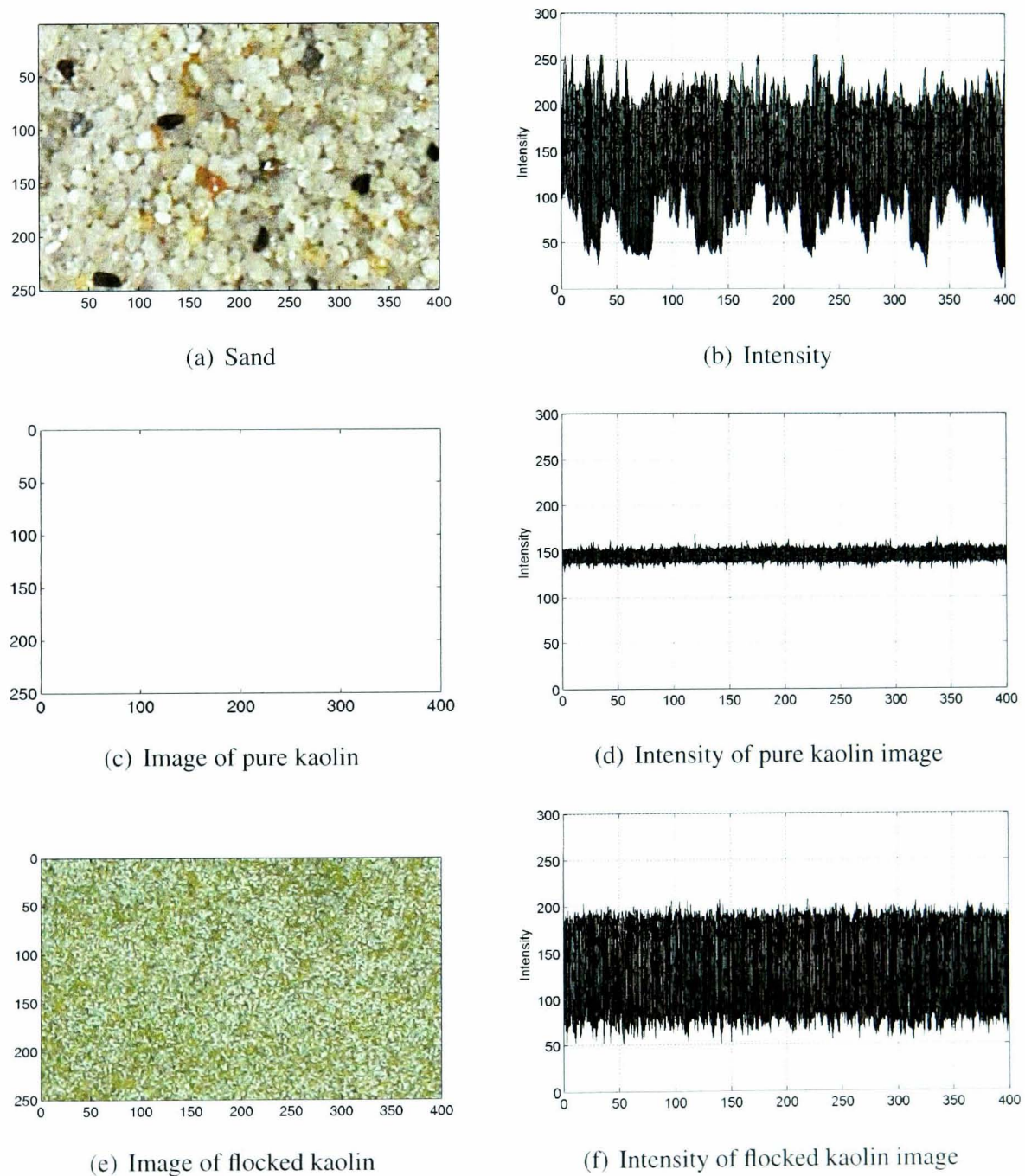
**Figure 4.2:** Typical intensity of sand image
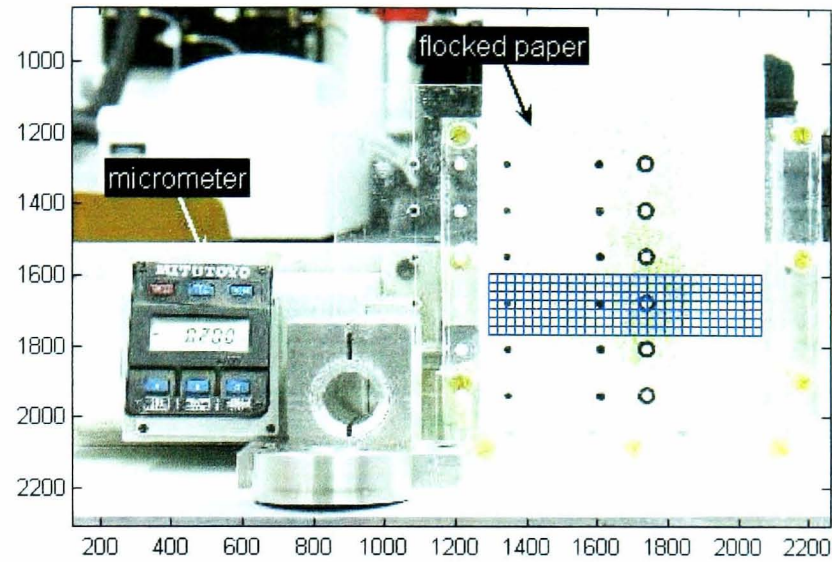
(a) Test setup
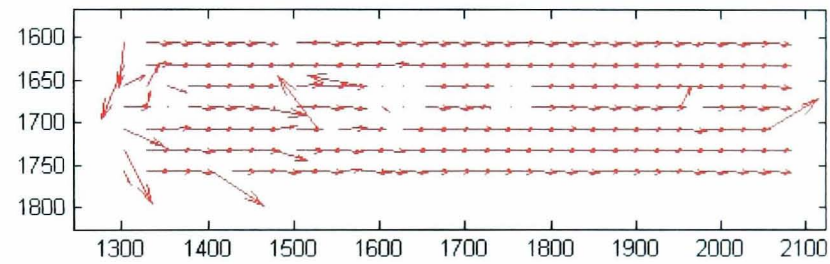


(b) Displacement vectors

**Figure 4.3:** Effect of flock distribution

centre of each patch in the mesh. Some wild vectors were encountered among those parallel to the displacement direction. The wild vectors indicated that the patches were not able to match the right areas over the search zones. The errors were attributed to flock that was sparsely distributed. It is indicated in Figure 4.4 (in which the intensity of the target marker has been removed) that the less dense flock resulted in a narrower bandwidth of the image intensity.
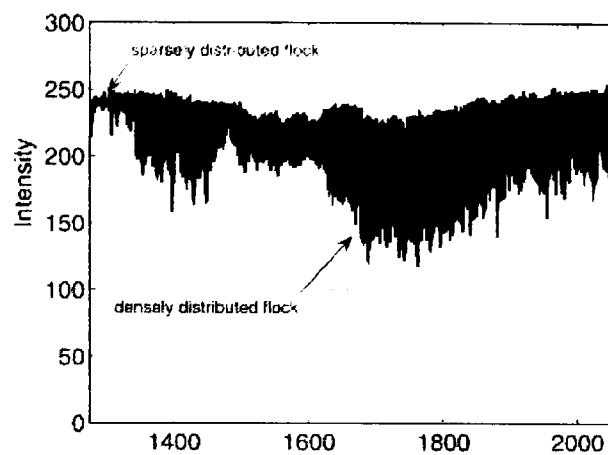
**Figure 4.4:** Intensity of flocked paper image

## 4.2.2 Effect of Patch Size

The success of the PIV analysis was also dependent on the size of patch. As shown in Figure 4.5(a), the PIV analysis tended to perform better when larger patch sizes were used. The larger patch size compensates for the scarcity of the texture of the flock. The greater the area covered by the patch the more unique was the texture (see Figure 4.5(b)).

Since the intensity depended on the density of flock, it was decided to apply dense flock onto the surface of the kaolin for the experiments. A further observation of the effect of patch size on the accuracy of the PIV analysis was then performed on this densely flocked kaolin. Similar to the procedures conducted by White et al. (2003), a cropped image was displaced by 10 pixels in the horizontal direction, using image processing (see Figure 4.6). The errors in the PIV results are shown in Figure 4.7.

The standard errors resulting from the validation agree very well with those found by White et al. (2003). When a patch size of 50 pixels was used, the mean error in both $u$ (horizontal) and $v$ (vertical) directions was 0.0016 pixel. The average standard error for this patch size was 0.004 pixel. These errors decrease with larger patch sizes. However, the size has to be limited if the area of interest lies close to the image border. In this case, the PIV analysis will be forcedly terminated if the dimension of the patch is larger than the available image matrix.
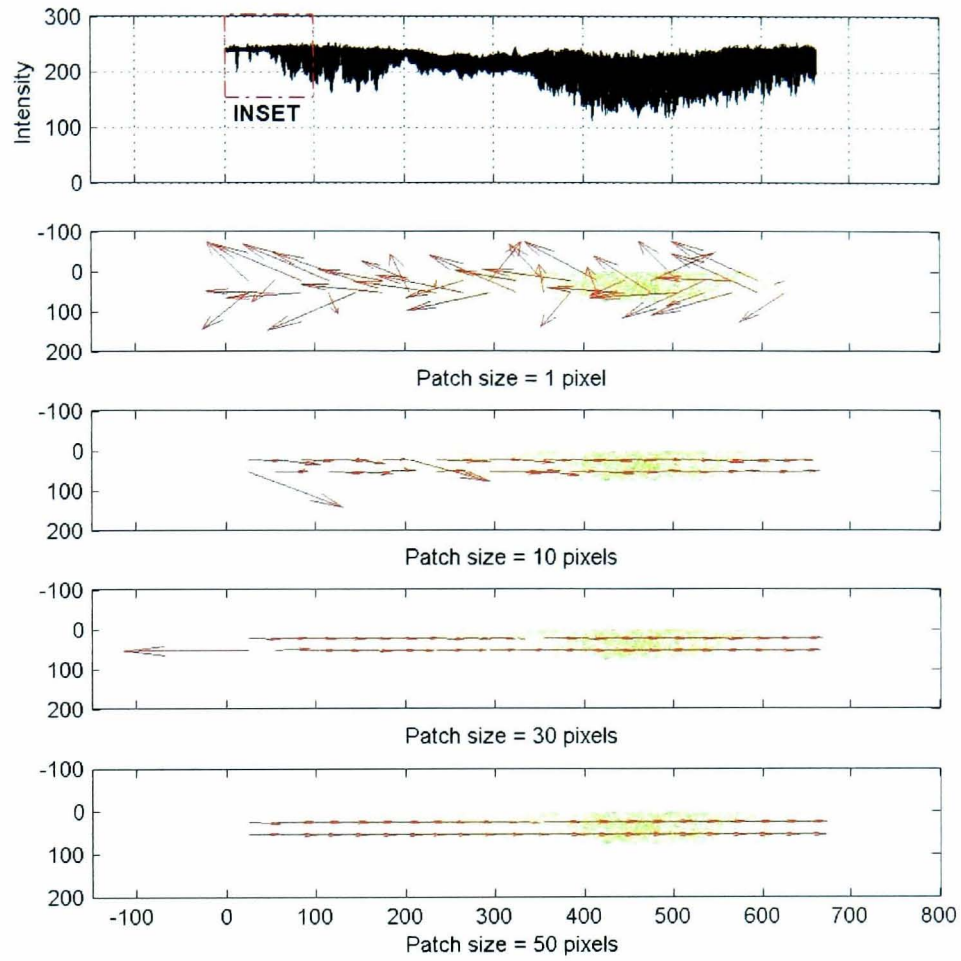
(a) Displacement vectors from different patch sizes
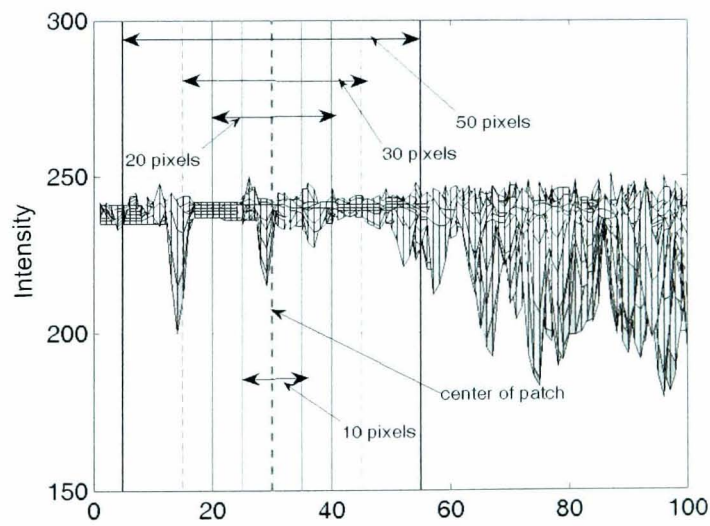


(b) Texture covered by different patch sizes (intensity taken from the inset in Figure 4.5(a))

**Figure 4.5:** Effect of patch size on PIV analysis
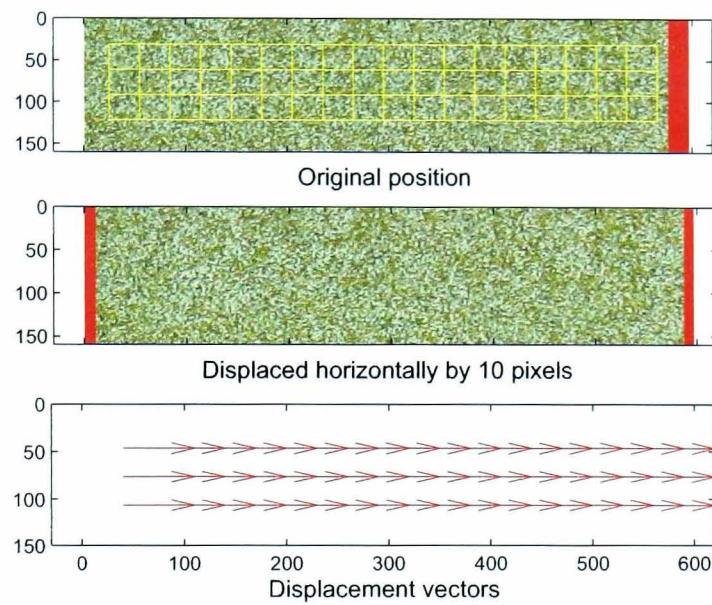
**Figure 4.6:** Accuracy test of PIV for the flocked kaolin used in the experiment
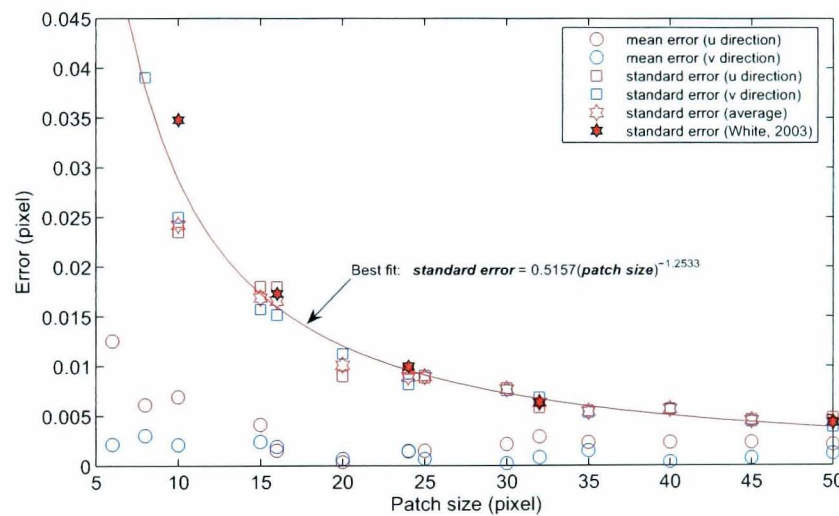


**Figure 4.7:** Accuracy and precision of PIV analysis with respect to patch size

### 4.2.3   Application to Experiments

In most of the PIV analysis for the experiments, a patch size of 30 pixels (corresponding to a distance of approximately 4 mm center-to-center of the patches) was implemented as shown in Figure 4.8. To cover all the soil sample, 5152 patches were required. When quite large displacements occurred, a pair of images sometimes was not sufficient to produce representative displacement vectors. In this case, intermediate images were needed. The analyses were then carried out using successive pairs of images. Large displacements often changed the texture drastically and caused difficulties for the PIV analysis to match the patches, resulting in wild vectors. The size of the
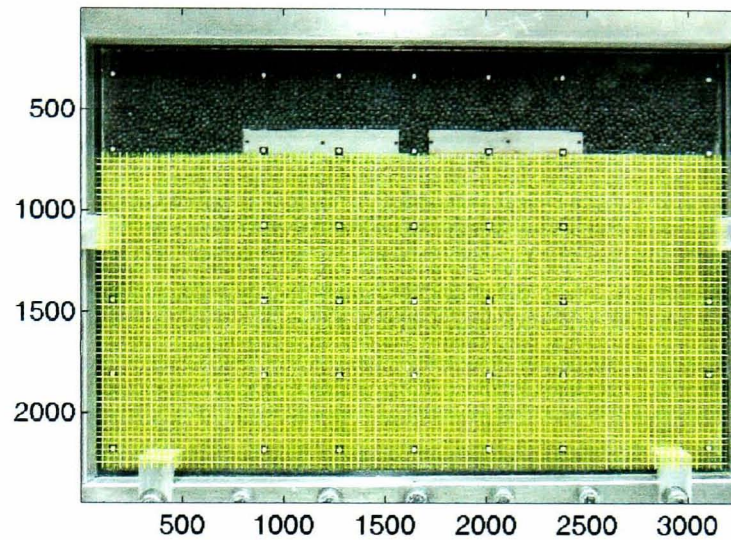
**Figure 4.8:** PIV mesh

search zone should not extend far beyond the actual displacement. Besides wasting analysis time, excessively large search zones tend to provide higher possibilities of erroneously matching areas. A search zone of 50 pixels was used in most analyses.

## 4.3  DISTORTION CORRECTION

As mentioned in Section 2.4.2 there are some factors that influence the accuracy of the measurement using a commercial digital camera. The pixels comprising an image taken with the camera might not be located in their "true" positions, but the errors can be corrected once the parameters contributing to the distortion are known. Usually the parameters are obtained through a calibration of the camera. The Canon Pro1 was calibrated using the Matlab$^{TM}$ toolbox developed by Heikkilä (2000a) using two images of the target markers (see Figure 3.21) with different camera positions.

Table 4.1 lists eight intrinsic parameters resulting from the camera calibration. The ratio of pixel dimensions, denoted as the scale factor $s$, was found to be approximately unity. The focal length $f$ of 13.092 mm was very similar to that in the manufacturer's specification of 13.1 mm. There was a slight offset between the coordinate of the principal point $(u_0, v_0)$ and the image centre. The coefficients of radial and tangential distortion were represented by $k$ and $t$. The overall standard error of the calibration was 0.08 pixels. Figure 4.9 illustrates an artificial image and its

**Table 4.1:** Output of camera calibration

| Parameter | Output |
|:---:|:---:|
| $s$ | 1.0001 |
| $f$ | 13.092 mm |
| $(u_0, v_0)$ | (1633.2673,1263.5144) |
| $k_1$ | $3.663 \times 10^{-4}$ mm$^{-2}$ |
| $k_2$ | $1.172 \times 10^{-5}$ mm$^{-4}$ |
| $t_1$ | $4.633 \times 10^{-4}$ mm$^{-1}$ |
| $t_2$ | $4.586 \times 10^{-4}$ mm$^{-1}$ |

distorted image after all camera parameters were incorporated in the inverse of the equation used in the calibration (see Heikkilä and Silvén (1997); Heikkilä (2000b)). It is evident that any apparent
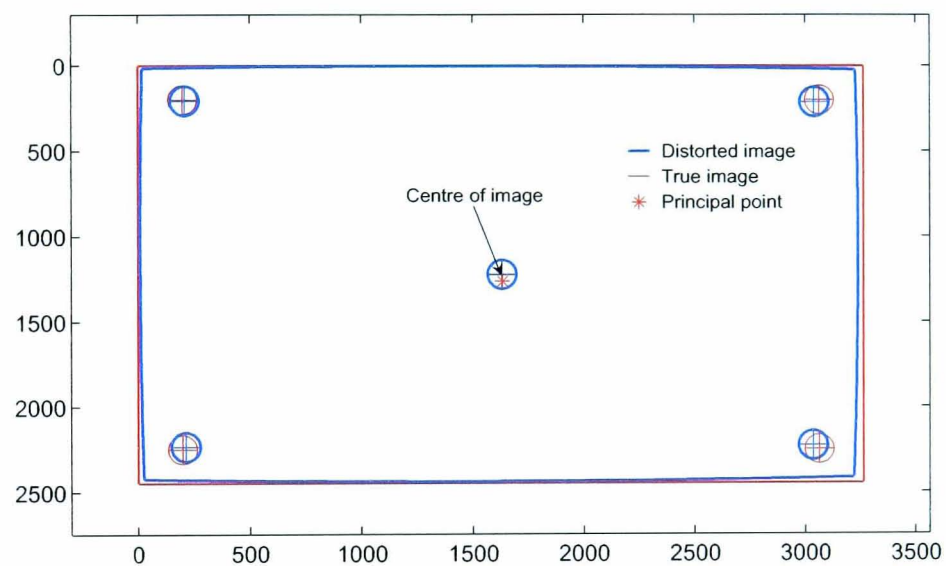


**Figure 4.9:** Illustration of distortion effect (artificial image)

pixel (composing an image) produced with this camera was not located at its "true" coordinate. In general, the distortion was more severe as the pixels were located further away from the principal point.

### 4.4 CLOSE RANGE PHOTOGRAMMETRY

#### 4.4.1 Target Markers

A thin perspex plate was used to accommodate 42 target markers that were spread over the plate (see Figure 3.21). Figure 4.10 shows the layout of the markers after the plate was attached outside the perspex window. Every marker comprised a white spot with a diameter of 3 mm on a black rectangular background. It was initially made by drilling blind holes in the plate with a positioning

accuracy ±0.01 mm. Each hole was then filled with the white correction fluid Tipp-Ex™ and
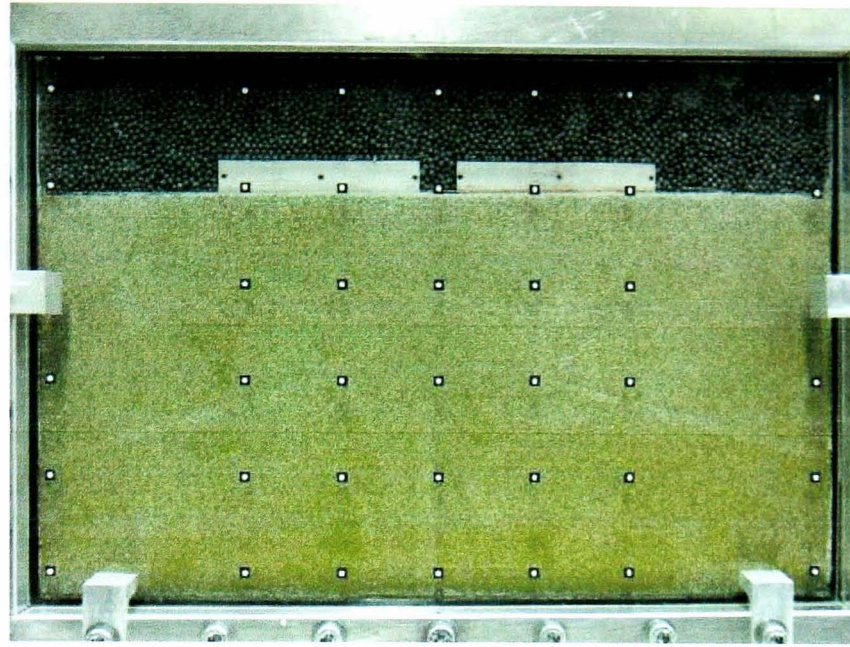


**Figure 4.10:** Layout of target makers on perspex plate

the background was made from insulation tape stuck on the other side of the plate. The position of the plate remained fixed throughout each test during which images of the target markers and the model were captured.

With the camera setup as mentioned in Section 3.3.2.2, the image consisted of approximately 8 million pixels. Every pixel possessed an intensity of brightness, so that, if the image was treated as an 8-bit grey colour, the intensity was scaled from 0 (pure black) to 255 (pure white). Although the images acquired during the tests were stored as "true-color" images which consisted of red, green, and blue colour-planes, only the red plane was used for image processing. When converted to grey scale, pure white pixels on the image indicated the highest concentration of each colour. The purpose of colouring the target markers with white and black was to achieve homogeneous and extreme values of the intensity. The black background was meant to differentiate the markers from the flocked kaolin. Figure 4.11 and Figure 4.12, respectively showing a marker with flocked kaolin behind and its intensity, demonstrate that this was achieved despite some noise on the face of the marker and the background.
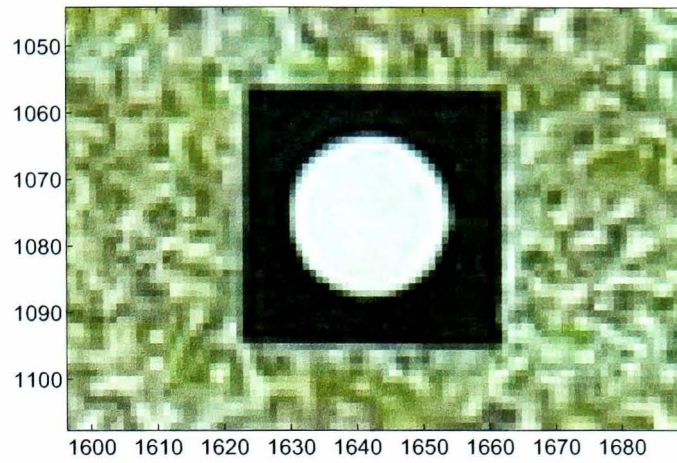
**Figure 4.11:** Patch of target maker and flocked kaolin
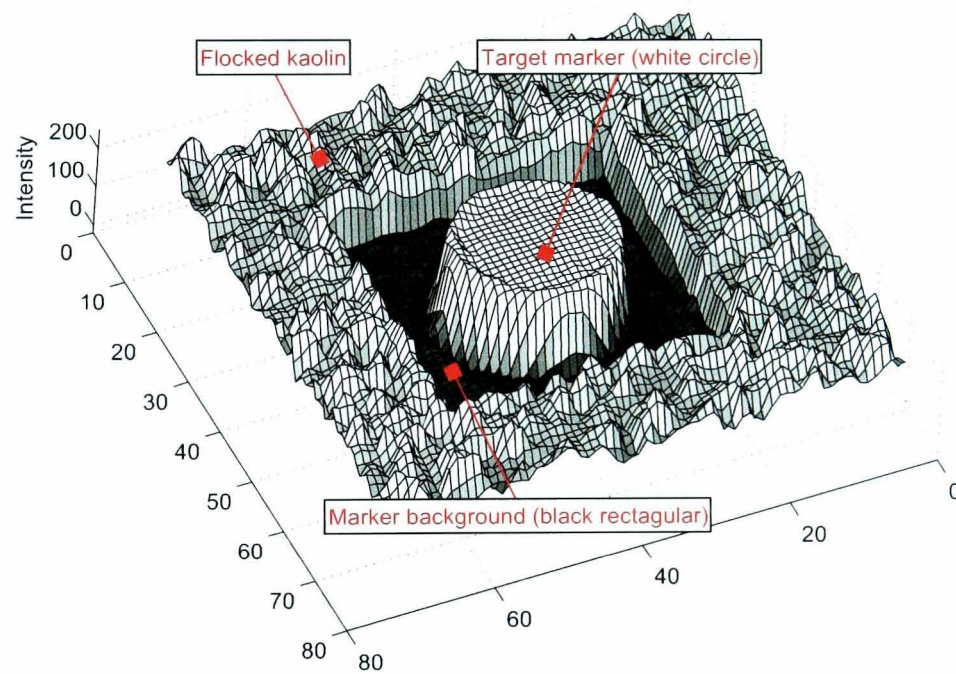


**Figure 4.12:** Intensity of the image of Figure 4.11

### 4.4.2 Centroiding

The transformation from image to object space required the positions of the target markers to be defined in each image. The positions were determined as the centroids of the markers, which were calculated according to the area moment as expressed in Equation 4.1. The coordinates of the centroids $(C_x, C_y)$ were determined from the ratio of the area moment of the individual pixels to

their total area $(A)$.

$$C_x = \frac{\int (x)dA}{A}$$
$$C_y = \frac{\int (y)dA}{A}$$

(4.1)

It was also possible to find the centroid by using the pixel intensities (Take, 2003), but this could only be achieved reliably if the intensity of the marker image was axisymmetric. Some noise that was observed in the intensity of the marker image discouraged the use of the method.

Thresholding was performed in order to isolate the marker pixels from those nearby. The image in which the pixels had smaller or larger intensities than an assigned value, the threshold, was converted to a binary form. The larger values were converted to ones, while the others were zeroed. As a result of non-uniform intensities among the markers, the centroiding had to be carried out individually for every marker using cropped images. An arbitrary size of cropping could lead to another problem. Figure 4.13 illustrates a single thresholding on the image of the marker shown in Figure 4.12. Because some pixels of the flocked kaolin image have intensities larger than the threshold value, they result in non-zero binary pixels around the marker (Figure 4.14). This would
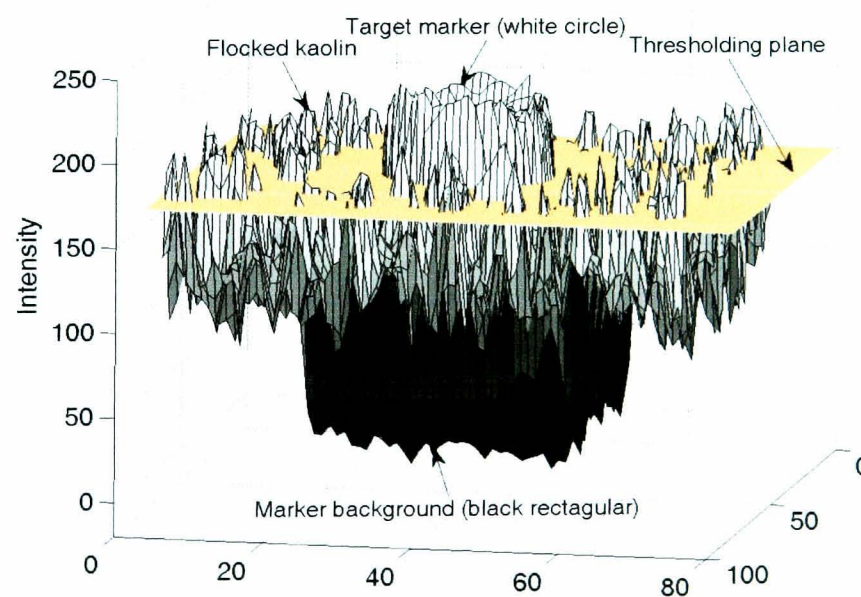


**Figure 4.13:** Single thresholding on the 20th target marker

contribute additional areas to the centroiding analysis and the resulting centroid might deviate from
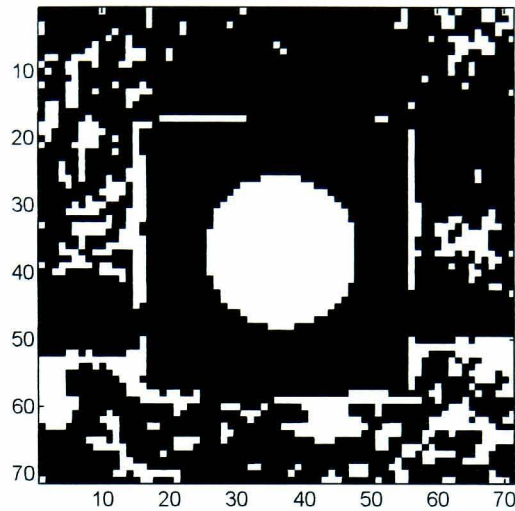
**Figure 4.14:** Pixels in a binary form of the 20th target maker

the centre of the circular marker. The marker images were cropped only inside the area of the black rectangular background.

The centroid was established by applying several thresholds to every marker. The centroid of each marker was then estimated by averaging the centroids resulting from using different thresholds. Figure 4.15 schematically shows the thresholding mechanism. The intensity of the marker
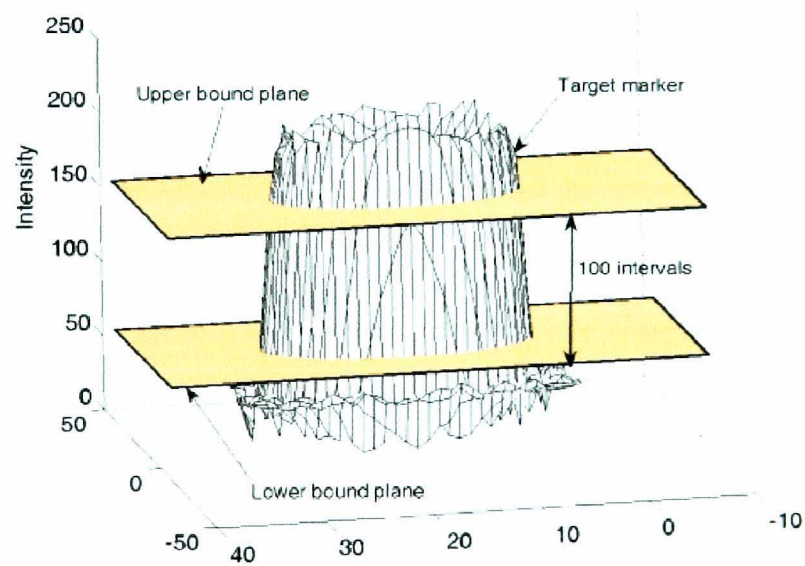


**Figure 4.15:** Multiple thresholding on the target marker

was divided by 100 thresholds between the upper and lower bounds. The bounds were predefined by excluding 10% of the extreme intensities. Since some noise was encountered at the top and the bottom (at the black rectangle), it would be misleading if the extreme values were considered.

Gaussian smoothing was implemented to exclude the noise (Haralick and Shapiro, 1992; Jain et al., 1995; Davies, 2005). This was performed using a 2-D convolution operator with a kernel representing the Gaussian bell shape. In the analysis, a standard deviation $\sigma = 1$ and mean (0,0) were used. Figure 4.16 demonstrates the application of the smoothing to remove some noise in the intensity of a marker image. Before the smoothing (Figure 4.16(a)), some noise is found around the



(a) Before smoothing      (b) After smoothing
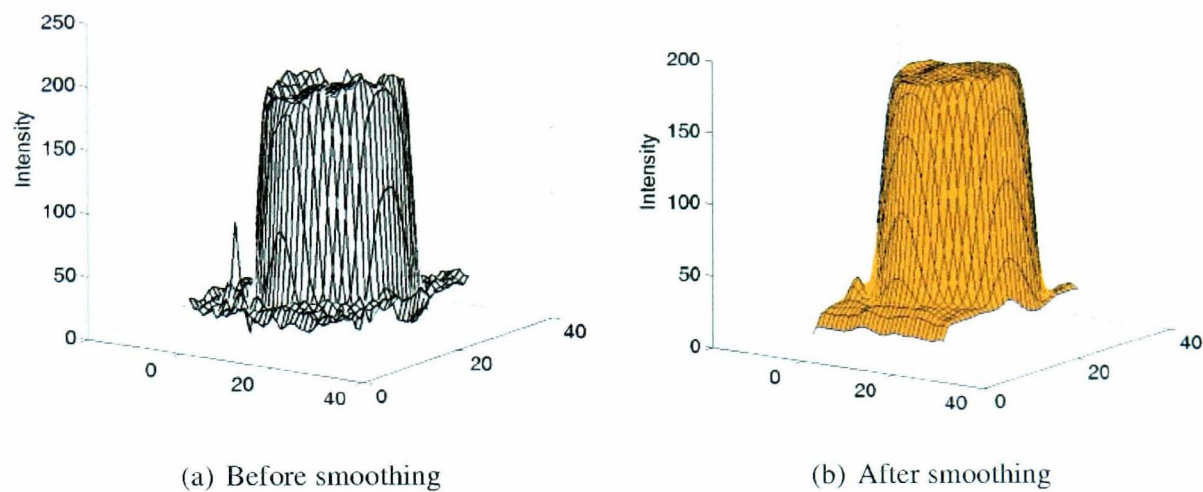
**Figure 4.16:** Gaussian smoothing to remove noise

top and the bottom of the cylinder (marker intensity). As shown in Figure 4.16(b) the noise disappears after the smoothing. However, it should be noted that the convoluted intensities could not be used in the centroiding calculations since some original intensities around the cylinder were also changed. Also, it was still possible to have pixels of non-zero binary intensities at the thresholds near the lower bound if noise was present. However, by implementing a cavity filling technique by a function provided by Matlab[TM], the non-zero intensities in the background image could be modified to zero (pure black) as shown in Figure 4.17.

The centroided marker is illustrated in Figure 4.18. The typical precision of the individual centroids is illustrated in Figure 4.19, with a standard deviation of about 0.04 pixel.

(a) Before filling  (b) After filling
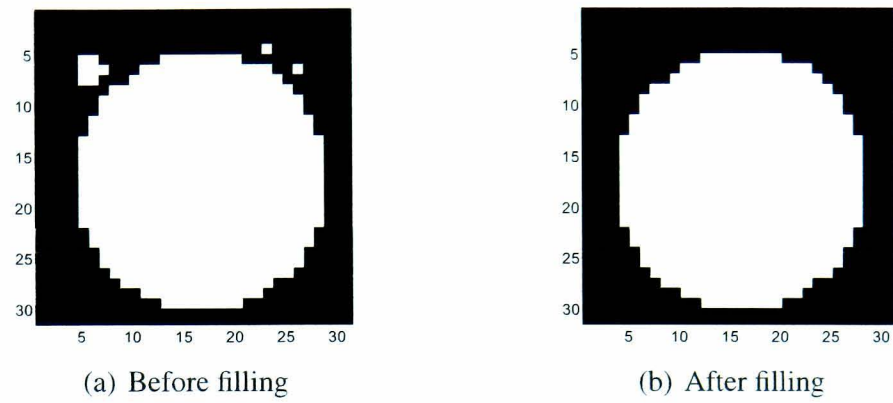
**Figure 4.17:** Filling non-zero pixels outside the marker
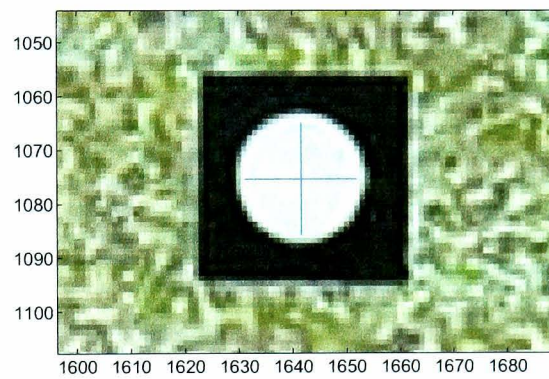


**Figure 4.18:** Centroid of target marker
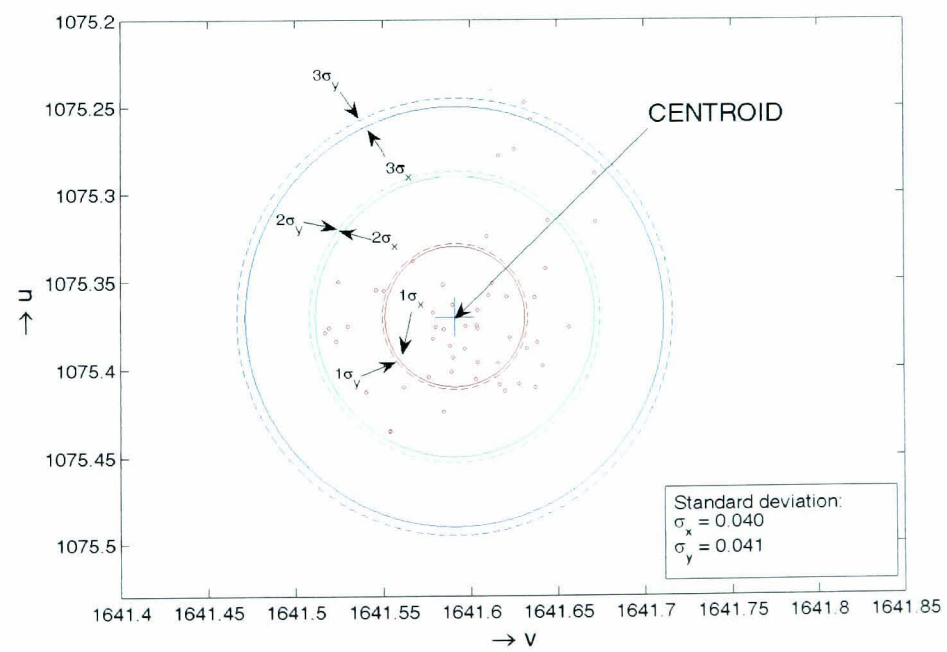


**Figure 4.19:** Typical precision of centroiding

### 4.4.3 Image-to-Object Transformation

If the camera was perfectly co-planar and did not move while acquiring the images, any points in the image space, after correction for distortion, could be linearly scaled to those in the object space. However, it was observed that movement of the camera occurred during successive image acquisition. Figure 4.20 shows the displacement vectors of the target markers of up to 0.3 pixels, analysed with PIV from an image pair remotely captured with an interval of 30 seconds. The
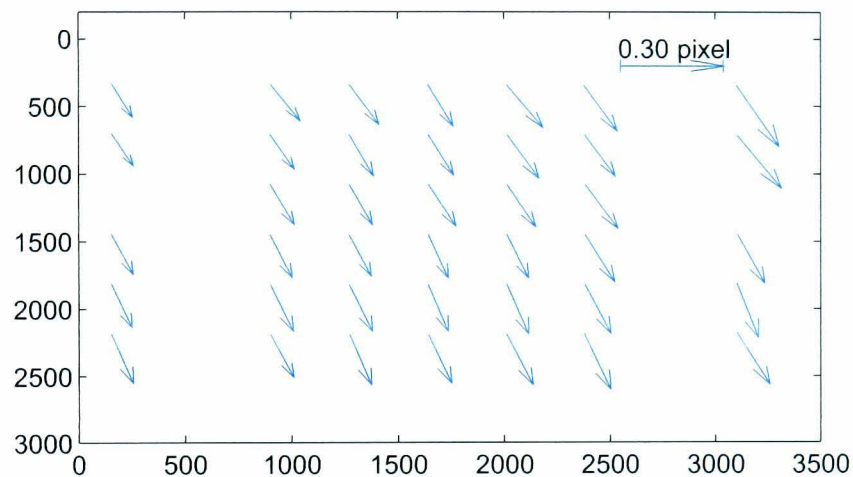
**Figure 4.20:** Typical displacement vectors of target markers due to camera movements, analysed from an image pair taken at a 30-second interval

direction of the vectors suggests that the movement was not only due to a translation but also a rotation. More severe movements of up to 3.6 pixels were encountered using a pair of images taken at the beginning of a test and at the end of a test, with an interval of a month. It was evident that camera movements during a test were inevitable. Correction for the "unexpected" movements is essential since the displacement vectors are, in fact, combinations of object and camera movements.

The images acquired by the camera were principally based on the pinhole camera model (Figure 2.19. Any points in the image plane were simply the perspective points in the object space,

transformed with Equation 4.2.

$$
\begin{bmatrix} u \\ v \\ 1 \end{bmatrix} \propto \begin{bmatrix} \lambda u \\ \lambda v \\ \lambda \end{bmatrix} = \begin{bmatrix} sf & 0 & u_0 & 0 \\ 0 & f & v_0 & 0 \\ 0 & 0 & 1 & 0 \end{bmatrix} \begin{bmatrix} \mathbf{R} & \mathbf{t} \\ 0 & 1 \end{bmatrix} \begin{bmatrix} X \\ Y \\ Z \\ 1 \end{bmatrix} \tag{4.2}
$$

The scaling factor $\lambda$ determined the overall magnification of the transformation, while the perspective, the rotation and the translation from the object to the camera frames were respectively governed by the first matrix containing focal length $f$ and aspect ratio $s$, $\mathbf{R}$ (Equation 4.3), and $\mathbf{t}$ (Equation 4.4).

$$
\mathbf{R} = \begin{bmatrix} \cos\varphi\cos\kappa & -\sin\kappa\cos\omega + \cos\kappa\sin\varphi\sin\omega & \sin\kappa\sin\omega + \cos\kappa\sin\varphi\cos\omega \\ \sin\kappa\cos\varphi & \cos\kappa\cos\omega + \sin\kappa\sin\varphi\sin\omega & -\cos\kappa\sin\omega + \sin\kappa\sin\varphi\cos\omega \\ -\sin\varphi & \cos\varphi\sin\omega & \cos\varphi\cos\omega \end{bmatrix} \tag{4.3}
$$

$$
\mathbf{t} = \begin{bmatrix} t_x \\ t_y \\ t_z \end{bmatrix} \tag{4.4}
$$

The Eulerian angles: $\varphi$, $\omega$, and $\kappa$ and the translation parameters of $\mathbf{t}$ could be readily obtained from the camera calibration algorithm by Heikkilä (2000a). The transformation from image to object coordinate systems was determined from the inverse of the equation. The application of this transformation was applied to the image of the target markers. The coordinates of the centroids of the markers in image space were transformed to their object coordinates. The discrepancies between the transformed and the real coordinates were observed with a mean error of 0.01 mm (standard deviation = 0.007 mm) in horizontal direction and 0.0065 mm (standard deviation = 0.005 mm) in vertical directions. This error was just about the same as the accuracy of the drilling machine used for manufacturing the markers.

To save calculation time, the transformations were carried out only on the points at which PIV analysis was conducted. The rotations and the translations of the camera were determined from the centroids of the markers in every image. Since the accuracy and the precision of the PIV analysis (see Section 4.2.2) was superior to that of the centroiding, the centroiding procedure (Section 4.4.2)

was established only on the first image. The centroids in the successive images were determined with the PIV analysis. The real displacement vectors were defined by transforming the initial and displaced coordinates of points in the output of the PIV analysis.

## 4.5 REFRACTION CORRECTION

The correction and transformation of the pixel coordinates discussed in the previous sections still disregarded the effects of refraction caused by viewing through the Perspex window. Because the object existed behind the Perspex window, light rays had to propagate through two different media, Perspex and air, in order to reach the camera. According to Snell's law, a light ray deviates once it enters medium with a different refractive index $n$. From the product specification of Perspex™(Ineos Acrylics UK Ltd., 2001), the refractive index of the Perspex was 1.49. To validate this figure, a refraction test was conducted, employing the same media used during the laboratory experiments.

Figure 4.21 schematically illustrates the validation test. The angle of refraction $\phi'$ was determined from $n_{\text{Perspex}} \sin \phi = \sin \phi'$, where $\phi$ was the angle of incidence of the ray originating from the object. The test used PIV analysis and the transformation described above, applied to a pair of images. The first image was captured from three interfacing Perspex plates. Closest to the camera was a 3 mm thick plate containing a set of target markers (Target Markers I). The middle and the farthest plates were the Perspex window and the 3 mm thick plate with the target markers (Target Markers II) that were used during the experiments. The Target Markers II replaced the flocked kaolin behind the Perspex window that would be present in the actual tests. Any points in this first image were subject to refraction due to the transition from the Perspex medium to air before light reached the camera.

The second image was taken on Target Markers II only after the Perspex window and the front plate were removed. No refraction occurred since the light propagated through only one medium, i.e., air. As expected, the centroids of the markers appeared at different positions on the two images. The differences are clearly depicted by the vectors of "displacement" in Figure 4.22 obtained using PIV. The vector directions show that due to refraction the centroids appeared to move away from their actual positions with respect to the principal point. It is also shown that the larger the distance from the principal point, the larger the deviation from the actual position. The error could reach

about 2 mm at a distance of 150 mm from the principal point (see Figure 4.23). In each case the value of $n_{\text{perspex}}$ needed to explain the error was calculated. Averaged from calculations for the 30 targets, the value of $n_{\text{perspex}}$ was 1.51 with a standard deviation of 0.03.
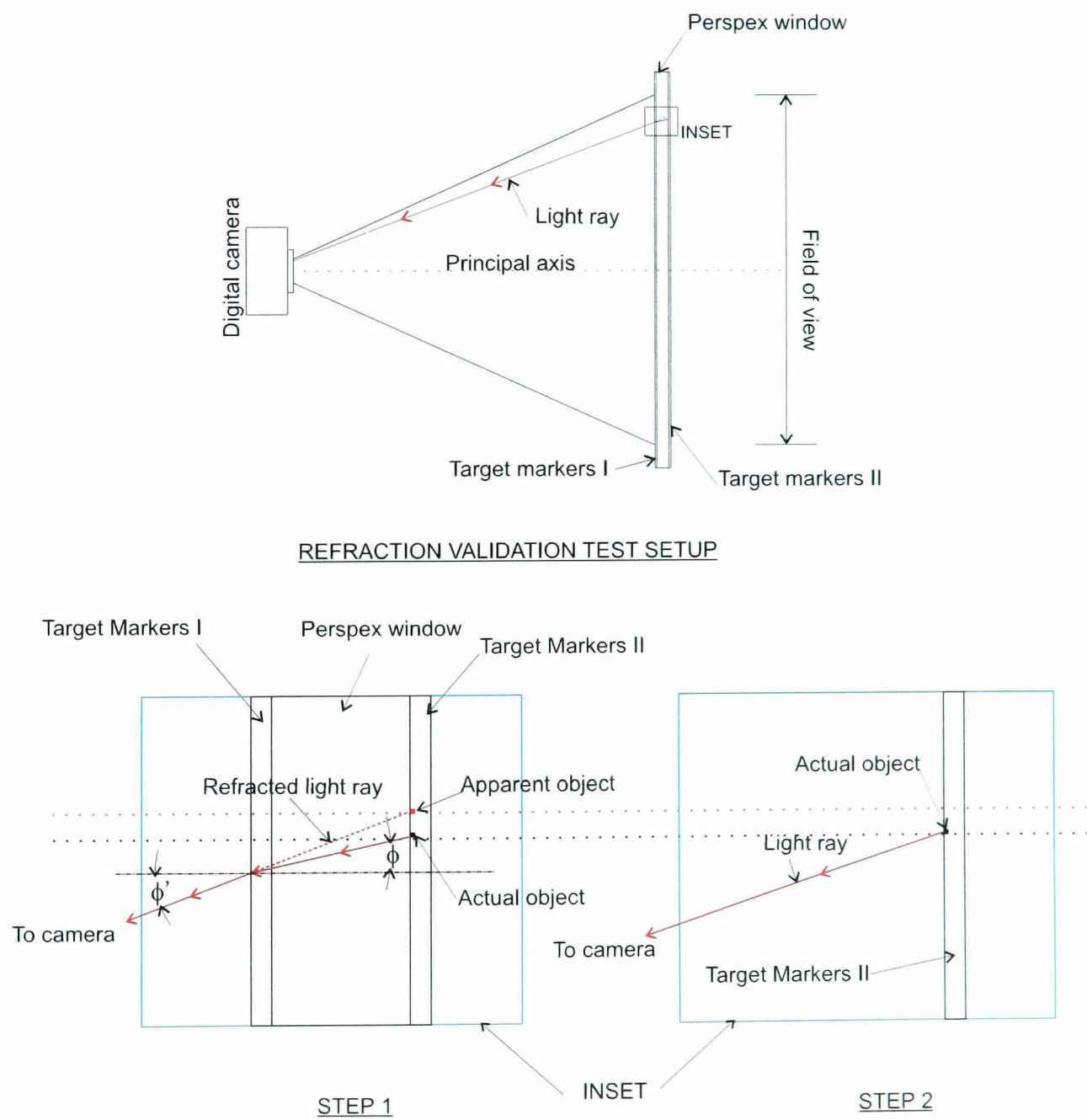


**Figure 4.21:** Refraction test
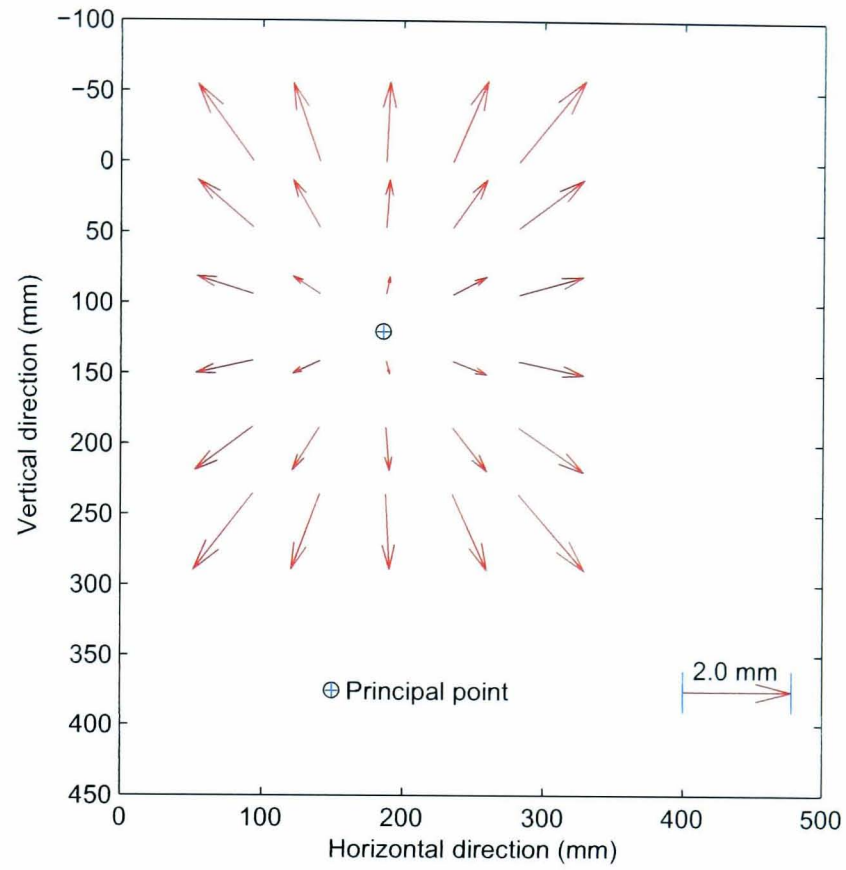
**Figure 4.22:** Vectors showing apparent and actual coordinates of markers
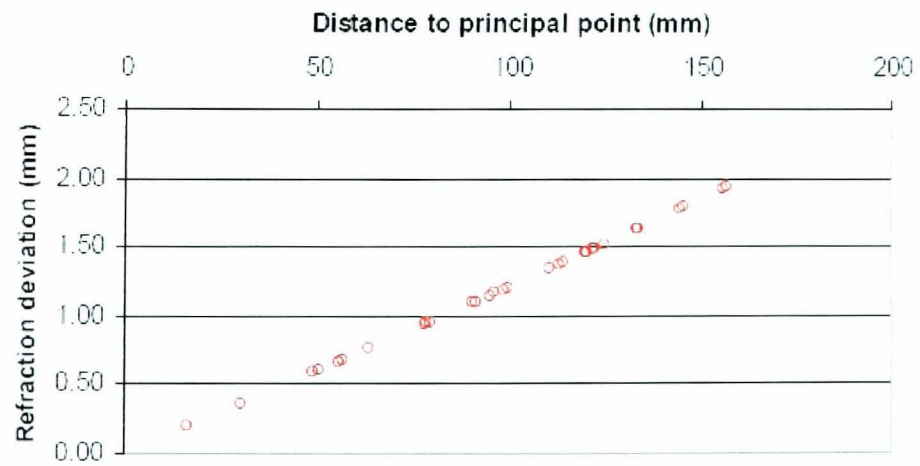


**Figure 4.23:** Measurement error due to the absence of refraction correction

Corrections of the position of every pixel due to refraction were performed using Equation 4.5 suggested by White (2002).

$$\delta \underline{R}^{\text{refraction}} = \begin{bmatrix} \delta X^{\text{refraction}} \\ \delta Y^{\text{refraction}} \end{bmatrix} = \lambda \begin{bmatrix} X_{\text{apparent}} - X_{\text{A}} \\ Y_{\text{apparent}} - Y_{\text{A}} \end{bmatrix}$$

$$\text{where} \quad \lambda = -\frac{t}{H} + \frac{t}{\sqrt{n_{\text{perspex}}^2 (H^2 + |\underline{R}_{\text{apparent}} - \underline{R}_{\text{A}}|^2) - (|\underline{R}_{\text{apparent}} - \underline{R}_{\text{A}}|^2)}}$$

(4.5)

$\delta \underline{R}^{\text{refraction}}$ is the deviation of an apparent point from its actual position (in two-dimensional coordinates) and the other parameters are explained in Figure 4.24.
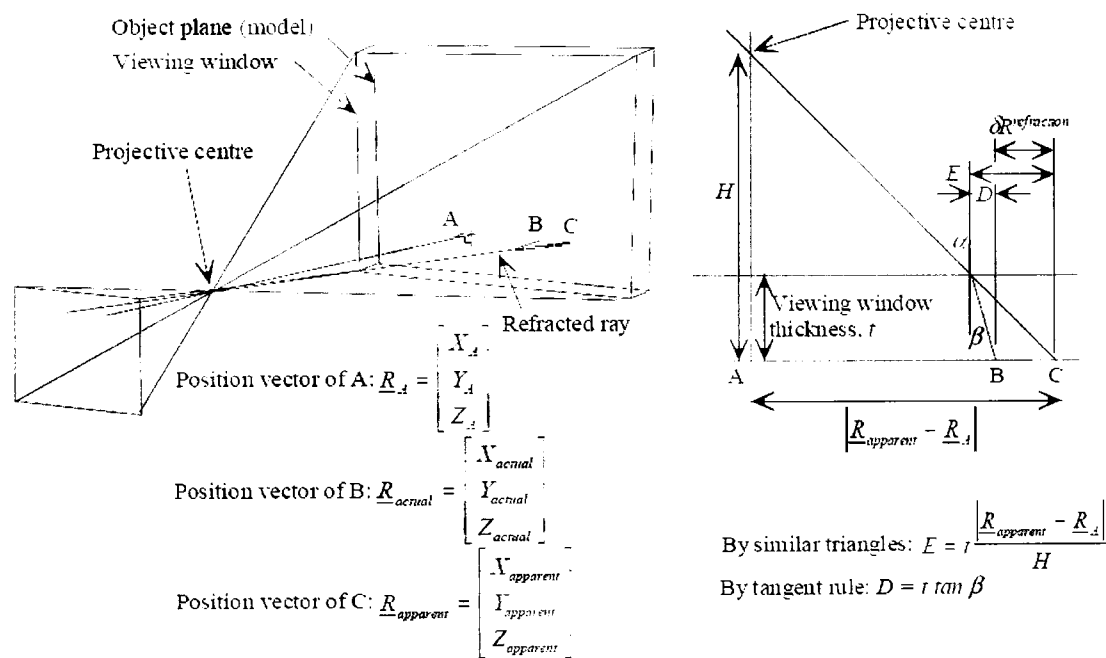


**Figure 4.24:** Derivation of refraction equation (Equation 4.5) by White (2002)

By knowing the deviation, the actual coordinates of every pixel in an image can be corrected. Figure 4.25 shows the discrepancies between the corrected coordinates (using Equation 4.5) of 30 target markers and their actual positions. The mean and standard errors in the horizontal direction 0.0480 mm and 0.021 mm, while those in vertical direction are 0.004 mm and 0.031 mm respectively.
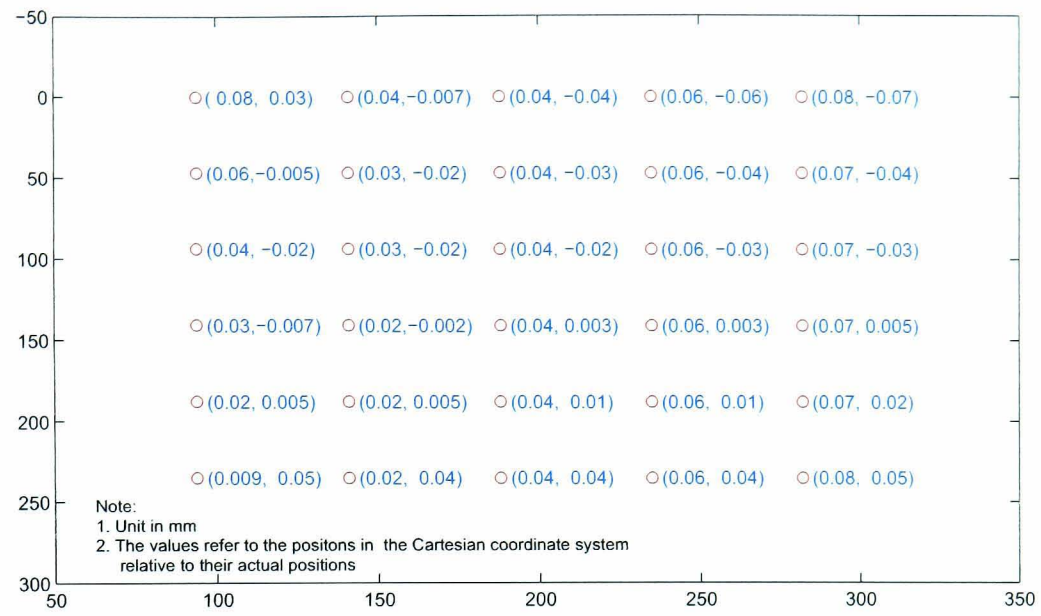
**Figure 4.25:** Distribution of errors resulting from refraction corrections on 30 target markers

# Chapter 5

# LABORATORY RESULTS

## 5.1 INTRODUCTION

The results from the laboratory work are presented in this chapter. The sections are generally organised in accordance with the order of the laboratory tests. Section 5.2 introduces the properties of soil used for all the tests, concentrating on the consolidation and the strength characteristics. The description includes the kaolin slurry properties, states during preconsolidation, and water content and soil strength before and after the model tests.

Section 5.3 discusses data obtained from two DF tests (see Section 3.5.1 for the test notation). The discussion is initiated with the effect of incremental loading on the settlement of a single footing and concluded with discussion of the effect of loading on the second footing on settlement and tilting of the previously loaded first footing.

Section 5.4 similarly describes the resulting data from two SP tests. However the discussion concentrates mainly on the effect of a floating sheet wall, inserted into the soil between two footings, on settlement and tilting of the footings.

Section 5.5 covers the data resulting from two FX tests during which a sheet wall, inserted between two footings, was vertically restrained. Here, the results from the FX tests are sometimes compared with those from the DF and the SP tests.

Some conventions are used through the chapter in order to aid the labelling of graphs. The symbols $\rho_{F2}(\sigma_{vF2})$ and $\rho_{F1}(\sigma_{vF2})$ respectively represent the settlements at the centres of Footing II and Footing I due to the loading applied on Footing II. On the other hand, $\rho_{F1}(\sigma_{vF1})$ and $\rho_{F2}(\sigma_{vF1})$ symbolise the settlements measured at the centres of Footing I and Footing II as a result of incremental loading on Footing I.

## 5.2 PRE- AND POST-TEST SOIL CONDITIONS

### 5.2.1 Water Content and Void Ratio

The slurry was designed to have an initial water content of 138% (see Section 3.4.1), slightly above twice the liquid limit of the kaolin. The homogeneity of the slurry was determined from the water contents of the slurry samples to be placed at the base, the middle, and the top of the soil model. Table 5.1 presents the resulting water contents of the slurry for all the tests. Although

**Table 5.1:** Initial water content and void ratio

| Type of Test | $\bar{w}_i{}^a$ (%) | $\sigma_{\bar{w}_i}{}^b$ (%) | $e_0{}^c$ |
|---|---|---|---|
| DF1 | 136.75 | 0.08 | 3.56 |
| DF2 | 135.03 | 0.05 | 3.51 |
| SP1 | 135.59 | 0.08 | 3.53 |
| SP2 | 136.70 | 0.26 | 3.55 |
| FX1 | 136.87 | 0.09 | 3.56 |
| FX2 | 137.43 | 0.08 | 3.57 |
| *Average* | 136.40 | 0.11 | 3.55 |
| *Standard deviation* | 0.90 | - | 0.02 |

[a] Averaged initial water content.
[b] Standard deviation of averaged initial water content.
[c] Initial void ratio.

a slight discrepancy of about 1.5% was encountered between the designed and the actual water content, which might stem from evaporation during preparation, the slurry for each individual test was considered homogenous, mostly with a standard error $\sigma_{\bar{w}_i}$ of less than 0.1%. Small differences of water content (with an averaged standard deviation of 0.11%) were also encountered among all the tests. The initial void ratio $e_0$ of the slurry was determined using Equation 5.1,

$$e_0 = \frac{w_i G_s}{S_r} \tag{5.1}$$

based on its initial water content $w_i$ and the specific gravity $G_s$ of 2.60 as reported in previous research that used Speswhite kaolin (Eid, 1978; Yong, 1979). Prior to the preconsolidation for each test, the slurry had an initial void ratio of 3.55 on average with the assumption that the slurry was fully saturated ($S_r = 1.00$).

### 5.2.2 Consolidation Characteristics

The consolidation characteristics of the soil during preconsolidation of kaolin slurry for all tests are depicted in Figure 5.1. The behaviour during compression and unloading of the preconsolidation pressures followed a consistent trend. This was comparable with the results from recent research
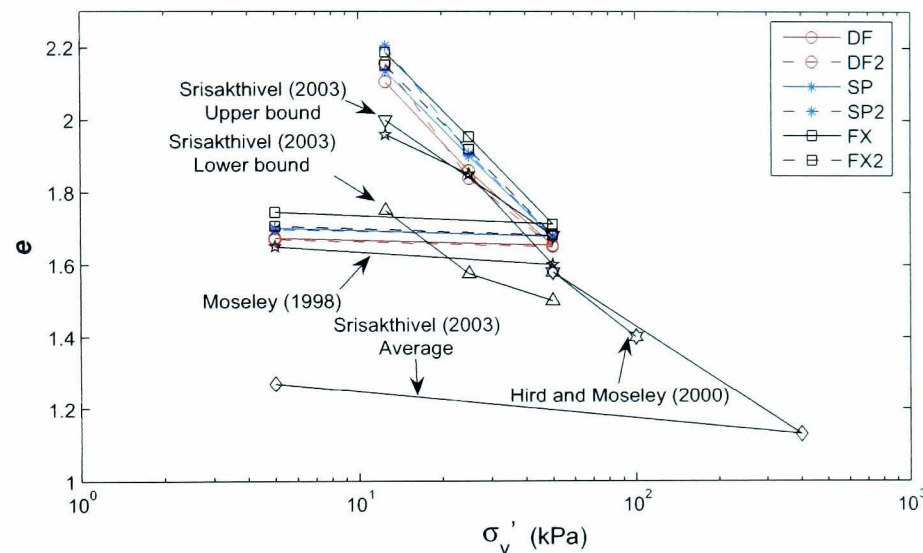


**Figure 5.1:** Preconsolidation characteristics

work using the same type of kaolin consolidated in a cylindrical chamber (Srisakthivel, 2003; Hird and Moseley, 2000; Moseley, 1998). The maximum applied pressure was 50 kPa before the soil was unloaded to 5 kPa to achieve an overconsolidation ratio of 10. At the end of the swelling, based on the height changes and the assumption $S_r = 1.00$, the samples had void ratios of approximately 1.7. Although the water contents of the samples were not taken at this stage to avoid disturbance, they could be estimated with Equation 5.1 resulting in a value of 65% on average. This value was also confirmed by the water content of the sample determined after the tests from furthermost regions with respect to the loading sources, i.e. the bottom corners of the chamber as shown from Figure 5.2 to Figure 5.4. These figures show the profiles of water content over the samples after the completion of every test. The areas with a water content of about 65% were considered to have been unaffected by the loading on the footings.
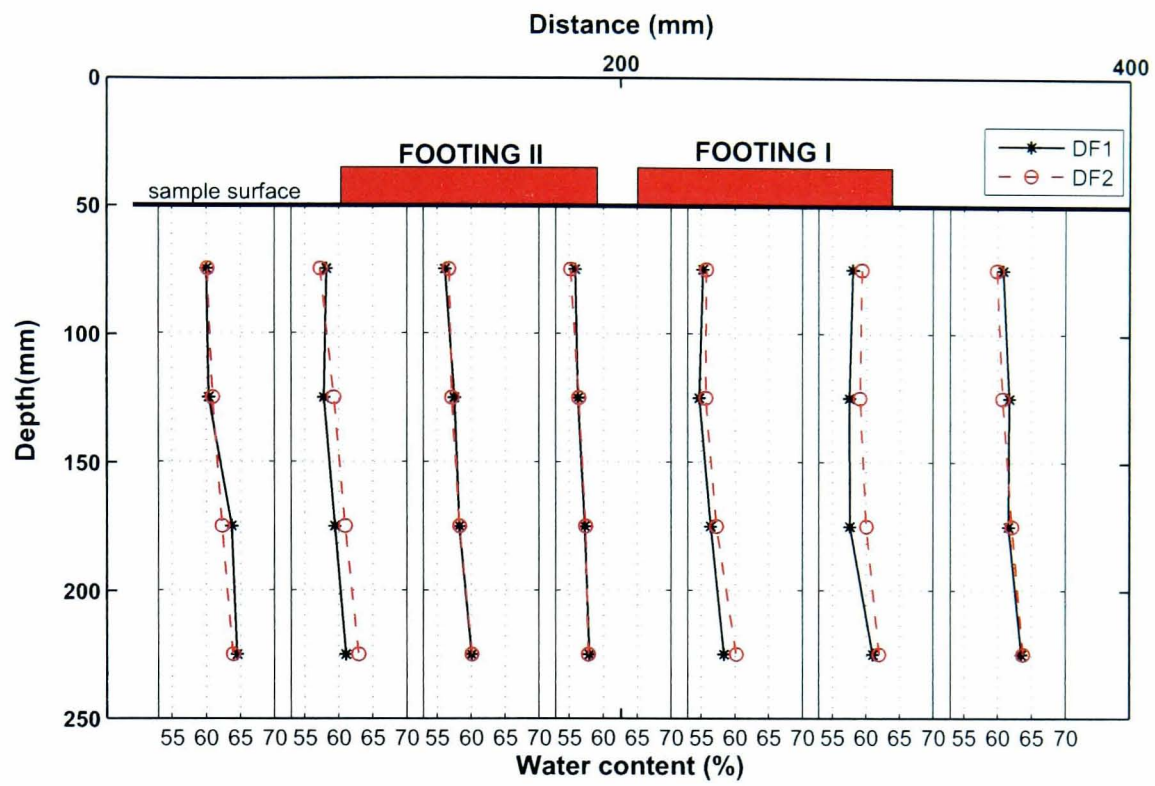
**Figure 5.2:** Water contents after DF tests
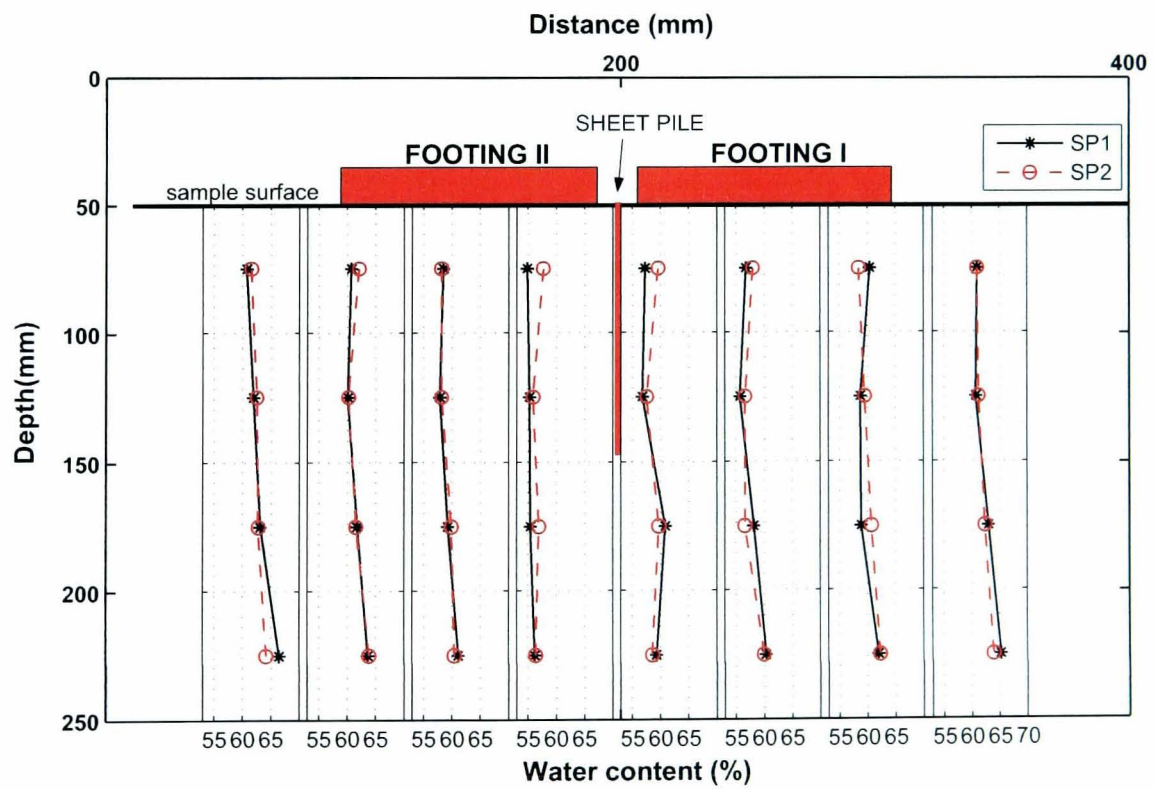


**Figure 5.3:** Water contents after SP tests
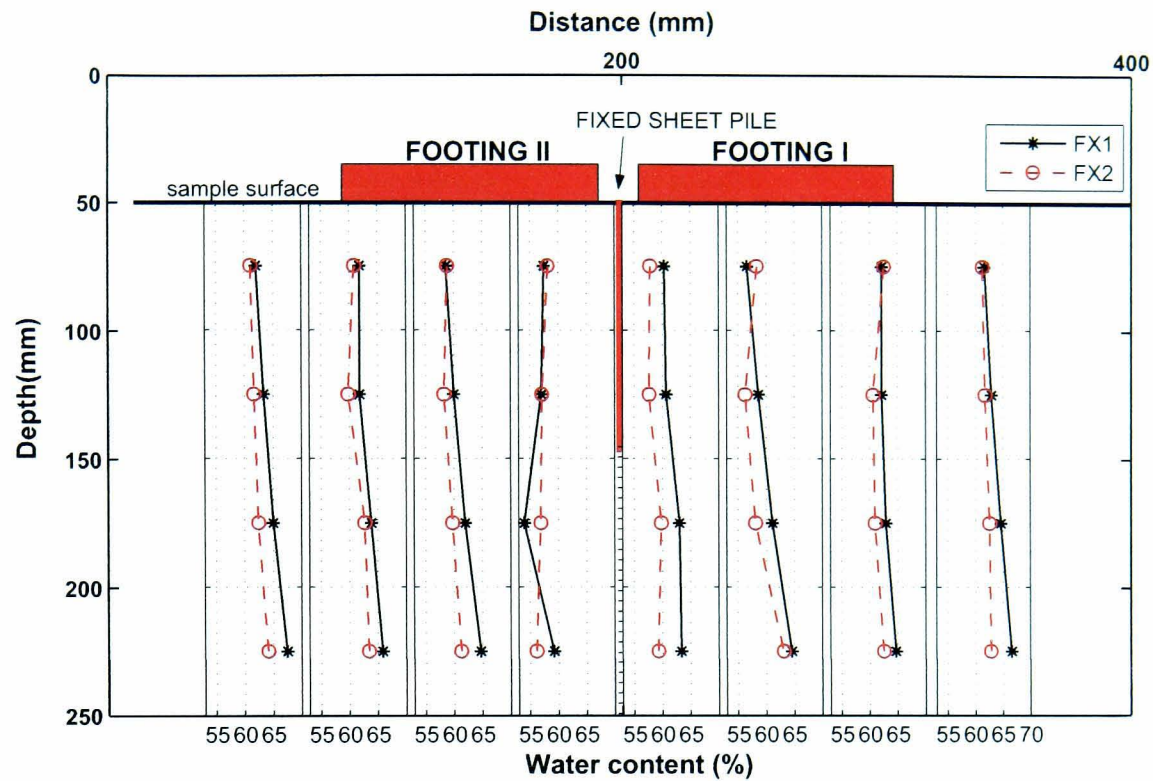
**Figure 5.4:** Water contents after FX tests

### 5.2.3  Undrained Shear Strength

After the completion of the tests, prior to sampling the water content, the distribution of undrained shear strength $s_u$ was determined with vane shear tests. The test points were taken as close as possible to those for the water content determination. Figures 5.5 to 5.7 show the profiles of undrained shear strength over the sample. Based on the assumption that in the areas furthermost from the footings the undrained shear strength and water content distributions were not greatly affected by the applied loading, a correlation between both variables was made, Figure 5.8. In making the correlation, some water content values were linearly interpolated to correspond to the undrained shear strength determined between two water content sampling points. It is evident from Figure 5.8 that the undrained shear strength of the soil was negatively correlated with the water content. It can be deduced from the correlation that the undrained strength of the soil sample after preconsolidation and before any test was about 4.3 kPa. The value was in good agreement with that found in a preliminary test in which a vane shear test was carried out in the soil sample under a lead shot surcharge. An undrained shear strength of approximately 4.5 kPa was observed.
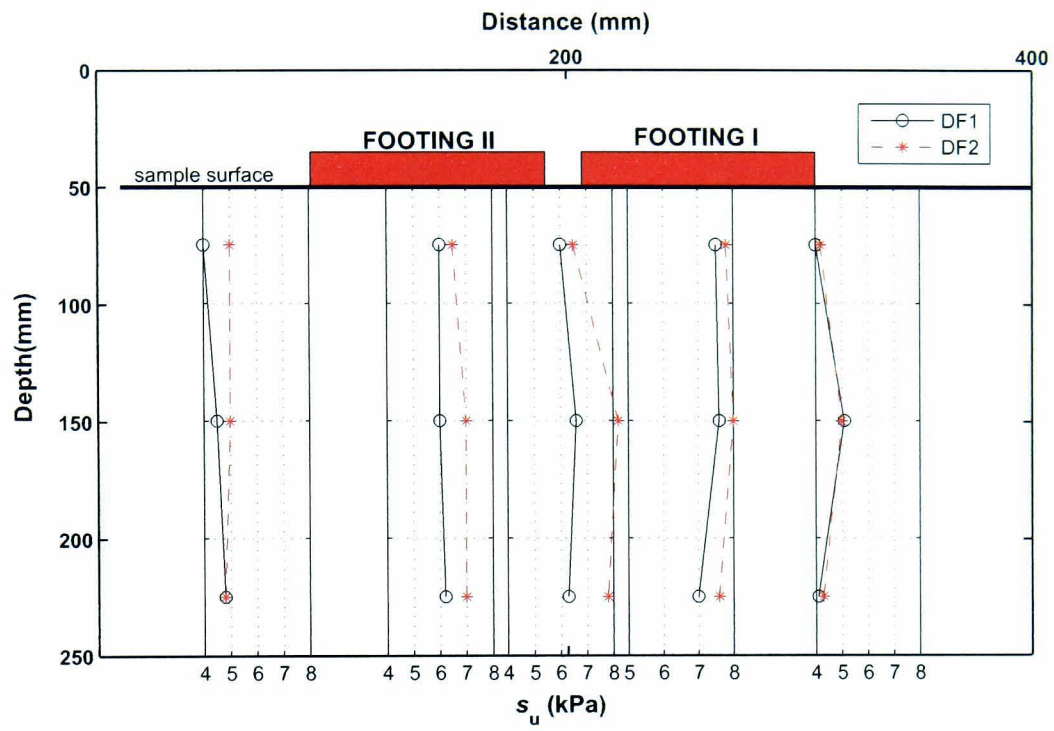
**Figure 5.5:** Undrained shear strength after DF tests
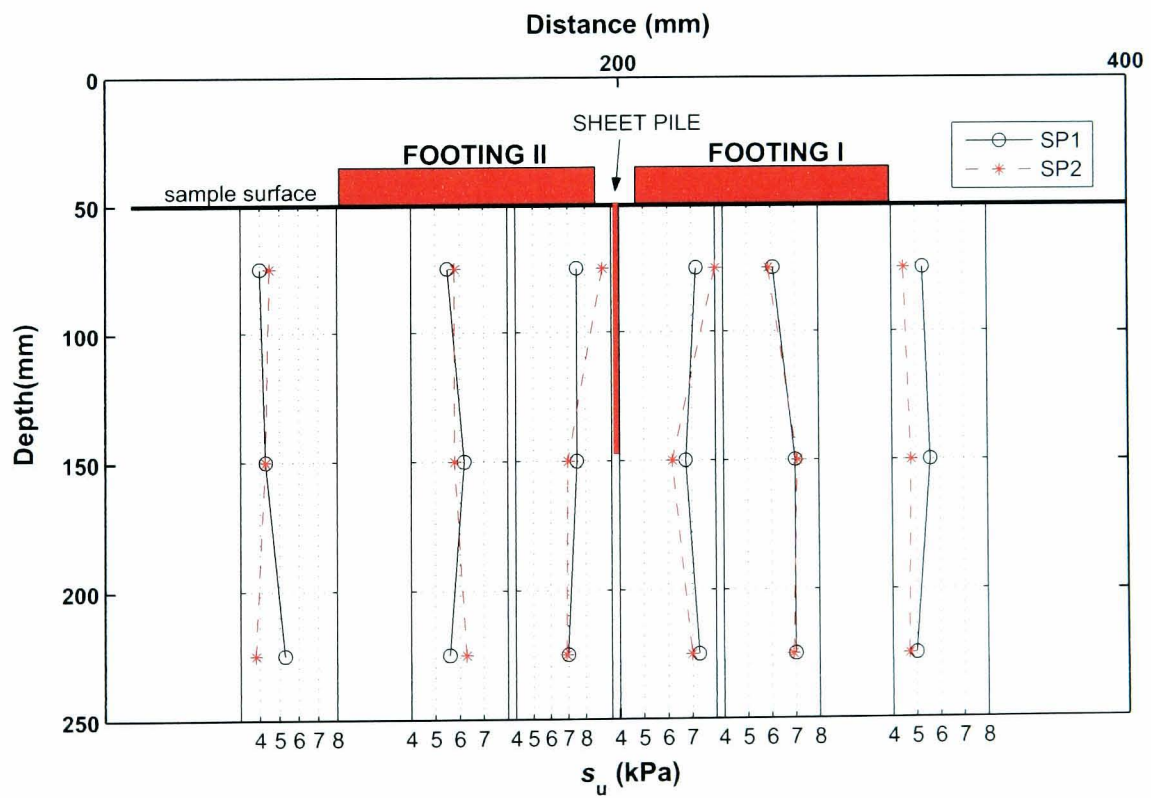


**Figure 5.6:** Undrained shear strength after SP tests
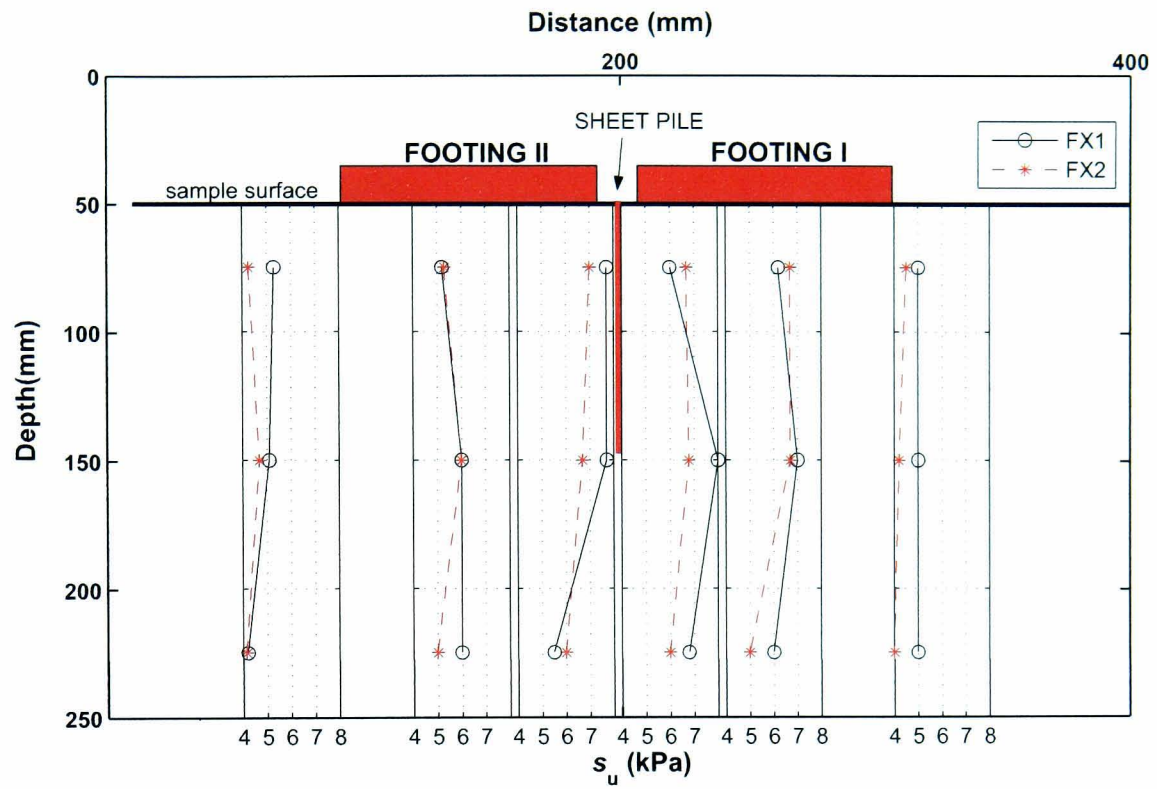
**Figure 5.7:** Undrained shear strength after FX tests
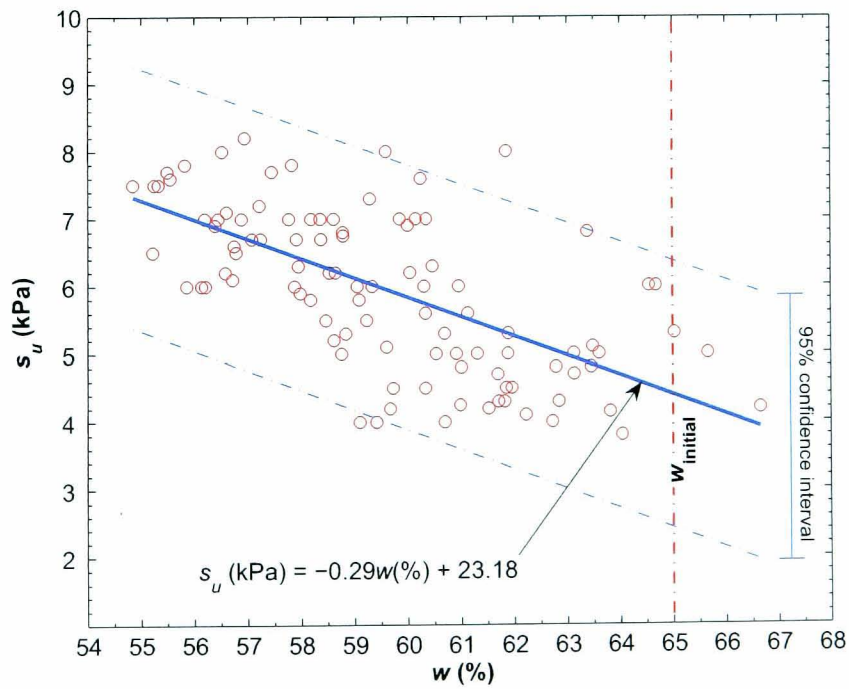


**Figure 5.8:** Correlation of water content $w$ and undrained shear strength $s_u$

## 5.3 DOUBLE FOOTING

### 5.3.1 Loading on Footing I

#### 5.3.1.1 Settlement of Isolated Footing

As a benchmark to which results from other tests were compared, two tests on a plain double foot-
ing (DF) were carried out. These tests, and all the others, were commenced by incrementally load-
ing Footing I, producing footing-soil contact pressures up to 80 kPa as described in Section 3.5.2.
This stage could be considered as a test on an isolated single footing. The vertical displacement
measured with an LVDT at the centre of the footing for all the tests is illustrated in Figure 5.9.
The figure also shows points at which consolidation ended in each test under the final increment of
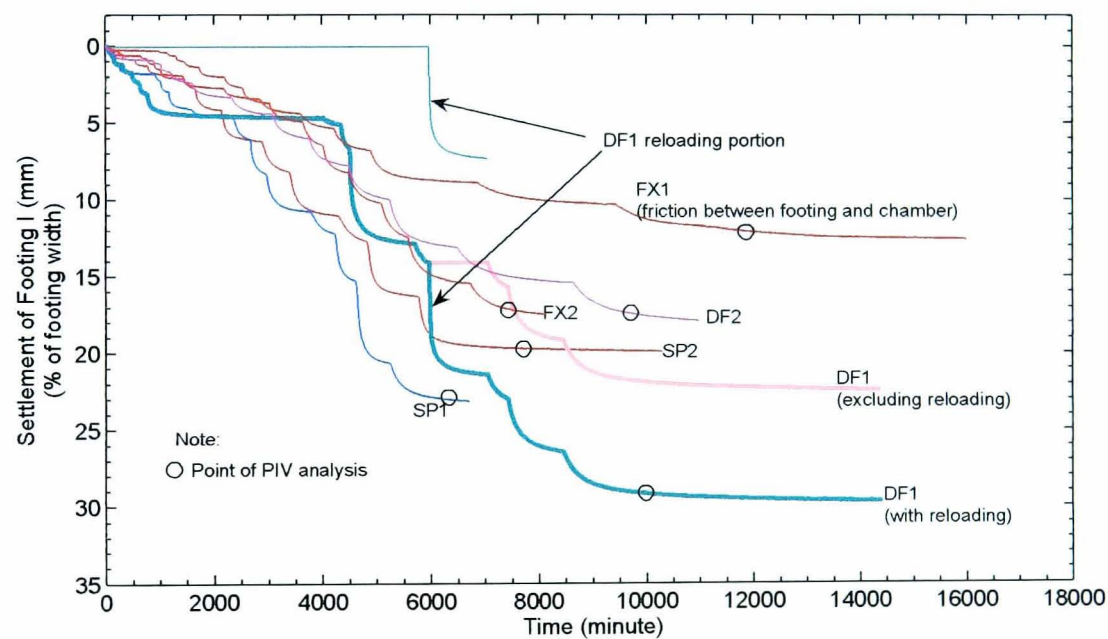


**Figure 5.9:** Vertical displacement at the centres of Footing I

80 kPa. Later, in PIV analyses the last images, representing the end of loading on Footing I, were
taken at the time of these points. Some variations in the total vertical displacements were encoun-
tered. The variations were attributed to factors discussed below. For the purposes of discussion the
tests will be classified into (1) DF1, (2) SP1 and SP2, (3) FX1, and (4) DF2 and FX2.

Test DF1 was interrupted by an unloading and a reloading in the middle of the test due to the
suspected failure of the footing material. During this test, at a contact pressure of 65 kPa, the
footing seemed to bend and the load was therefore released. It was found that only the thin rubber
glued on the footing side was partly detached, so the load was then quickly applied to the previous

magnitude of 65 kPa. From the LVDT measurement (see Figure 5.9), an instantaneous vertical displacement was observed, followed by another consolidation. By excluding this portion the total displacement fell into the range of the results from Tests SP1 and SP2. Yasuhara et al. (1992, 2001) described immediate settlement that occurred when fine grained soils experienced cyclic loading. Excess pore pressure generated resulted in effective stress decreases and caused instability. Hyde and Brown (1976) and Hyde and Ward (1985) similarly observed that the stress path in cyclic triaxial tests shifted to left side on a $p'-q$ plot so that the mean normal effective stress decreased. Using a Universal Testing Machine, Das and Shin (1996) applied a cyclic load of 1 cycle/sec to a model strip foundation on a clayey soil and observed initial rapid settlement contributing up to 80% of the total settlement. They also found that the undrained shear strength of the soil increased by between 8% to 12% compared to that measured at the beginning of test. It was believed that the increase was partially due to by consolidation.

Tests SP1 and SP2, despite a slight discrepancy in the final deformation of approximately 2.5% of the footing width, were considered normal. The tests were carried out according to the procedures that were described in Section 3.

Test FX1 had a mechanical problem. After the completion of the test, both footings, Footing I and Footing II, were observed to stick between the back wall and the Perspex window of the chamber. This occurred when extra silicon glue was inserted between the folded ends of the porous plastic and the ends of the footings (see Figure 3.8 and also Section 3.2.3). An additional length of about 1 mm was effectively added to the length of each footing. It was intended to stop soil intruding into the gap between the footing side and the Perspex window. Unfortunately, although no friction was found at the initial setup, when footing loading equalled the maximum past pressure of 50 kPa it was discovered that the footing had experienced less settlement than expected. After the entire test was completed, both footings were placed into the empty chamber where the test had been performed. Friction between the footing sides and the walls was felt when each footing was lowered by about 2 mm. The footing was supported by friction at this position. A force of approximately 150 N (equivalent to 10-kPa footing pressure) was required to push the footing further down using the pressure cylinder with a mounted load cell.

Finally, two repeat tests, DF2 and FX2, were carried out on soil that had experienced unloading and reloading during preconsolidation. At some loadings during the preconsolidation of slurry, the

consolidation piston was found to be slightly tilted due to an eccentricity occurring between the tip of the loading shaft and the piston. In order to bring the tip to the centre of the piston, the pressure was fully released. This was not the case for the previous tests in which a tilt of less than 0.25% was ignored. It was thought that the reloading path would continue along the normal consolidation line. No change in soil behaviour was expected from the treatment. However, a simulation with a finite element analysis, as discussed in Chapter 6, suggested that the unloading and reloading had changed the soil behaviour. Less settlement was observed on the soil that had experienced such cyclic loading.

When the vertical displacements are plotted with respect to the applied pressures (Figure 5.10), it is evident that the relationships follow a very similar trend. The Test FX1 data has been corrected by subtracting 10 kPa from the applied pressures to allow for the friction. The data from the Test DF1 seem to fall near the rest if the deformation owing to the reloading is omitted.
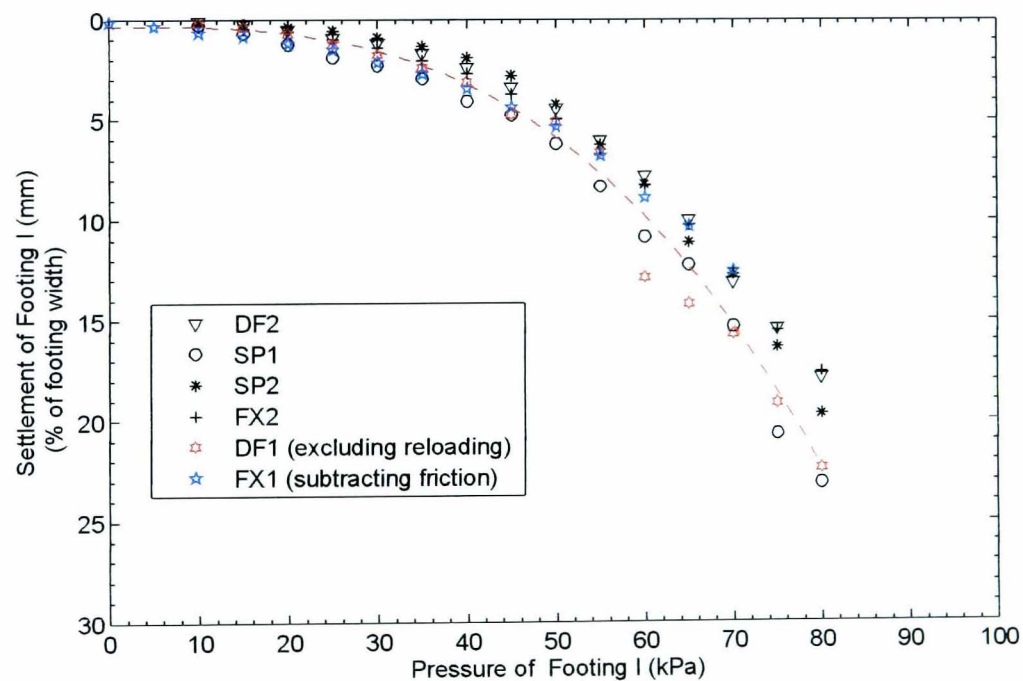


**Figure 5.10:** Load and settlement relationship at the centre of Footing I

### 5.3.1.2 Overall Soil Displacement

The LVDTs were utilised only to measure the vertical displacement at the centre of both footings. The displacements of the points of interest over the model soil face were observed through PIV analyses. Figure 5.11 and Figure 5.12 show the displacement vectors derived from the analyses over a series of images taken before the first loading and after the end of consolidation under the final loading on Footing I during Tests DF1 and DF2.
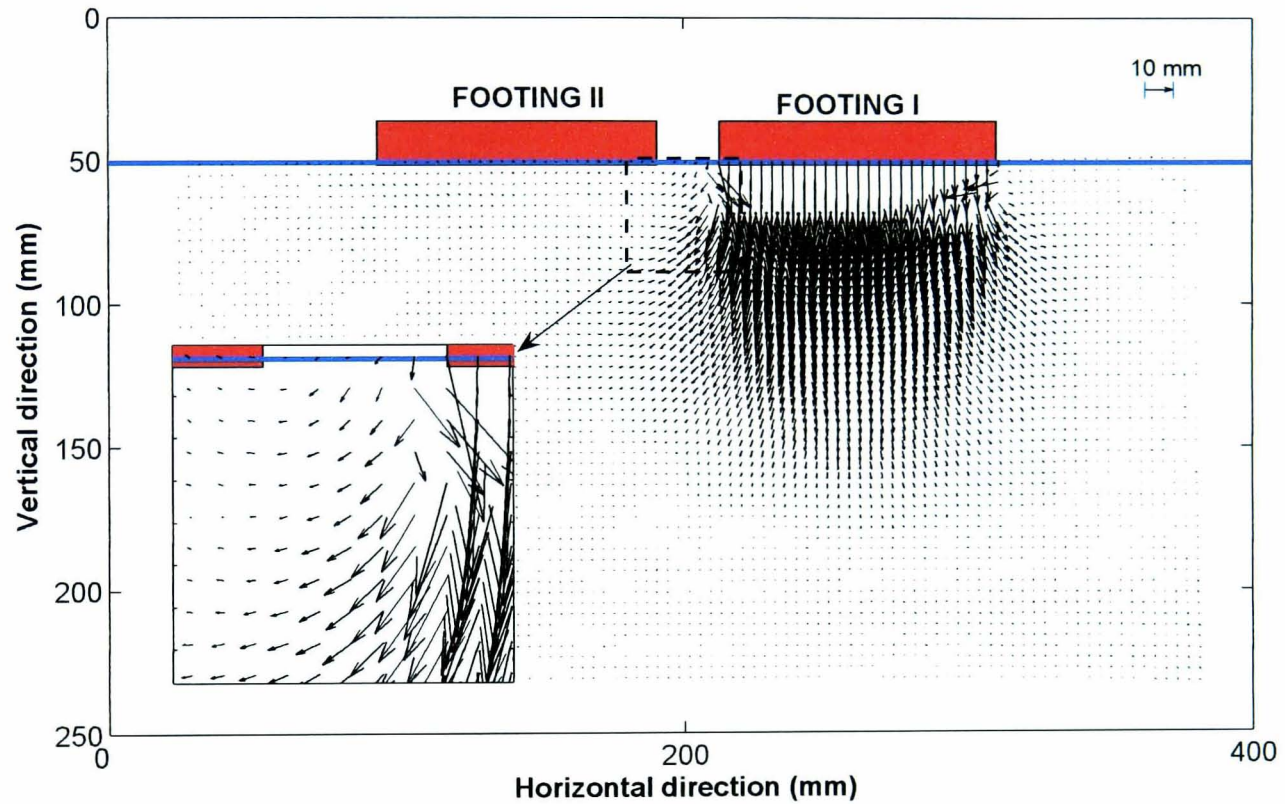


**Figure 5.11:** Vectors of cumulative displacement due to final loading on Footing I in Test DF1

To enable a better understanding of the vertical displacements over the entire area, Figures 5.13 to 5.16 depict the displacement contours from Tests DF1 and DF2. The corresponding numbers on the contours represent the displacement of the soil in millimetres which is equivalent to a percentage of the footing width. The pressure of the footing displaced the underlying soil symmetrically. At the end of Test DF1, the vertical displacement contours show a cumulative soil heave of about 0.4% of the footing width around the footing, while only 0.1% appeared in Test DF2. The heaving observed in Test DF1 was mostly undrained deformation during the quick reloading described in Section 5.3.1.1. Although the heave was very small and visually unobservable, unsymmetri-
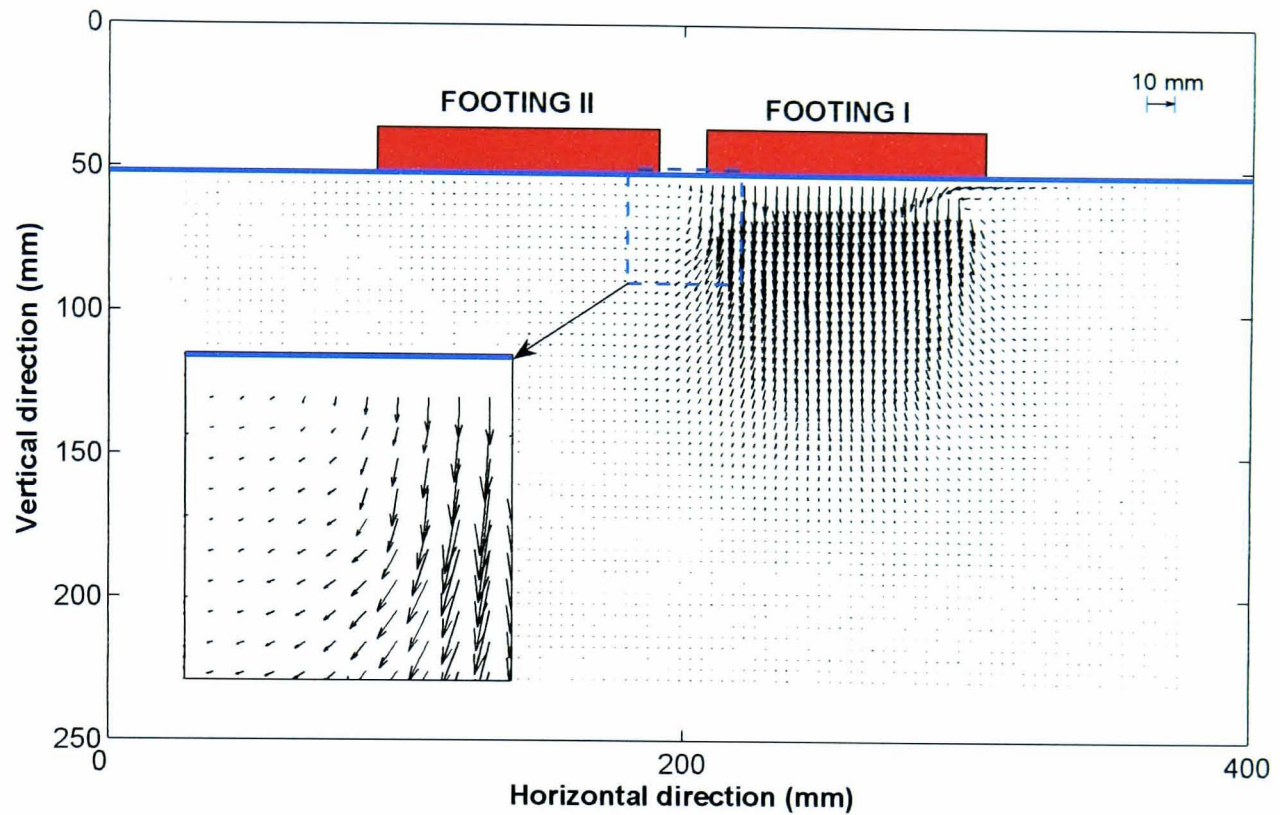
**Figure 5.12:** Vectors of cumulative displacement due to final loading on Footing I in Test DF2

cal displacements had occurred. This was confirmed by the horizontal displacement contours in Figure 5.14 and Figure 5.16 from both tests.

Figure 5.17 shows the contours of immediate settlement resulting from the application of the reloading pressure. It proves that the reloading caused about 70% of the total heaving. The inset of vectors depicting the soil movement after the immediate deformation adjacent to the footing is shown in the figure. During this process the soil was immediately rotated upwards in a spiral pattern but this did not occur in the consolidation stage, as shown in the other inset. A similar pattern shown by the inset in Figure 5.12 indicated that during Test DF2 the soil had undergone smaller undrained deformation. The total settlement at the centre and the corners of the footing was determined with a PIV analysis in which three markers on the footing side were used as tracing points. Figure 5.18 shows the vector magnitudes of the vertical displacements of the soil beneath the footing and those of the tracing points. A significant discrepancy was observed between the vector magnitudes obtained from the points in the soil directly underneath the footing and these from the markers on the footing side. This was attributable to intrusion of the soil into the gap between the footing side and the Perspex window during the tests. As a consequence, the soil immediately beneath

the footing and also close to the window was not displaced by the same amount as the footing. Nevertheless, the total displacement at the surface can be well estimated from an extrapolation of the linear portion of the settlement curves as depicted in the figure. A slight dissimilarity of surface settlement was observed in comparison with that measured from the LVDT. It was assumed that the larger displacement from the LVDT was caused by deflection of the Perspex footing under the point loading. In a deflection test in which its edges were simply supported, the footing centre deflected to about 2 mm under the same force that was applied to the footing at the final loading during the test. Another possible contribution of the LVDT displacement was from the longitudinal tilting of the footing. Similar discrepancies were also found in the measurements in the other tests. The results are summarised in Table 5.2 and shown in Figure 5.19. The table also lists the net vertical displacement excluding the cumulative creep over all loading increments.
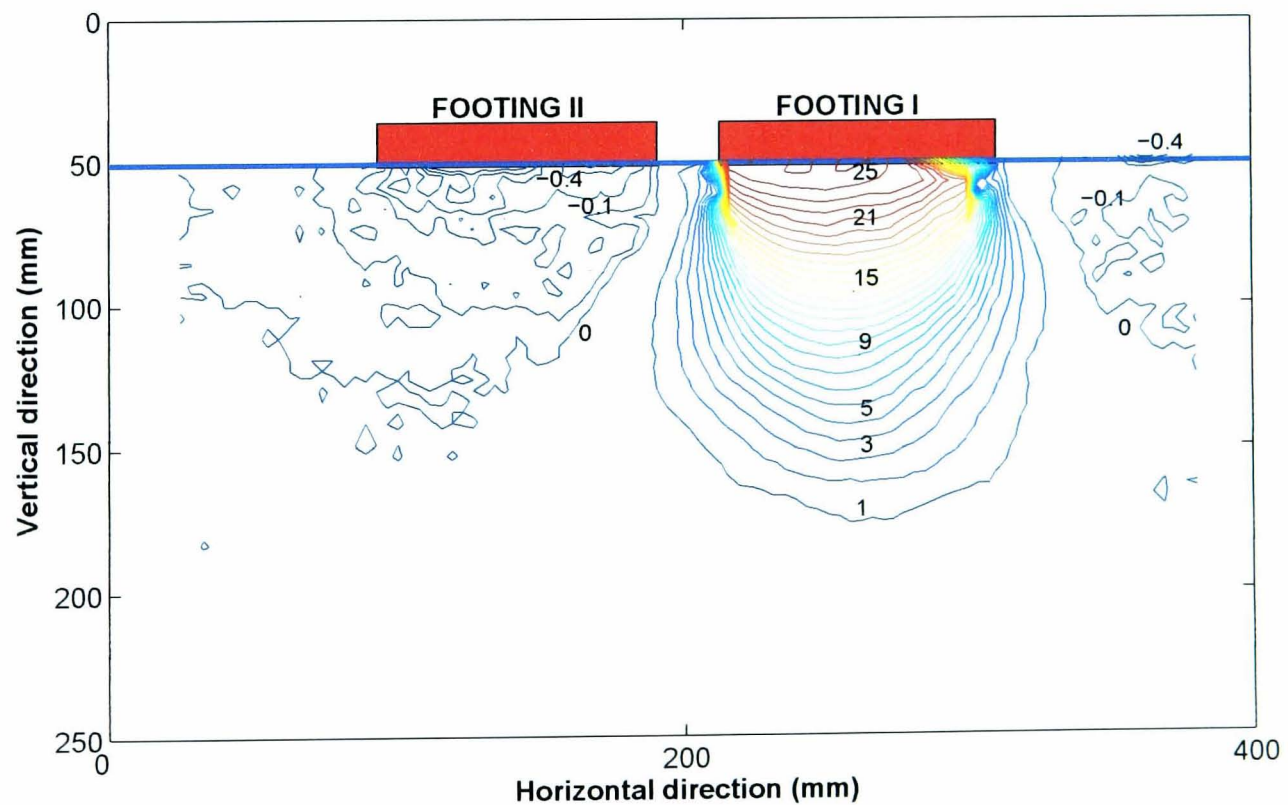


**Figure 5.13:** Contour of cumulative vertical displacement due to final loading on Footing I in Test DF1
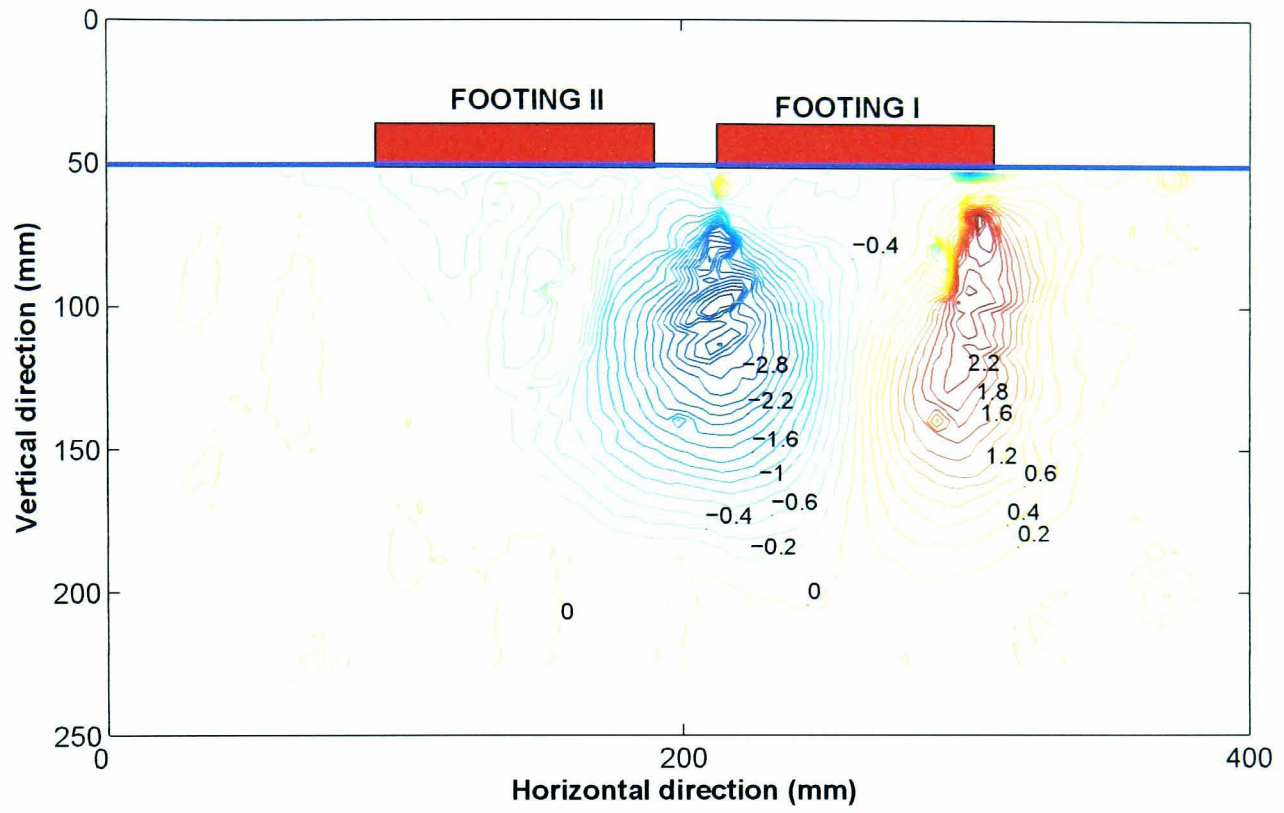
**Figure 5.14:** Contour of cumulative horizontal displacement after final loading
on Footing I in Test DF1
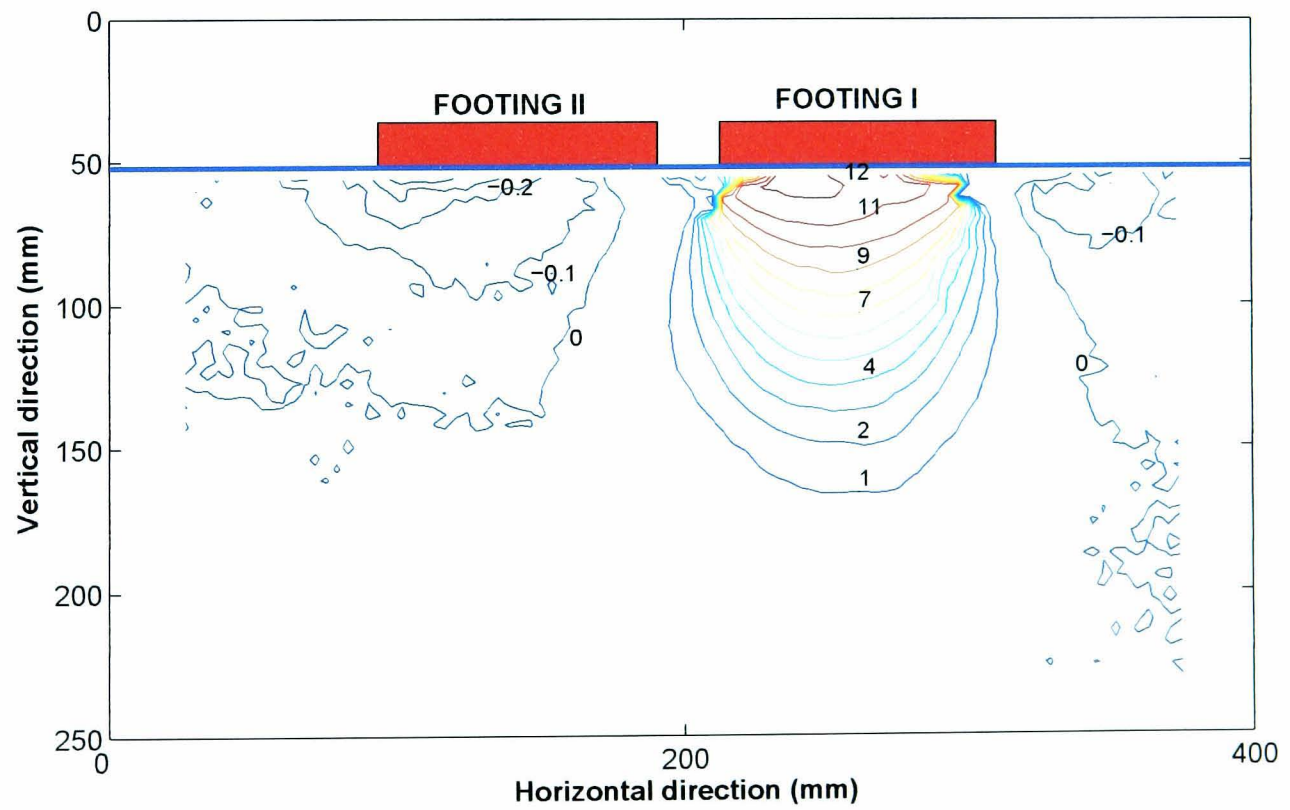


**Figure 5.15:** Contour of cumulative vertical displacement due to final loading
on Footing I in Test DF2

**Figure 5.16:** Contour of cumulative horizontal displacement after final loading
on Footing I in Test DF2

**Table 5.2:** Vertical displacements ($\rho$) measured with PIV at markers and with
LVDT on Footing I

| Test | $\rho_{left}$ (mm) | $\rho_{centre}$ (mm) | $\rho_{right}$ (mm) | $\rho_{average}$ (mm) | LVDT (mm) | Discrepancy[a] (mm) | Creep (mm) | LVDT (excl. creep) (mm) |
|------|-------|--------|-------|---------|-------|-------------|-------|-------------------|
| DF1 | N/A | N/A | N/A | $27.35^b$ | 29.26 | 1.92 | 1.61 | 27.65 |
| DF2 | 16.04 | 16.24 | 16.19 | 16.16 | 17.43 | 1.27 | 2.50 | 14.93 |
| SP1 | 21.63 | N/A | 21.52 | 21.57 | 23.23 | 1.65 | 2.60 | 20.63 |
| SP2 | 18.40 | 18.44 | 18.21 | 18.35 | 19.68 | 1.33 | 2.29 | 17.39 |
| FX1 | 10.32 | N/A | 10.38 | 10.35 | 12.10 | 1.75 | 1.88 | 10.22 |
| FX2 | 15.16 | 15.23 | 14.96 | 15.12 | 16.80 | 1.68 | 2.71 | 14.09 |

Note:

N/A = Markers were not available.

[a] Between $\rho_{average}$ and LVDT.

[b] Predicted from soil deformation beneath the footing centre.
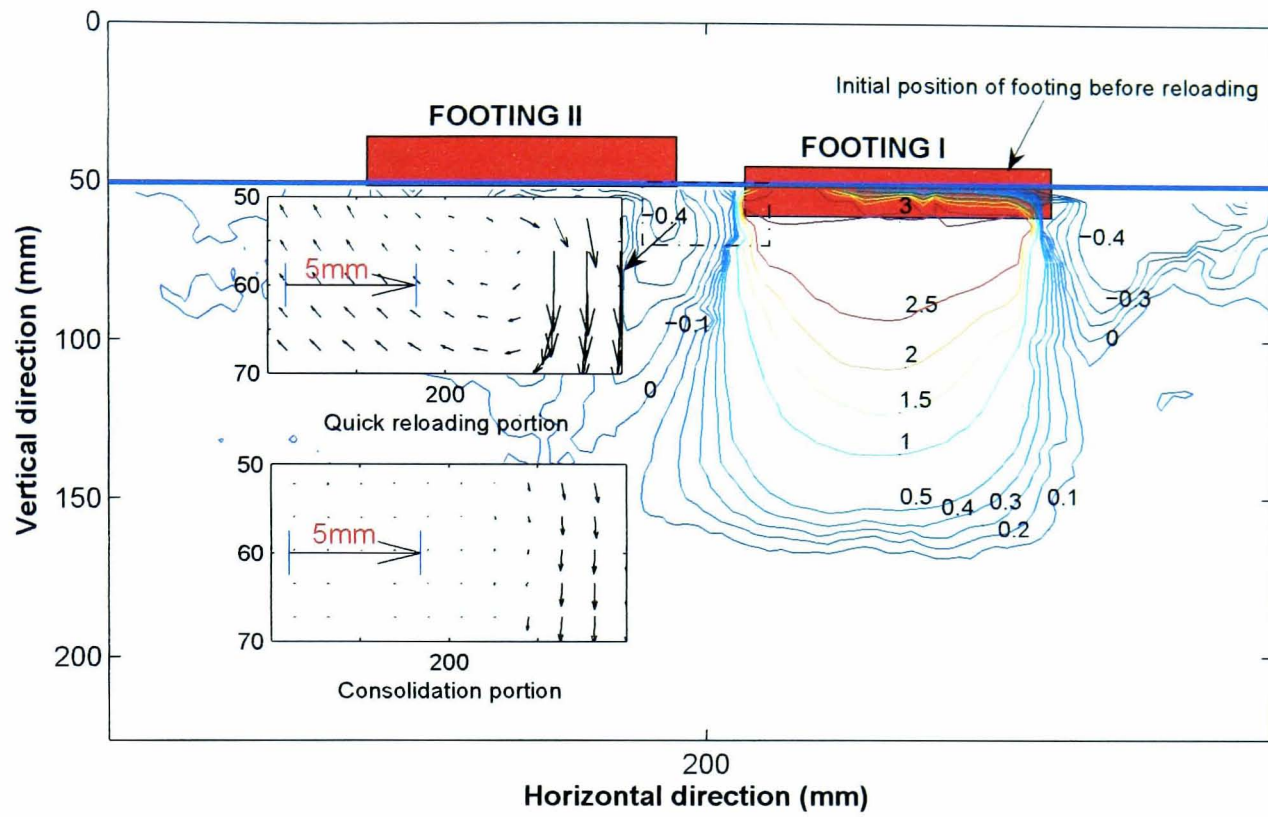
**Figure 5.17:** Contour of vertical displacement due to quick reloading on Footing I in Test DF1
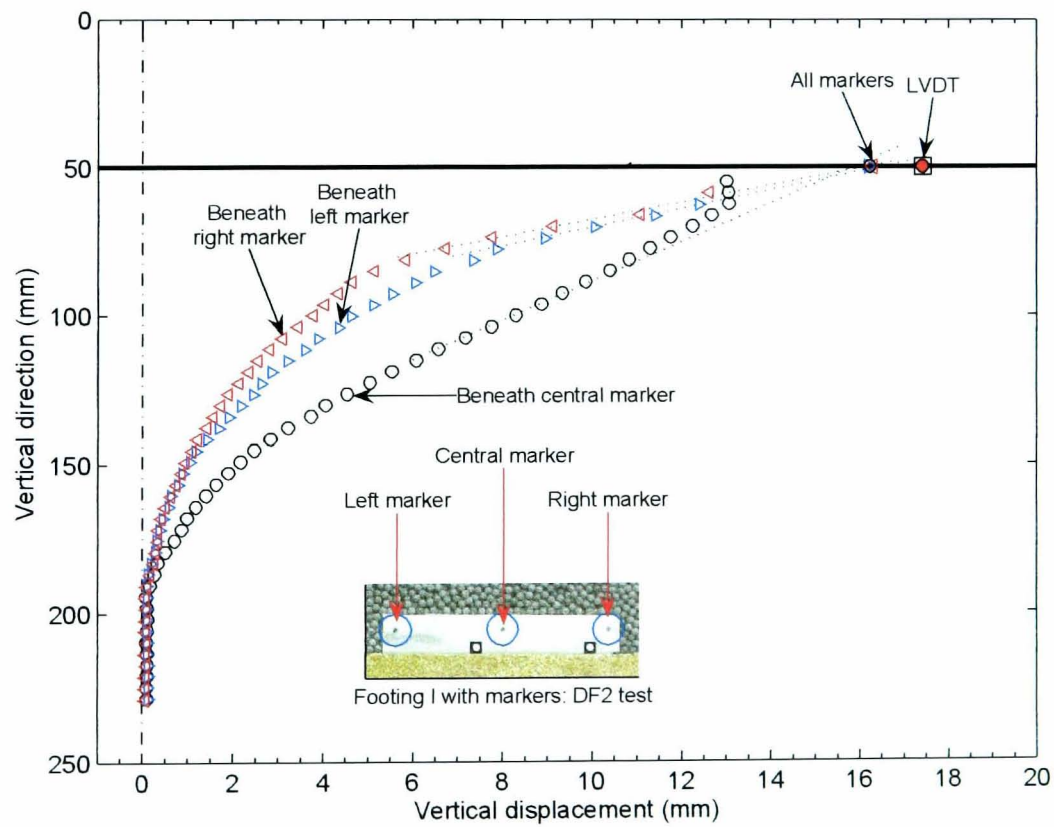


**Figure 5.18:** Vertical displacement beneath Footing I in Test DF2
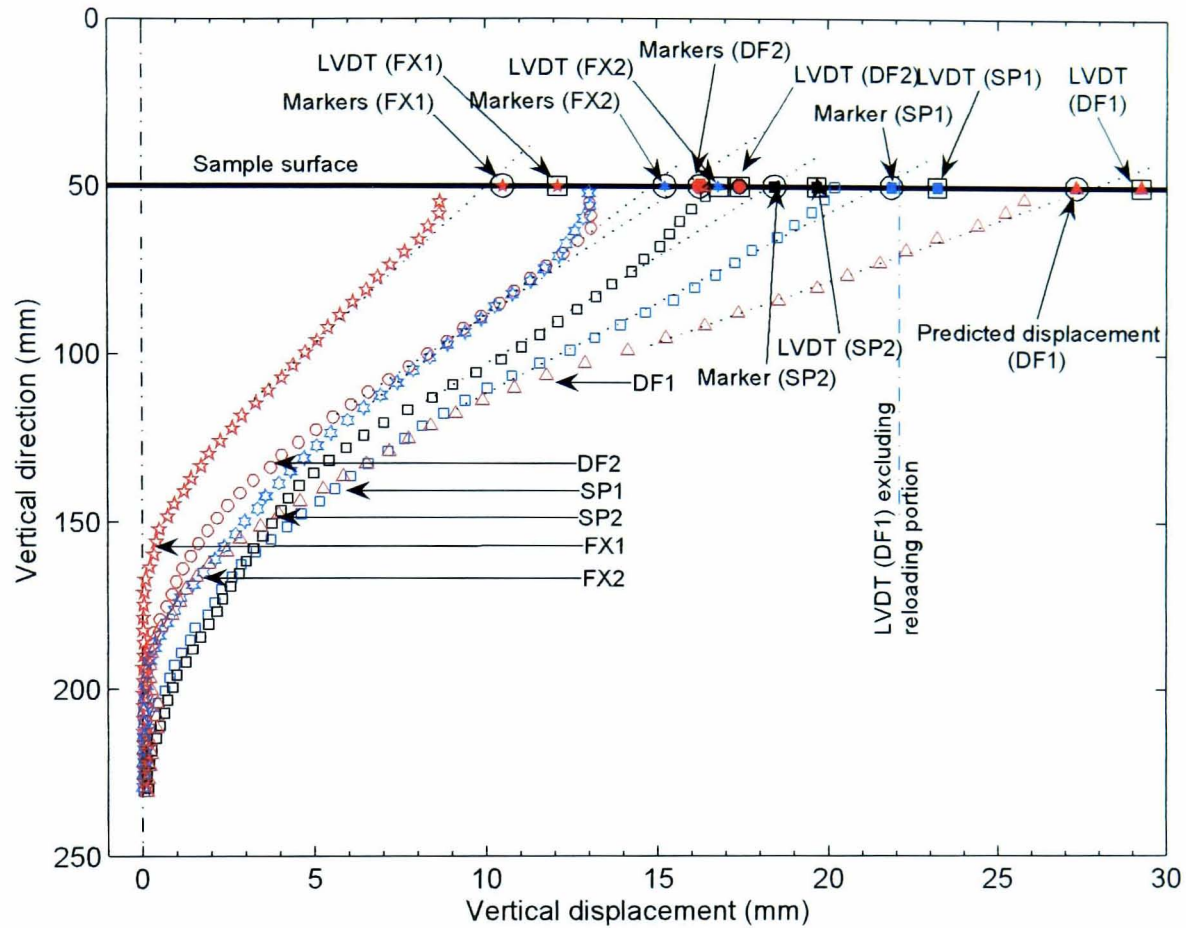
**Figure 5.19:** Vertical displacement beneath Footing I

### 5.3.2  Loading on Footing II

#### 5.3.2.1  *Effect of Interference*

Once creep under the final increment of loading on Footing I had developed (i.e.consolidation had ended), successive 5-kPa increments of loading on Footing II were applied. The loading procedures exactly repeated those for Footing I (see Section 3.5.2), finishing with a contact pressure of 80 kPa. Figure 5.20 shows the LVDT measurements of the vertical displacement at the centres of Footing I and Footing II for both the DF tests as well as the SP and the FX tests. The settlements and the respective creep components are summarised in Table 5.3. A stiffer soil response beneath Footing II was observed in all the tests, resulting in less settlement than that of the single footing (Figure 5.9). This phenomenon was also observed by Graham et al. (1984) from tests on closely-spaced footings on sand.
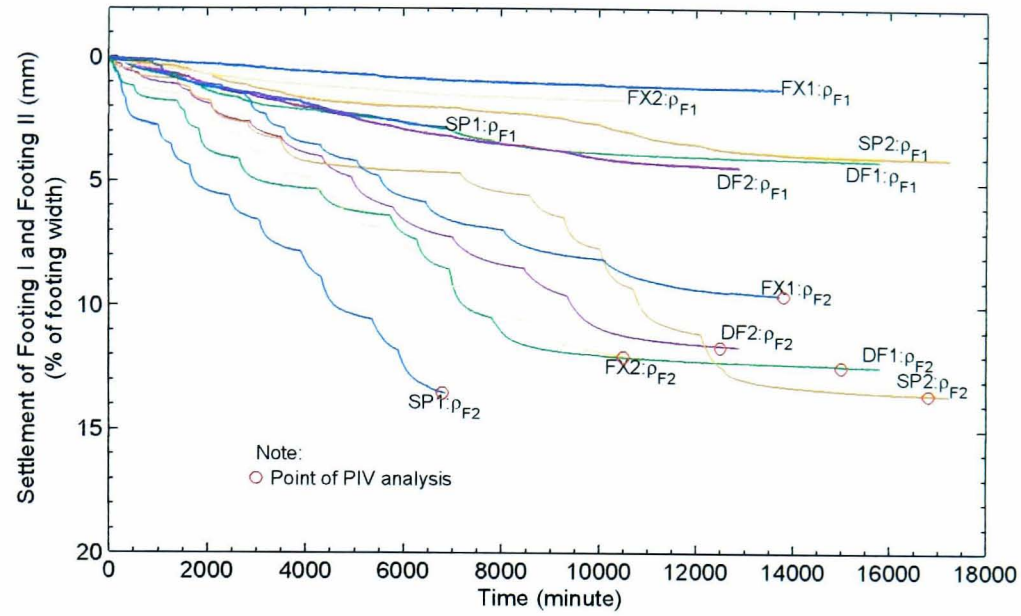
**Figure 5.20:** Settlement of Footing I and Footing II due to loading on Footing II

**Table 5.3:** Settlement ($\rho_{tot}$) and creep ($\rho_s$) of Footing I and Footing II due to loading on Footing II

| Test | FOOTING II | | | FOOTING I | | |
|------|-----------|---|---|----------|---|---|
| | $\rho_{tot}$ (mm) | $\rho_s$ (mm) | $\rho_{net}$ (mm) | $\rho_{tot}$ (mm) | $\rho_s$ (mm) | $\rho_{net}$ (mm) |
| **DF1** | 12.46 | 1.18 | 11.28 | 4.14 | 0.49 | 3.65 |
| **DF2** | 11.66 | 2.00 | 9.66 | 4.42 | 1.47 | 2.95 |
| **SP1** | 13.54 | 2.07 | 11.47 | 2.82 | 0.45 | 2.37 |
| **SP2** | 13.58 | 1.71 | 11.87 | 4.06 | 0.52 | 3.54 |
| **FX1** | 9.58 | 1.74 | 7.84 | 1.22 | 0.55 | 0.67 |
| **FX2** | 12.06 | 3.03 | 9.03 | 1.74 | 1.11 | 0.63 |

Figure 5.21 presents the relationship of the displacements extracted from Figure 5.20 at the end of each loading increment and the corresponding pressures. Although each type of test (DF, SP, or FX) had different treatments of the soil prior to imposing incremental loading on Footing II, they displayed similar settlement behaviour. For comparison, the best fit curve of the pressure–settlement relationship of the single footing is also incorporated in the figure. The lower parts of both curves almost tally in the range less than the preconsolidation pressure of 50 kPa. The two curves then start diverging. When they are correlated as shown in Figure 5.22, it indicates that the presence of the loaded Footing I did not affect the settlement characteristics of the soil beneath the Footing II until the preconsolidation pressure of the soil was exceeded. The correlation above the preconsolidation pressure indicates that the pressure of the Footing I reduced the settlement in Footing II by approximately 50%.
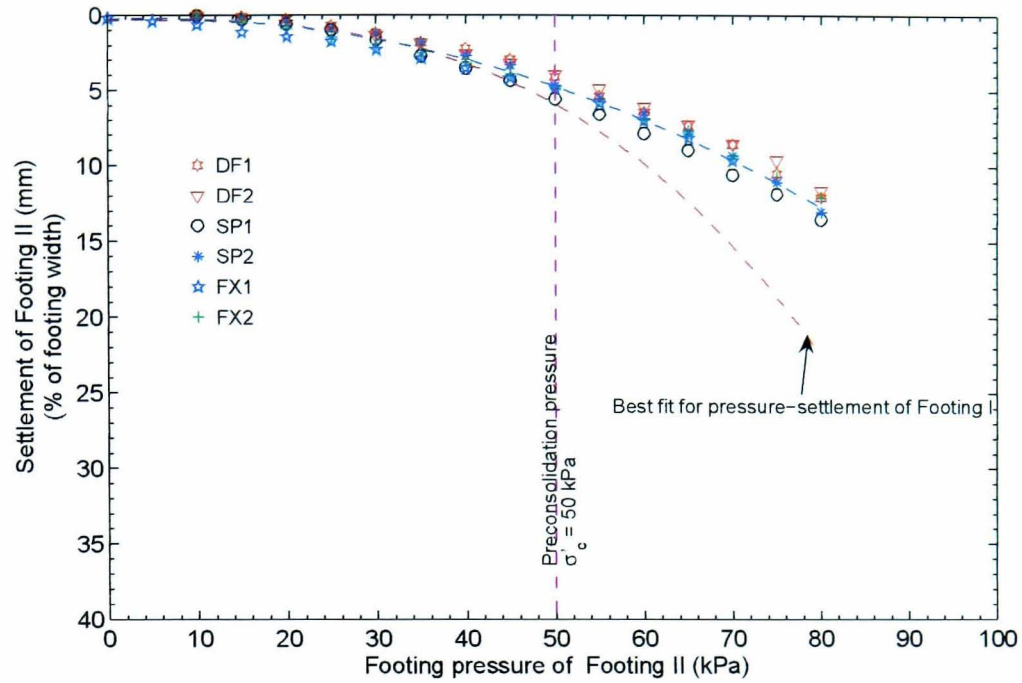
**Figure 5.21:** Load and settlement relationship at the centre of Footing II
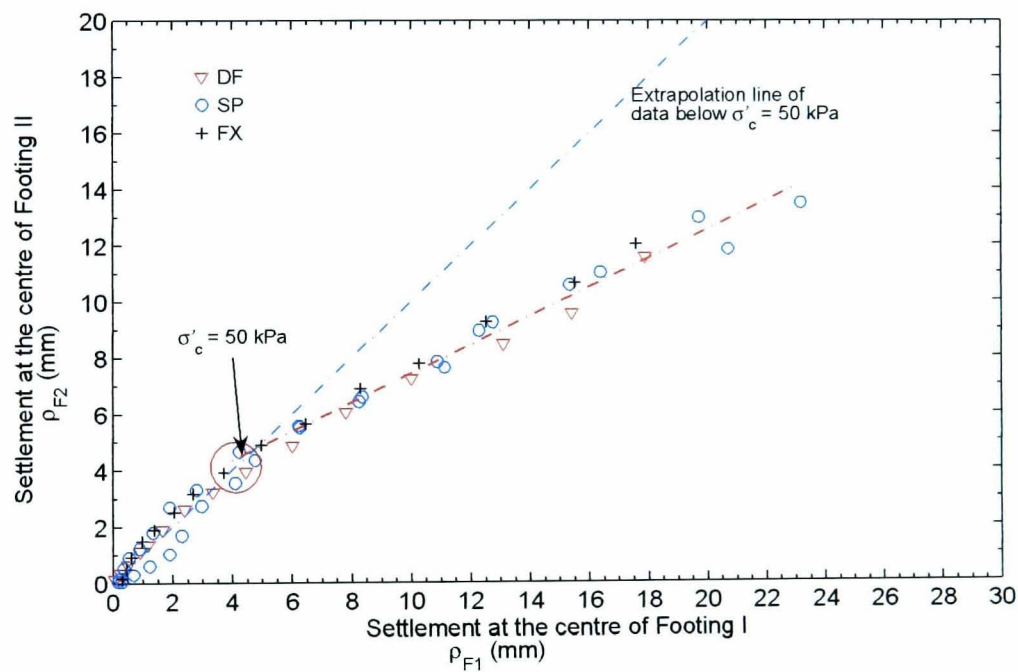


**Figure 5.22:** Correlation of settlement of Footing I and Footing II

Cumulative soil movement relative to the situation at the beginning of incremental loading on Footing II for Tests DF1 and DF2 is respectively shown with vectors in Figure 5.23 and Figure 5.24. The vectors were derived from PIV analyses on a series of images taken just before the application of the first loading on Footing II and at the end of consolidation of every pressure

increment. It is noted in Figure 5.23 that some displacement vectors below Footing II are shown as zero magnitudes. This was caused by some grease unintentionally rubbed on the Perspex window blocking the texture of the soil. The PIV could not therefore detect the soil displacement. Later, this problem also affected the calculated displacement contours around the area concerned. The vertical displacement contours are shown in Figure 5.25 and Figure 5.26. Although at the end of the tests, Footing I and Footing II were subjected to the same amount of loading, asymmetric vertical displacements were observed in both tests. The total displacements in Tests DF1 and DF2, from the initial loading on Footing I to the final loading on Footing II, are shown in Figure 5.27 and Figure 5.28. As already indicated, Footing II always had less settlement than Footing I.

Unlike the tests on single footing (loading on Footing I) where the soil nearby was pushed laterally away from the footing, the soil in the region between the footings seemed to move straight down. This indicates that the stressed region beneath Footing I passively resisted the lateral pressure from Footing II. Figure 5.29 details changes of the horizontal displacement midway between the footings, caused by footing pressures of 55 kPa, 65 kPa, and 80 kPa. By convention, negative values mean that the soil was horizontally displaced to the left and positive values imply the op-
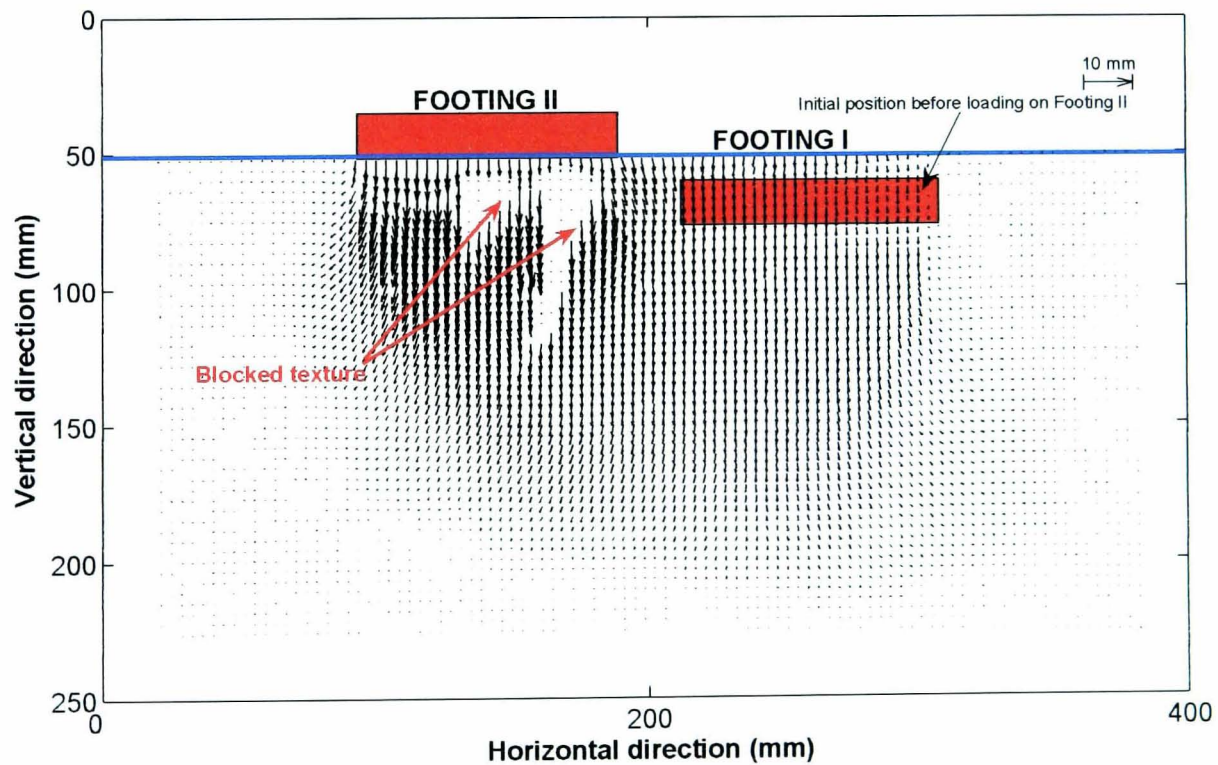


**Figure 5.23:** Vectors of cumulative displacement due to final loading on Footing II in Test DF1
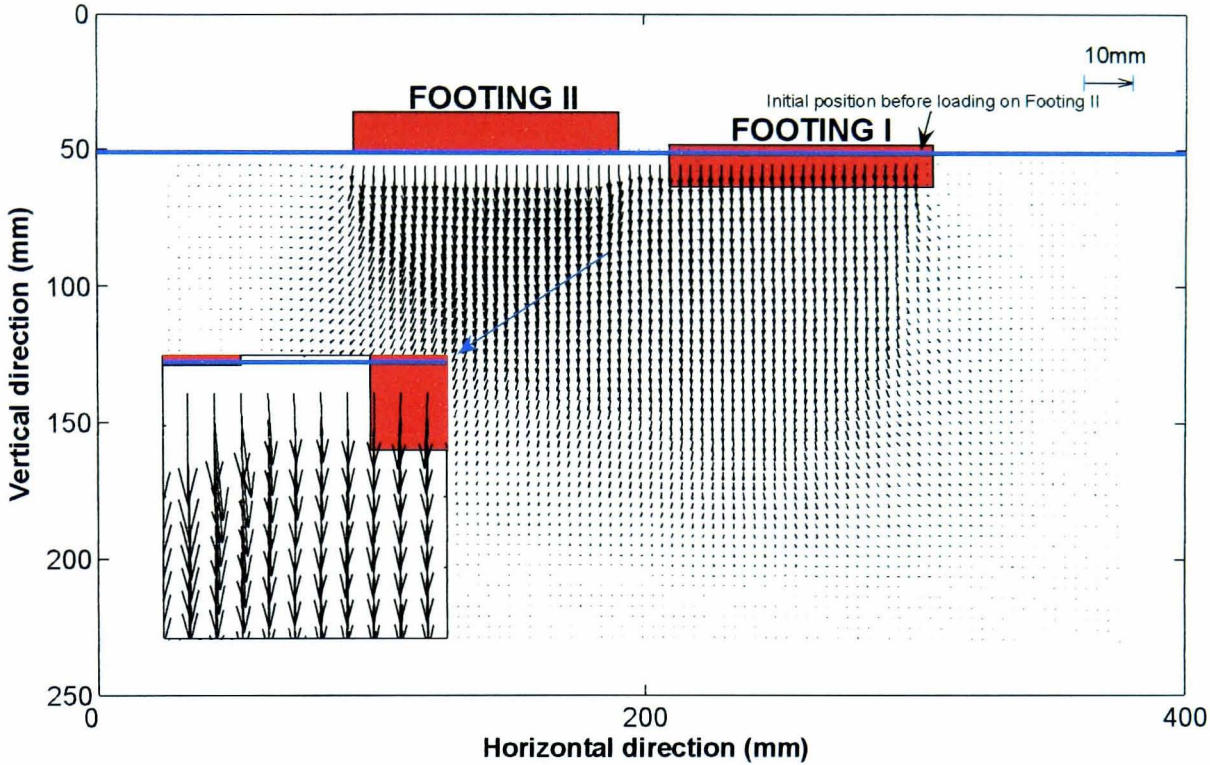
**Figure 5.24:** Vectors of cumulative displacement due to final loading on Footing II in Test DF2
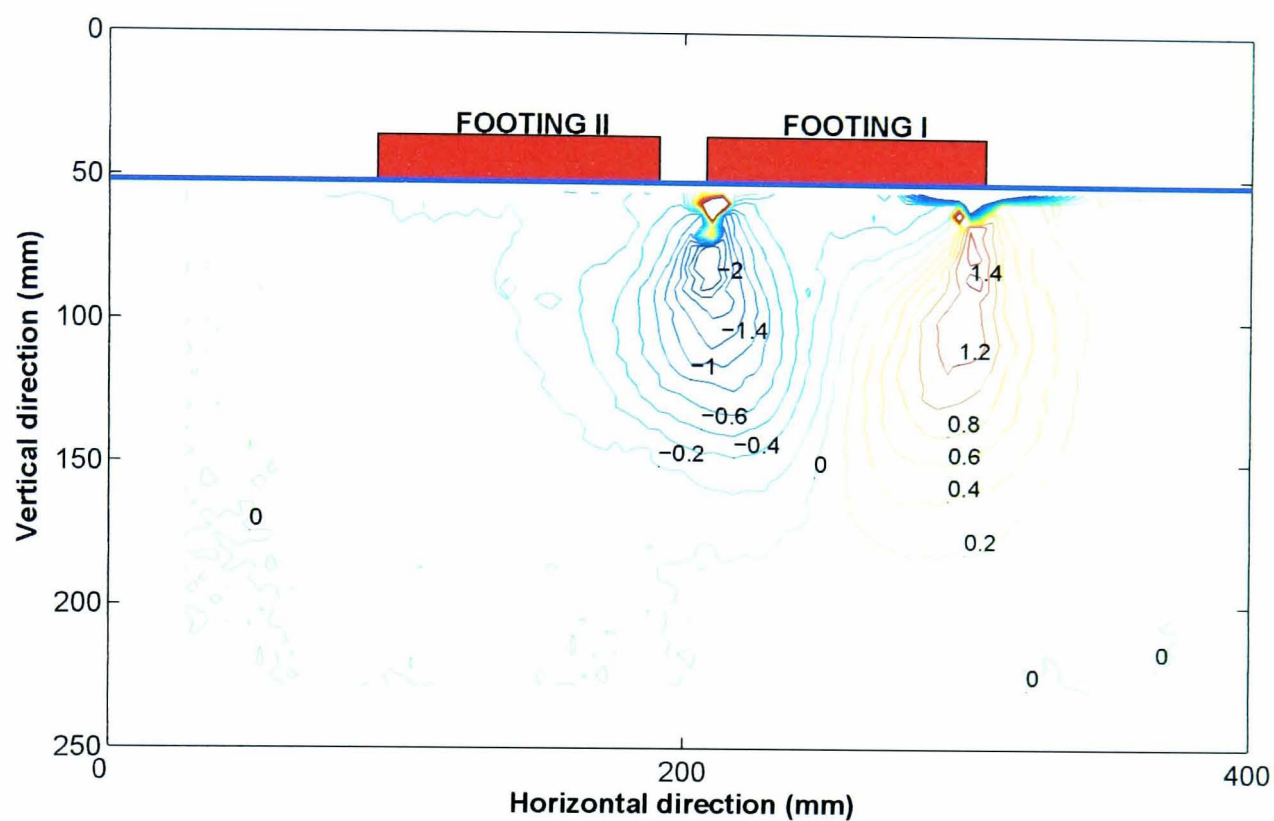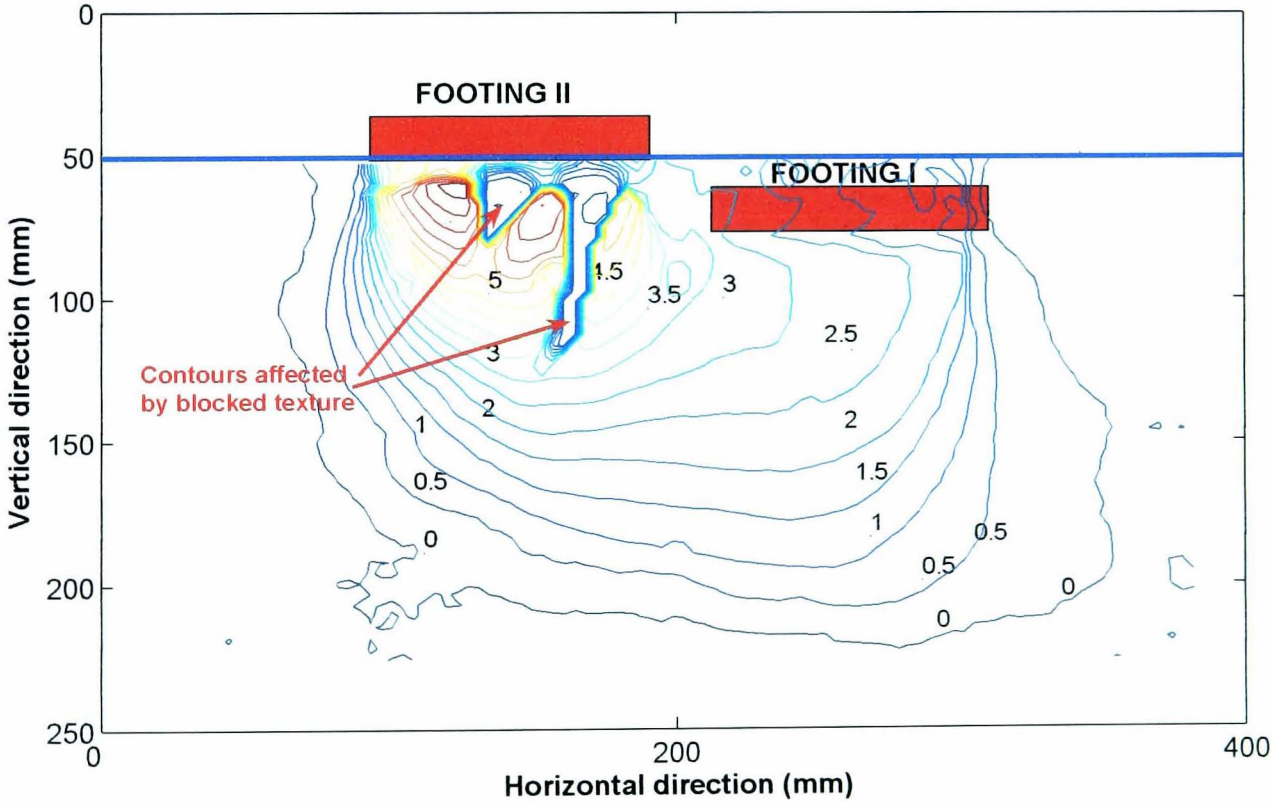


**Figure 5.25:** Contour of cumulative vertical displacement due to final loading on Footing II in Test DF1
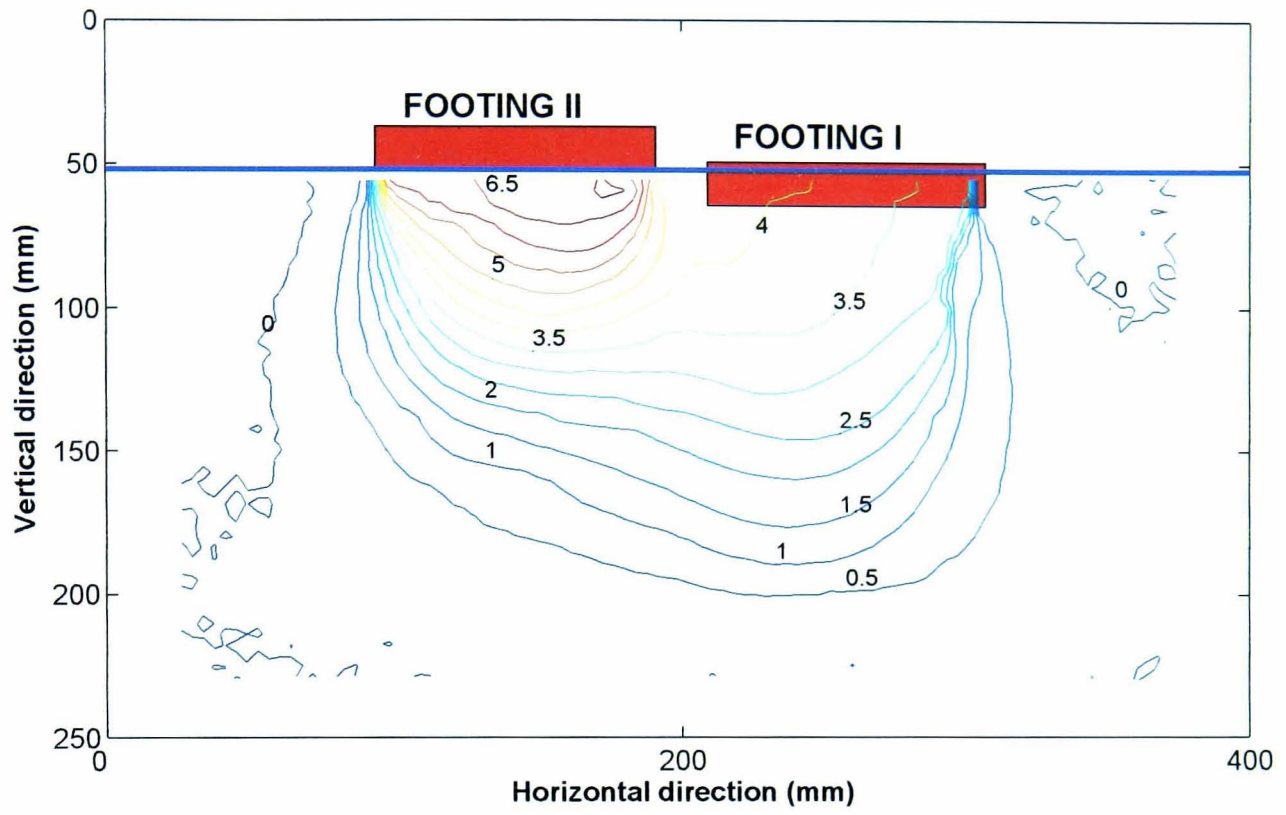
**Figure 5.26:** Contour of cumulative vertical displacement due to final loading
on Footing II in Test DF2
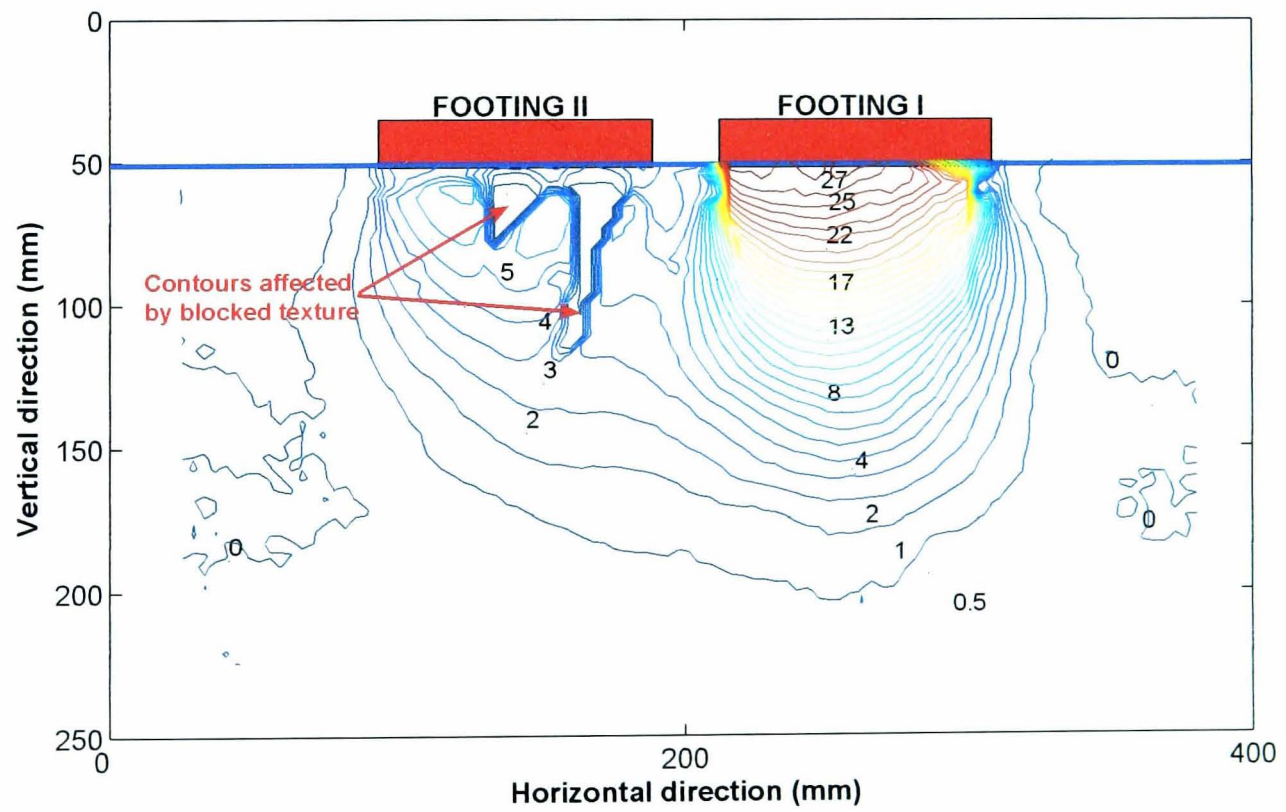


**Figure 5.27:** Contours of total vertical displacement at the end of Test DF1
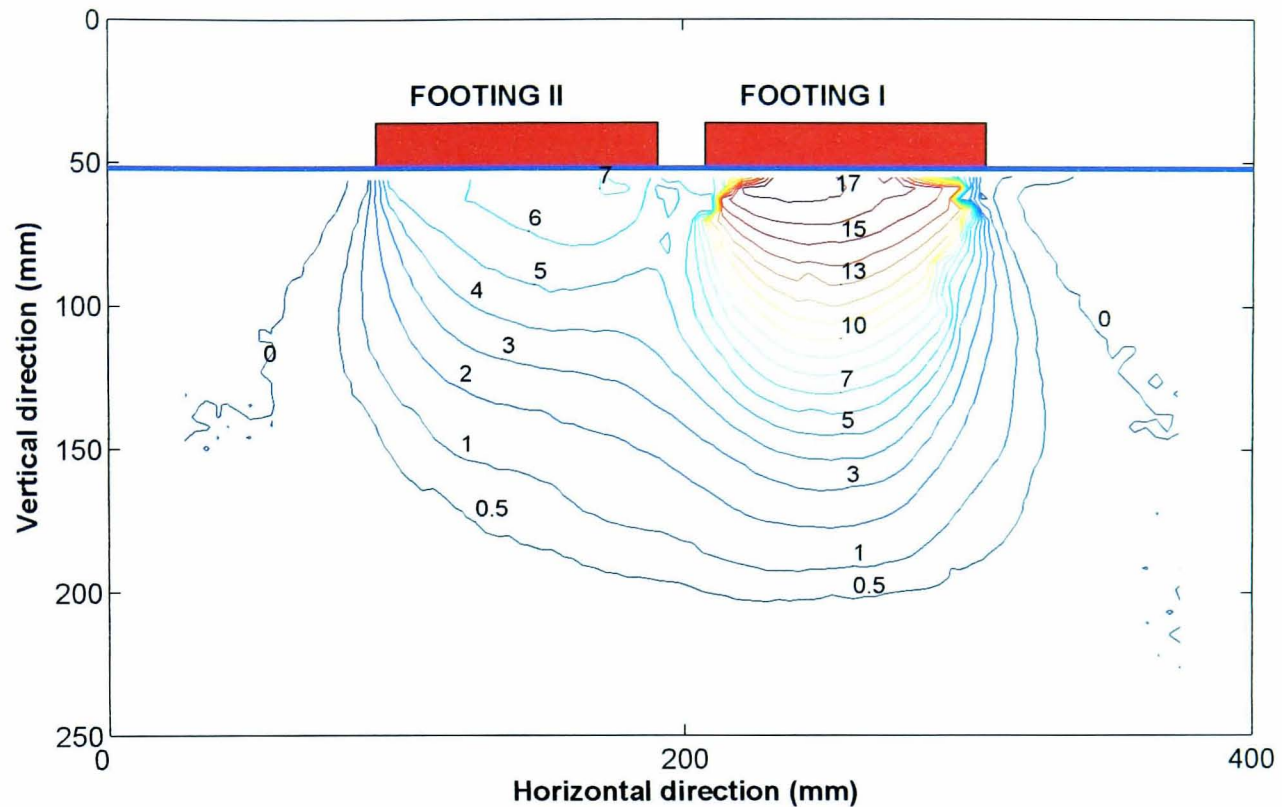
**Figure 5.28:** Contour of total vertical displacement at the end of in Test DF2

posite. Although the displacement magnitude was very small, i.e. a maximum of only about 0.4% of the footing width, it is evident that the lateral pressure induced by Footing I still prevailed in this region. It is shown that up to a pressure of 55 kPa, or about the preconsolidation pressure, the soil moved horizontally towards Footing II. At higher pressures, a pivoting point of different deformation characteristics was observed at a depth of approximately $0.9B$, where $B$ was the footing width. Above this point, the soil moved back towards Footing I with increasing pressure, while the soil below the point to a depth of about $1.4B$ still moved towards the Footing II. This behaviour is depicted in Figure 5.30. The lower region from a depth of $2B$ seemed unaffected by the pressures from both footings.

The effects of loading on Footing II on the vertical displacement at the centre of Footing I and Footing II were also observed from the results of LVDT measurement as shown in Figure 5.20. The curves resulting from Tests DF1 and DF2 are plotted again in Figure 5.31 and Figure 5.32. The displacement was measured with respect to the soil level at the beginning of the loading on Footing II. In both figures the previous time–settlement curves for Footing I from the last incremental pressure of 80 kPa are incorporated. Each creep portion at the curve's tail is extended to the end of
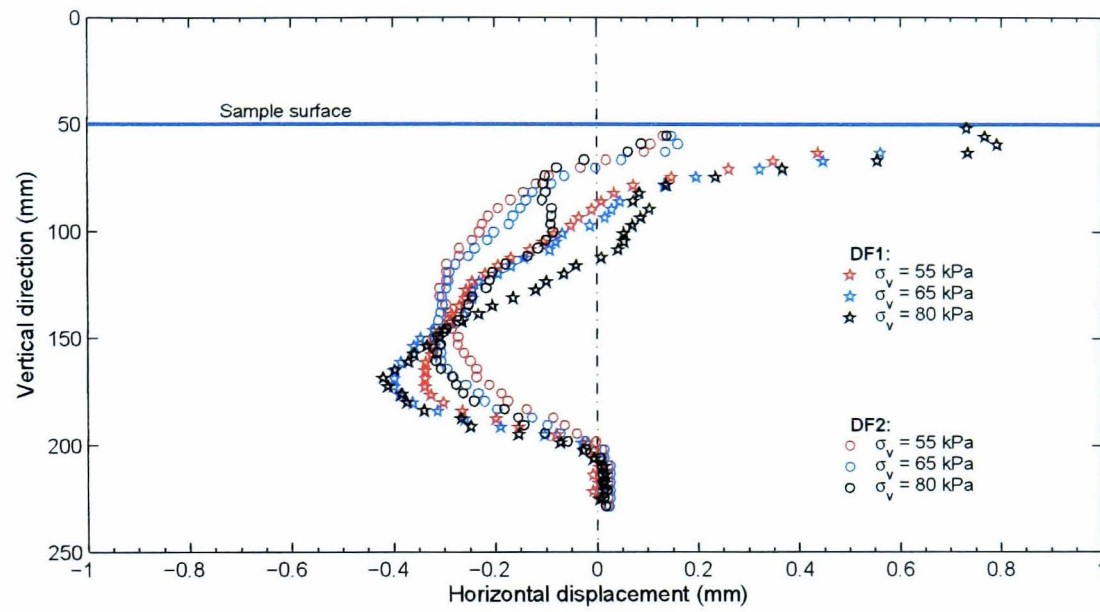
**Figure 5.29:** Effect of incremental loading on Footing II on horizontal displacement at centre of sample.
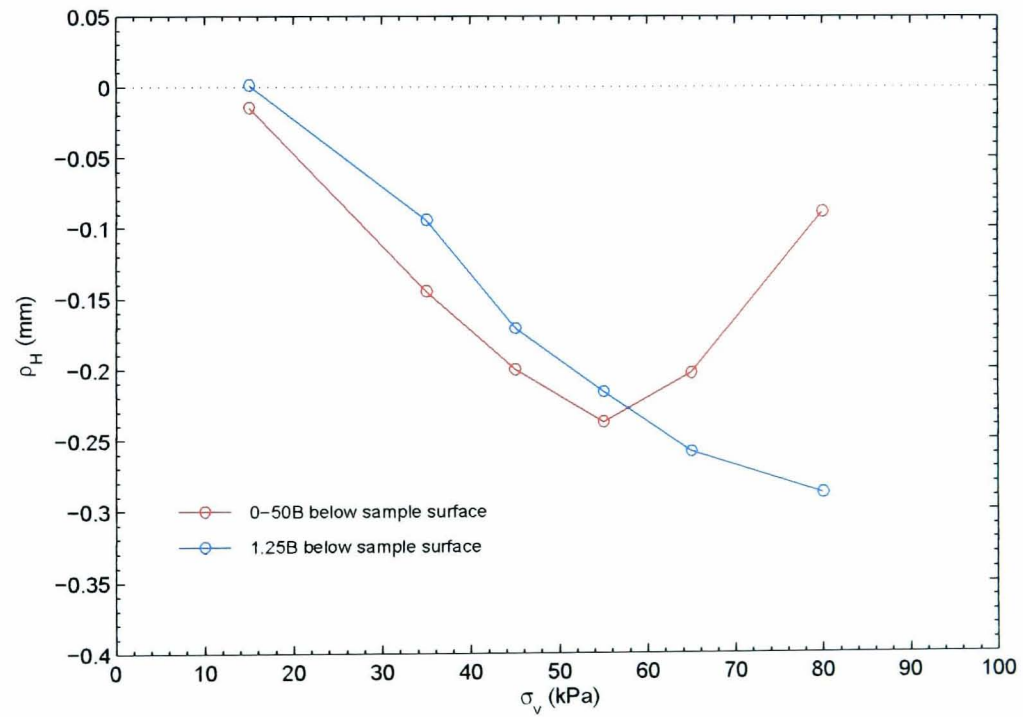


**Figure 5.30:** Effect of incremental loading on Footing II, in Test DF2, on horizontal displacement at centre of sample at the depth of 0.5B and 1.25B from the sample surface
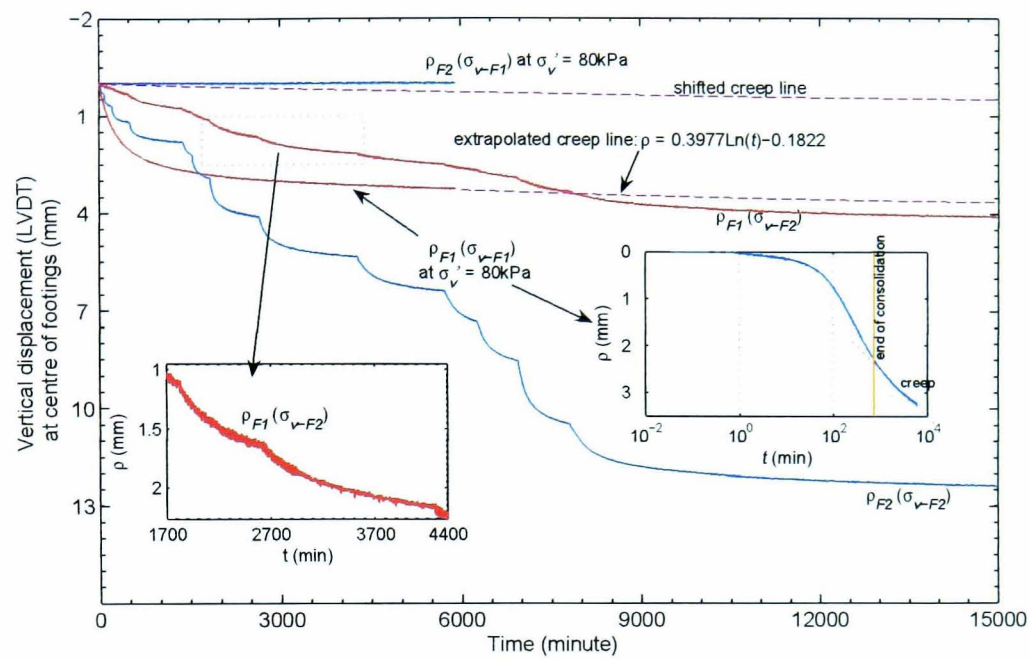
**Figure 5.31:** Effect of loading on Footing II on the vertical displacement of Footing I and Footing II in Test DF1
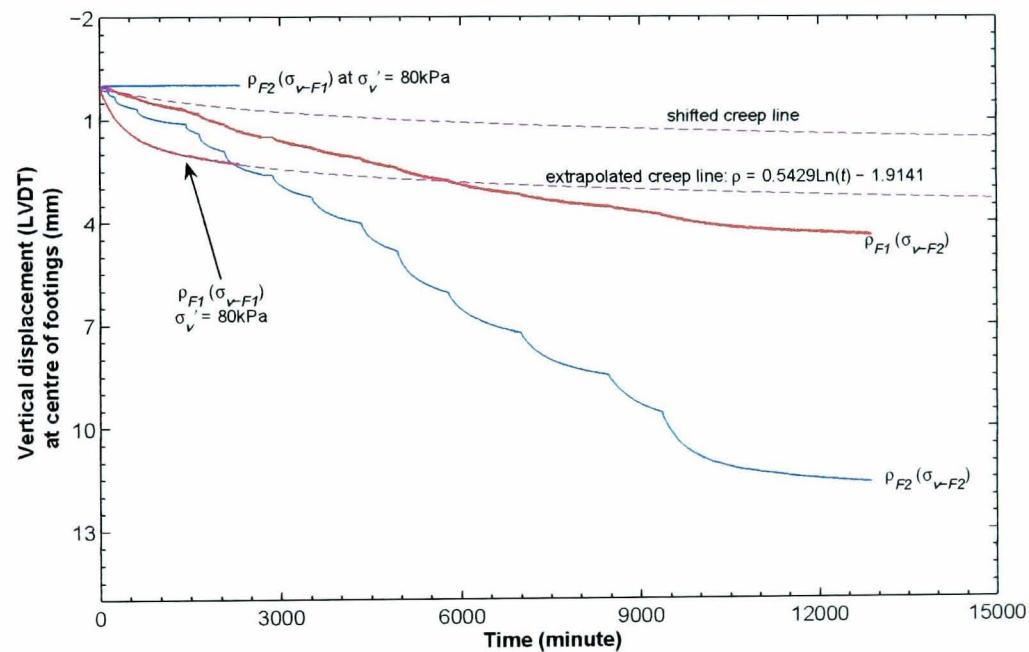


**Figure 5.32:** Effect of loading on Footing II on the vertical displacement of Footing I and Footing II in Test DF2

the test. The extrapolated line was obtained from the best fit of the creep line. For the purpose of observing whether the current settlements of Footing I were induced by the incremental loading on Footing II or were due to creep, the line was then reset to zero settlement. It is clearly evident from the figure that the pressures from Footing II influenced the settlement of Footing I. This is indicated

by additional small deformations in the settlement curve of Footing I under every pressure increment. The divergence of the settlement curve of the Footing I from the shifted creep line further explains that the settlement was mainly caused by consolidation. In Test DF1, the total settlements of Footing II and Footing I were 12.46 mm and 4.14 mm respectively from the loading on Footing II, i.e. Footing I settled by only about 33% of the settlement of Footing II or $\rho_{F1}/\rho_{F2} = 0.33$. In Test DF2, Footing II settled 11.66 mm and Footing I by 4.42 mm or $\rho_{F1}/\rho_{F2} = 0.38$. Over the loading increments, the cumulative creep developed in the settlement of Footing II and Footing I in Test DF1 was 1.18 mm and 0.49 mm consecutively. In Test DF2, the cumulative creep was 2.00 mm for Footing II and 1.47 mm for Footing I. Disregarding the displacement caused by the creep, the ratios $\rho_{F1}/\rho_{F2}$ were 0.32 for Test DF1 and 0.31 for Test DF2.

### 5.3.2.2  Tilting

Both footings suffered tilting and tended to tilt toward each other. Similar behaviour was also found by Jao et al. (2002) from a finite element simulation of footings supported by cohesive soil. Unfortunately the magnitude of tilting obtained from their research could not be compared with this study since the soil properties and loading intensity were considerably different. In their research the soil was modelled with parameters $c = 158.5$ kPa and $\phi = 8°$. The footing pressure was more than 200 kPa. They concluded that the tilting angles depended on the footing spacing as well as the pressure intensity.

To cope with the problem described in Section 5.3.1.2, namely that the visible soil directly under the footings did not settle at as much as the footings, and to accurately record the tilting, at least two horizontally separated markers were inscribed on the footing side facing the Perspex window. Patches covering the markers were used in PIV analysis to trace the footing movement. Figure 5.33 shows the markers on the footing sides and the resulting vectors analysed with PIV for Test DF2. The vector magnitudes represent the footing movement after the first loading increment was applied on Footing II. The footing movements could also be estimated by extending the plot of vertical displacement versus depth, obtained with PIV analysis, to the soil surface under the footings as illustrated in Figure 5.34. The footing tilting in Test DF1 (where no markers were employed) was then calculated using this interpretation. The tilting was quantified by the angular distortion, $\delta/l$ as defined by Skempton and MacDonald (1956), where $\delta$ and $l$ were respectively a
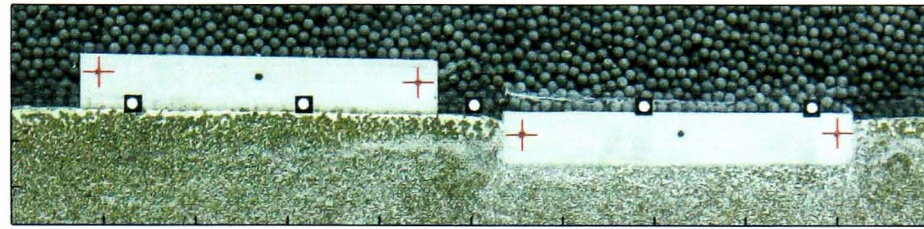
(a) Tracking markers
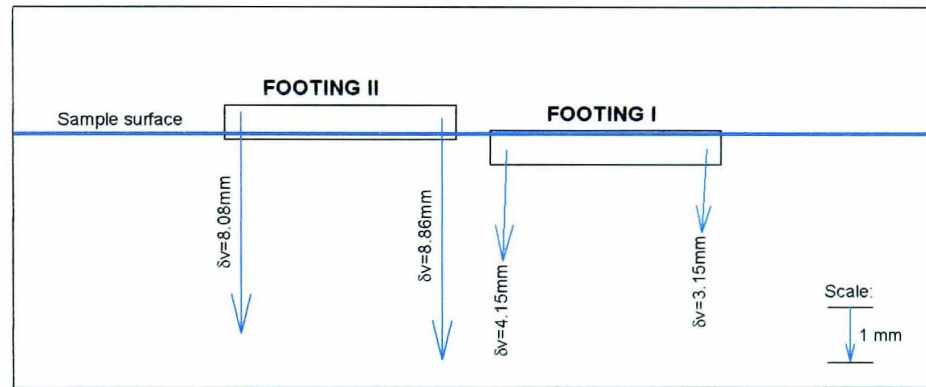


(b) Tilt of Footing I due to loading on Footing II

**Figure 5.33:** Tilting in Test DF2
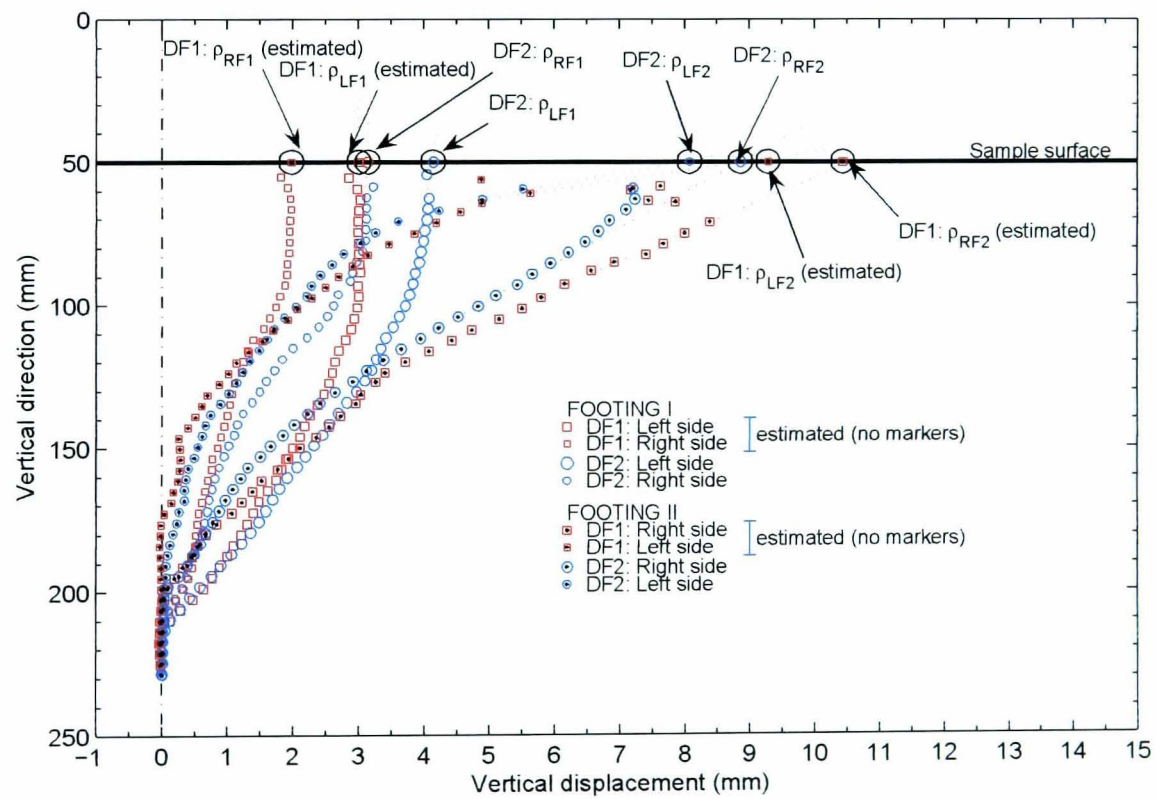


**Figure 5.34:** Vertical displacement of soil beneath the tracing markers

differential vertical movement and a horizontal distance between two markers. Since the footings were almost rigid, this effectively defined a rotation of the footing. At the end of loading on Footing II in Test DF1, Footing I had tilted with $\delta/l \approx 1/97$ and at the same time Footing II had $\delta/l \approx 1/87$. In Test DF2, Footing I tilted with $\delta/l \approx 1/87$ and Footing II with $\delta/l \approx 1/112$. Skempton and MacDonald (1956) postulated that $\delta/l \approx 1/300$ was a limiting value for buildings to crack (especially panels in frame buildings or load-bearing walls).

### 5.4   DOUBLE FOOTING WITH FLOATING SHEET WALL

#### 5.4.1   Loading on Footing I

The contours of cumulative vertical soil displacement from the first to the last increment of loading on Footing I for Tests SP1 and SP2 are depicted in Figure 5.35 and Figure 5.36. Apart from their magnitude, the patterns of the contours for these tests are very similar to those encountered in the DF tests (see Section 5.3.1.2). An unsymmetrical horizontal displacement, as found in the DF tests, was also observed in these two tests (e.g. Figure 5.37 for Test SP1).
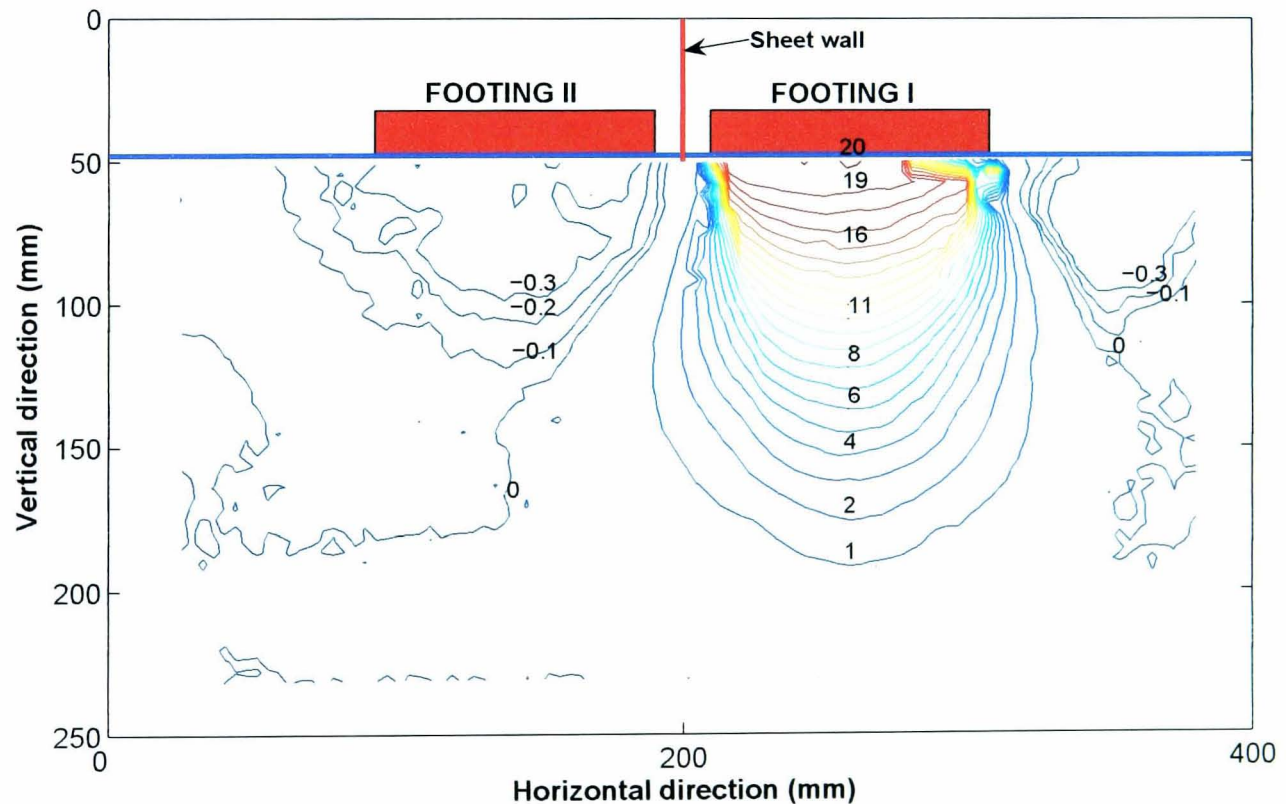


**Figure 5.35:** Contours of cumulative vertical displacement due to final loading on Footing I in Test SP1
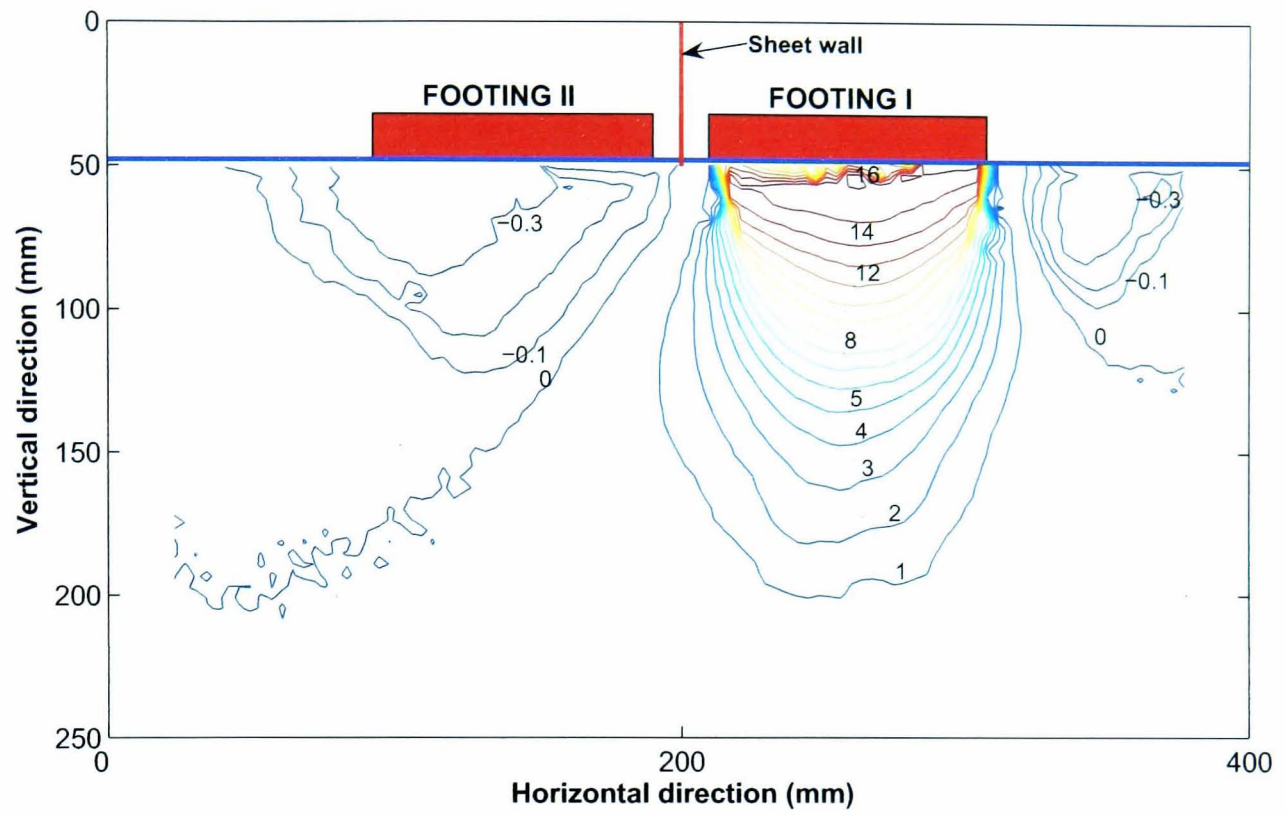
**Figure 5.36:** Contours of cumulative vertical displacement due to final loading on Footing I in Test SP2
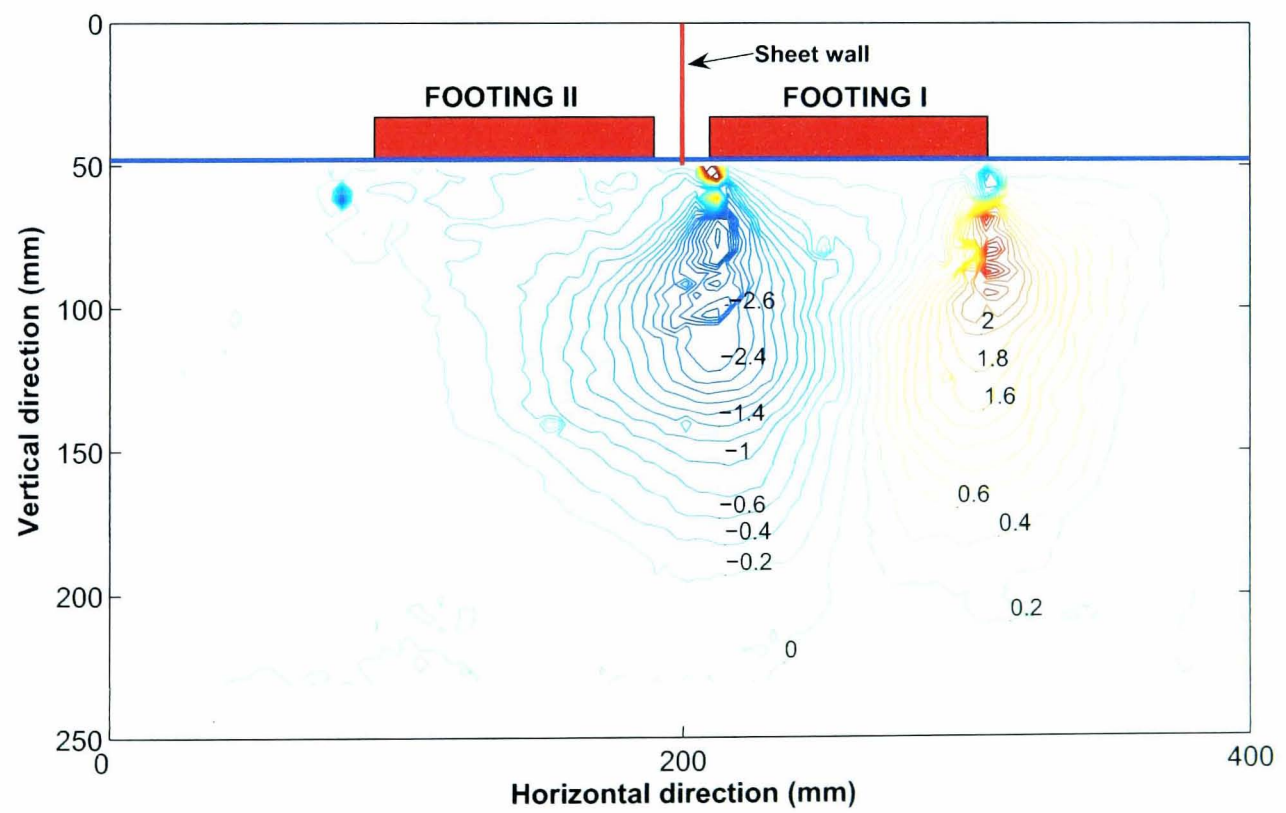


**Figure 5.37:** Contours of cumulative horizontal displacement due to final loading on Footing I in Test SP1

### 5.4.2 Sheet Wall Insertion

In these two tests, Tests SP1 and SP2, an aluminium sheet wall with a length of 100 mm and thickness of 1.5 mm was inserted between Footing I and Footing II, prior to applying the incremental loading onto Footing II. The top of the wall was level with the sample surface. It remained floating in the upper half of the sample thickness of 200 mm. A typical pattern of soil movement due to the insertion of the sheet wall is illustrated in Figure 5.38. The soil was immediately displaced by
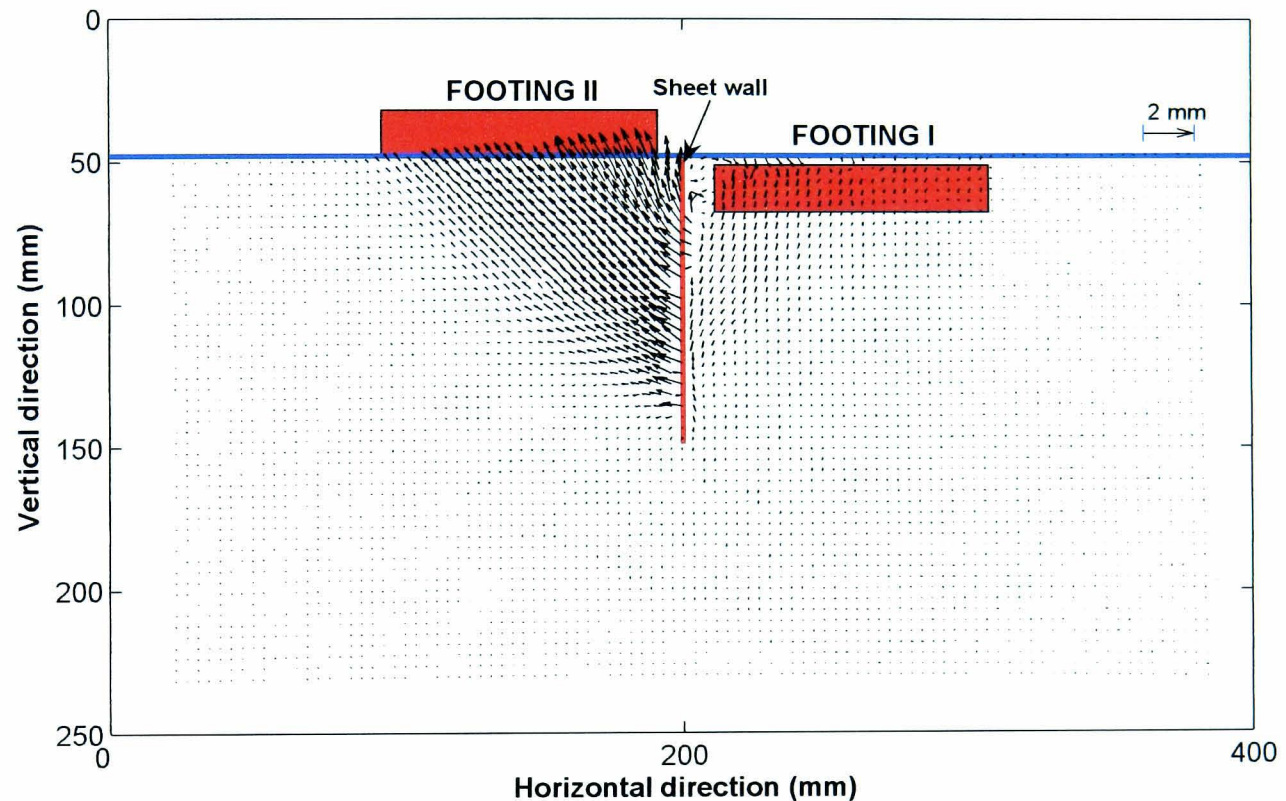


**Figure 5.38:** Soil movement by the insertion of sheet pile (Test SP1)

the penetration of the sheet. As depicted in the figure, the soil along the left side of the sheet wall was pushed towards Footing II with movement vectors at an angle of approximately 45° to the soil surface. The contours of vertical displacement in Figure 5.39 suggest that up to 1.6 mm of heaving occurred in the region beneath Footing II. This was further confirmed by an LVDT measurement that is plotted in Figure 5.40. The insertion of the sheet in ten 10-mm pushes is indicated by the steps in the curve $\rho_{F2}$. At the same time, the soil beneath Footing I was dragged down, illustrated by the curve $\rho_{F1}$. The completion of the sheet wall installation was followed by a dissipation of excess pore water pressure during which the soil displacement beneath Footing I was skewed towards the sheet wall, Figure 5.41. The loading on Footing II was delayed until consolidation ended and
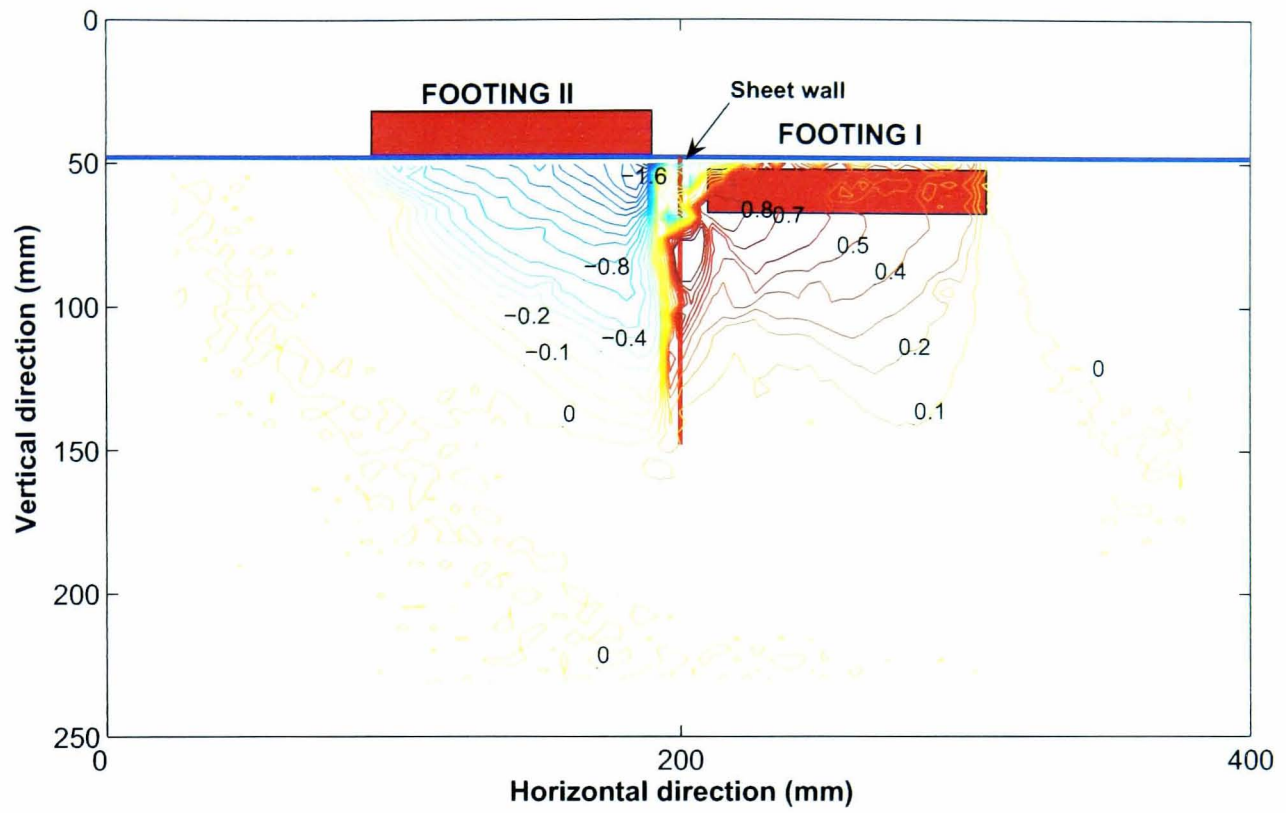
**Figure 5.39:** Contours of vertical displacement immediately after a sheet wall installation in Test SP1
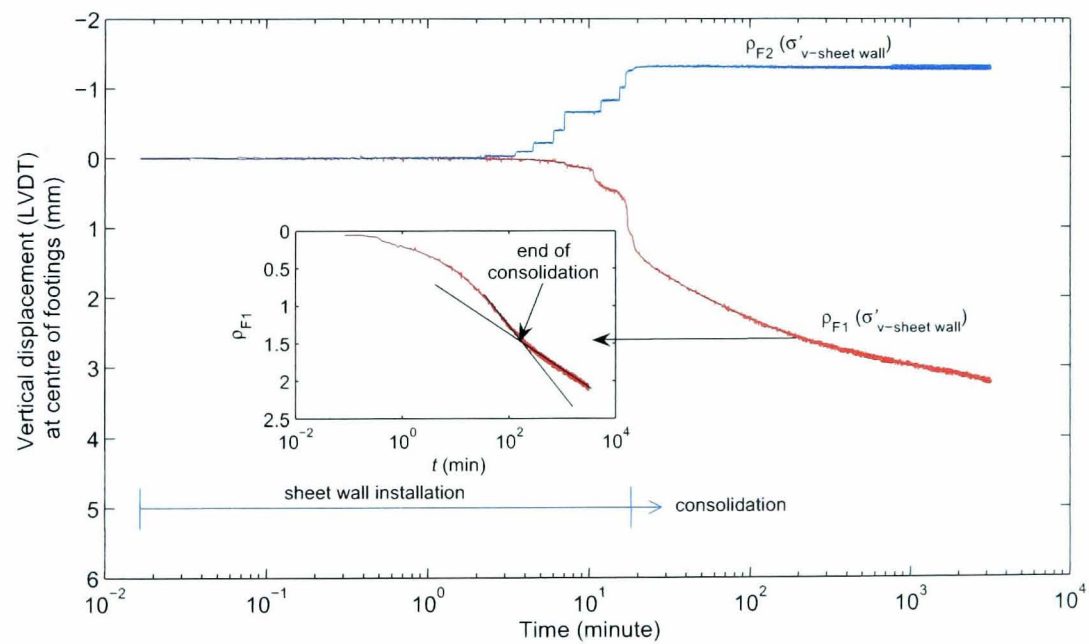


**Figure 5.40:** Settlement of footings from an LVDT measurement due to sheet wall installation (Test SP1)
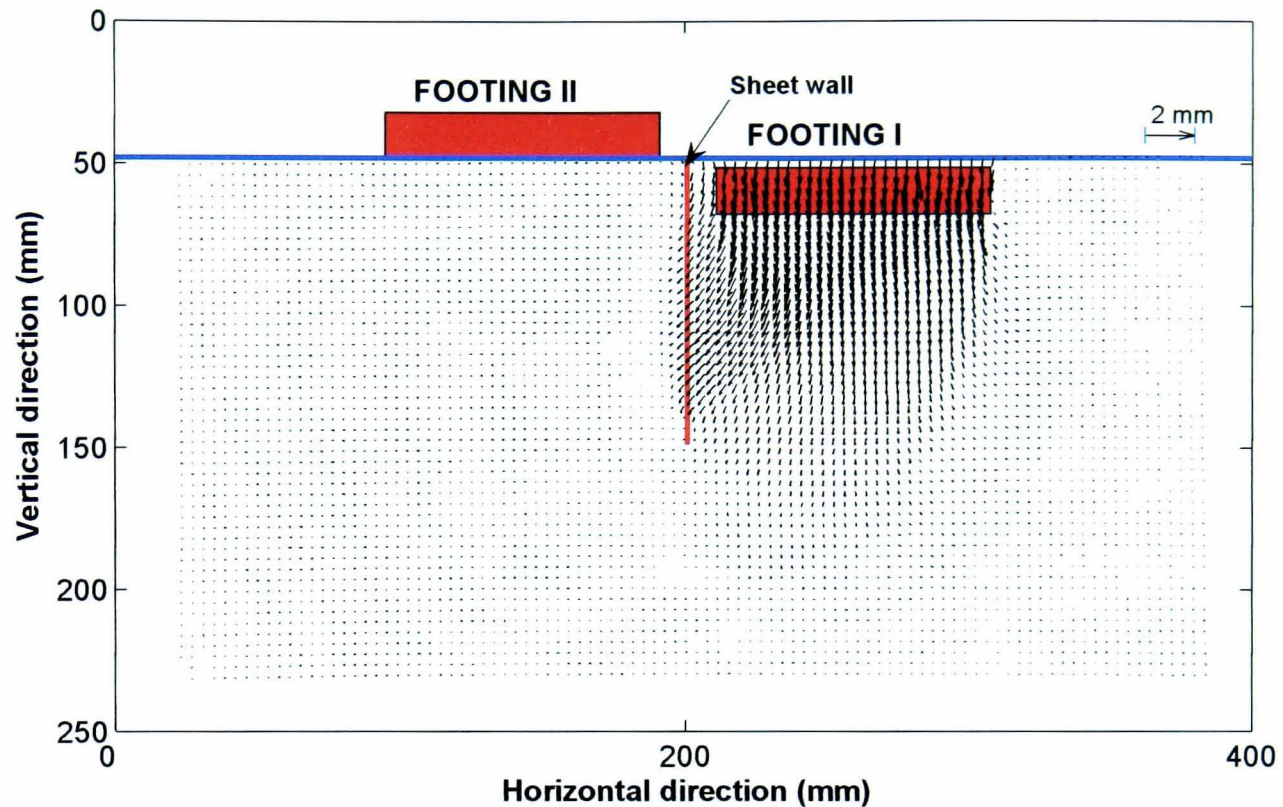
**Figure 5.41:** Soil movement after consolidation relative to the end of sheet wall installation (Test SP1)

creep developed. This was determined from the curve $\rho_{F1}$ in Figure 5.40. At the commencement of loading on Footing II, only an insignificant tilt of Footing I (due to wall insertion) with an angular distortion of $\delta/l \approx 1/667$ was detected from PIV analysis on the markers on the footing side.

### 5.4.3   Effect of Surface Roughness of Sheet Wall

The total settlements due to wall installation for Tests SP1 and SP2, relative to the beginning of the sheet wall installation, are presented in Figure 5.42 and Figure 5.43. The installation in Test SP1 caused Footing I to settle by about 3% of the footing width. Less effect was observed during the sheet wall insertion in Test SP2. As shown in Figure 5.44, the total vertical displacement at the centre of Footing I was only about 50% of that encountered in Test SP1 (see Figure 5.40). The variation is probably attributable to the roughness of the surface of the sheet wall. This phenomenon also occurred during the wall insertion in Tests FX1 and FX2 (see Figure 5.59 and Figure 5.60). The aluminium sheet walls that were used in Tests SP1 and FX2 had been previously installed into the soil during a trial test and Test FX1 respectively. In contrast, smoother new sheets were used in Tests SP2 and FX1 .
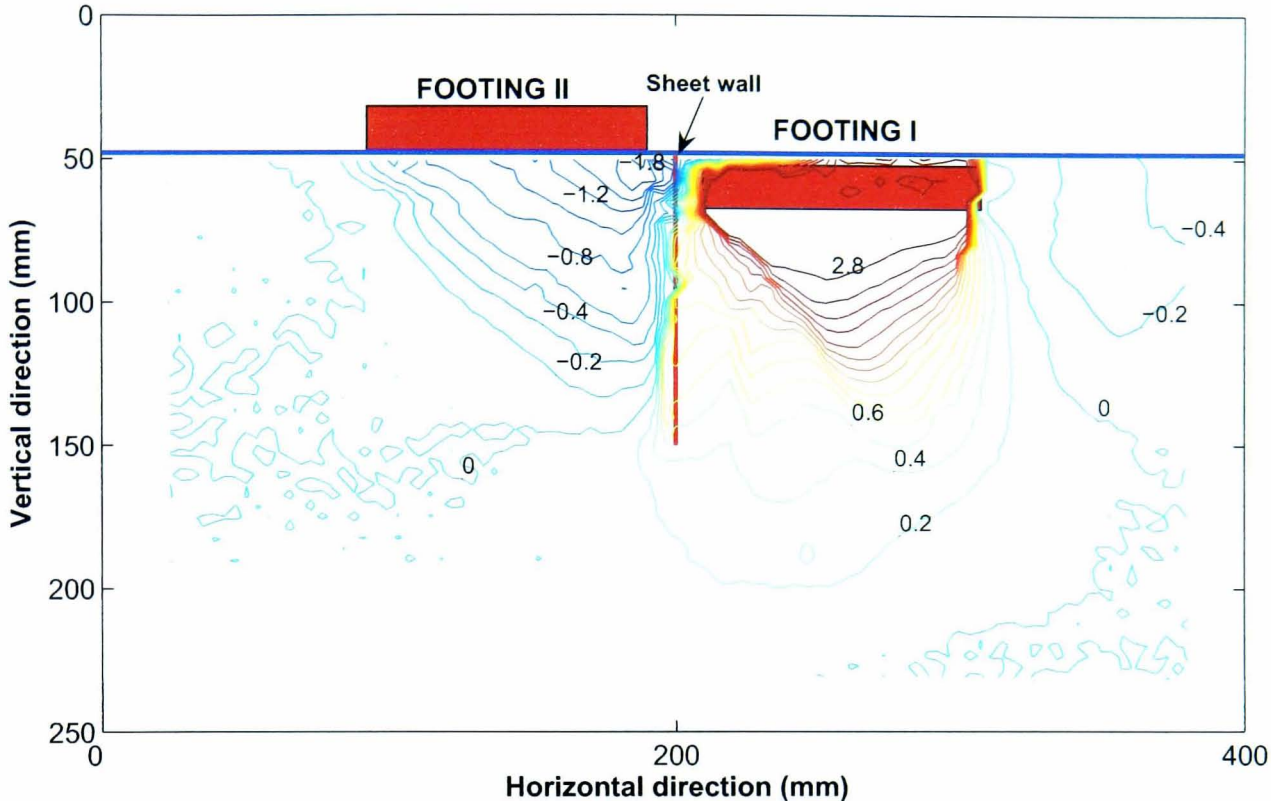
**Figure 5.42:** Contour of total settlement measured after consolidation due to sheet wall installation in Test SP1
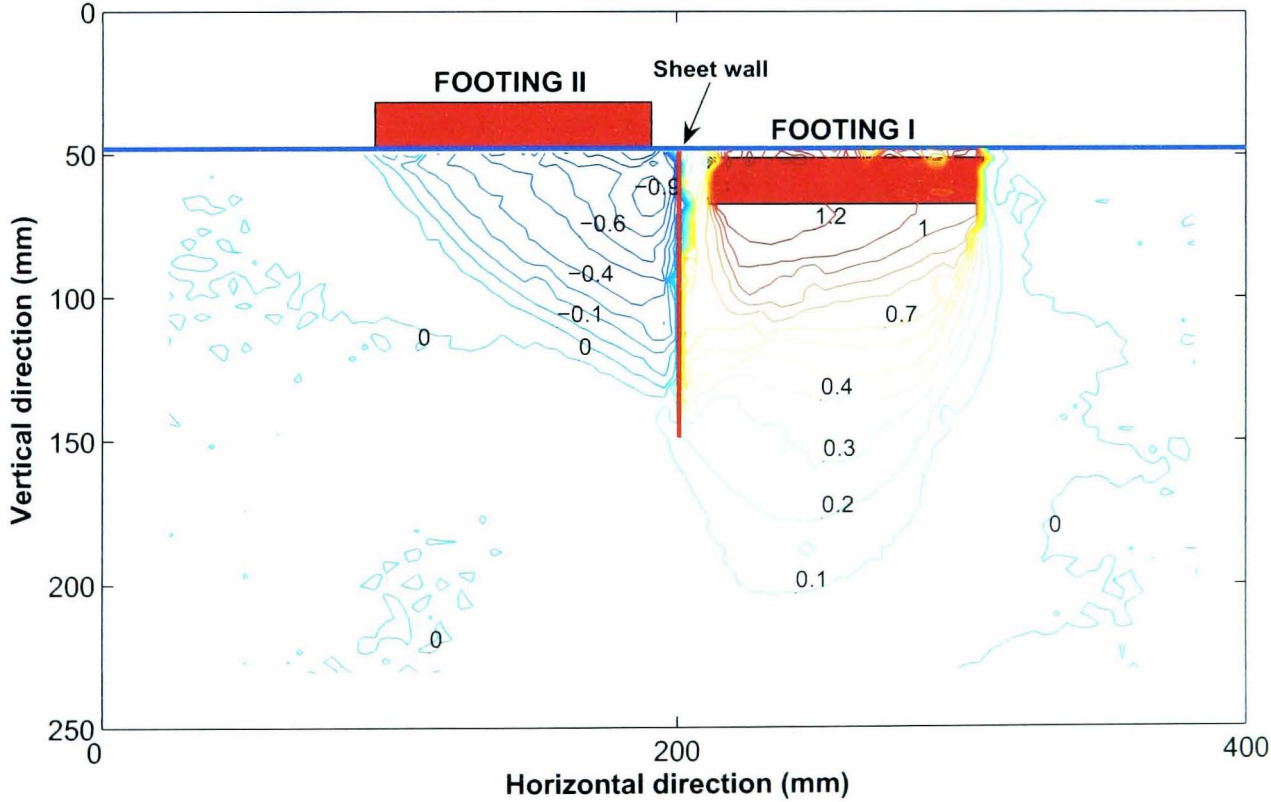


**Figure 5.43:** Contour of total settlement measured after consolidation due to sheet wall installation in Test SP2
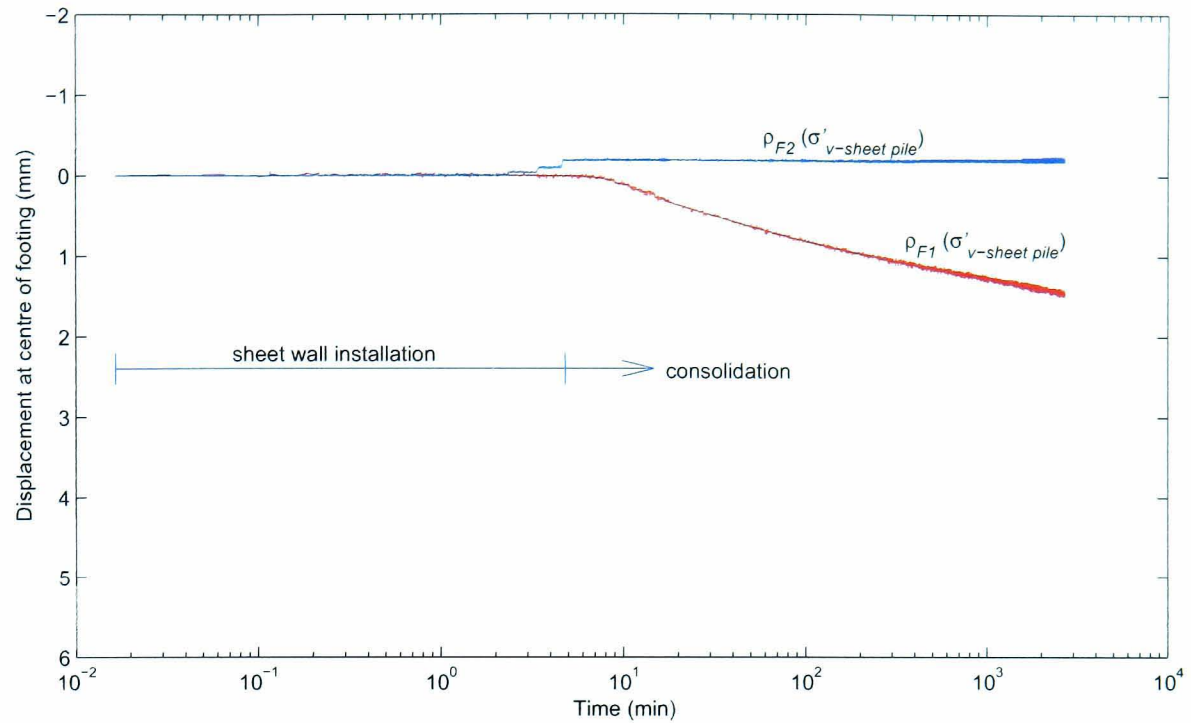
**Figure 5.44:** Settlement of footings from an LVDT measurement due to sheet wall installation in Test SP2

### 5.4.4   Loading on Footing II

*5.4.4.1   Settlement of Footings*

The incremental loading on Footing II was commenced while creep induced by the sheet wall installation was occurring. The settlement measurements from Tests SP1 and SP2 are respectively illustrated in Figure 5.45 and Figure 5.46.    Relative to an extension of the end of previous creep
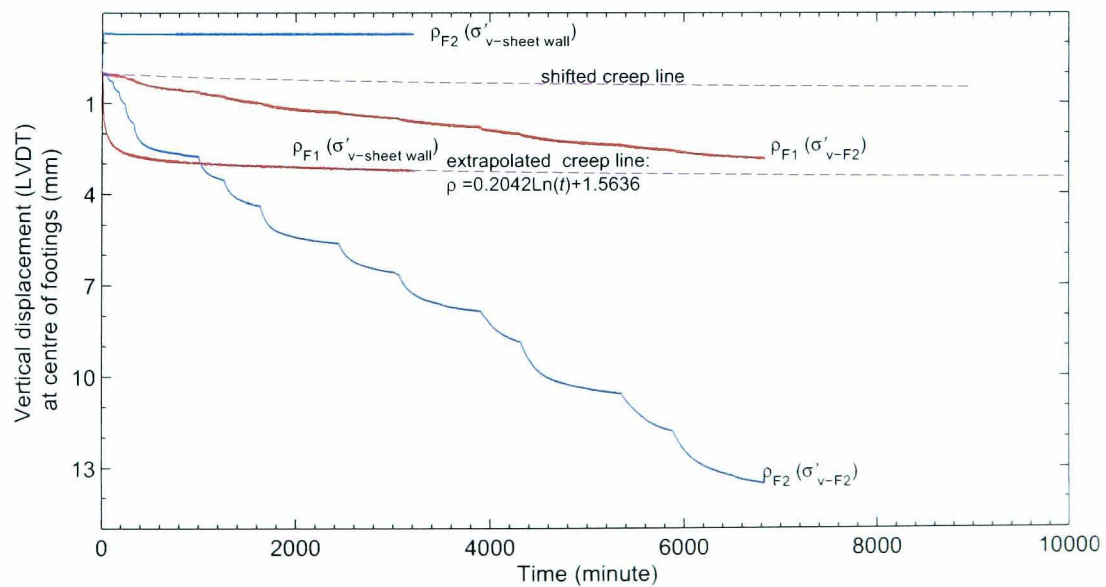


**Figure 5.45:** Vertical displacement and creep in Test SP1
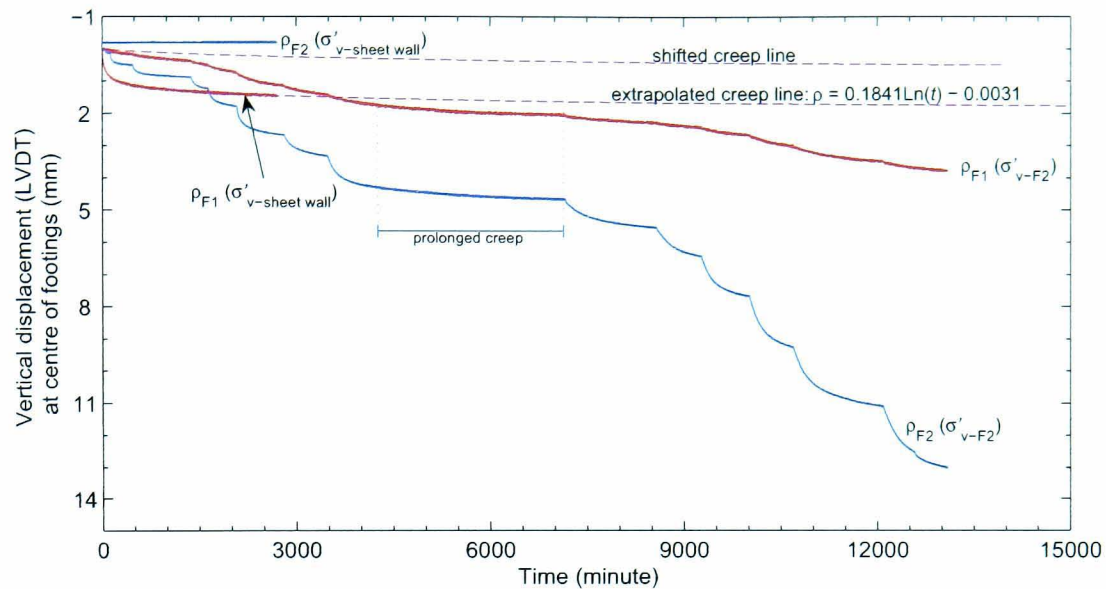
**Figure 5.46:** Vertical displacement and creep in Test SP2

settlement, shown as the shifted creep line, the settlement curve of Footing I ($\rho_{F1}(\sigma'_{v\text{-}F2})$) for either test departed from the line as each loading increment on Footing II was applied. This shows that incremental loading on Footing II influenced the settlement of Footing I. A further verification of this can be obtained from Figure 5.46 for Test SP2 during which the creep under the incremental pressure of 50 kPa was prolonged. During this creep period the settlement curves of Footing I ($\rho_{F1}(\sigma'_{v\text{-}F2})$) and Footing II ($\rho_{F2}(\sigma'_{v\text{-}F2})$) remained parallel to the extended creep line. This suggests that the earlier and later divergence of the curve $\rho_{F1}(\sigma'_{v\text{-}F2})$ from the line was due to the influence of the pressures of Footing II.

During the loading on Footing II, the settlements of Footing II and Footing I were respectively 13.54 mm (including creep of 2.07 mm) and 2.82 mm (creep = 0.45 mm) in Test SP1. The settlements of Footing II and Footing I in Test SP2 were 13.58 mm (creep = 1.71 mm) and 4.06 mm (creep = 0.52 mm). Excluding creep settlement, the settlement ratios $\rho_{F1}/\rho_{F2}$ were 0.21 and 0.30 for Tests SP1 and SP2 respectively. Although the ratio observed in Test SP1 was lower than those observed in Tests DF1 and DF2 (see Section 5.3.2.1), in general, the settlement ratios in all tests were quite similar. As also observed in DF tests, the settlement of Footing II was significantly less than that of Footing I. This was shown in Figure 5.21 and Figure 5.22. Beyond the maximum preconsolidation pressure the settlement of Footing II measured with LVDTs was only about 54% of that occurring at Footing I as it was first loaded.

*5.4.4.2   Effect of Floating Sheet Wall*

Cumulative soil movement due to the incremental loading on Footing II in Tests SP1 and SP2 is depicted in Figure 5.47 and Figure 5.49 (vector plots) and Figure 5.48 and Figure 5.50 (vertical displacement contours).      Compared with that found in DF tests, in these SP tests the vertical soil deformation subsided more abruptly beyond the sheet wall in the direction from Footing II to Footing I. This can be clearly seen in Figure 5.51 in which the vertical deformations of both types of test at a depth of 50 mm from the sample surface are shown. It is evident that the sheet wall had slightly reduced the stress interference between the footings. The movement of the sheet wall, in Test SP2, was traced using PIV. For this purpose, a small Perspex cap with a target marker (see Figure 5.53(a)) was placed on the top of the wall. At the end of the test the vertical movement of the sheet wall was 3.92 mm as shown in Figure 5.53(b).
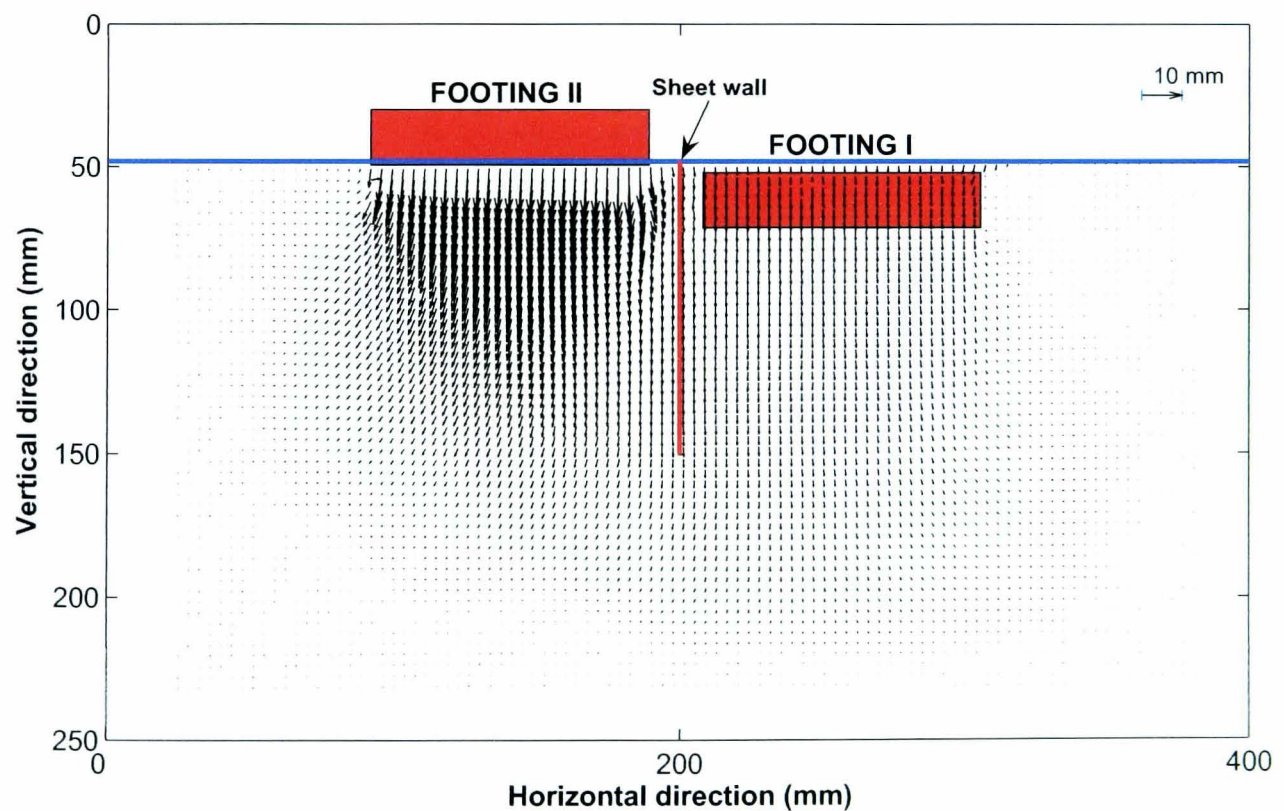


**Figure 5.47:** Vectors of cumulative vertical displacement due to final loading on Footing II in Test SP1
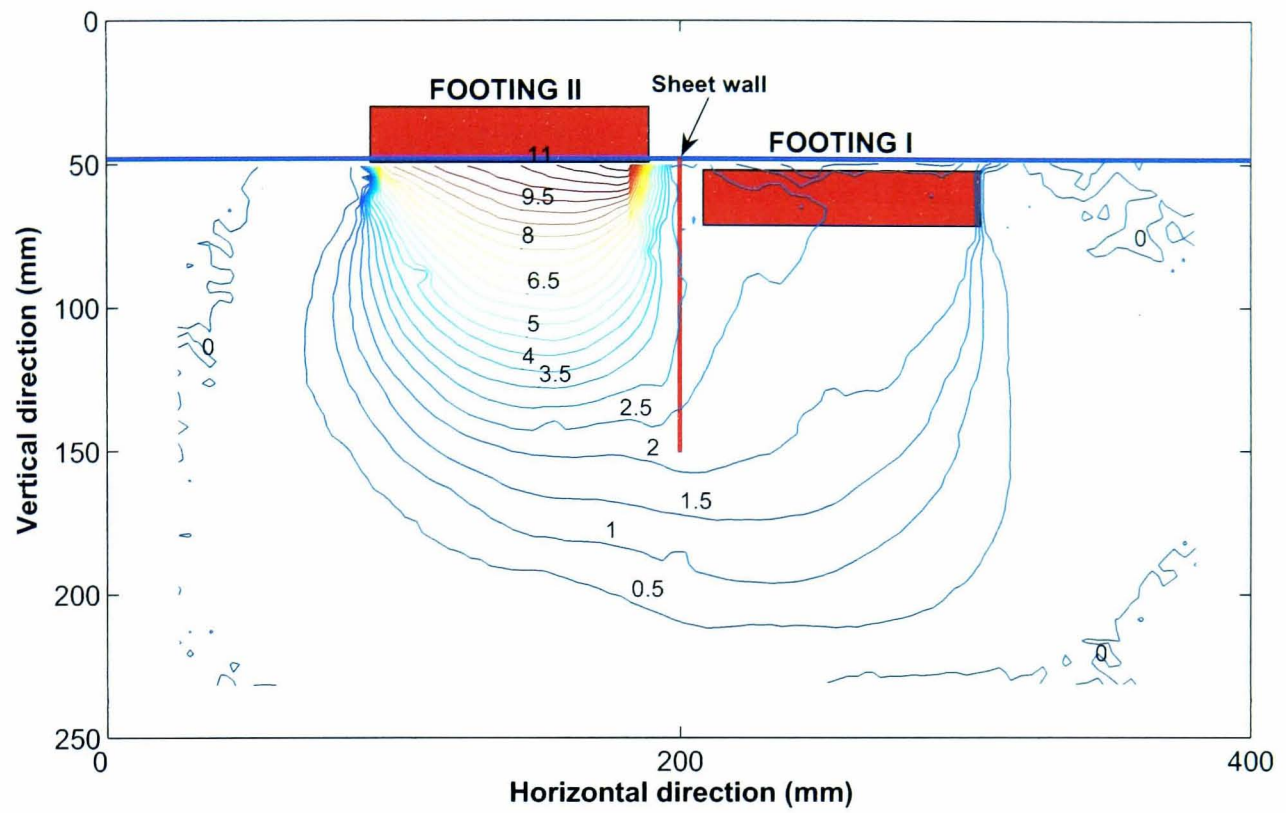
**Figure 5.48:** Contours of cumulative vertical displacement due to final loading on Footing II in Test SP1
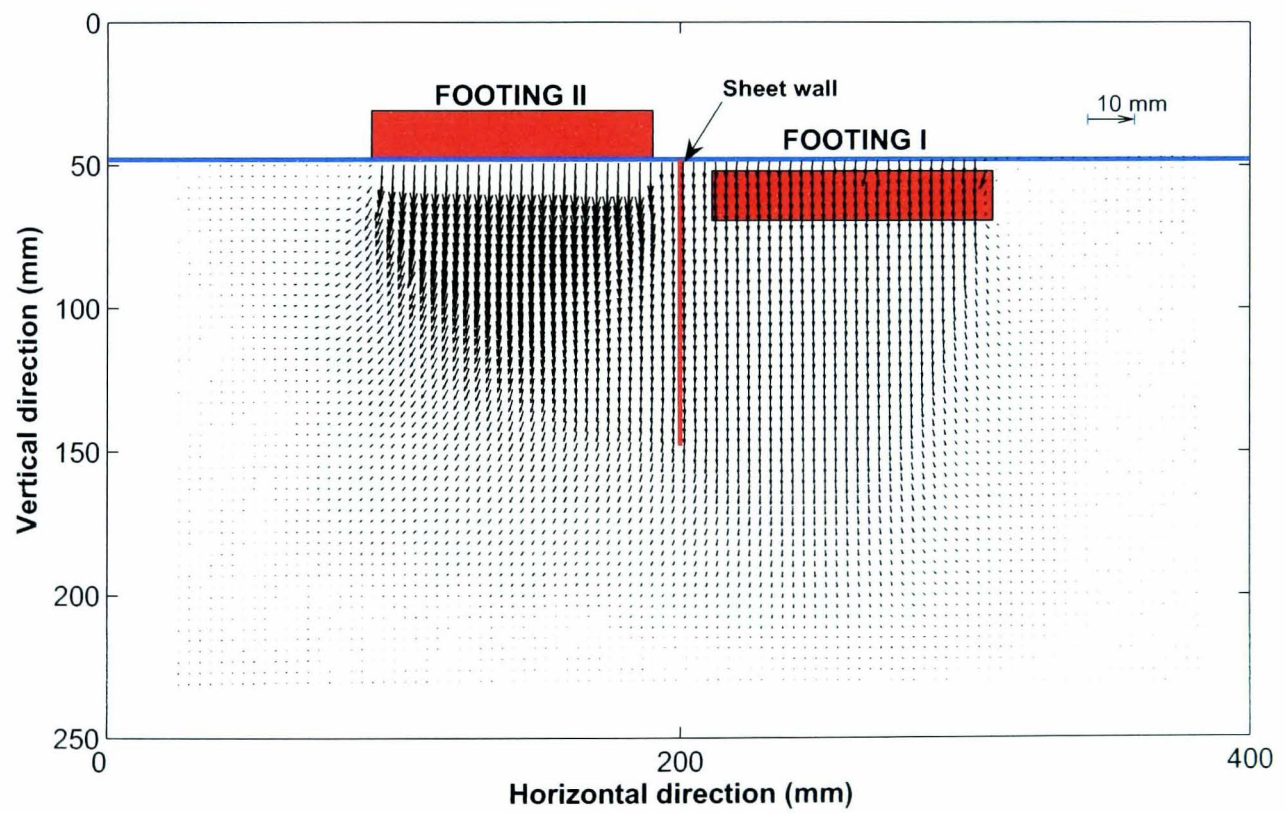


**Figure 5.49:** Vectors of cumulative vertical displacement due to final loading on Footing II in Test SP2
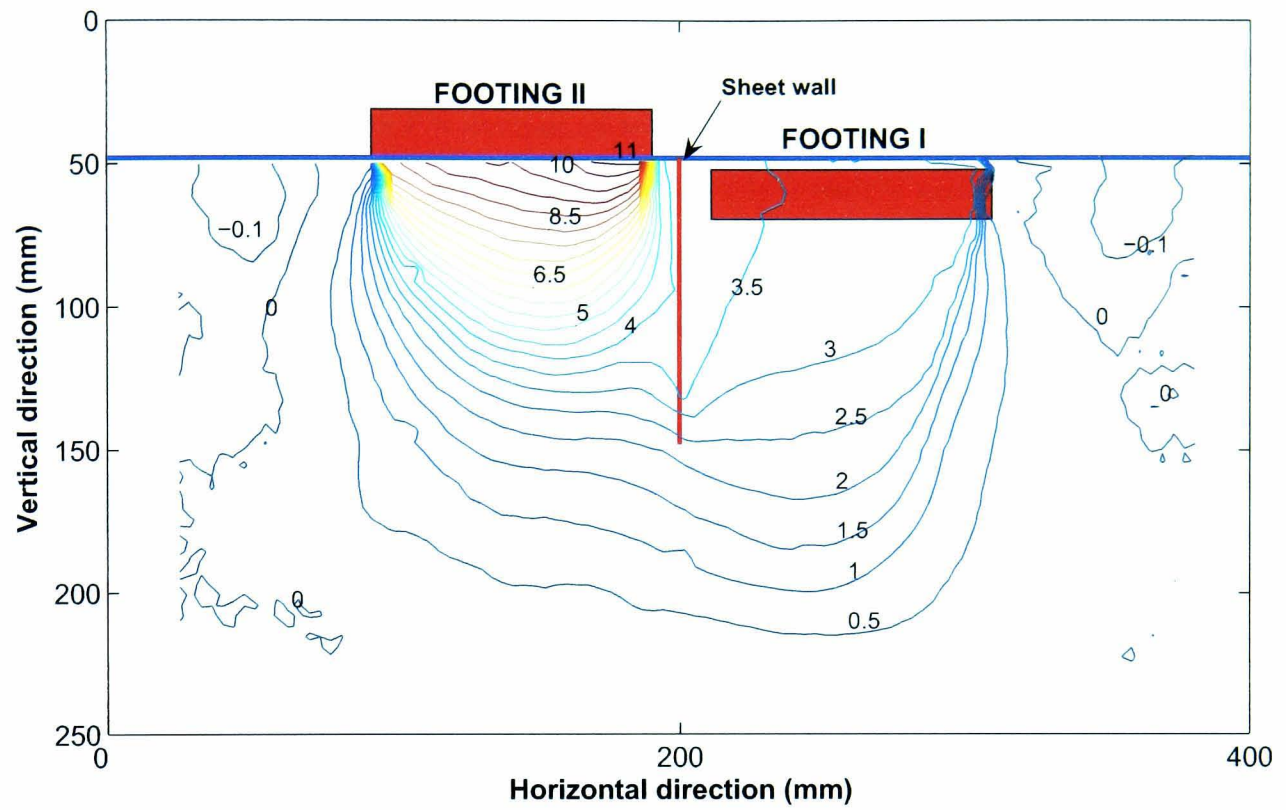
**Figure 5.50:** Contours of cumulative vertical displacement due to final loading on Footing II in Test SP2
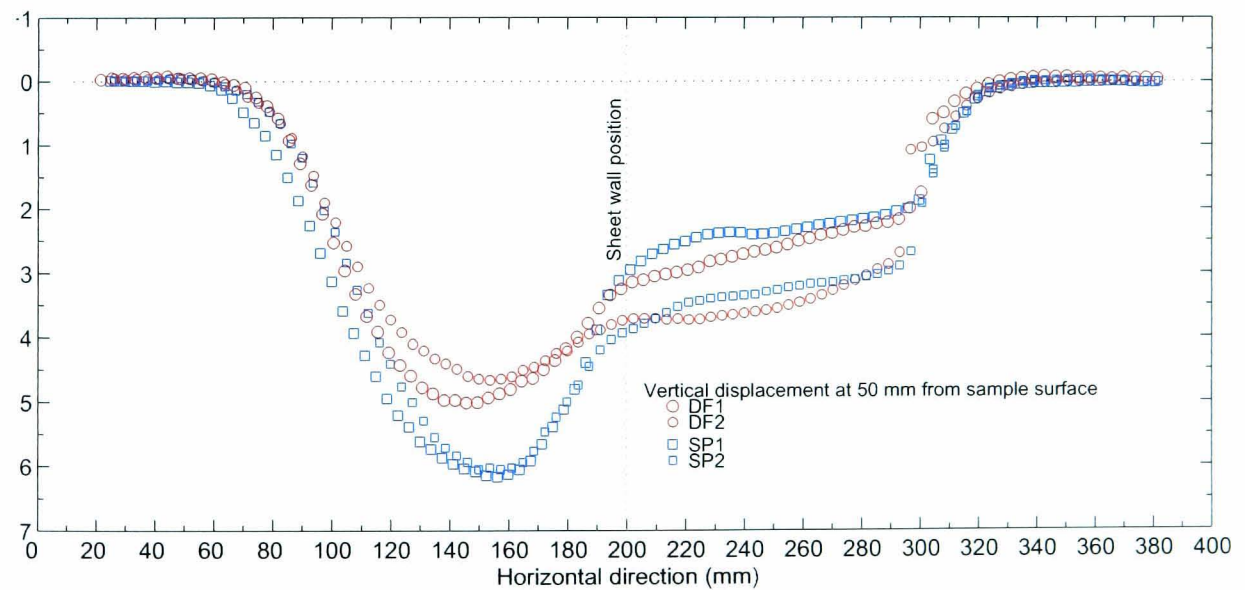


**Figure 5.51:** Vertical displacement at a depth of 50 mm from the surface of sample

### 5.4.4.3 Tilting

Tilting of Footing I and Footing II as a result of incremental loading on Footing II during Tests SP1 and SP2 was determined with PIV analysis on markers inscribed on the footing sides. Figure 5.52 and Figure 5.53 show images of the footings with the markers and the vectors of the traced cumulative vertical movements of the markers. As for the results from the DF tests that were discussed in Section 5.3.2.2 (see Figure 5.34), the settlement magnitude of the footings could also be estimated by extending the vertical displacement profile of the underlying soil as shown in Figure 5.54.

Based on the vertical displacements of the markers, the tilting of the footings was determined using the angular distortion $\delta/l$ as described in Section 5.3.2.2. In Test SP1, the loading on Footing II had caused Footing I and Footing II to tilt with $\delta/l = 1/181$ and $\delta/l = 1/123$ respectively. In Test SP2, Footing I tilted with $\delta/l = 1/147$, while Footing II had $\delta/l = 1/80$. Compared with the results from DF tests, the tilts of Footing I in these two tests were reduced by about 50% on average. However, insignificant differences in tilting were observed for Footing II. The reduced tilting of Footing I in SP tests was attributable to alteration of the stress distribution by the sheet wall.
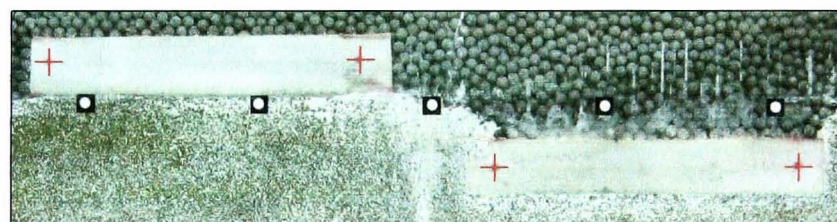


(a) Markers on footings
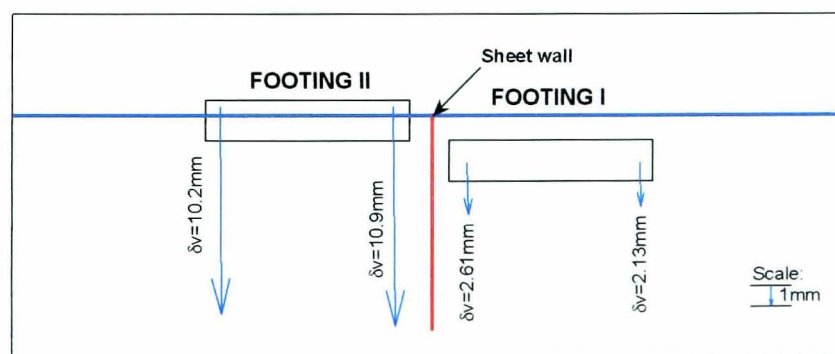


(b) Movement of markers due to loading on Footing II

**Figure 5.52:** Tilting of footings in Test SP1
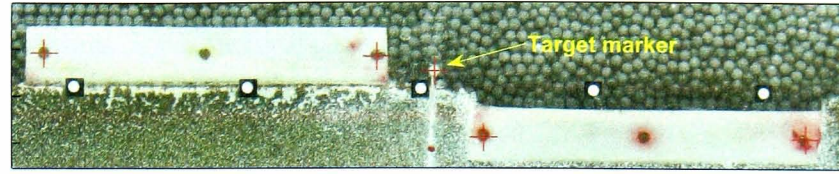
(a) Markers on footings and top of sheet wall
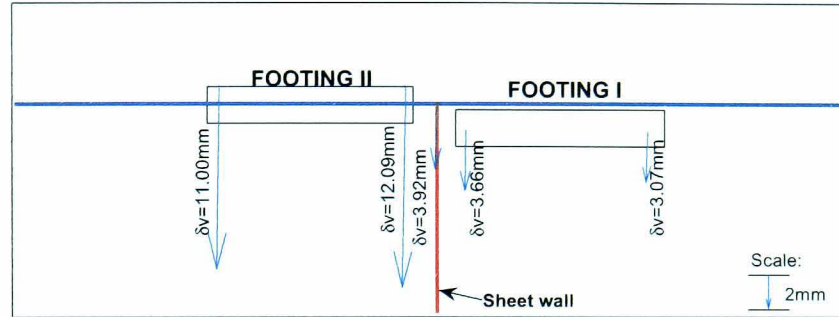


(b) Movement of markers due to loading on Footing II

**Figure 5.53:** Tilting of footings in Test SP2
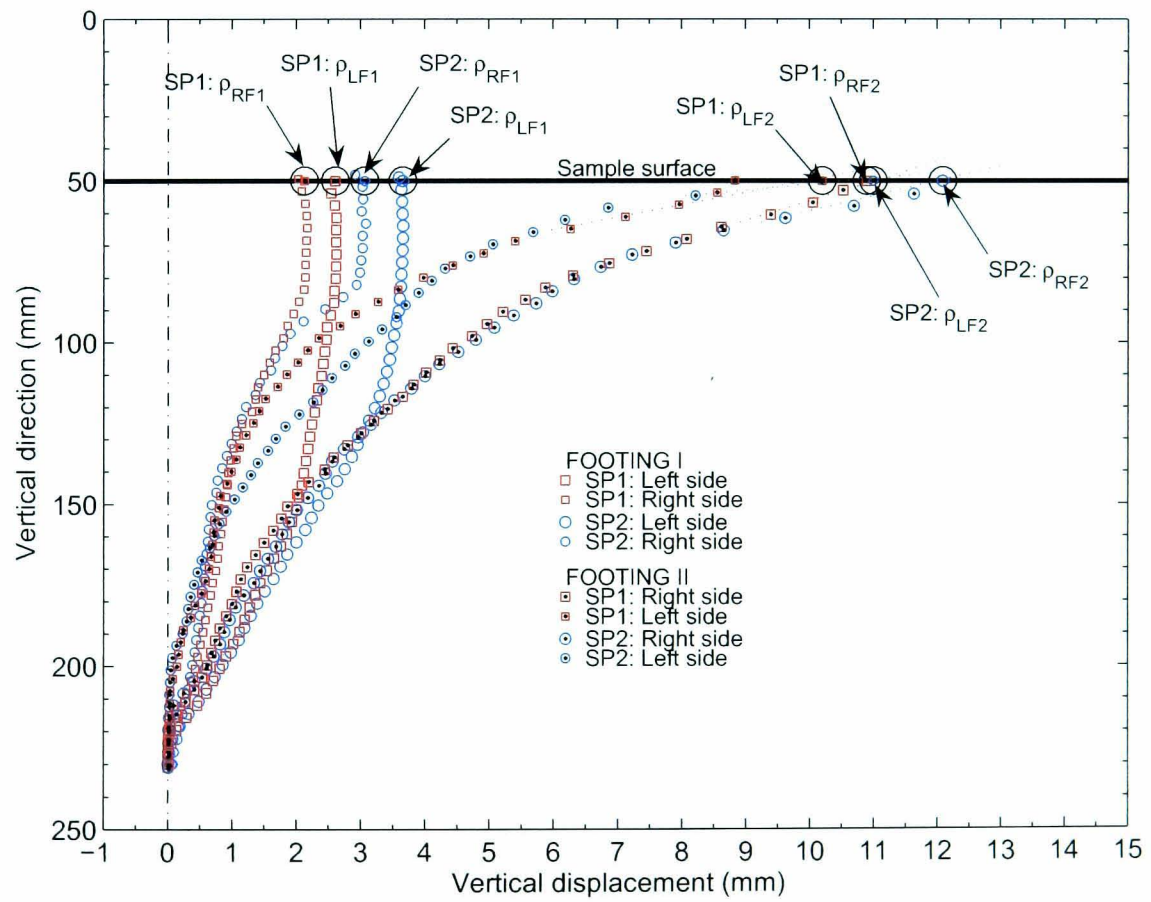


**Figure 5.54:** Vertical displacements of footings based on the markers and the displacements of the soil beneath the markers due to loading on Footing II in SP tests

## 5.5   DOUBLE FOOTING WITH FIXED SHEET WALL

### 5.5.1   Loading on Footing I

As in the DF and the SP tests, incremental loading on Footing I was applied to commence two identical FX tests, Tests FX1 and FX2. The vertical displacements measured with LVDTs at the centre of the footings in the two tests have already been presented in Figure 5.9. The displacement of Footing I in Test FX2 did not much deviate from those in the other tests. As mentioned in Section 5.3.1.1, the smaller displacement in Test FX1 was traceable to friction between the footing sides and the chamber wall and the Perspex window. The displacement vectors and settlement contours at this stage of the test, obtained with PIV analysis, are presented in Figures 5.55 to 5.58 for both Test FX1 and Test FX2.
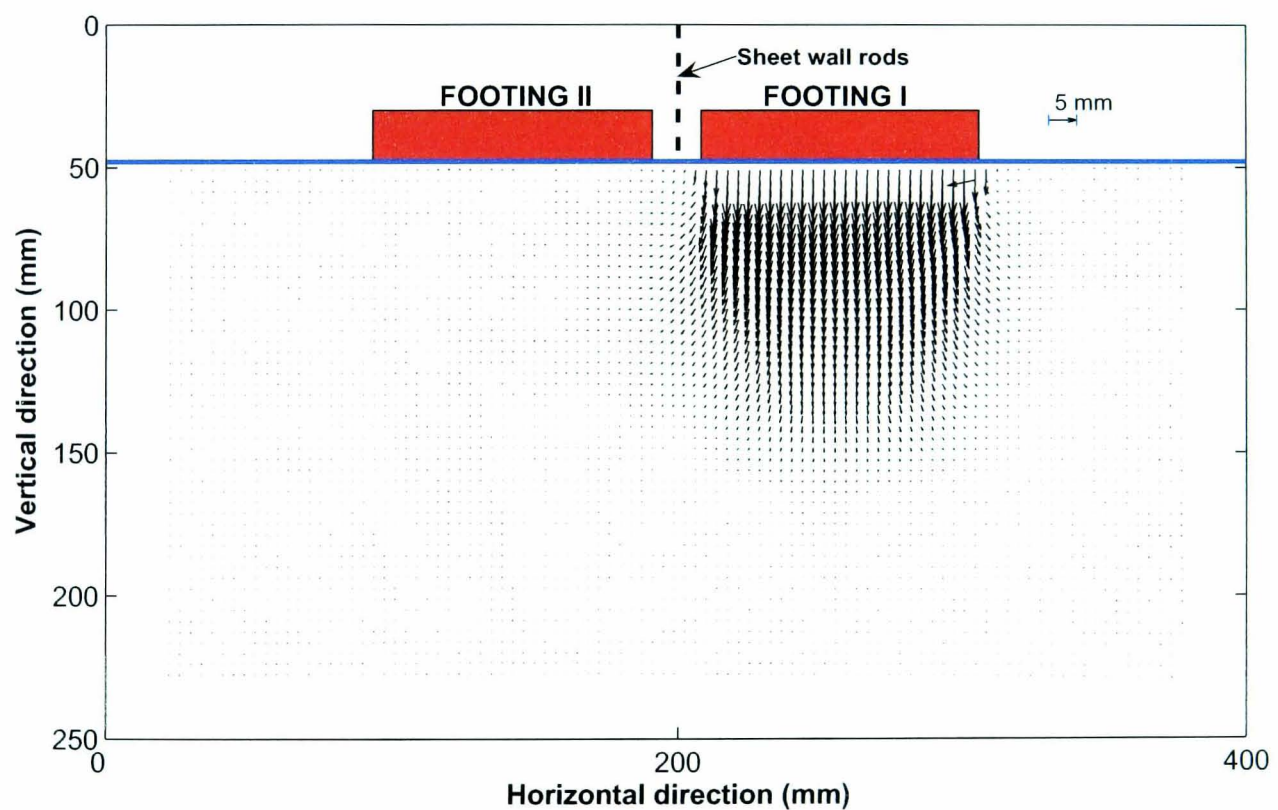


**Figure 5.55:** Vectors of cumulative displacement due to final loading on Footing I in FX1 test
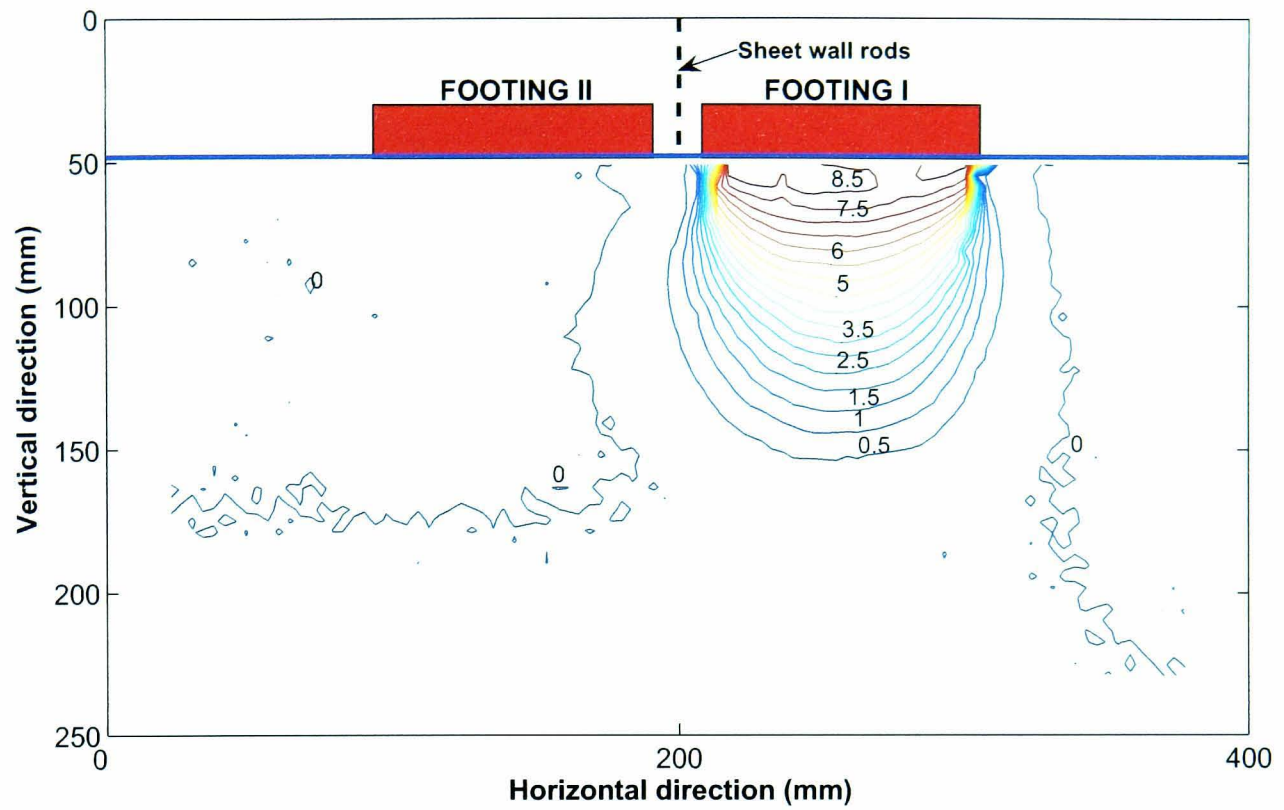
**Figure 5.56:** Contours of cumulative vertical displacement due to final loading
on Footing I in FX1 test
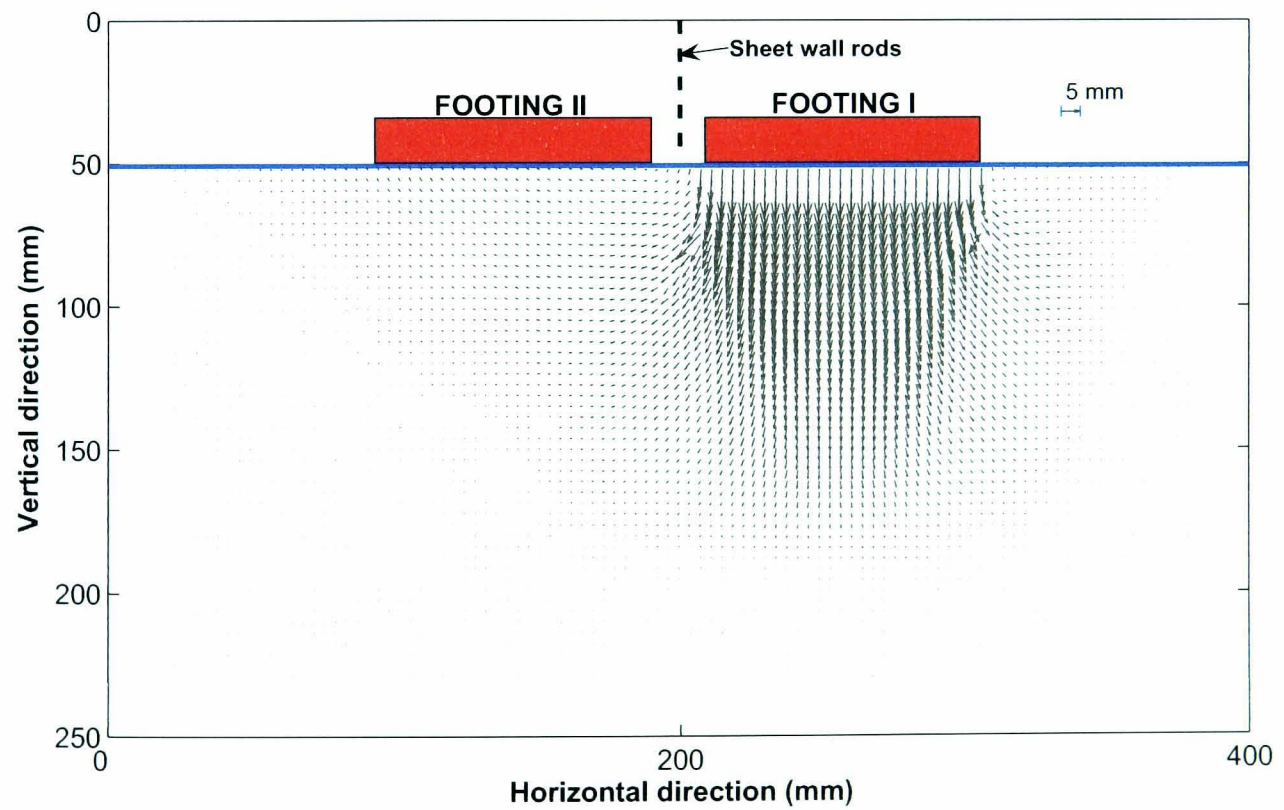


**Figure 5.57:** Vectors of cumulative displacement due to final loading on Foot-
ing I in FX2 test
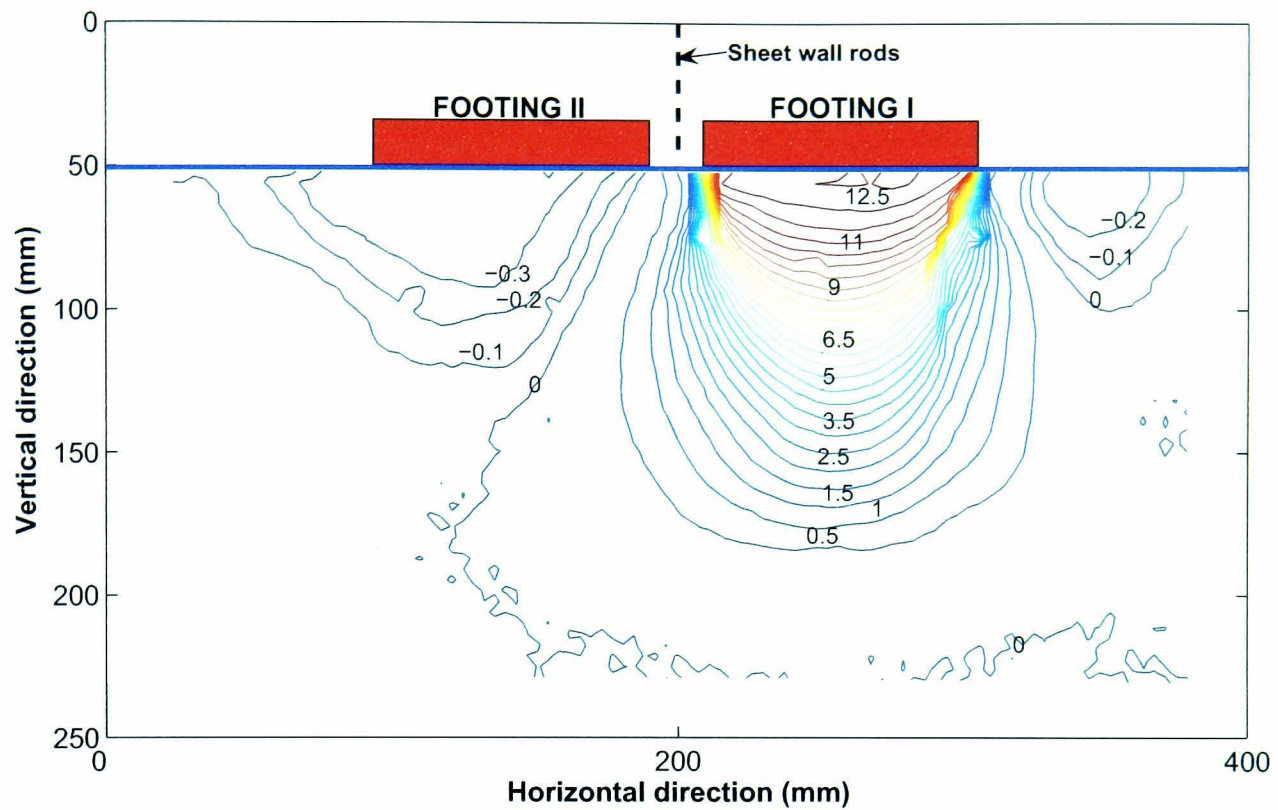
**Figure 5.58:** Contours of cumulative vertical displacement due to final loading on Footing I in FX2 test

## 5.5.2 Sheet Wall Insertion

Unlike the floating sheet wall in the SP tests, throughout the FX tests the wall was vertically restrained by rods resting on the chamber base. The sheet wall insertion was initiated by penetrating the two small rods fixed at the tip of the wall (recall Section 3.5.2). This penetration took about 1.5 to 3 minutes. The wall sheet was then slowly pushed down in three stages, until the rods reached the base of the consolidation chamber. The complete installation resulted in the top of the 100 mm deep sheet being level with the sample surface.

The effect of the installation during Tests FX1 and FX2 on the soil regions beneath Footing I and Footing II are illustrated in Figure 5.59 and Figure 5.60. The effect of rod penetration was almost unnoticeable for the two tests. The wall insertion was always followed by sudden step-ups of the curve $\rho_{F2}(\sigma'_{v\text{-sheet wall}})$ and gradual drops of the curve $\rho_{F1}(\sigma'_{v\text{-sheet wall}})$. This indicates that heaving on the left and subsidence on the right sides of the wall occurred as a result of every push of the wall. This phenomenon was also observed in SP tests. The discrepancies between the magnitudes of the vertical displacements in Tests FX1 and FX2, as discussed in Section 5.4.3, were

suspected to stem from differences in the roughness of the wall surface. Moreover, the friction on

the footings during Test FX1 (see Section 5.3.1.1) might also have contributed.
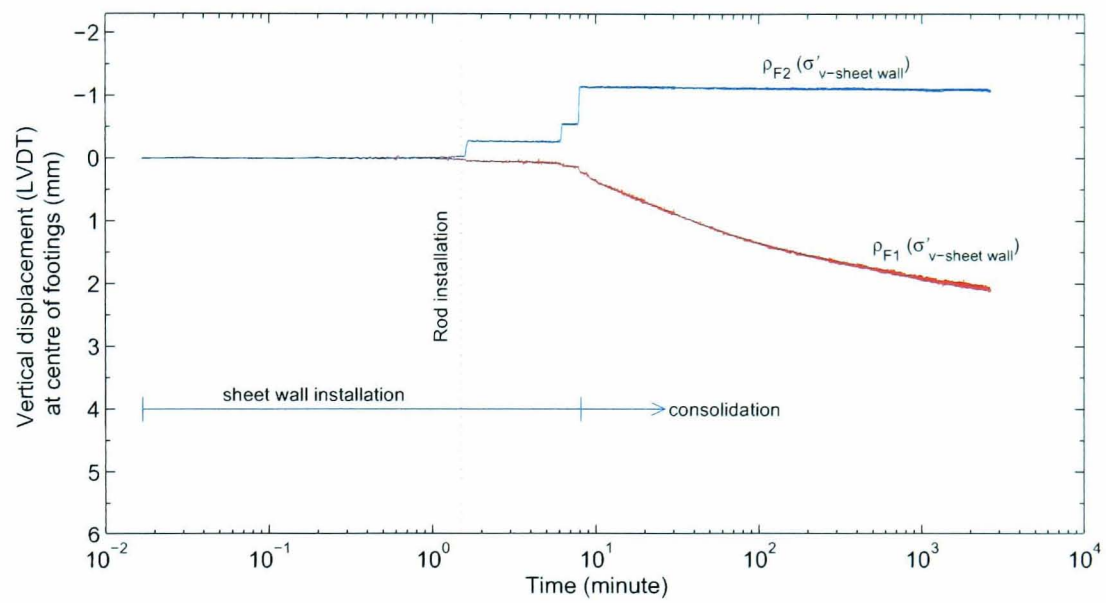


**Figure 5.59:** Vertical displacement due to sheet wall installation in FX1 test
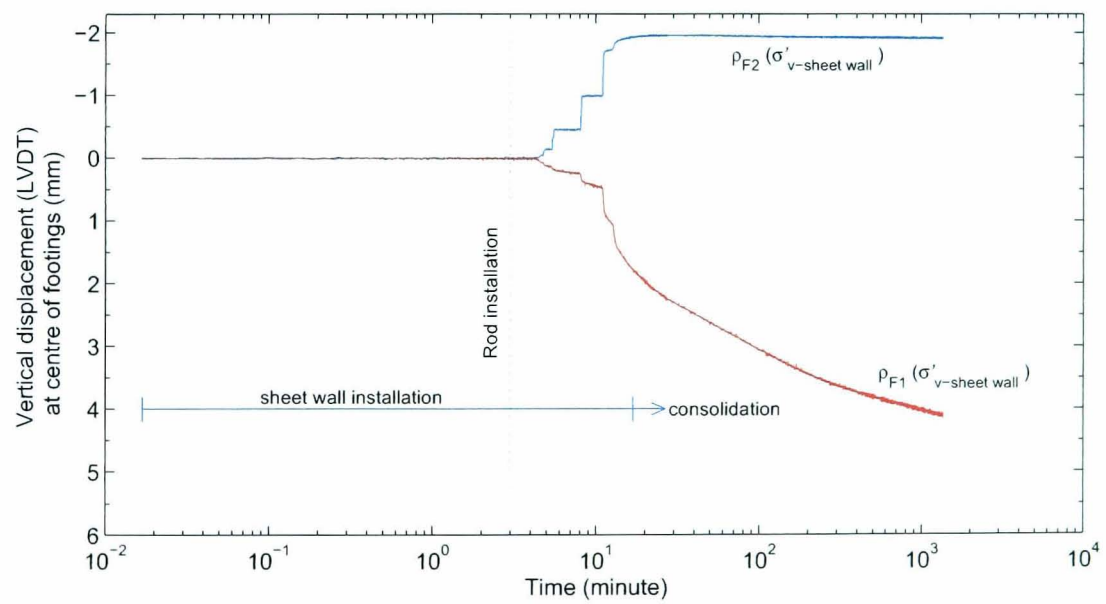


**Figure 5.60:** Vertical displacement due to sheet wall installation in FX2 test

### 5.5.3    Loading on Footing II

#### 5.5.3.1    Settlement of Footings

As in the SP tests, incremental loading on Footing II was initiated once consolidation had ended after the wall insertion and creep was observed. The displacements during the tests are plotted against time in Figure 5.61 and Figure 5.62. Except for their magnitudes, the settlement profiles
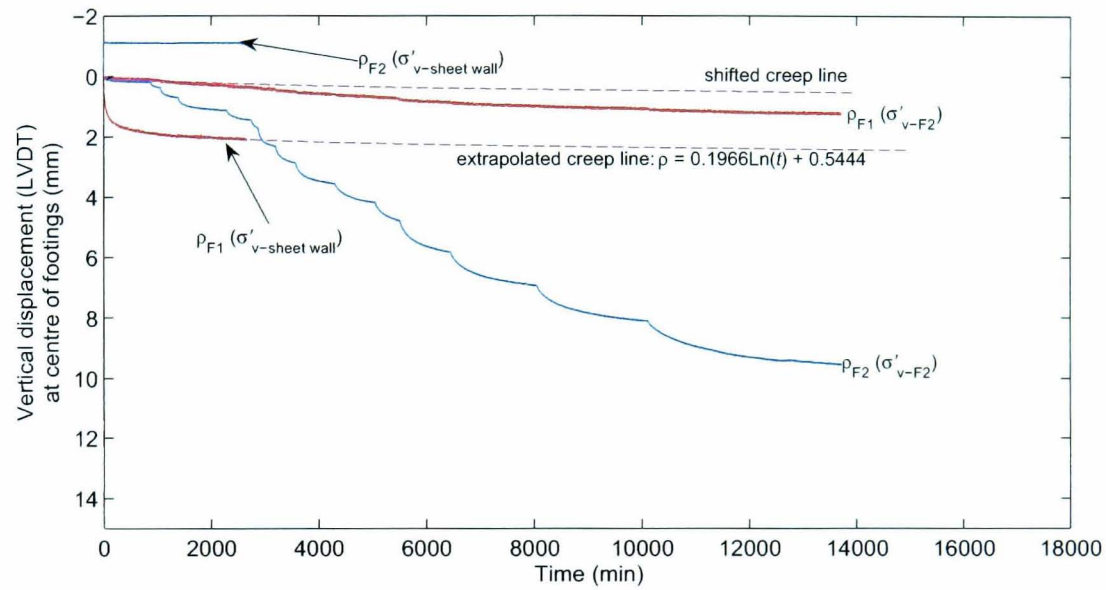


**Figure 5.61:** Effect of loading on Footing II on the vertical displacement of Footing I and Footing II in FX1 test
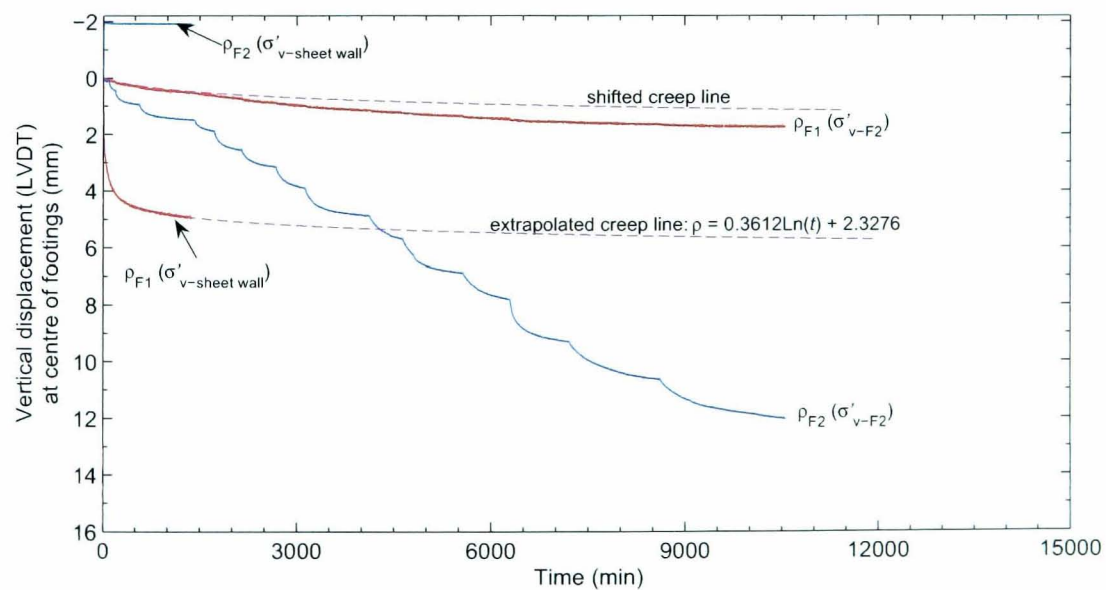


**Figure 5.62:** Effect of loading on Footing II on the vertical displacement of Footing I and Footing II in FX2 test

for both tests are very similar. At the end of Test FX1, the settlements of Footing II and Footing I after the beginning of the incremental loading on Footing II were 9.58 mm (creep = 1.74 mm) and 1.22 mm (creep = 0.54 mm) respectively. The settlement ratio $\rho_{F1}/\rho_{F2}$ was about 0.13. The final loading in Test FX2 resulted in settlements of 12.06 mm (creep = 3.03 mm) for Footing II and 1.74 mm (1.11 mm) for Footing I, giving a ratio $\rho_{F1}/\rho_{F2}$ of 0.14. Without creep, the ratios $\rho_{F1}/\rho_{F2}$ were 0.09 and 0.07 for Test FX1 and Test FX2 respectively. In general the ratios $\rho_{F1}/\rho_{F2}$ in these tests were roughly a quarter of those in the DF and the SP tests (see Section 5.3.2.1 and Section 5.4.4.1).

The soil movement vectors and vertical displacement contours resulting from the loading on Footing II, are depicted in Figures 5.63 to Figure 5.66. At a glance, there is an indiscernible difference between the displacement vectors from these tests and those from the SP tests (see Figure 5.47 and Figure 5.49). However, the contour patterns confirm the indication in Figure 5.61 and Figure 5.62 that the pressure from Footing II had virtually no impact on Footing I.
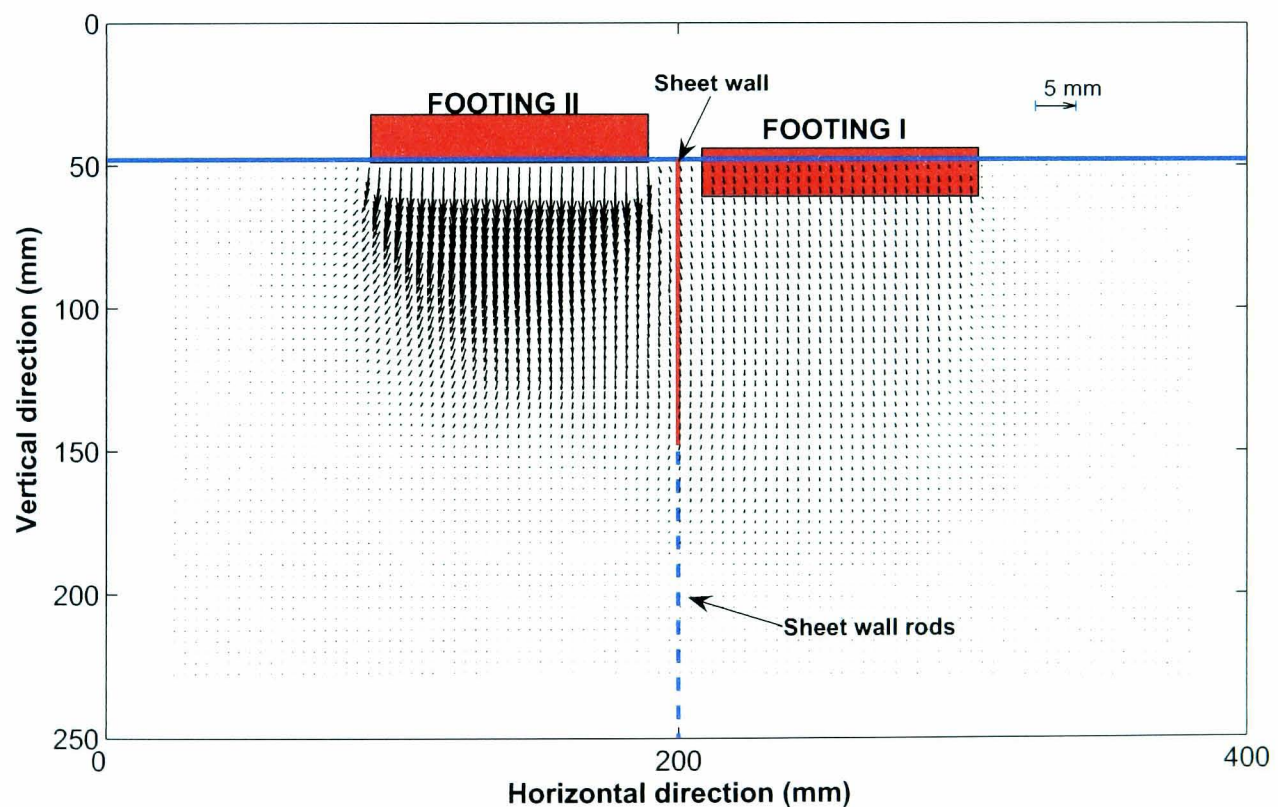


**Figure 5.63:** Vectors of cumulative displacement due to final loading on Footing II in FX1 test
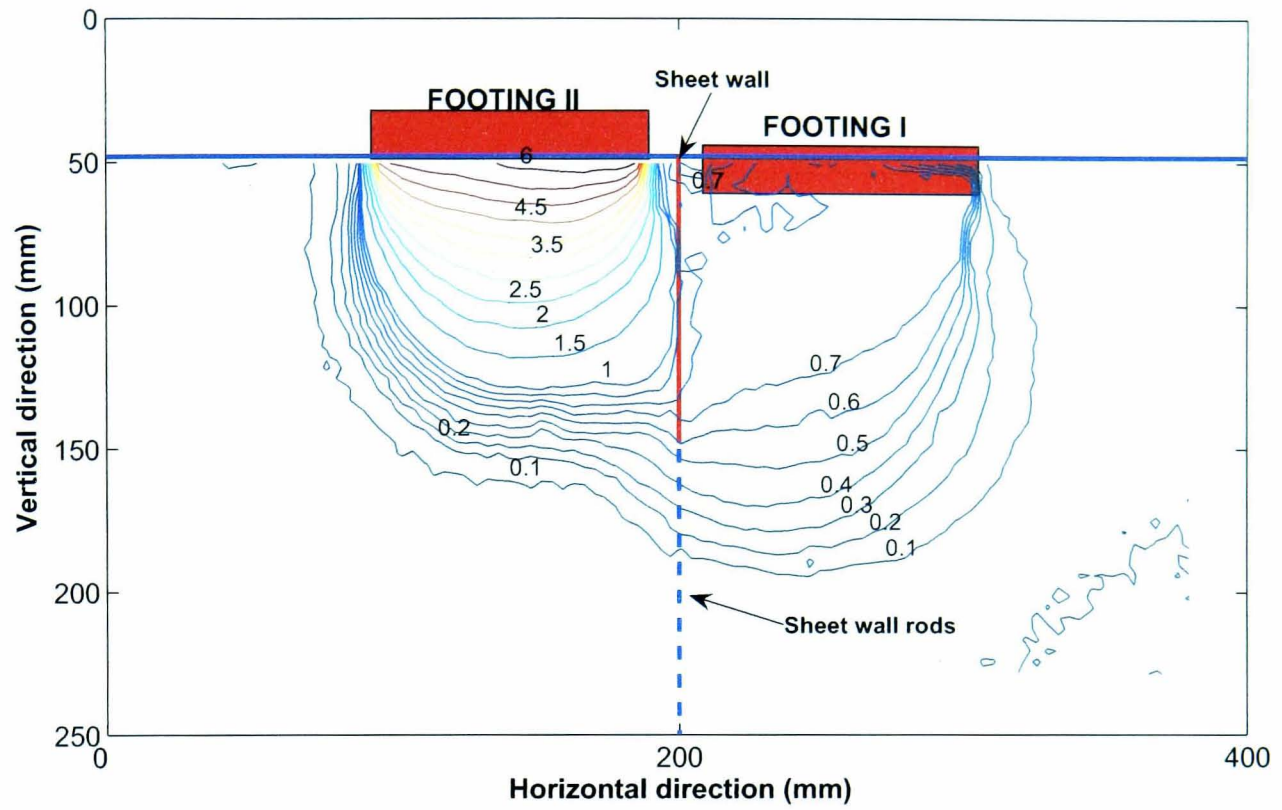
**Figure 5.64:** Contours of cumulative vertical displacement due to final loading on Footing II in FX1 test
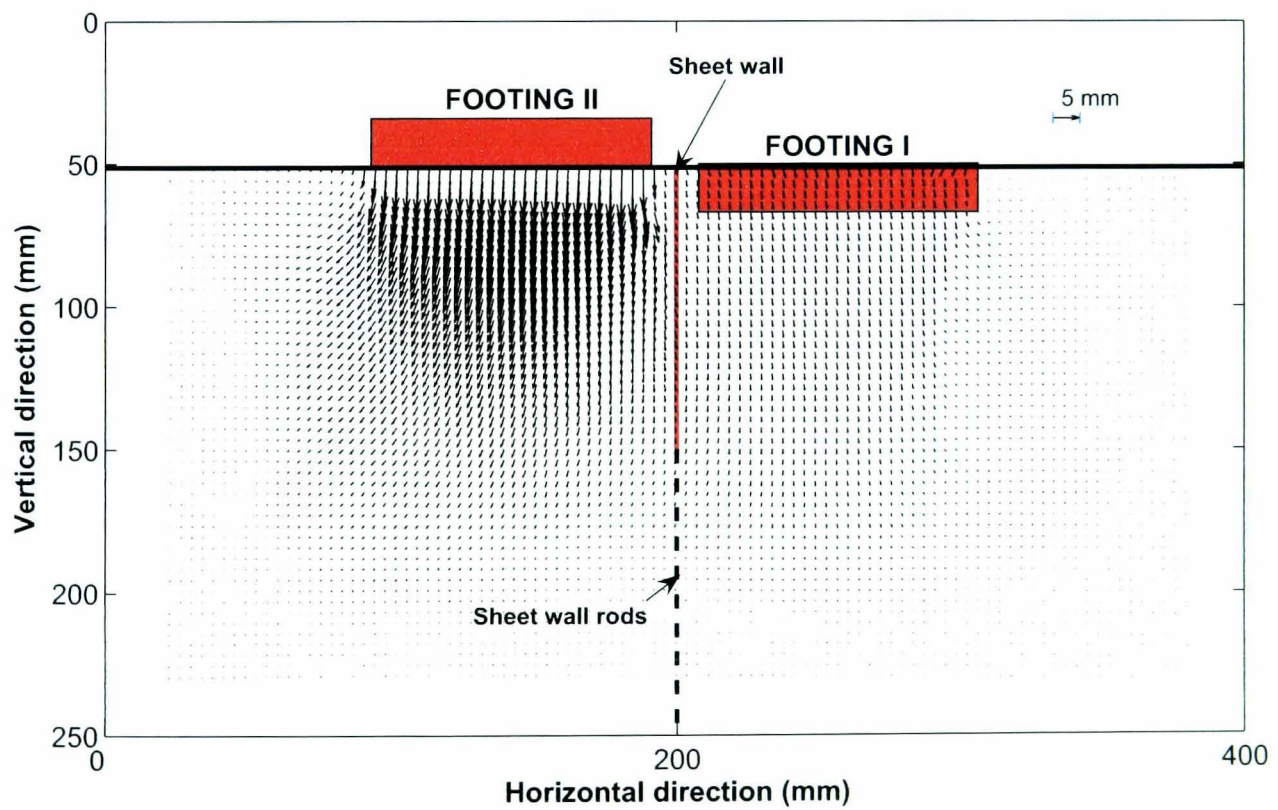


**Figure 5.65:** Vectors of cumulative displacement due to final loading on Footing II in FX2 test
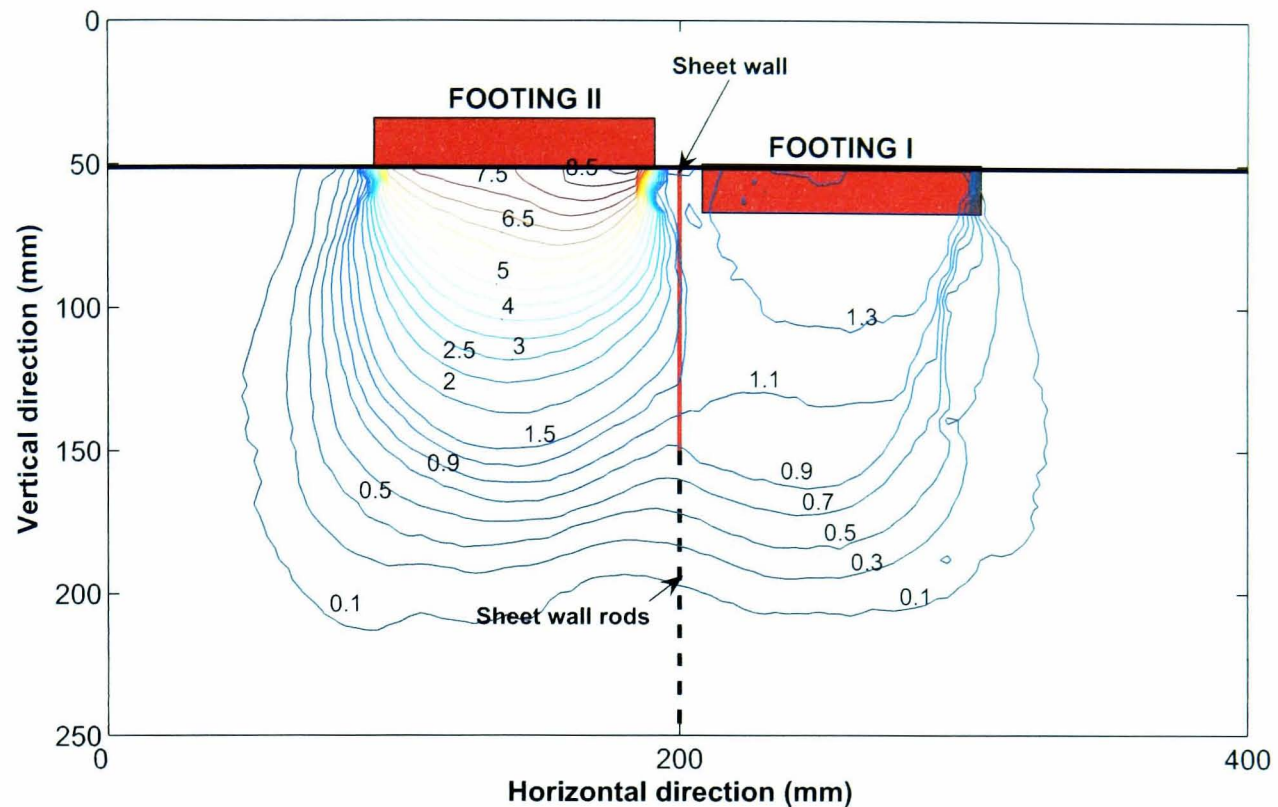
**Figure 5.66:** Contours of cumulative vertical displacement due to final loading on Footing II in FX2 test

### 5.5.3.2 *Effect of Fixed Sheet Wall*

Figure 5.67 shows the vectors of soil displacement around the sheet wall in SP and FX tests, at a depth of 50 mm from the sample surface. There are at least two marked distinctions that can be observed. The first concerns the magnitude of the displacements and the second concerns the change of the vector magnitude from left to right. Excluding the result from Test FX1, known to be affected by boundary friction, the settlement of the soil around the fixed sheet in Test FX2 was still only about 50% of that observed in the SP tests. This can be also clearly seen in Figure 5.68 showing the vertical displacements at this depth across the sample. The smaller settlement in Test FX2 might also result from the soil treatment during preconsolidation, as explained in Section 5.3.1.1. The profiles of the displacements on the left and on the right of the wall are presented in Figure 5.69. As discussed in the Section 5.4.4.2, in the SP tests the upper level of soil settled together with a floating sheet wall. This resulted in the vertical displacements on the left and the right of the sheet wall being almost equal. On the other hand, since the sheet wall in the FX tests was vertically restrained, the vertical displacement on the right of the sheet wall was almost unaffected by the soil

displacement on the left side. Consequently, the figure shows a considerable distinction between the vertical displacements on the left and the right of the sheet wall.
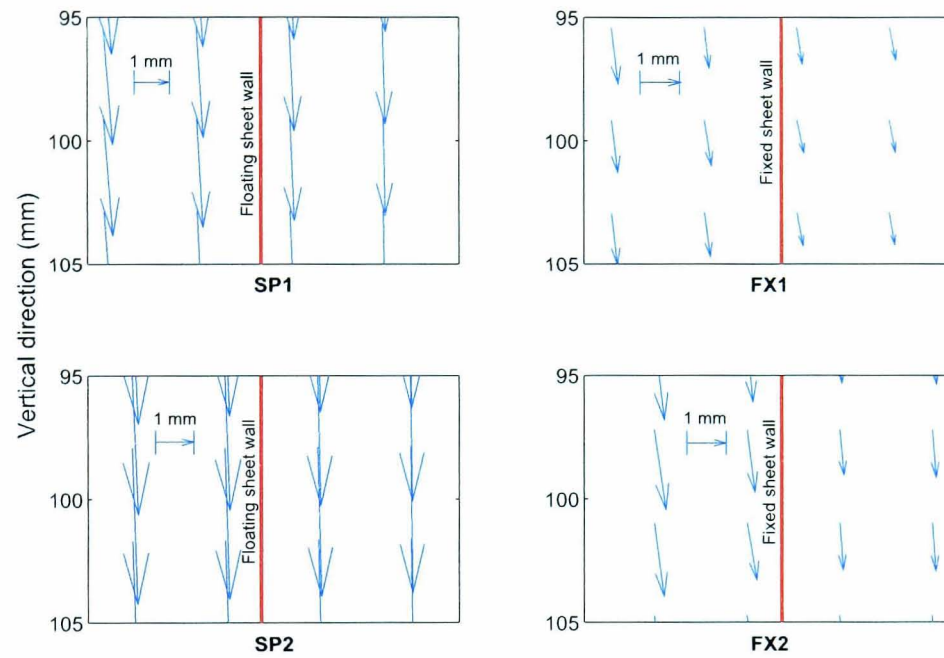


**Figure 5.67:** Vector of vertical displacement around sheet pile
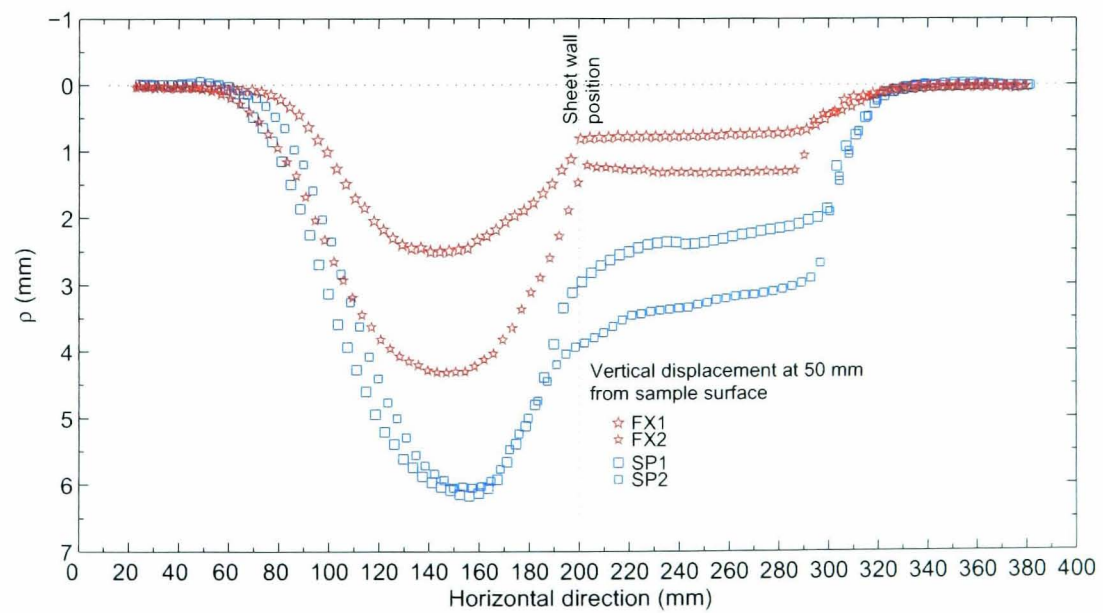


**Figure 5.68:** Vertical displacement along the depth of 50 mm from the sample surface
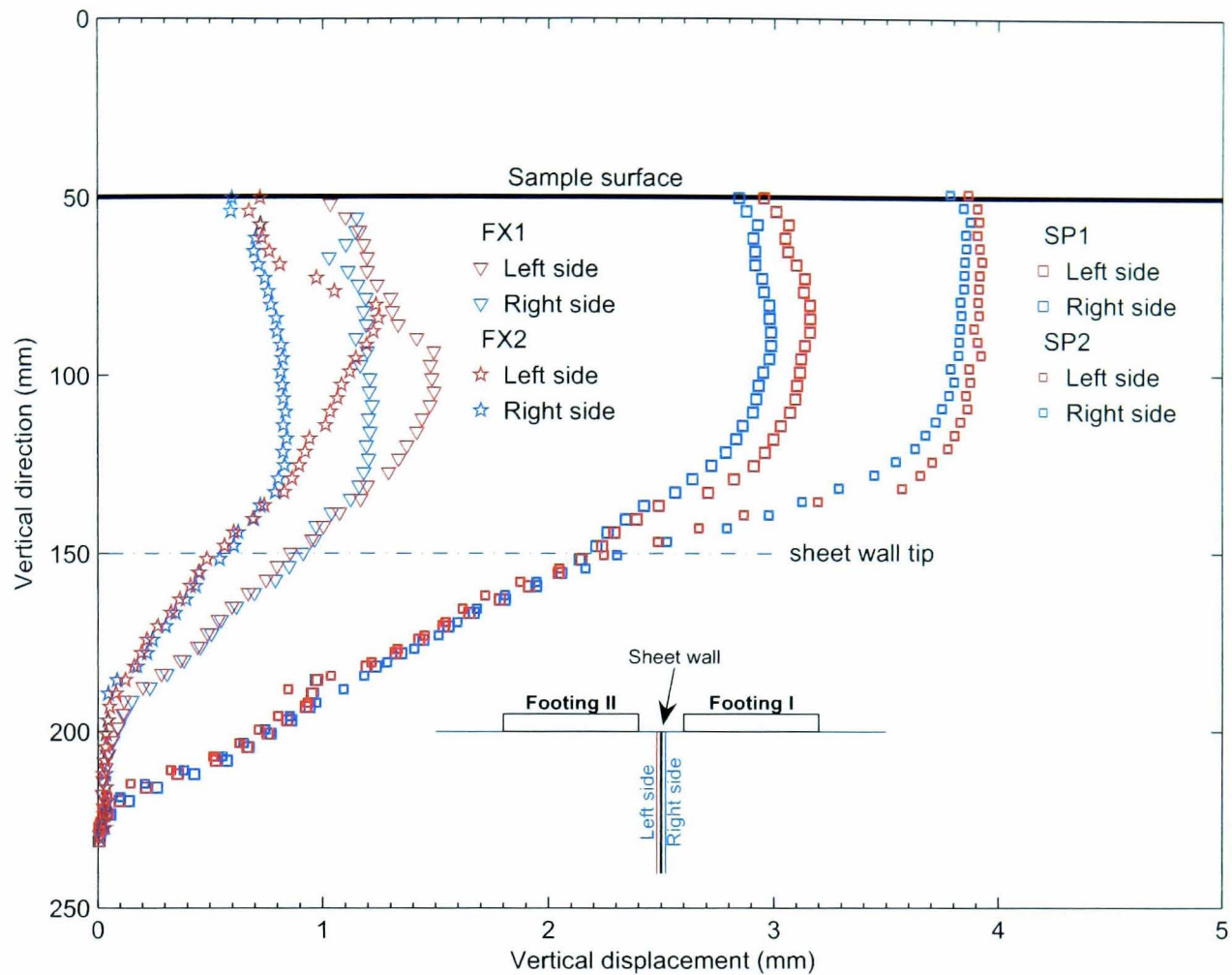
**Figure 5.69:** Displacement around sheet wall in FX and SP tests

### 5.5.3.3 Tilting

Figure 5.64 and Figure 5.66 in Section 5.5.3.1 show the non-uniform settlement of the soil beneath Footing I and Footing II. The tilting of both footings was analysed with PIV using markers on the footing sides (see Figure 5.70(a) and Figure 5.71(a)). The vectors of the vertical footing movement at the marker coordinates are shown in Figure 5.70(b) and Figure 5.71(b). These movements, together with the soil settlement profiles beneath the markers, are summarised in Figure 5.72. The figure reveals that, although insignificant tilting of Footing I was detected in both tests, the tilting of Footing II was larger than that in the DF and SP tests. In Test FX1, Footing I and Footing II tilted with $\delta/l = 1/1583$ and $\delta/l = 1/80$, while in Test FX2, Footing I and Footing II tilted with $\delta/l = 1/870$ and $\delta/l = 1/51$ respectively.
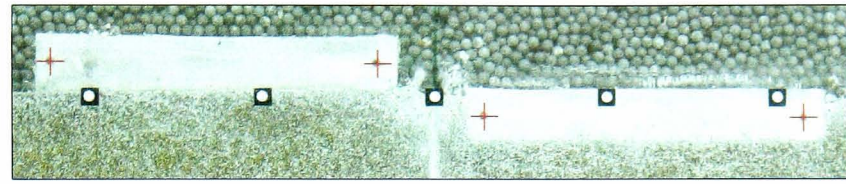
(a) Tracking markers on Footing II
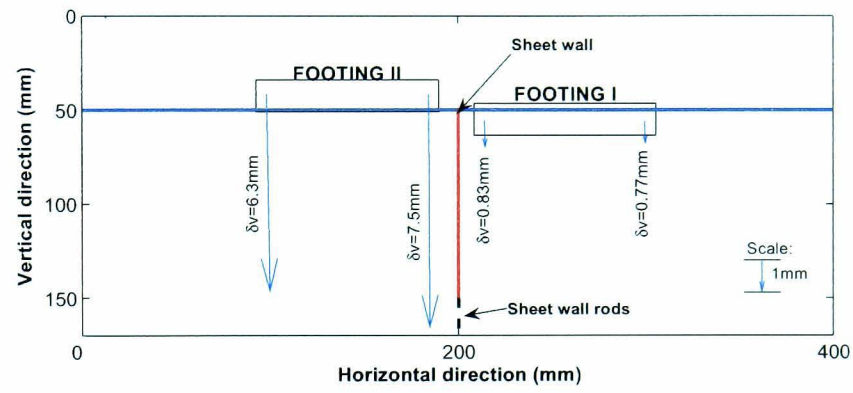


(b) Displacement vectors at the markers due to loading on Footing II

**Figure 5.70:** Tilting in FX1 test
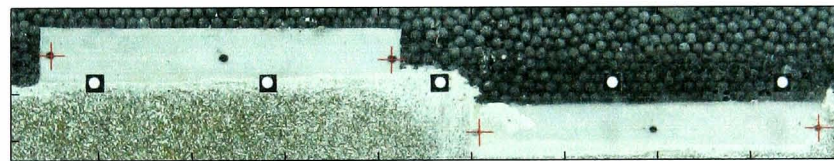


(a) Tracking markers
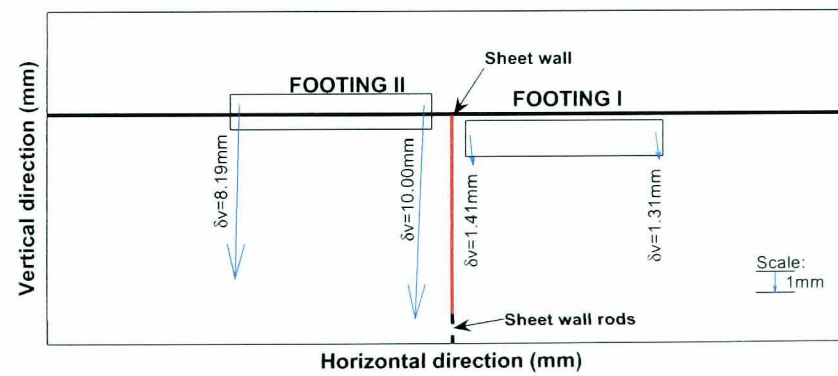


(b) Displacement vectors at the markers due to loading on Footing II

**Figure 5.71:** Tilting in FX2 test
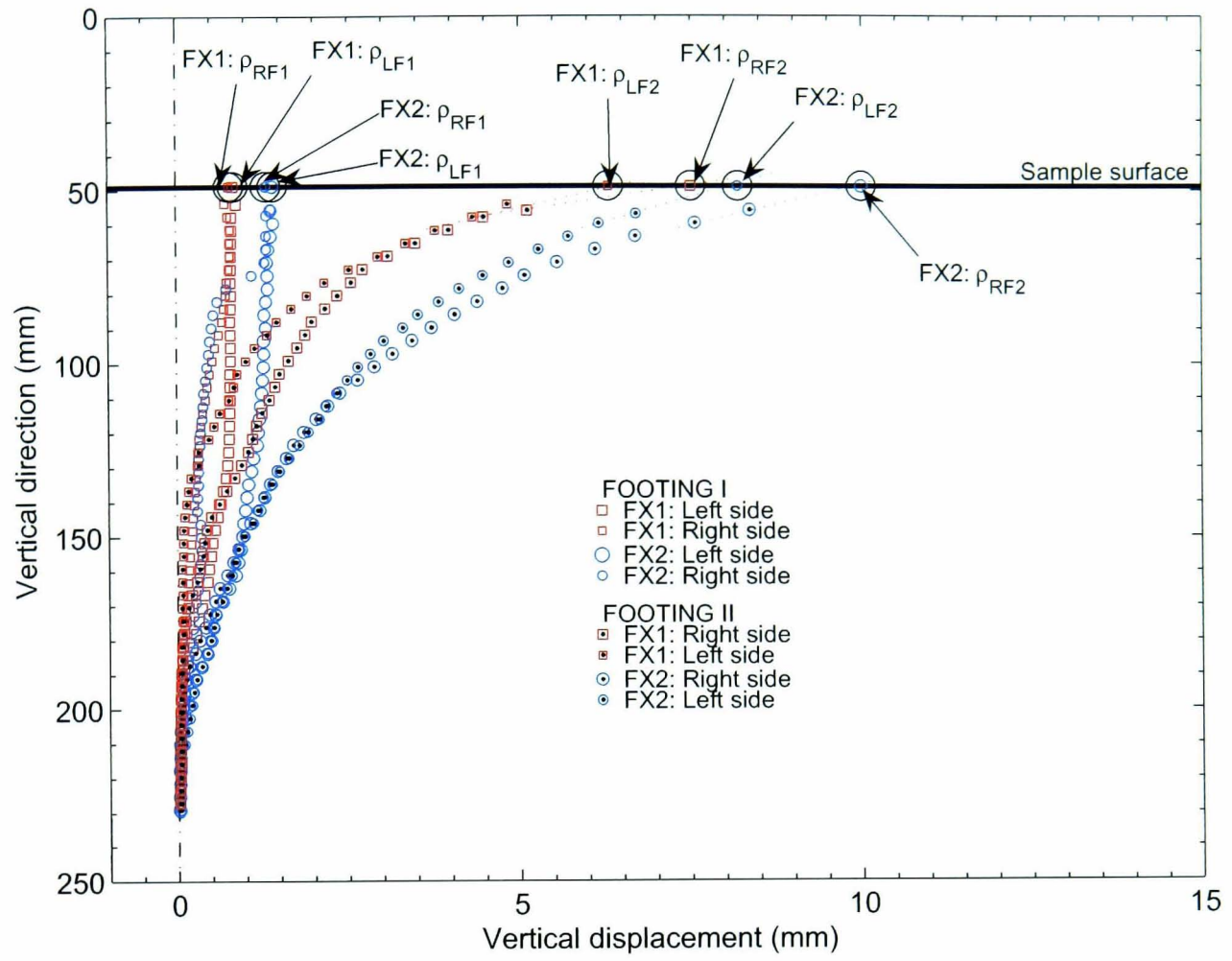
**Figure 5.72:** Vertical displacements of markers and the soil beneath the markers due to loading on Footing II

# Chapter 6

# FINITE ELEMENT ANALYSIS

## 6.1 INTRODUCTION

Two series of finite element analyses were carried out: (1) simulations of the model used in laboratory experiments and (2) simulations of the prototype of the laboratory model. The simulations deployed the program SAFE, part of the Oasys GEO Suite provided by Oasys Ltd. The stress–strain behaviour of the soil was represented with the BRICK constitutive model developed by Simpson (1992). Both simulations were conducted assuming a two-dimensional mode of deformation (plane strain).

The main objective of the first simulations was to use the results obtained from the physical modelling, discussed in Chapter 5, to validate the finite element analyses. This will be discussed in Sections 6.2–6.2.3 where selected outcomes from the physical modelling are compared with finite element predictions.

The second simulations are addressed in Section 6.3. These analyses involved the application of the model used in the first simulations to field cases. Singapore Lower Marine Clay was represented as the field soil. The section discusses the mitigation of settlement achieved by the presence of sheet piles. In the simulations the effects of different lengths of floating and fixed sheet piles on the mitigation are examined. Furthermore, the effects of stiffness variation of the sheet piles are also addressed.

## 6.2  SIMULATION OF PHYSICAL MODELLING

### 6.2.1  Input Data

There were three main categories of data input for the analyses, i.e., geometry, boundary conditions, and material properties.

#### 6.2.1.1  Geometry

Figure 6.1 shows the mesh geometry of the model implemented in these finite element analyses. The dimensions of the finite element model were identical to those of the physical model. The finite element model, geometrically, consisted of three material zones: the soil sample, the footings, and the sheet pile wall. All were represented by regular rectangular shapes. The horizon-
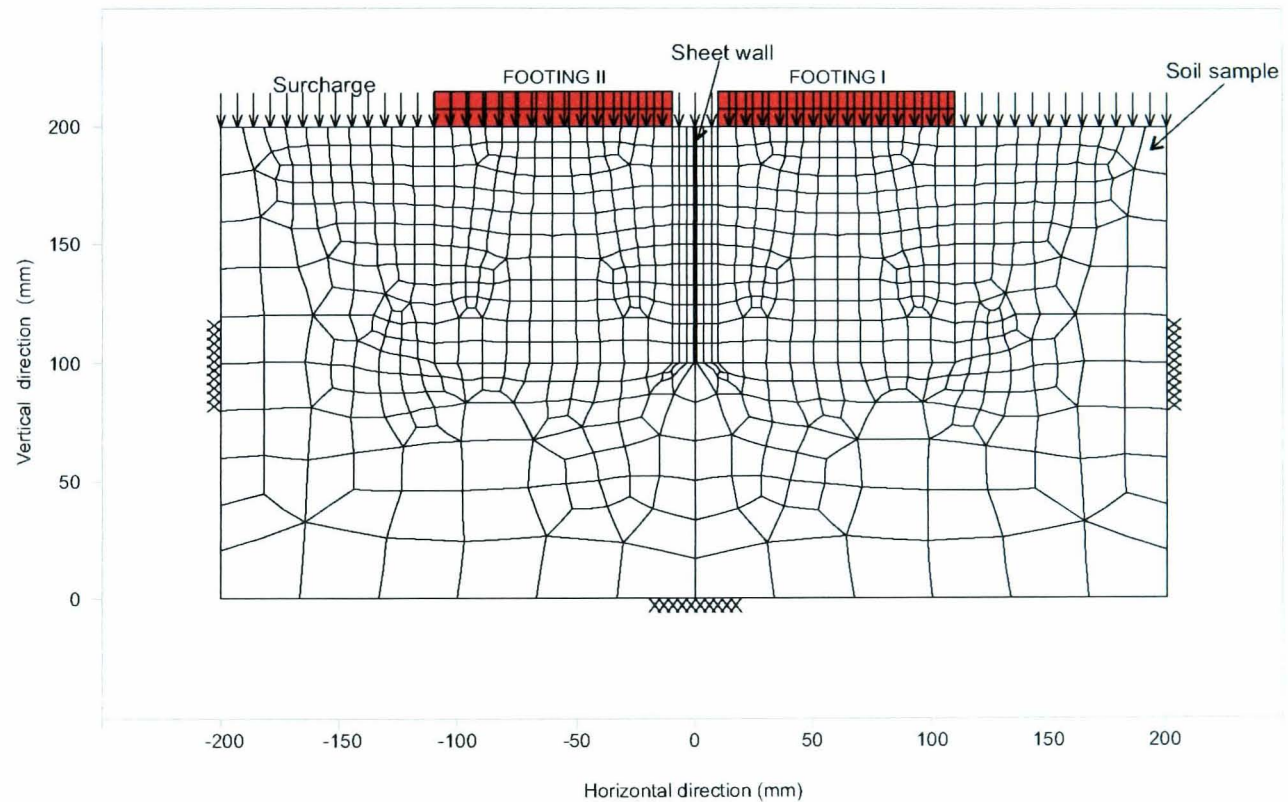


**Figure 6.1:** Geometry and mesh used in SAFE

tal and vertical dimensions of the soil sample, each footing, and the sheet wall were respectively 400 mm×200 mm, 100 mm×15 mm, and 1.5 mm×100 mm. Since SAFE does not facilitate special interface elements, relative movements at common nodes of the footings or the sheet wall and the soil were not simulated. Springs in SAFE can only be used to fix nodes to points outside the mesh, not for connecting opposite nodes as an alternative interface element. However, the thin (3.1 mm

thick) continuum elements around the sheet wall were expected to serve as interface elements as explained by Potts and Zdravković (2001a).

The soil model, including the footings and the sheet wall, was discretised into 830 8-noded isoparametric elements with 2587 nodes. The discretisation of the footings was intended to include the stiffness of the foundation in the analyses (Potts and Zdravković, 2001b). The element shapes were maintained as square as possible. Their aspect ratios, were generally close to 1.00, except around the sheet wall between the two neighbouring footings. This was due to the transitions from a very thin sheet wall. The aspect ratio for elements in this region was 2.7. The slender elements of the wall had a quite large aspect ratio of 11.1. Desai and Abel (1972) compared pure bending of a beam resulting from its exact solution with those using finite element analyses with different aspect ratios ranging from 1.125 to 8. They found that the horizontal displacement at a point, using meshes with an aspect ratio of 1.125, deviated by only about 3% from the exact solution. The largest aspect ratio of 8 resulted in an error of 13%. According to their regression fit, an aspect ratio of 2.7 might have an error of around 5.6%.

To verify the accuracy of the mesh used for the wall, five different mesh aspect ratios (66.7, 11.1, 5.6, 2.8, and 1.0) were examined using the same wall dimensions, as shown Figure 6.2. One of them had the same geometry as that implemented in all the main analyses, i.e. an aspect ratio of 11.1.
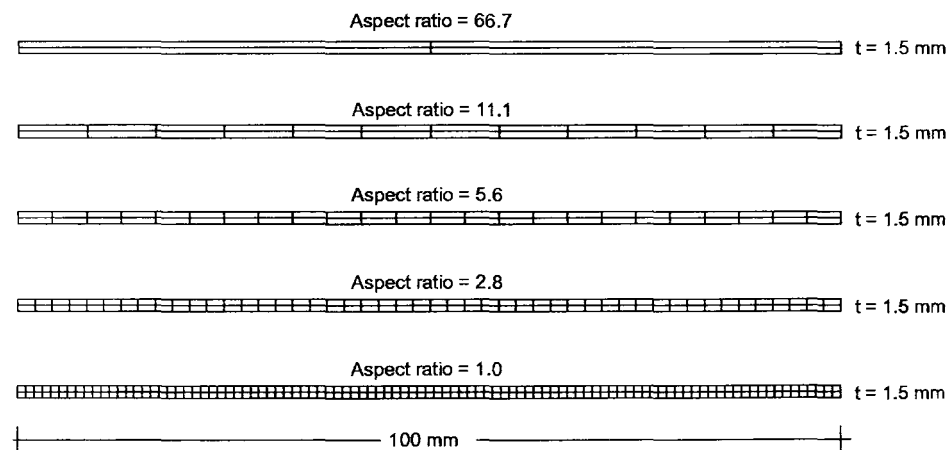


**Figure 6.2:** Various mesh aspect ratios used for accuracy verification
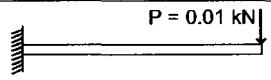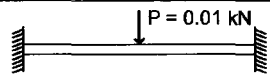
For comparison with numerical results, the deflection equations (British Steel, 1997) for a cantilever (Equation 6.1) and a beam fixed at both ends (Equation 6.2) were used as exact solutions.

$$\delta = \frac{P.L^3}{3EI} \qquad \text{Cantilever} \qquad (6.1)$$

$$\delta = \frac{P.L^3}{192EI} \qquad \text{Beam} \qquad (6.2)$$

In these equations, $\delta$ represents the deflection at the position of the point load $P$, i.e. at the unsupported end of the cantilever or at the centre of the span ($L$) of the beam fixed at both ends. In the calculation, $P = 0.01$ kN and the modulus of elasticity $E = 6.9 \times 10^7$ kPa was taken from the aluminium properties given by Dwight (1999). The second moment of inertia $I$ was based on the thickness of the wall. Table 6.1 shows that the deflections resulting from implementing the five different aspect ratios in a finite element analysis of these two problems exhibit insignificant discrepancies, either from those obtained with an aspect ratio of 1.0 or from the exact solution. As illustrated in Figure 6.3, with an aspect ratio of 11.1 the deviations from both comparisons are less than 0.5%.

**Table 6.1:** Effect of aspect ratio variation of mesh on deflection

| | P = 0.01 kN | | P = 0.01 kN | |
|---|---|---|---|---|
| | Cantilever[a] | | Beam[b] | |
| Aspect ratio | Deflection (mm) | Deviation (%) | Deflection (mm) | Deviation (%) |
| 66.7 | 0.1697 | 1.28 | 0.002632 | 2.16 |
| 11.1 | 0.1715 | 0.23 | 0.002680 | 0.37 |
| 5.6 | 0.1717 | 0.12 | 0.002685 | 0.19 |
| 2.8 | 0.1718 | 0.06 | 0.002688 | 0.07 |
| 1.0 | 0.1718 | 0.06 | 0.002690 | 0.00 |

Beam theory:
        [a]0.1719 mm                    [b]0.00269 mm
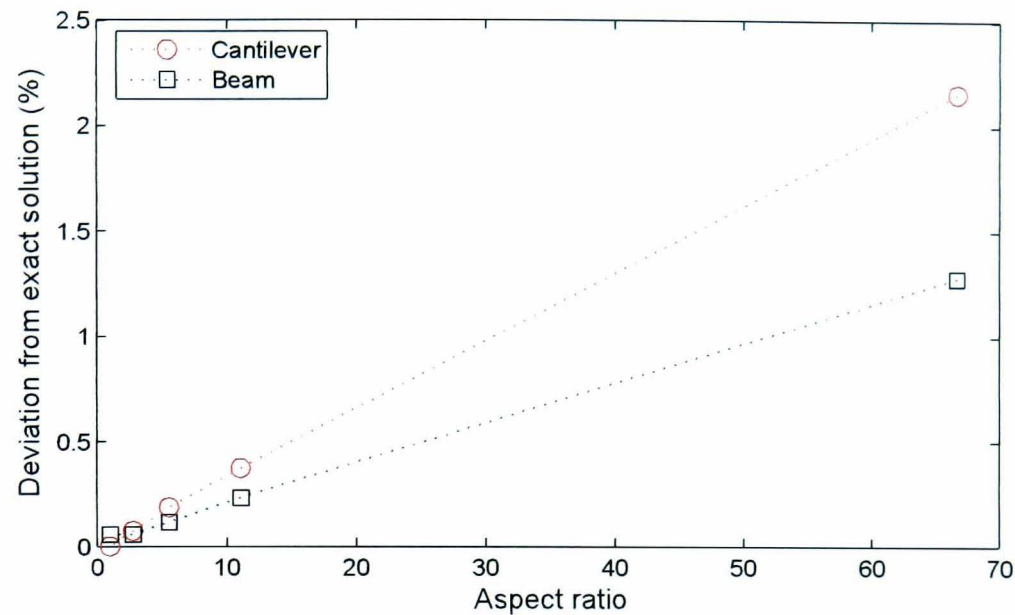
**Figure 6.3:** Deviation of finite element analysis results from exact solution for various mesh aspect ratios

### 6.2.1.2  Boundary Conditions

The boundary conditions prescribed in the analyses included the soil initial conditions. With the BRICK model, a stress history had to be incorporated as an initial condition. The soil was designed to have an OCR of 10 with a maximum past pressure of 50 kPa. The current pressure of 5 kPa was maintained using a surcharge along the soil surface, simulating the presence of the lead shot in the physical model.

The right, the left, and the bottom edges of the mesh were assumed to be fixed. The nodes along these edges were not permitted to move either vertically or horizontally. This assumption related to the PIV results in which no slip was ever found along any of the edges of the soil model. The remaining nodes at the surface and wall were left unrestrained, except in the special case when the sheet wall was restrained vertically. The construction stages were simulated using incremental loading concentrated at the centres of the footings.

### 6.2.1.3  Material Properties

Some of the soil parameters used in the analyses were derived from the laboratory test results. The soil unit weight of 15.62 kN/m$^3$ was determined using the initial void ratio $e_0 = 1.7$ which corresponded to the water content of 65%, as discussed in Section 5.2.2. SAFE also required coefficients of vertical and horizontal permeability of the soil to be specified. These parameters

were derived from the expressions in Equation 6.3, suggested by Al-Tabbaa and Wood (1987) for kaolin.

$$k_v = 0.53e^{3.16} \times 10^{-6} \quad \frac{mm}{s}$$

$$k_h = 1.49e^{2.03} \times 10^{-6} \quad \frac{mm}{s}$$

(6.3)

The soil was treated as a BRICK material. Its stress–strain behaviour followed the mechanism proposed by Simpson (1992), as explained in Section 2.5.2. The string parameters input in the analyses are listed in Table 6.2 and depicted in Figure 6.4. The string properties were the same as those adopted by Simpson (1992) for Singapore clay.

Table 6.2: Material properties for Brick model

| Shear strain $\gamma$ | $\frac{G_t}{G_{max}}$ | Material proportion |
|---|---|---|
| 0.00008 | 0.9200 | 0.0800 |
| 0.00020 | 0.7500 | 0.1700 |
| 0.00040 | 0.5300 | 0.2200 |
| 0.00080 | 0.2900 | 0.2400 |
| 0.00200 | 0.1300 | 0.1600 |
| 0.00400 | 0.0750 | 0.0550 |
| 0.00800 | 0.0440 | 0.0310 |
| 0.01800 | 0.0170 | 0.0270 |
| 0.03600 | 0.0035 | 0.0135 |
| 0.07500 | 0.0000 | 0.0035 |
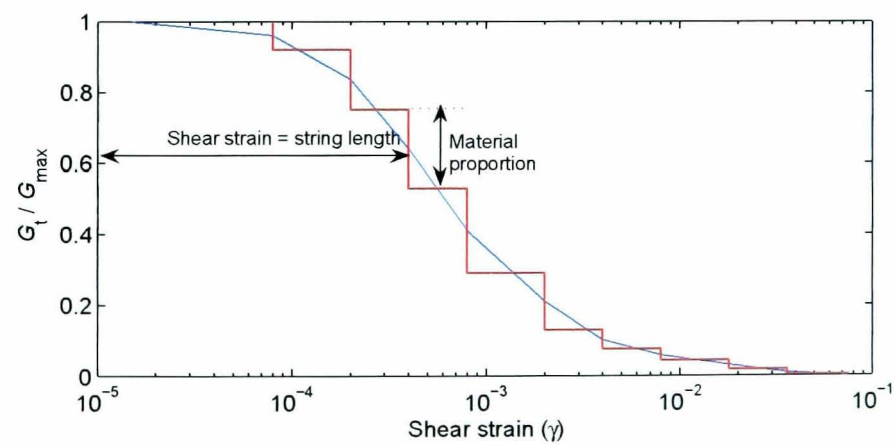


Figure 6.4: String properties used in Brick model

The constants $\lambda$ and $\kappa$ required for the BRICK model were determined from the observed behaviour of the soil. As described in Section 2.5.2, the magnitudes of $\lambda$ and $\kappa$ are identical to $\lambda^*$ and $\kappa^*$ proposed by Houlsby and Wroth (1991). The coefficient $\lambda^*$ and $\kappa^*$ are the gradients of the consolidation and the swelling lines in $\log_e(v) - \log_e(p')$ space. Since mean effective stresses $p'$ were required instead of effective vertical stresses $\sigma'_v$, the coefficient of lateral earth pressure at rest, $K_0$, was needed to calculate the lateral pressures in the soil. The following equation (Equation 6.4) shows this derivation.

$$p' = \frac{(\sigma'_v + 2\sigma'_h)}{3}$$

$$\text{where } \sigma'_h = K_0 \sigma'_v$$

$$K_0 = K_{0nc} \text{OCR}^{\sin \phi'}$$

$$K_{0nc} = (1 - \sin \phi')$$

(6.4)

The coefficient of $K_0$ was taken according to the empirical relation proposed by Mayne and Kulhawy (1982), with $K_{0nc}$ based on Jaky's relation. At the initial condition, the soil model had a stress history giving OCR = 10. The internal friction angle ($\phi'$) of the soil was chosen by referring to those listed by Springman (2004). Under triaxial compression conditions, $\phi'$ varied from $20.9°$ to $22.6°$ for kaolin with $I_p = 32\%$. The value of $\phi' = 22.6°$ was selected. The values of $\lambda^*$ and $\kappa^*$ based on these assumptions were 0.1 and 0.017 respectively (see Figure 6.5). By using the Oasys BRICK program, the consolidation behaviour of the model soil with the combination of these values and the proposed BRICK model's string lengths was checked. As shown in Figure 6.6 the resulting slope of the normal consolidation line seemed higher than that obtained from laboratory data. After some adjustment, the values of $\lambda^* = 0.08$ and $\kappa^* = 0.017$ seemed to produce a better fit to the data and they were implemented throughout the analyses. In the analyses, the Poisson's ratio, $\nu = 0.2$, was specified. It was suggested by Simpson (1992) that most soils have Poisson's ratios around this value. In this constitutive model, at very small strain, the elastic volumetric stiffness was assumed to be proportional to current mean stress, i.e. $\delta s = s\delta v_e/\iota$ where $\delta s$, $s$, $\delta v_e$, and $\iota$ are mean stress increment, mean stress, elastic volumetric increment, and proportionality constant respectively. The constant $\iota = 0.0032$ was used in the analyses. The effects of overconsolidation on stiffness and strength were controlled by $\beta_G = 4$ and strength $\beta_\phi = 2$ respectively.
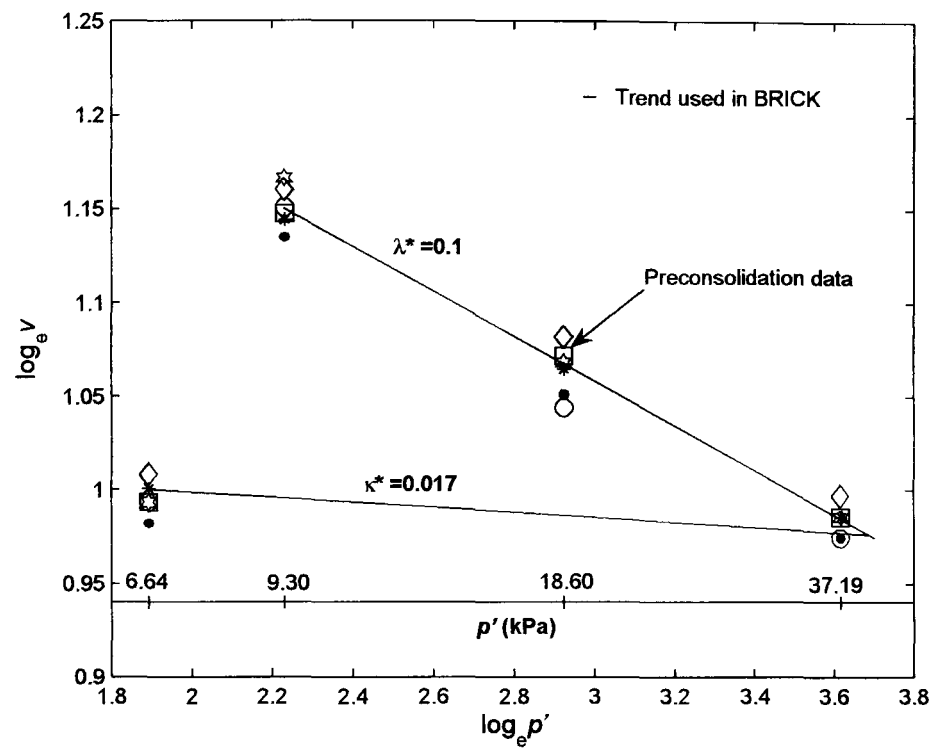
**Figure 6.5:** Determination of $\lambda^*$ and $\kappa^*$ proposed by Houlsby and Wroth (1991)
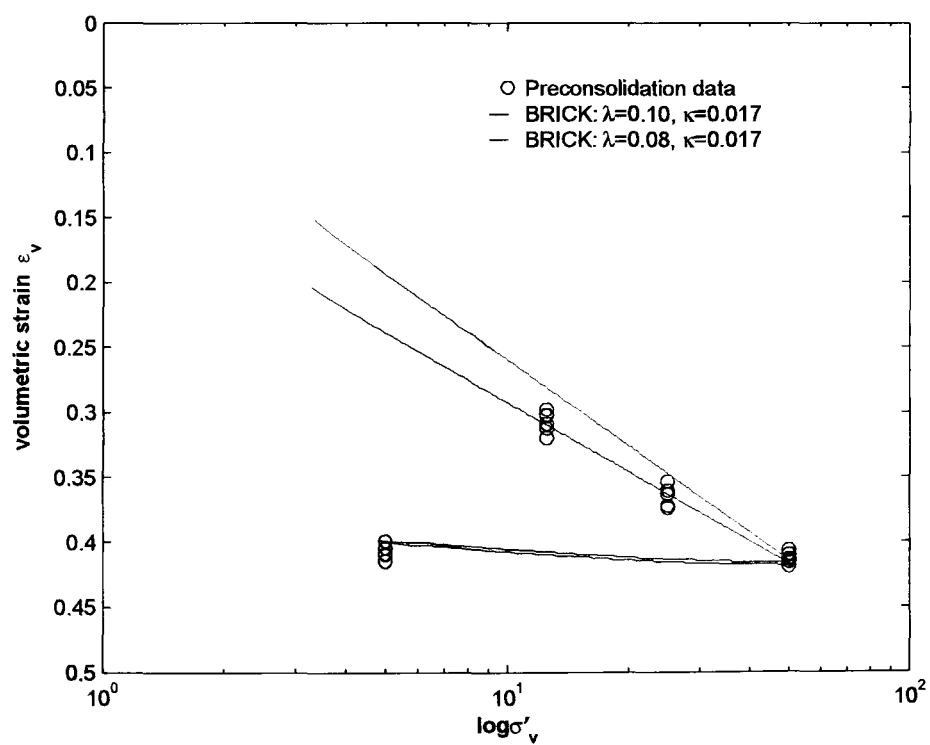


**Figure 6.6:** Resulting data from BRICK software and from preconsolidation

The implied $\phi'$ obtained from Oasys BRICK software was 24° which is larger than the initial assumption. In order to obtain lower soil strength, a larger $\iota$ or $\nu$ was required. However when larger values were tried, the adjustment seemed to result in convergence failure of the finite element analyses before the maximum pressure of 80 kPa on Footing I was reached.

The footings and the sheet wall were treated as linear elastic materials. Since the analyses were carried out in plane strain and as the physical model was designed according to a plane strain mode (see Section 3.2.1.1.6), no adjustment of stiffness was required in the analyses. The elastic moduli $E$ of the footings and the sheet wall were respectively $3 \times 10^6$ kPa (Ineos Acrylics UK Ltd., 2001) and $6.9 \times 10^7$ kPa (Dwight, 1999). As discussed in Section 3.2.1.1, Poisson's ratios $\nu = 0.38$ for the Perspex and $\nu = 0.33$ for the aluminium were used. To simulate the perforated nature of the Perspex footings, a coefficient of permeability $k$ of 0.01 m/s was assigned, which was much higher than that of the interfacing soil. On the other hand $k = 0$ was specified for the aluminium sheet wall.

### 6.2.2 Analysis Procedures

As already mentioned, the finite element analyses were performed in plane strain. The soil model was assumed to be fully saturated in a drained condition with a pore pressure of zero magnitude at the surface of the sample. The analyses consisted of four stages. Figure 6.7 illustrates the flow diagram of the stages.
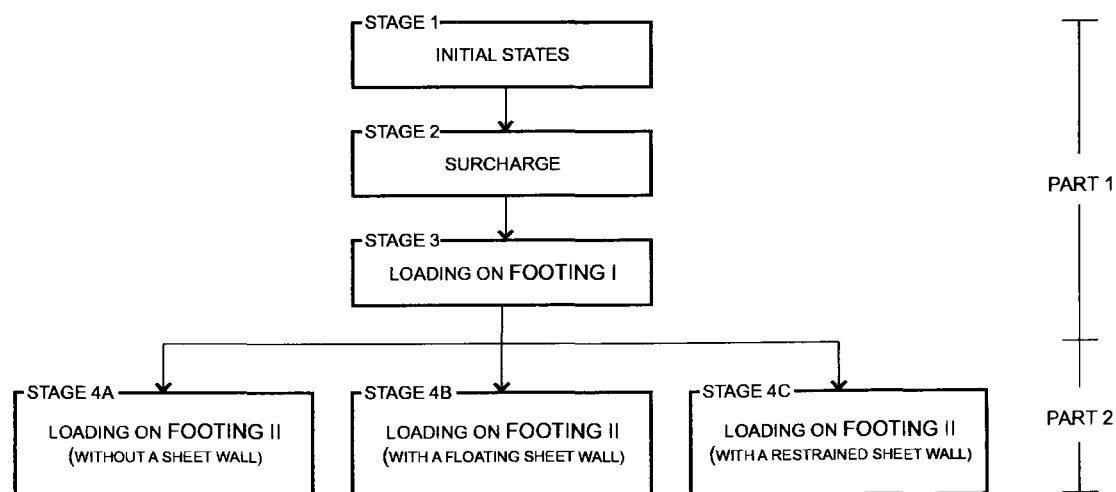
**Figure 6.7:** Stages of finite element analyses implemented in this research

In general the whole analysis could be divided into two parts. The first part comprised the first three stages which were run in order. In the first stage, using a feature in SAFE, the stress history was included in the BRICK model parameters. The maximum past pressure of 50 kPa during the preconsolidation in the physical modelling was simulated with an assumption that the sample previously had a higher surface level. The missing soil thickness was then replaced with a surcharge of 5 kPa in the second run. The pressure was subsequently maintained through the rest of analysis. This created an OCR of 10 in the soil model. In the third stage, a concentrated load of 7.5 kN was applied on the centre of Footing I in order to produce a contact pressure of 80 kPa including the surcharge. The loading was applied incrementally in 15 stages of 0.5 kN. Up to this stage the material of Footing II was set to void. Otherwise the displacement at the nodes interfacing the footing and the soil would have been affected by the compatibility enforcement between the two extremely different materials.

The second part constituted three different and independent studies (denoted as Stage 4A, Stage 4B, and Stage 4C) related to observations on the settlement mitigation due to the presence of a sheet wall. The first study (Stage 4A) was considered as a benchmark to which the results from the other parts were compared. The effects of the interaction between two footings without any barrier on soil displacements were first scrutinised. In this study the incremental loading on Footing II was applied using the same loading increments that had been applied to Footing I. In the second study (Stage 4B), similar procedures were applied except a floating sheet wall 100 mm long was placed in the soil between the two footings. The last study (Stage 4C) also involved analyses with a sheet placed between the footings but vertically restrained at its tip.

### 6.2.3  Results

The outcomes from the finite element analyses are generally presented as vectors and contours on a cross-section. The following conventions will be used if no units are specified: a scale of unity is used if displacement vectors are used i.e. vectors are plotted to the same scale as the footings and soil boundaries, displacement contours are presented in millimetres, a negative sign indicates downward deformation for vertical displacement or leftward movement for horizontal displacement, and a positive sign represents the reverse. When contours are used to show the proportion

of strength mobilised, they are presented as percentages. Strain contours usually represent strain ratios.

### 6.2.3.1    Loading on Footing I

**6.2.3.1.1    Overall Soil Displacement**    Figure 6.8 and Figure 6.9 show the vectors and contours of cumulative displacements due to incremental loadings on Footing I. The patterns of both the vectors and contours are very similar to the results from the PIV analysis for the same problem in Section 5.3.1.2 (Figures 5.11, 5.12, 5.13 and 5.15). The horizontal displacements are shown in Figure 6.10. It is revealed that the horizontal dimension of the consolidation chamber was not adequate to allow the soil to behave symmetrically with respect to the centre of the footing. Again, similar patterns were encountered in the results of PIV analyses of the physical model (see Figures 5.14 and 5.16 in Section 5.3.1.2). Although the magnitudes of the horizontal displacements in the physical model tended to decrease more quickly than those obtained from the finite element analysis, both show that the displacements beneath the left side of the footing were always larger than those beneath the right side which was closer to the chamber wall.
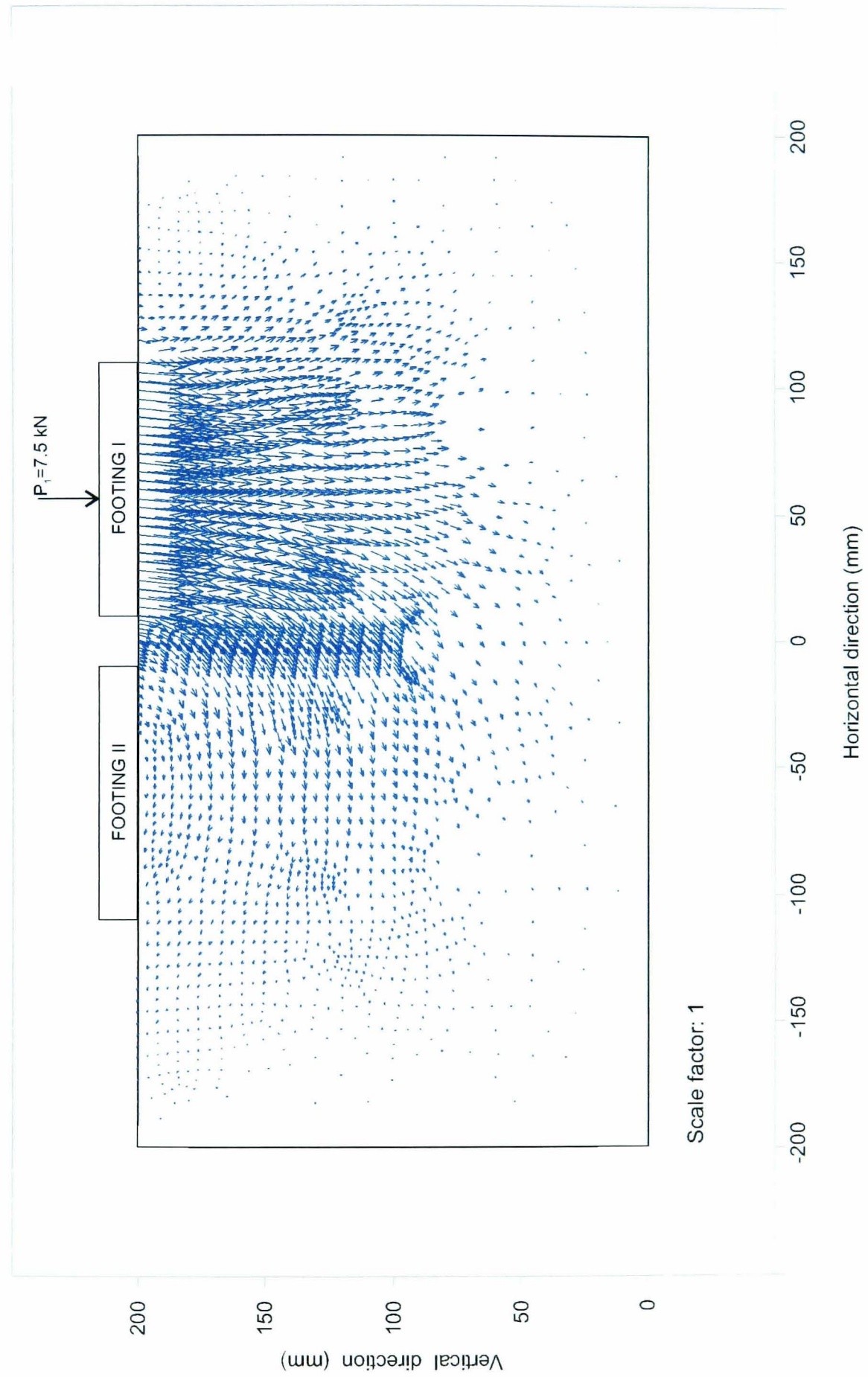
**Figure 6.8:** Vectors of displacement due to loading on Footing I
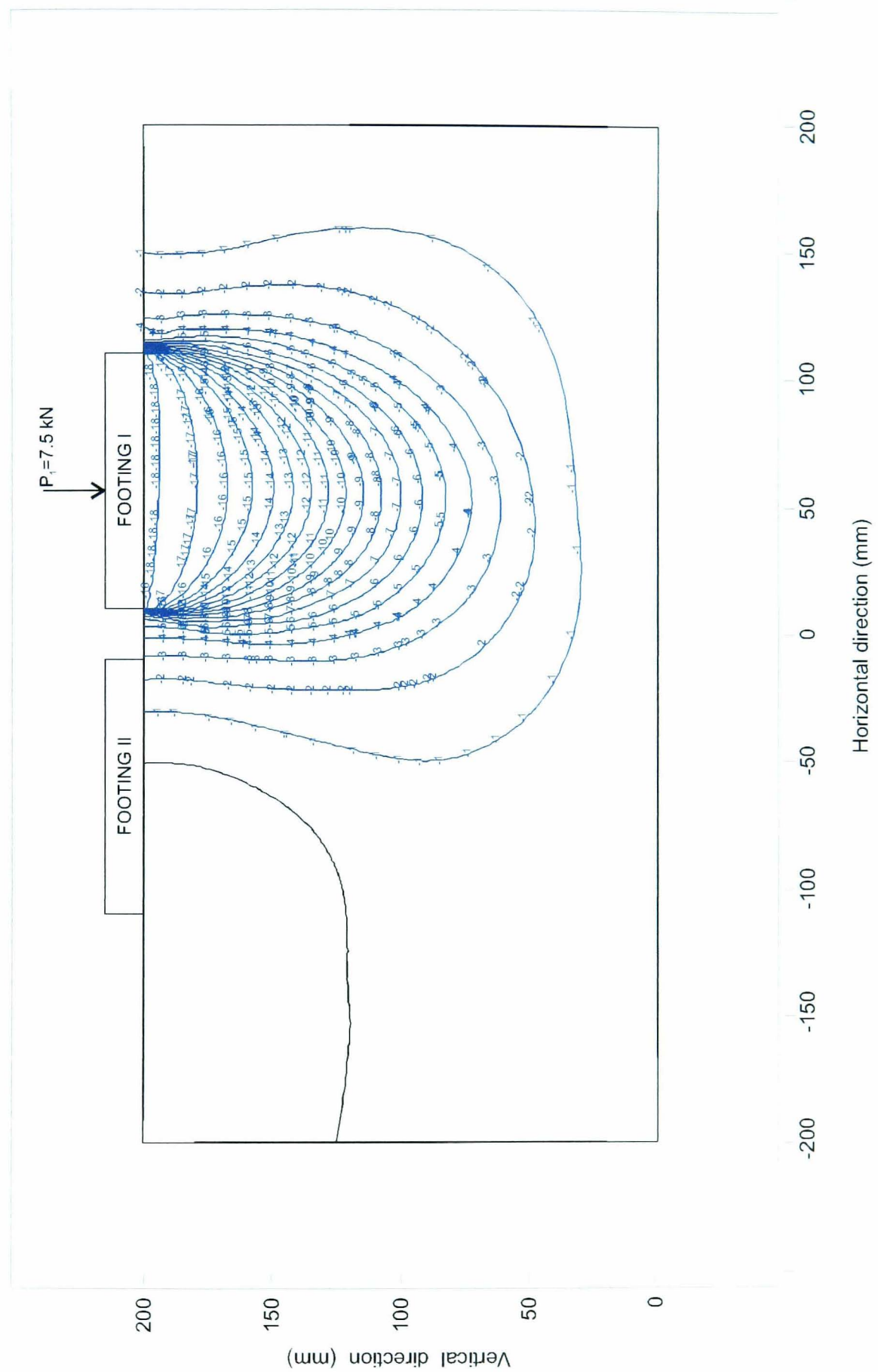
**Figure 6.9:** Contours of vertical displacement due to loading on Footing I
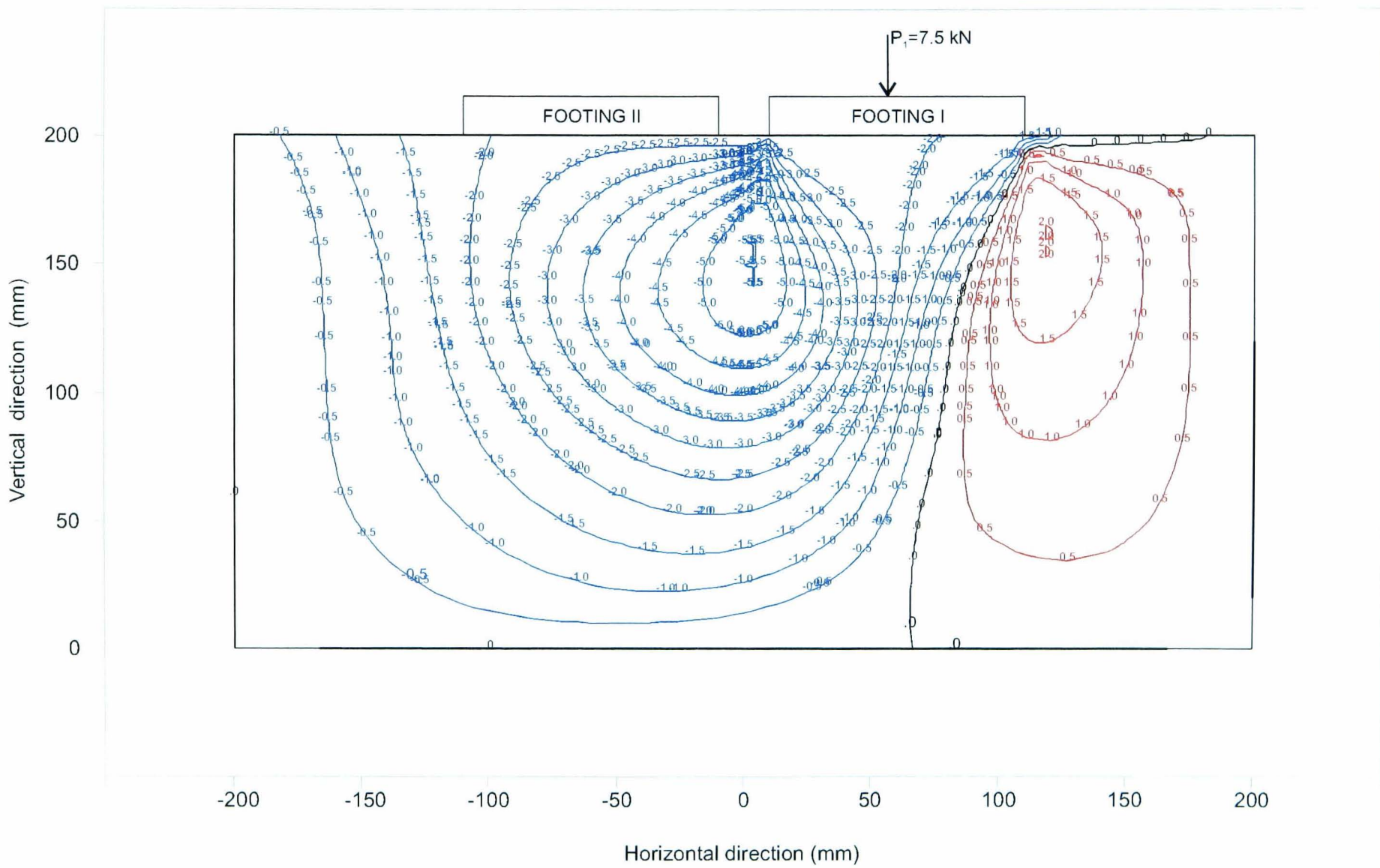
**Figure 6.10:** Contours of horizontal displacement due to loading on Footing I

**6.2.3.1.2 Displacement Profiles: PIV versus FEM** Compared to those in the physical model, the displacements in the finite element analysis seemed to propagate over a larger area. The vertical displacement profiles beneath the centre of Footing I are depicted in Figure 6.11. The magnitude of the predicted surface settlement at this location was inside the range of the
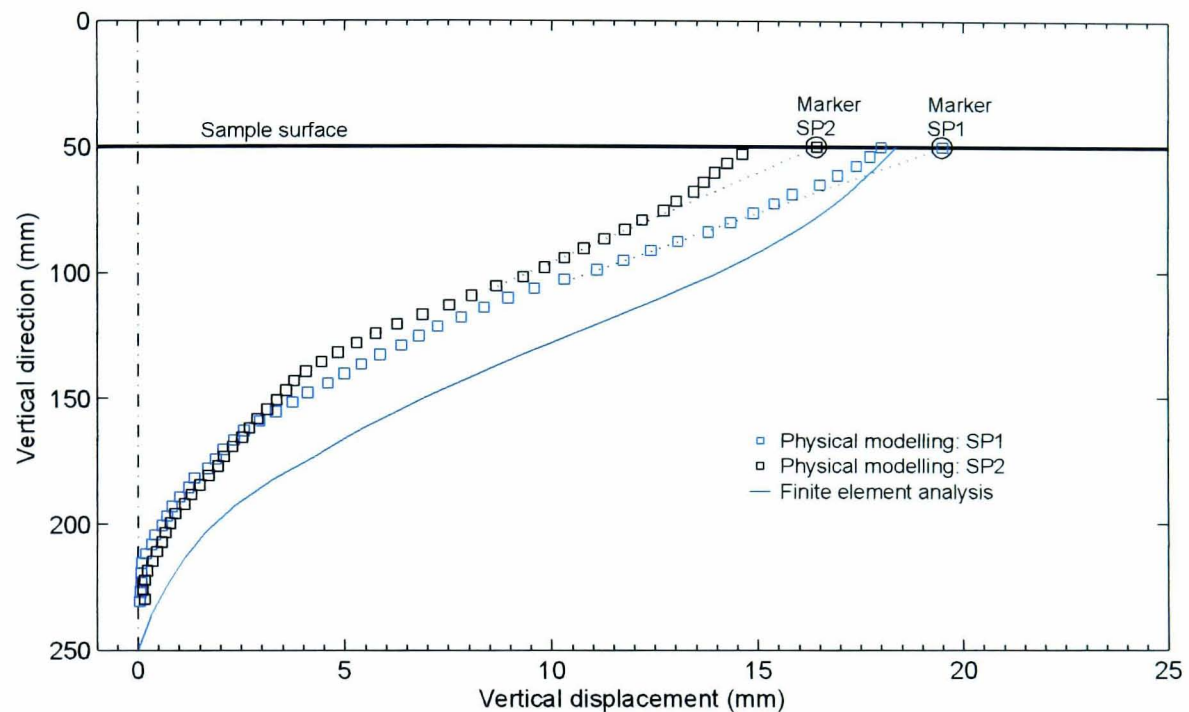


**Figure 6.11:** Vertical displacement beneath the centre of Footing I, resulting from PIV and finite element analyses

results from the physical model that were considered the most representative (Test SP1 and Test SP2). In the figure above, creep has been subtracted from the vertical displacement profiles of the physical model, assuming that the creep proportion measured with LVDTs (see Table 5.2 in Section 5.3.1.2) is constant with depth. The vertical displacements observed in the physical models seem to decrease more rapidly with depth. In the finite element analysis the sample face was assumed frictionless. This was not the case for the physical modelling. The friction between the sample face and the Perspex window could have diminished either the vertical or horizontal displacements over the whole area.

**6.2.3.1.3 Load–Settlement Behaviour of Single Footing** The settlements with respect to the incremental loading on Footing I are shown in Figure 6.12. A good agreement was noted,
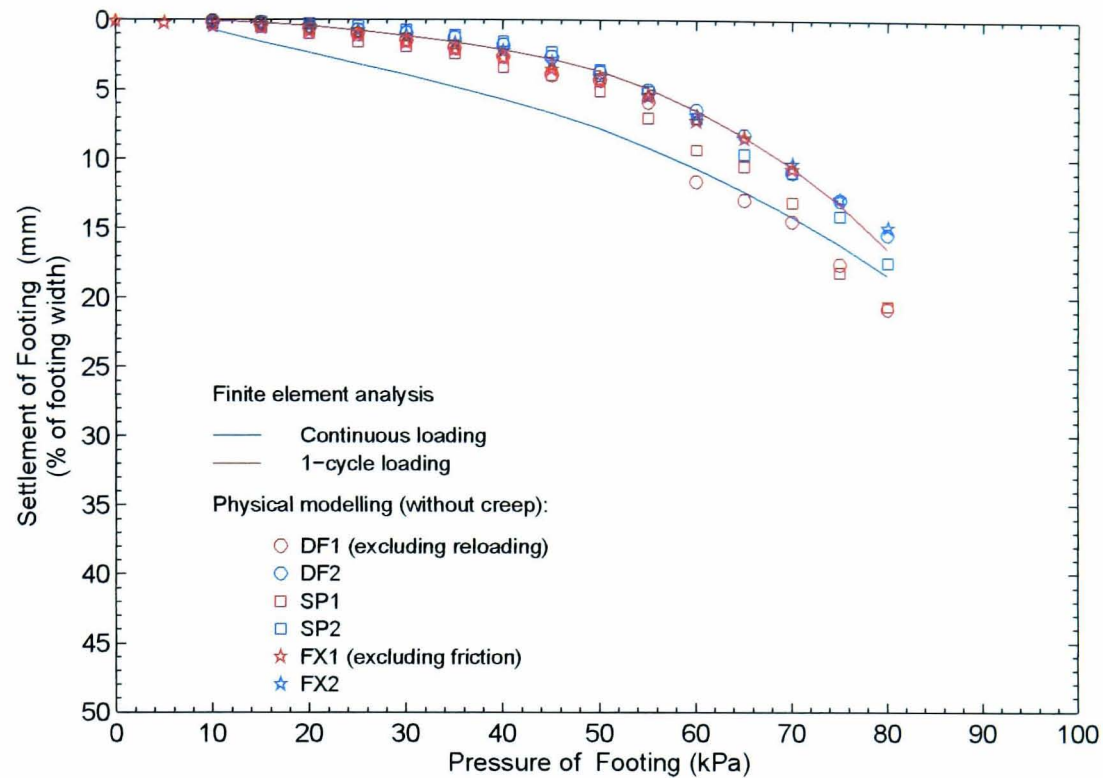
**Figure 6.12:** Relationship of pressure and settlement of Footing I

for higher footing stresses, between the outcome obtained from the analysis and that from the physical modelling with the creep settlements excluded. The finite element analyses seem slightly to overestimate the settlement below the preconsolidation pressure (50 kPa). However, the result from a "1-cycle loading simulation", discussed in Section 6.2.3.1.4 (see Figure 6.17), fits very well with all data of the physical modelling. At a footing pressure of 80 kPa the settlement had already reached about 18% of the footing width. The proportion of the strength mobilised at this stage is shown in Figure 6.13. Higher proportions of 70% to 80% prevailed beneath and around the sides of the footing while only about 60% of the strength was mobilised beneath the centre of the footing.
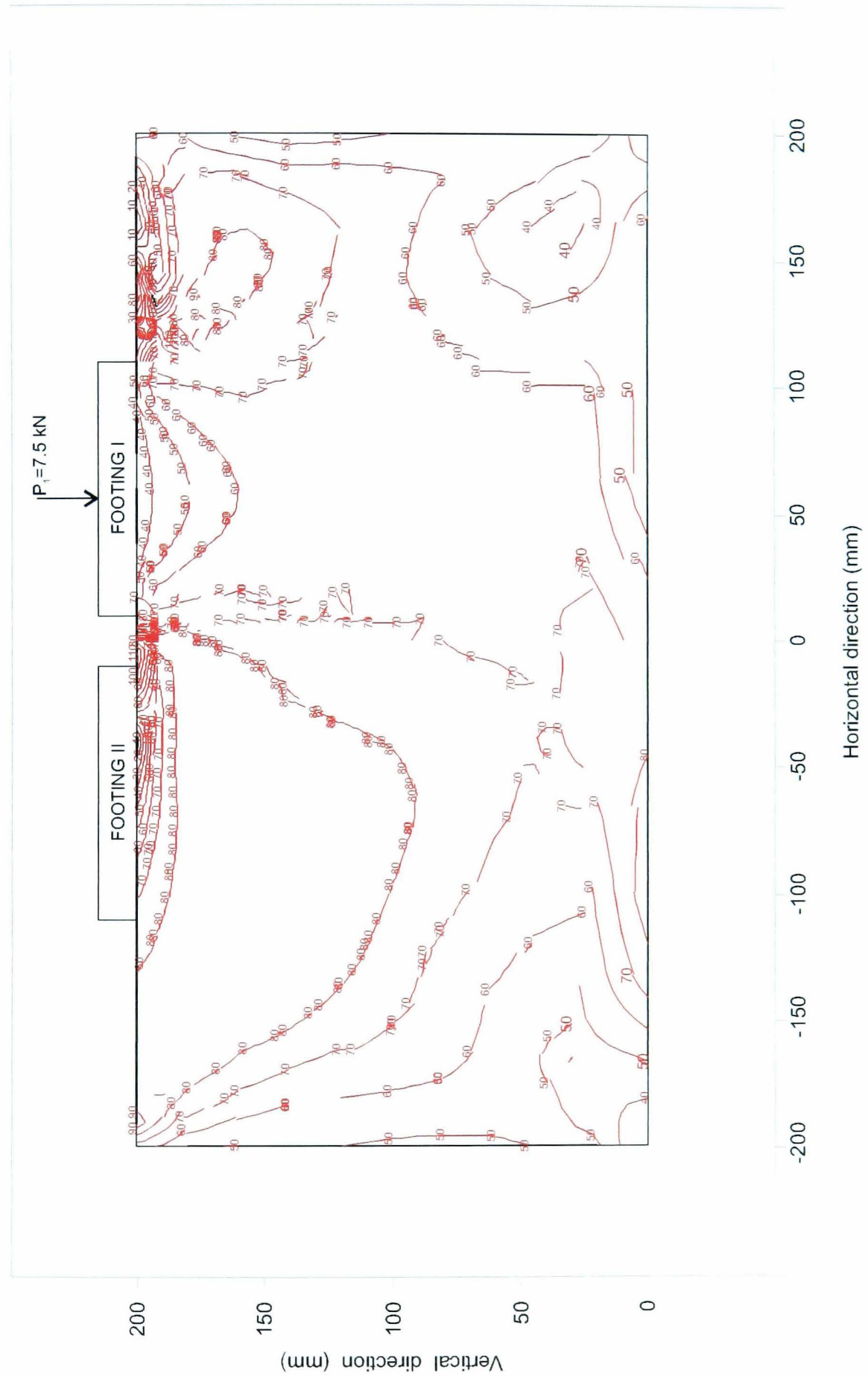
**Figure 6.13:** Proportion of strength mobilised of model soil due to a pressure of
80 kPa of Footing I

**6.2.3.1.4   Effects of Cyclic Loadings**   The cyclic loadings thought to be the cause of discrepancies in the soil displacements between different physical models, as discussed in Section 5.3.1.1, were simulated in finite element analyses. Previously, the test results were placed in one of four categories. For the discussion here, they will be reclassified into Case 1 for Test DF1, Case 2 for Tests SP1 and SP2, Case 3 for Test FX1, and Case 4 for Tests DF2 and FX2. The models which experienced loading cycles were Case 1 and Case 4.

Case 1 was simulated with a cycle of an unloading-reloading of Footing I. The footing was first incrementally loaded to a contact pressure of 65 kPa and then unloaded to 0 kPa in a single stage. The soil was reloaded back to 65 kPa in 5-kPa increments. The result is shown in Figure 6.14. When plotted together with that of the physical modelling, it is evident that the settlements follow
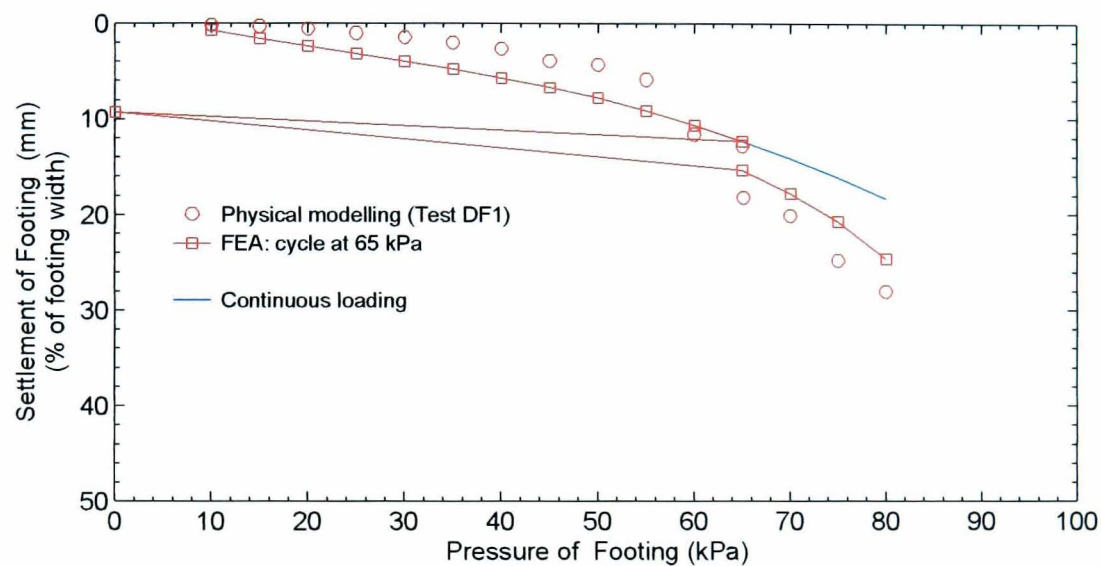


**Figure 6.14:** Effect of unloading and reloading at 65 kPa on Footing I

a similar trend. The settlement after 65 kPa due to the reloading was larger than that before the unloading. Compared with the result from the analysis on the normal case, i.e. continuous loading, from Figure 6.12, it is revealed that there is an offset of the settlement after reloading. This offset was caused by some plastic straining around both sides of Footing I. Figure 6.15 shows that the strength of the soil was fully mobilised in these regions.

Case 4 was modelled with zero, one or two stress history loading cycles as described in Figure 6.16. The Point A represents the maximum stress experienced by the soil. This was specified in the stress history parameters of the BRICK model. In the initial equilibrium states, the soil had not yet been subjected to any loading (Point B). The soil is defined as "zero cycle" at Point C after
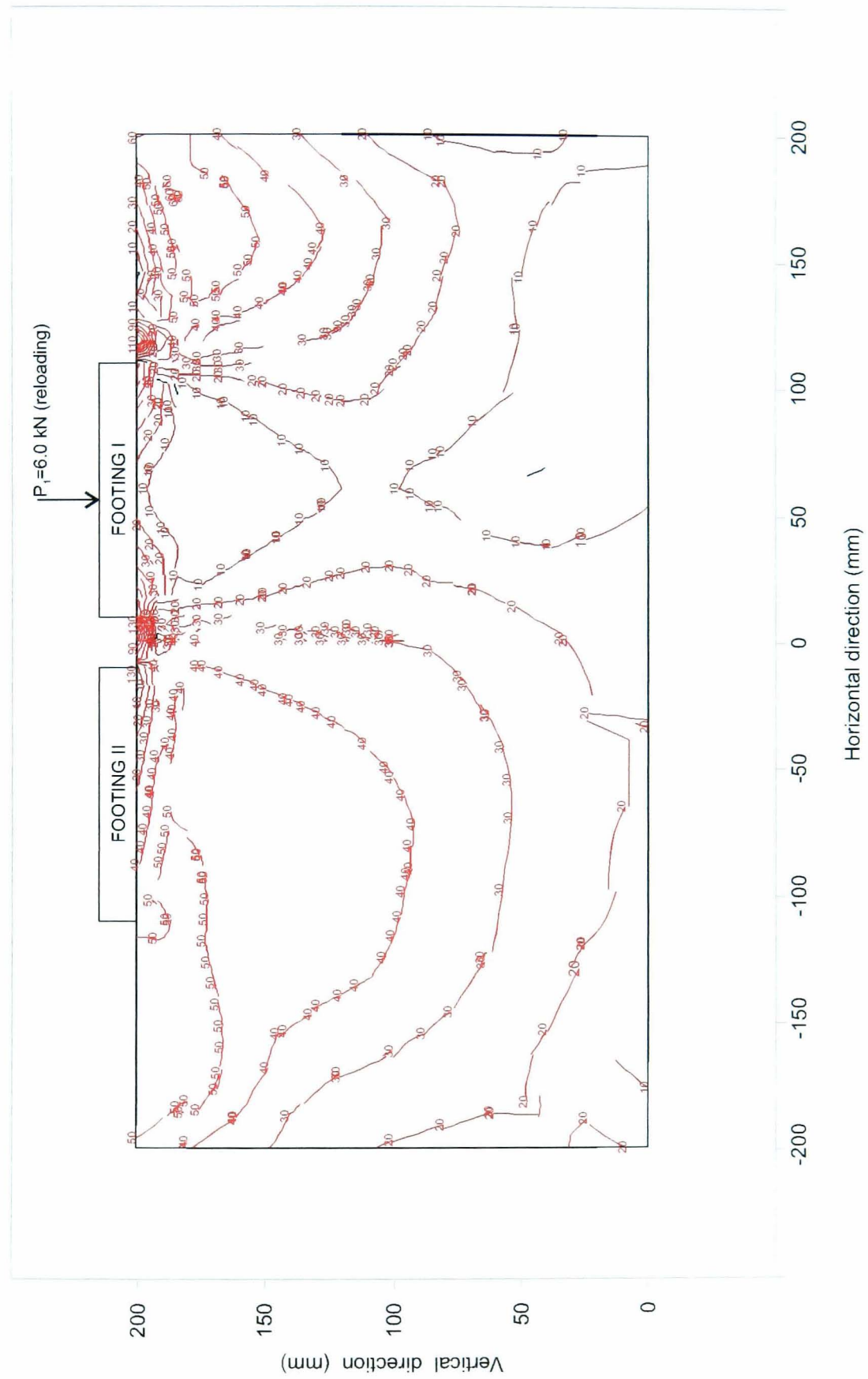
**Figure 6.15:** Contours of strength mobilised due to unloading and reloading at 65 kPa on Footing I

applying a surcharge of 5 kPa on the soil surface. An additional cycle (50→0→5 kPa) from this point is considered as one cycle and so on. Figure 6.17 illustrates the resulting pressure–settlement relationship and the effect of cycling. The soil behaved more stiffly with more loading cycles.
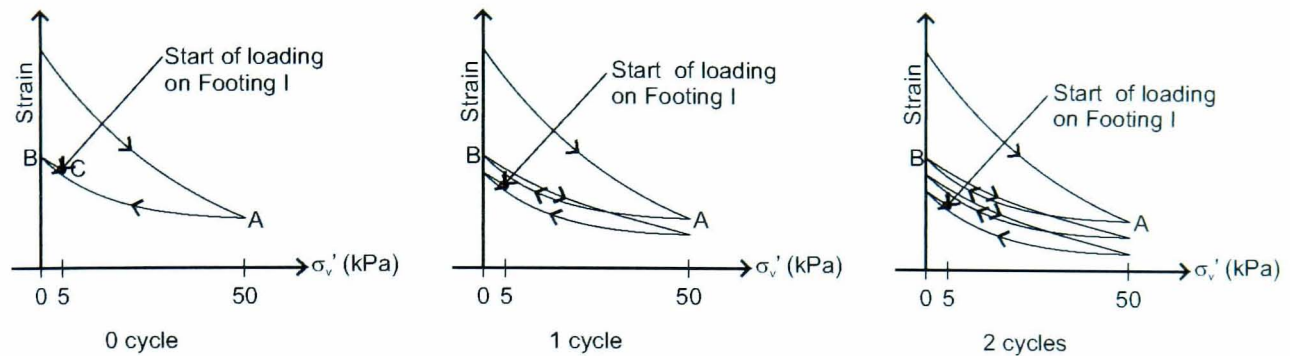


**Figure 6.16:** Definition of cycles in the finite element simulation of unloading and reloading during preconsolidation
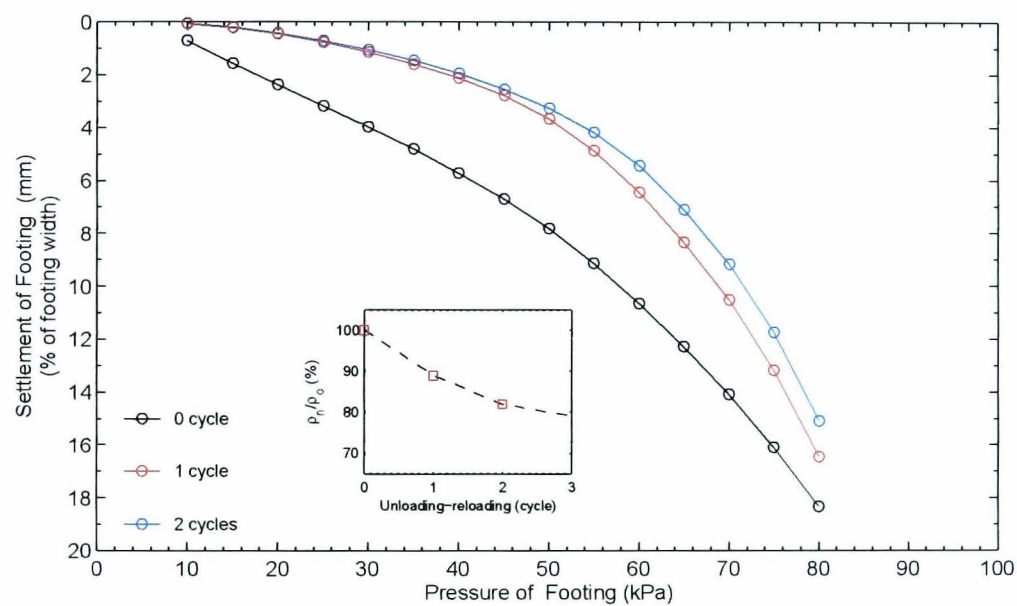


**Figure 6.17:** Effect of unloading and reloading during preconsolidation

The settlement profiles with depth beneath the centre of Footing I for both of the cyclic loadings and the other cases are plotted in Figure 6.18. Since the pressure loss due to friction of the footing sides and the chamber wall in the physical modelling was measured as about 10 kPa (see Section 5.3.1.1), the settlement profile for Case 3 was established using the result from the Case 4 simulation at 70 kPa (zero cycle). In the case of total settlement, good agreements are evident between the results from the physical and numerical modelling. However, the finite element method seems to overestimate the settlement profiles at the lower levels, as noted in Section 6.2.3.1.2.
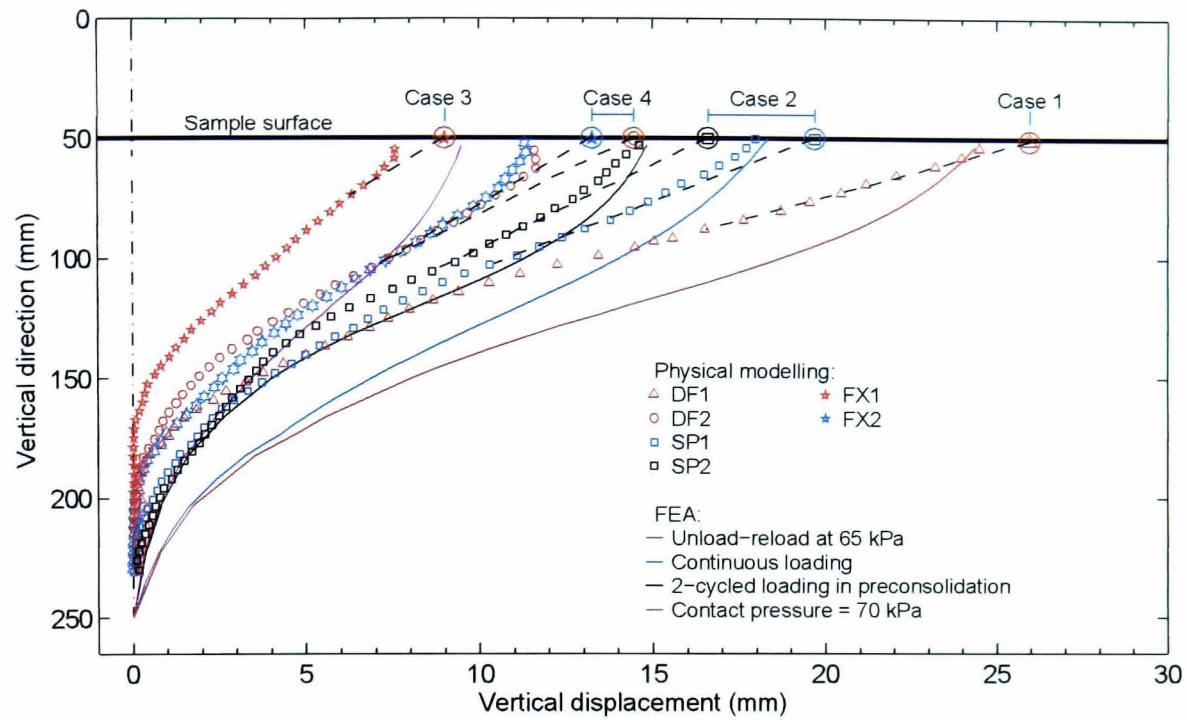
**Figure 6.18:** Comparison of results from finite element method and physical modelling (without creep)

### 6.2.3.2  Loading on Footing II

As observed in the physical modelling, a stiffer response from the soil beneath Footing II than beneath Footing I was evident as the footing was loaded. The vectors and the contours of the overall vertical soil displacement are shown in Figure 6.19 and Figure 6.20. At the end of the incremental loading on Footing II, Footing I tilted towards Footing II with $\delta/l \approx 1/169$. However, Footing II did not tilt towards Footing I. Unlike in the physical model, the cumulative vertical displacement caused this footing to tilt towards to the opposite side, although during the first five loading increments the footing did incline towards Footing I. Also, taking the start of loading on Footing I as a datum, the footings tilted towards each other, similar to the phenomenon found by Jao et al. (2002) in their finite element analysis (Section 2.2.2). This evidence is illustrated in Figure 6.21. At the end of loading on Footing II, the cumulative displacement contours (Figure 6.21) reveal that the settlement of the two footings was not symmetrical. This would not occur, i.e. the settlement would have been symmetrical, if the soil behaved as a linear elastic medium, as often assumed in design practice.

**Figure 6.19:** Displacement vectors due to loading on Footing II
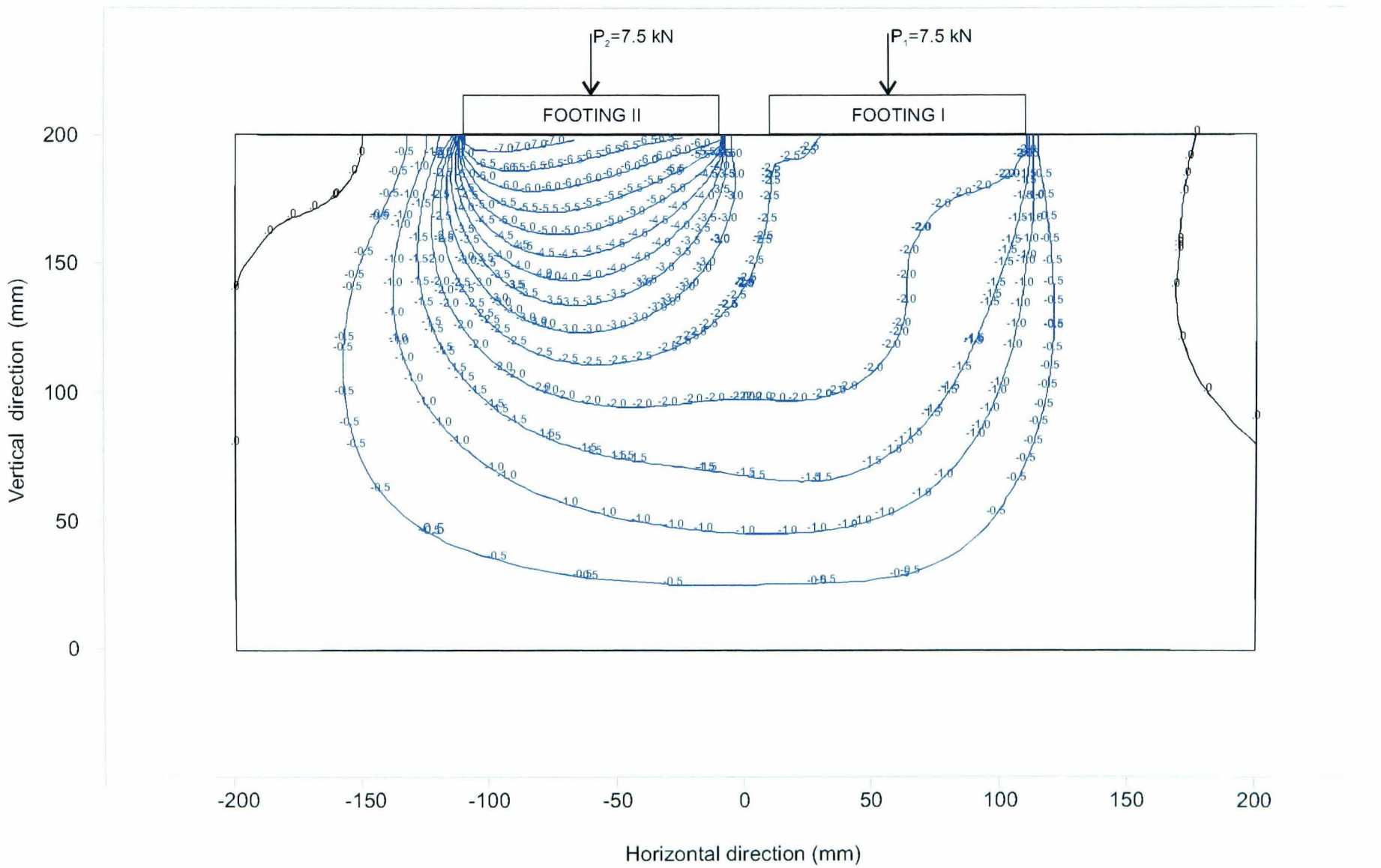
**Figure 6.20:** Vertical displacement contours due to loading on Footing II
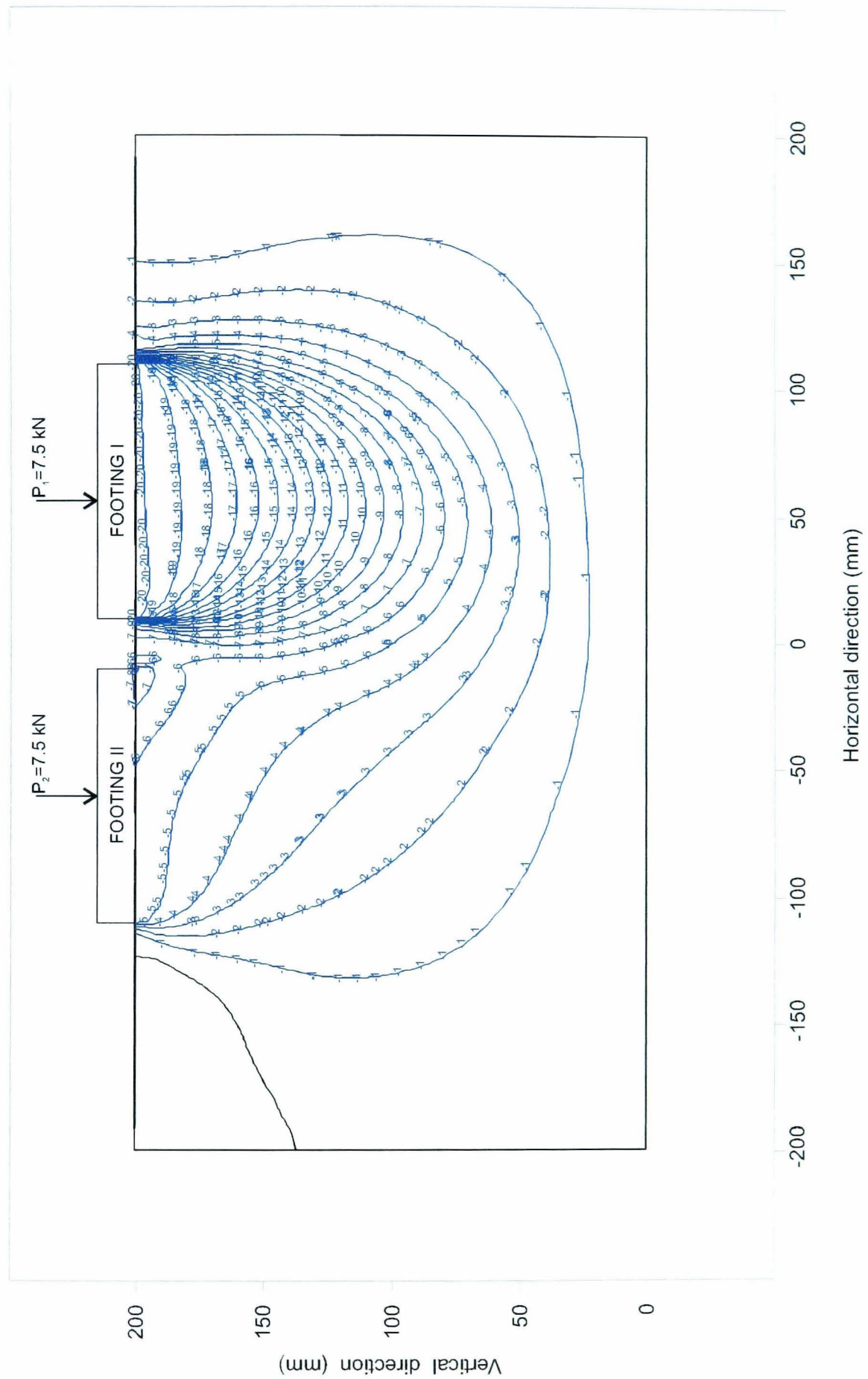
**Figure 6.21:** Cumulative vertical displacement contours due to loading on Footing I and Footing II

**6.2.3.2.1  Load–Settlement Behaviour of Double Footing**  The relationship between the contact pressures and the settlement at the centre of Footing II is shown in Figure 6.22. The
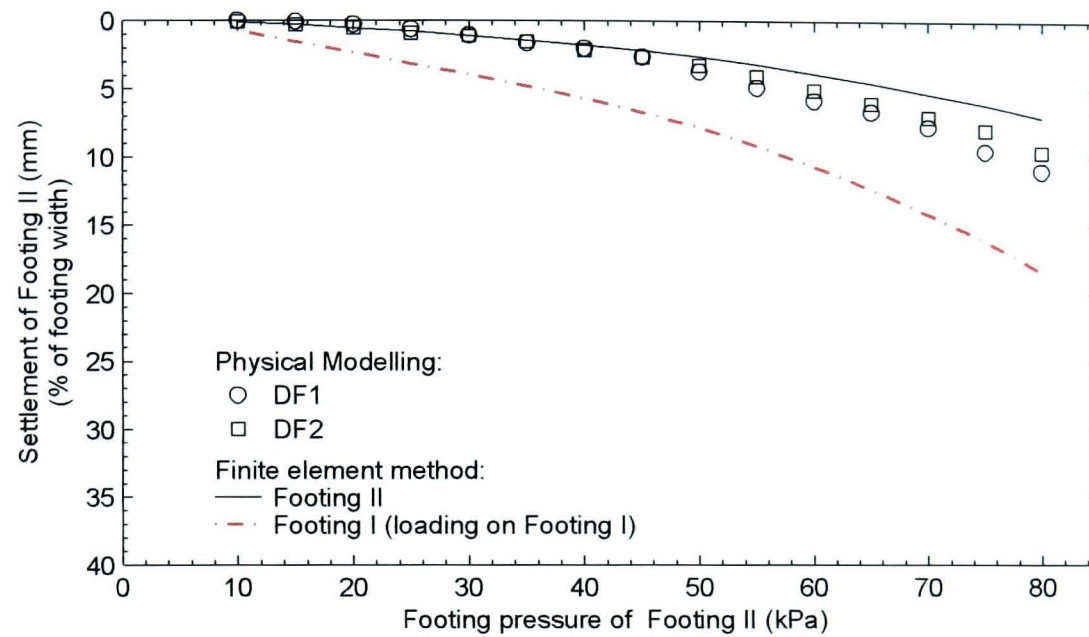


**Figure 6.22:** Relationship of pressure and settlement (excluding creep) of Footing II due to loading on Footing II

outcome demonstrated a similar trend and a good agreement with that of the DF tests although the settlement of the physical model at the end of tests was slightly underestimated by the finite element method. The final settlement of Footing II was about 7% of the footing width, which was only 39% of the settlement of Footing I (as an isolated footing) for the same magnitude of load. The settlement ratio $\rho_{F1}/\rho_{F2}$ was 32%. The stiffer response of the soil beneath Footing II was confirmed by the contours of the mobilised strength in Figure 6.23. The strength mobilised beneath Footing II was less than that beneath Footing I.
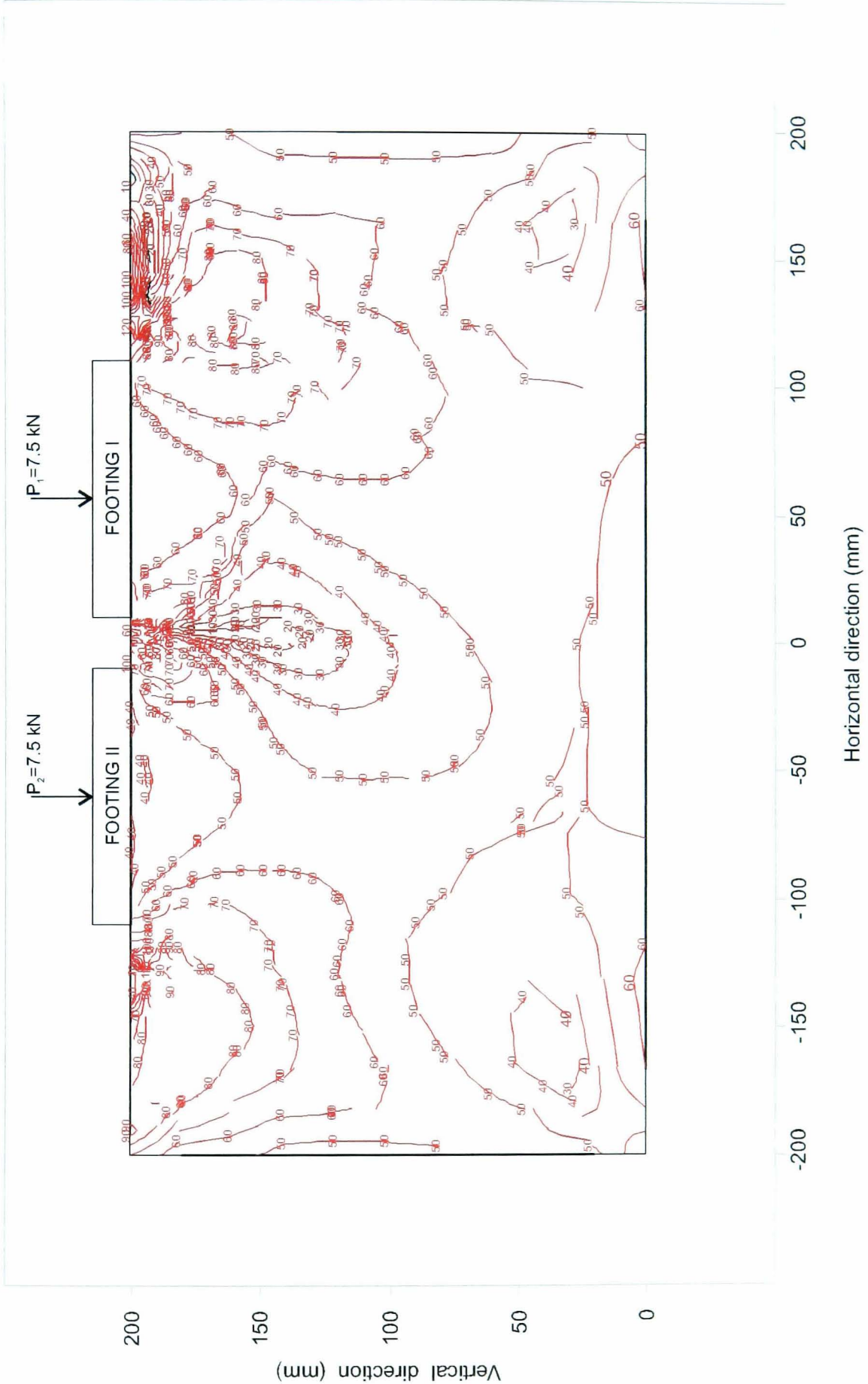
**Figure 6.23:** Proportion of strength mobilised due to loading on Footing I and Footing II

**6.2.3.2.2   Effect of Sheet Wall**   The effects of a 100-mm long aluminium sheet wall placed between the two footings, on the settlement of Footing I due to Footing II pressures were analysed. Two types of analysis were carried out with different fixity conditions for the sheet wall. In the first analysis, the sheet wall was placed between the footings without any restraint (floating wall). During the second analysis, the wall was vertically restrained (fixed wall). This simulated the FX tests in which an aluminium sheet wall of the same length was supported with two small rods reaching to the base of the consolidation chamber.

The overall vertical soil displacement vectors and contours obtained from the analyses on the footings with a floating sheet wall are successively shown in Figure 6.24 and Figure 6.25. There was no significant discrepancy in the overall displacements resulting from the analyses on the footings without a sheet wall and those with a floating wall. The settlement of Footing II was only 33% of that of Footing I loaded as a single footing. The settlement ratio $\rho_{F1}/\rho_{F2}$ was 30%, slightly less than that resulting from the footings without a sheet pile wall (Section 6.2.3.2.1). Footing I tilted (counter clockwise) towards Footing II, with $\delta/l \approx 1/588$, while Footing II tilted away from Footing I with $\delta/l \approx 1/105$.

During incremental loading on Footing II, the wall was dragged down by the negative skin friction over the upper part of the wall. Figure 6.26 illustrates shear stress distribution in the interfacing soil elements on the right and the left of the wall during 15 increments of loading on Footing II. The progressive shear stress development is described based on the sign conventions in the inset. At low pressures, only very small areas the upper part of the sheet wall were sheared down by the soil on the left side. Simultaneously, the right side of the sheet wall was pushed down by the surrounding soil induced by the pressure of Footing I of 80 kPa. While the stresses along the sheet wall were dominated by the pressure of Footing I, the sheet wall was moved towards Footing II with a larger displacement at its lower part (see Figure 6.27). Gradually, as the loading on Footing II was increased, the dragging-down shear stresses on the right side of the wall decreased and on the left side they increased. Towards the end of loading the whole wall was still displacing towards Footing II but at this time larger horizontal displacement took place at the upper part of the wall.

In general, the resultants of the shear stresses on both sides of the wall, as visualised in Figure 6.28, indicated that the upper part of the wall was always pushed down. The same behaviour was encountered during the physical modelling with a floating sheet wall (SP Tests). The ratios of
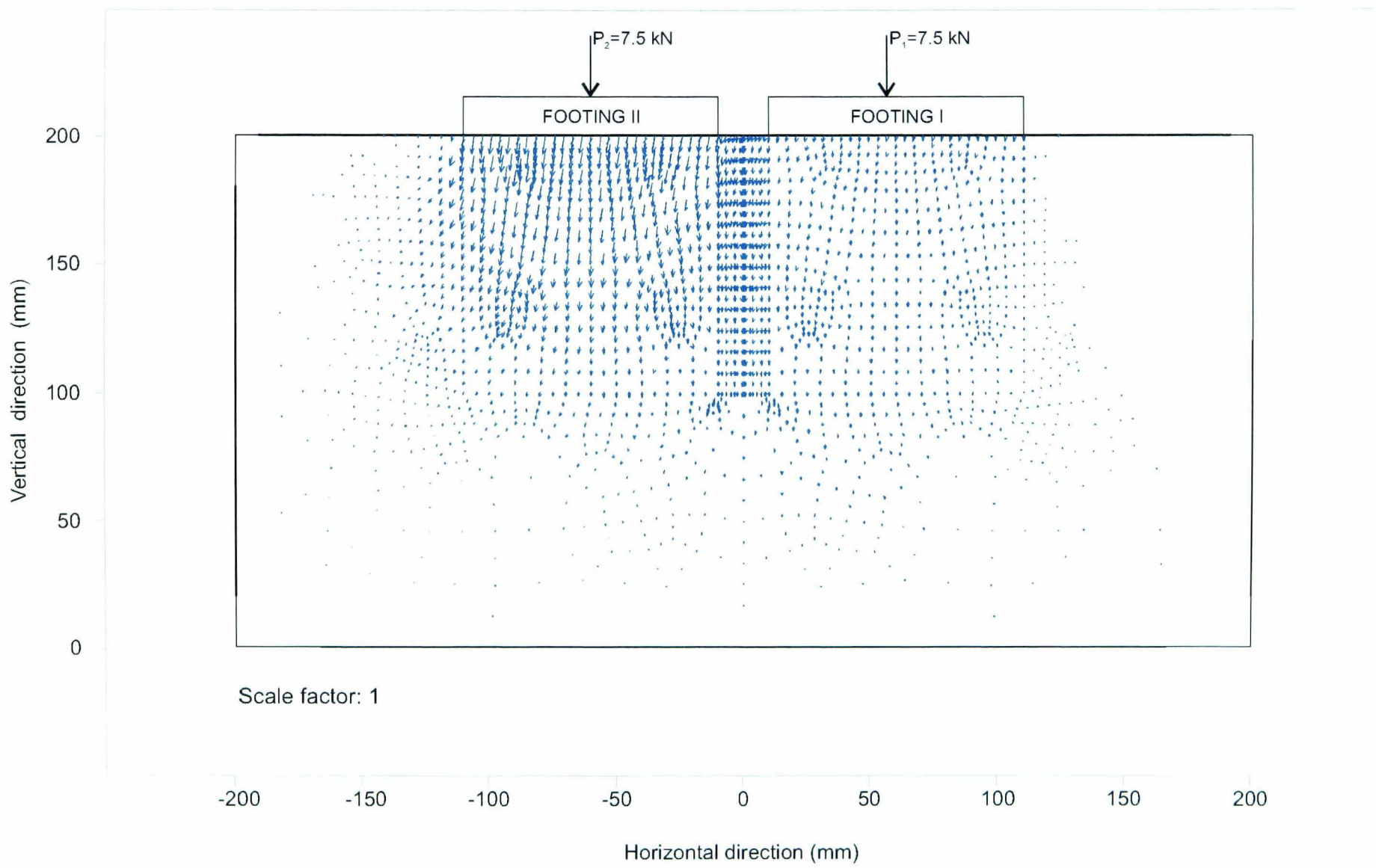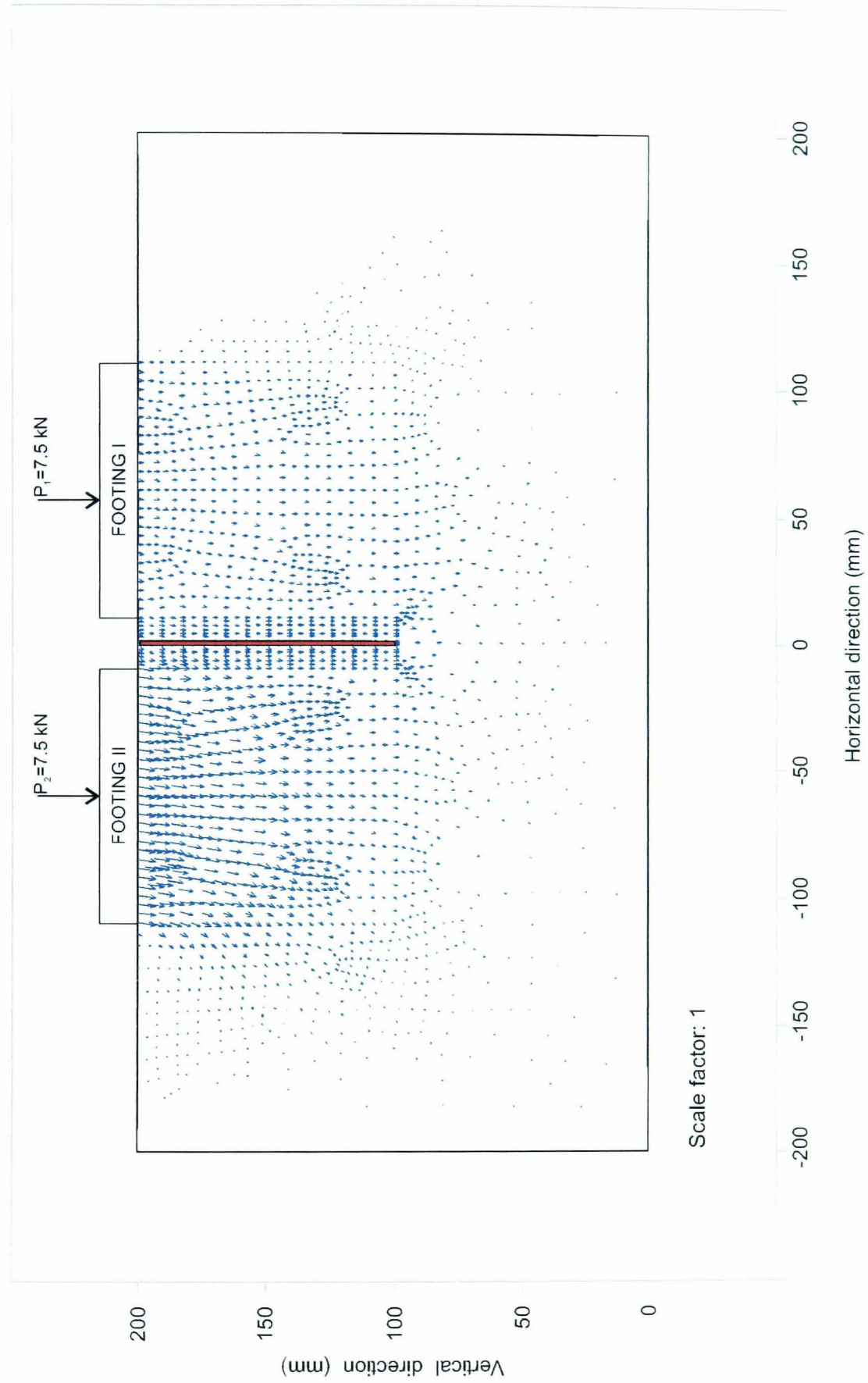
**Figure 6.24:** Displacement vectors of due to loading on Footing II with a floating sheet wall
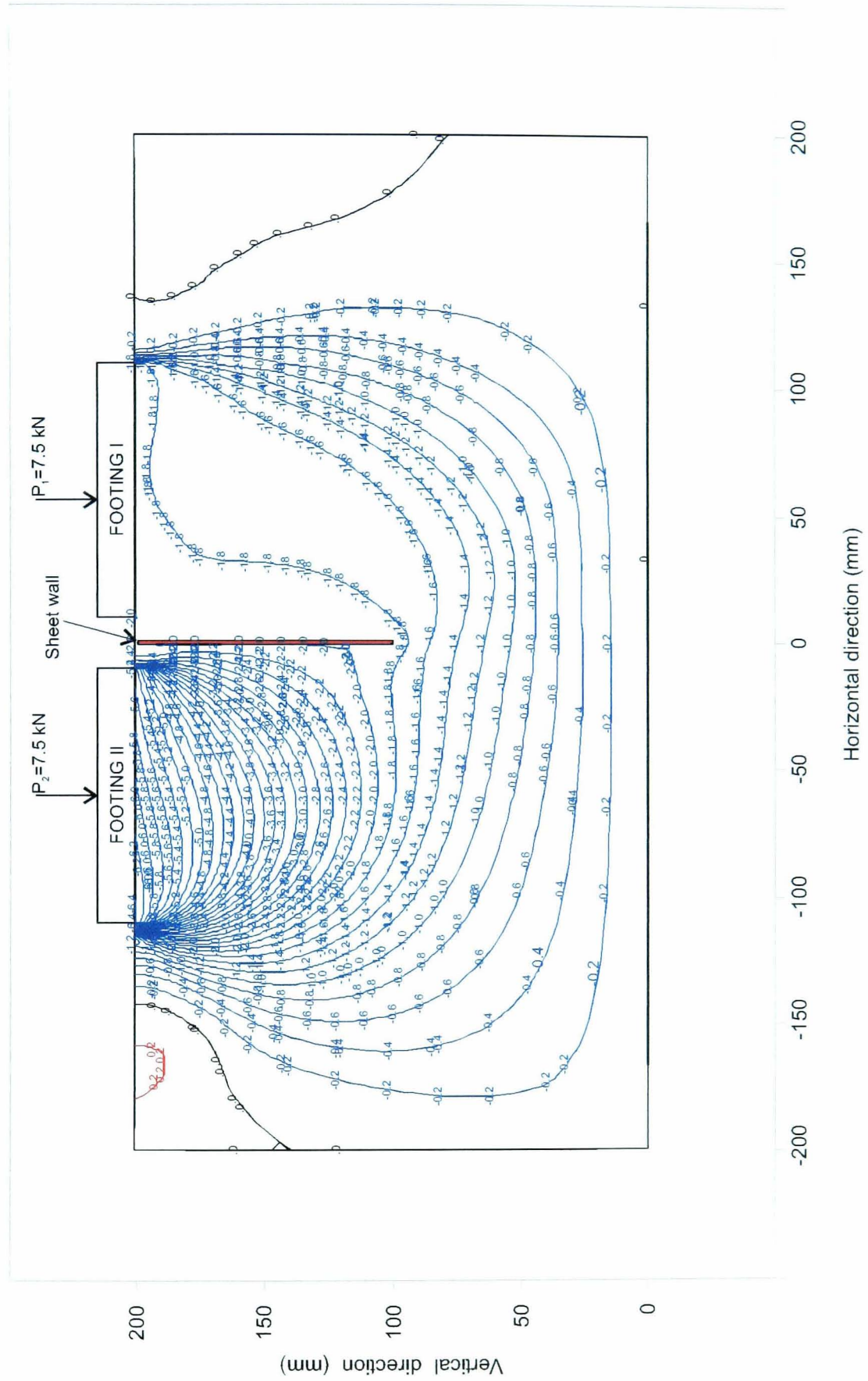
**Figure 6.25:** Vertical displacement contours of due to loading on Footing II with a floating sheet wall
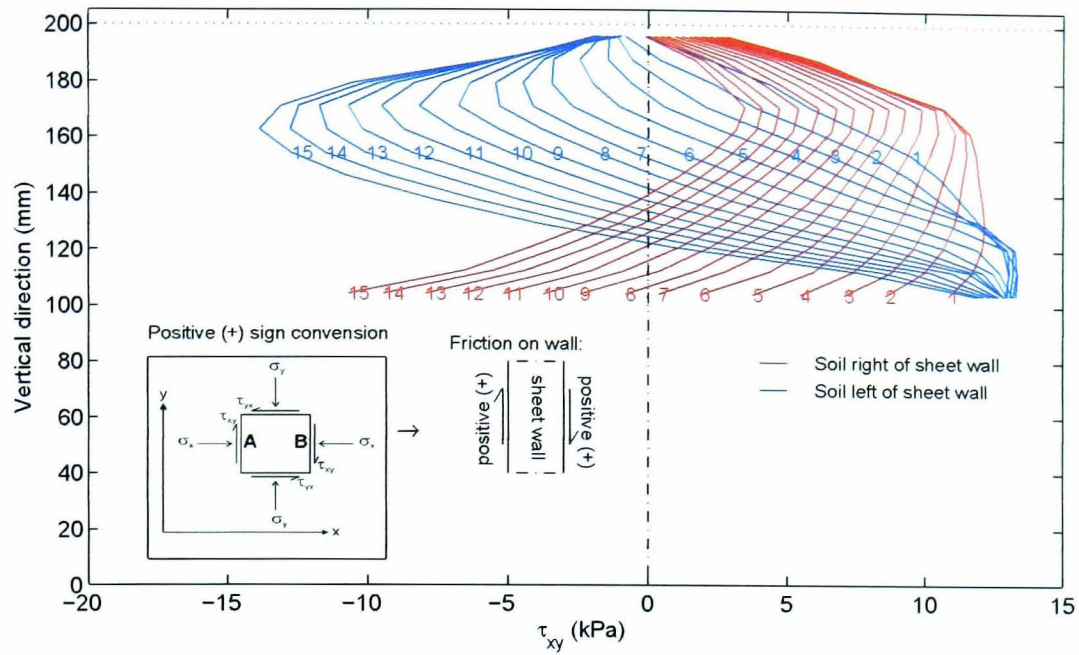
**Figure 6.26:** Progressive shear stresses around floating sheet wall due to loading increments on Footing II
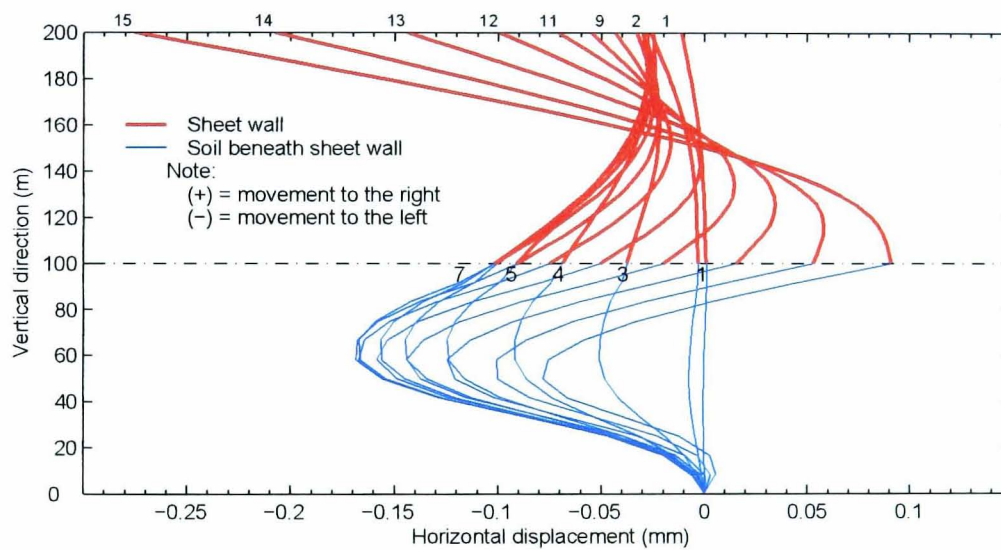


**Figure 6.27:** Progressive horizontal displacements along the centre of sheet wall and the underlying soil due to loading increments

the resultant shear forces on the lower part to those on the upper part during normalised pressure increments are depicted in Figure 6.29. They were increasing as the pressure of Footing II was increased up to 35% of its maximum design pressure of 80 kPa. The ratios remained constant at about 0.35 until the pressure of Footing II was equal to that of Footing I. This suggests that the upper part of the sheet wall was settling together with the soil while the lower part of the wall penetrated into the soil beneath its initial tip level. This phenomenon was similar to that observed in the
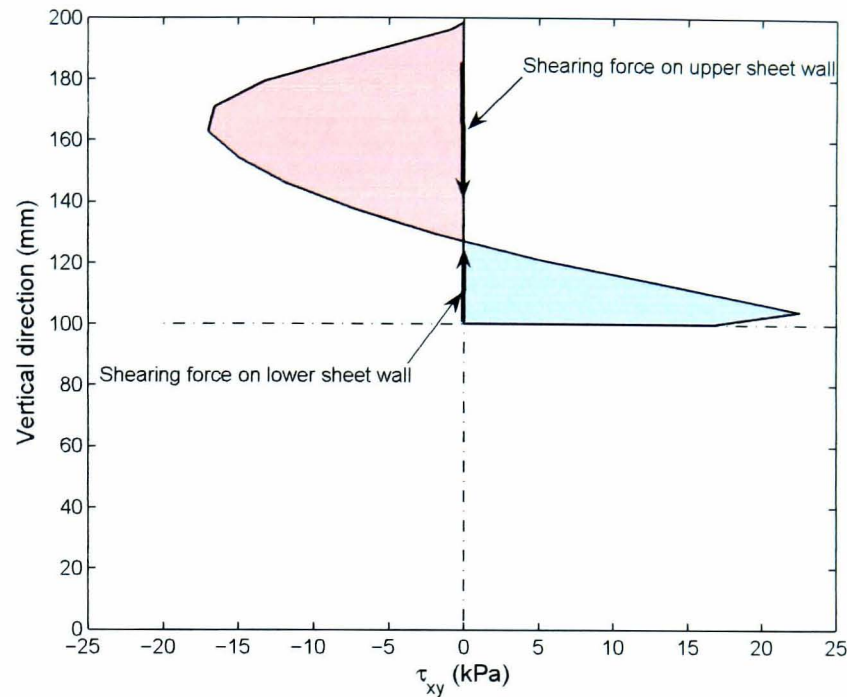
**Figure 6.28:** Total shear stress around floating sheet wall at the end of loading on Footing II

physical modelling. This behaviour is reflected through Figure 6.30 showing contours of strength mobilised due to the loading on both footings. In the soil near the upper part of the sheet wall, the strength mobilisation is higher than that near the lower part. This indicates that the shearing against the wall was also higher.

By comparison with those from analyses on the footings with the floating wall, distinctive displacement characteristics were obtained from the analyses on the footings with a fixed sheet wall, Figure 6.31. The vectors beneath Footing II were remarkably larger than these beneath Footing I. The displacement contours are depicted in Figure 6.32. The contours show a very small settlement of only 0.3 mm ($\rho_{F1}/\rho_{F2} = 4\%$) experienced by Footing I as a result of cumulative incremental loading on Footing II. With the floating wall, the soil beneath Footing I was very much affected since it was still dragged down by the settling wall. This was not the case for the footings with the fixed wall. Footing II settled 32% of the single footing (Footing I), slightly less than those with a floating sheet wall, and tilted with $\delta/l \approx 1/141$ away from Footing I. Footing I was almost unaffected. It only tilted with very insignificant $\delta/l$ of 1/3448 towards Footing II. The small settlement and tilting of Footing I was induced by horizontal movements of the wall. Figure 6.33 illustrates the movement of the finite element nodes along the centre of the wall. During the pressure increments of up to 50% of the final pressure (80 kPa), the wall was moved towards Footing II. At
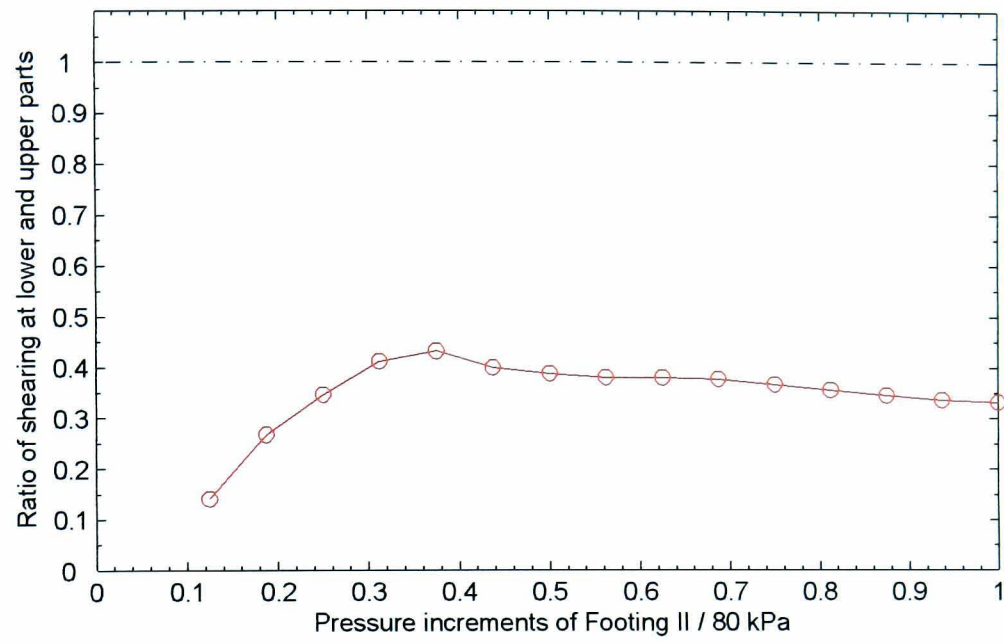
**Figure 6.29:** Development of shearing along a sheet wall during pressure increments of Footing II
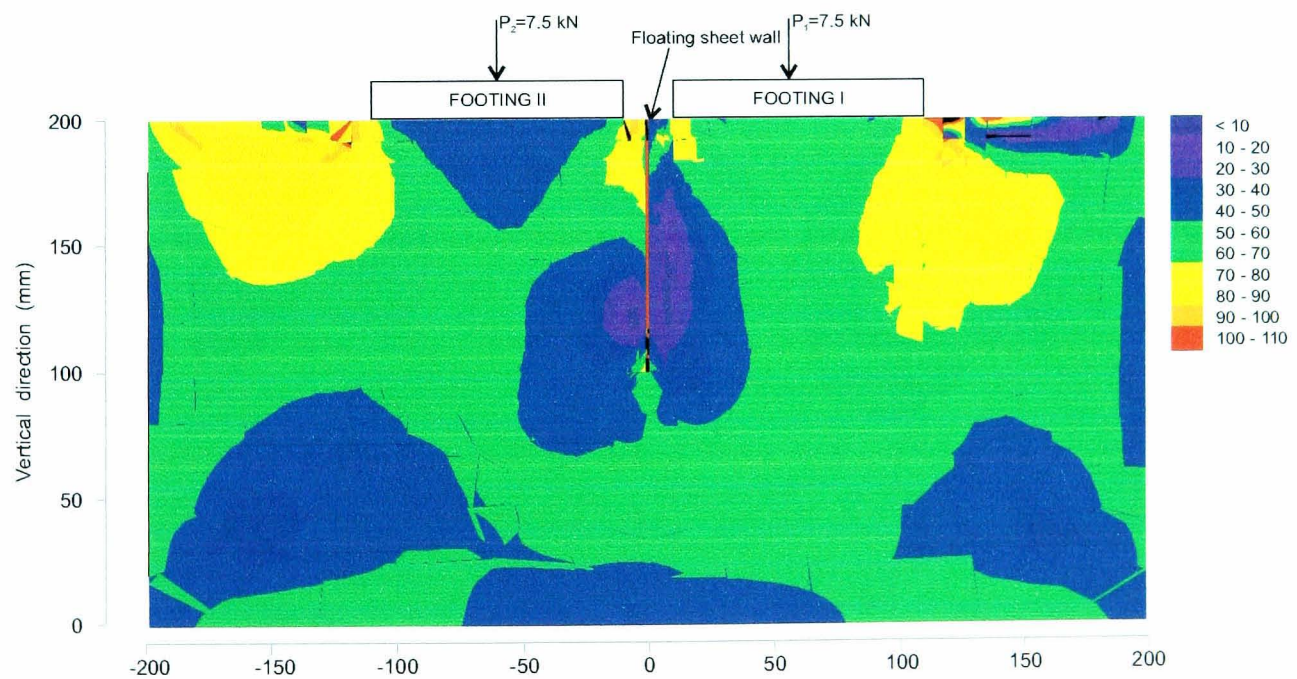


**Figure 6.30:** Strength mobilised due to loading on Footing I and Footing II with a floating sheet wall
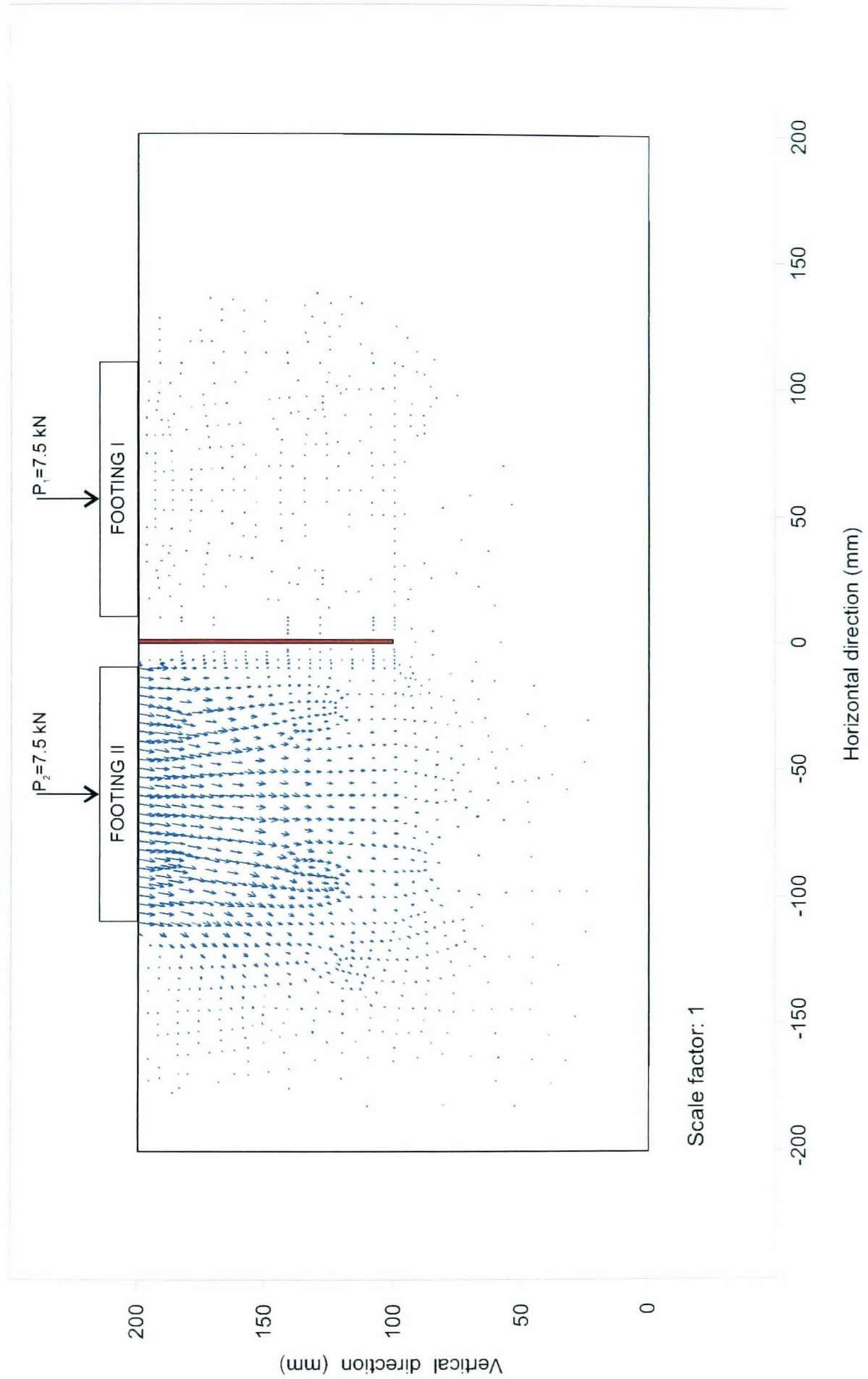
**Figure 6.31:** Displacement vectors of due to loading on Footing II with a fixed sheet wall
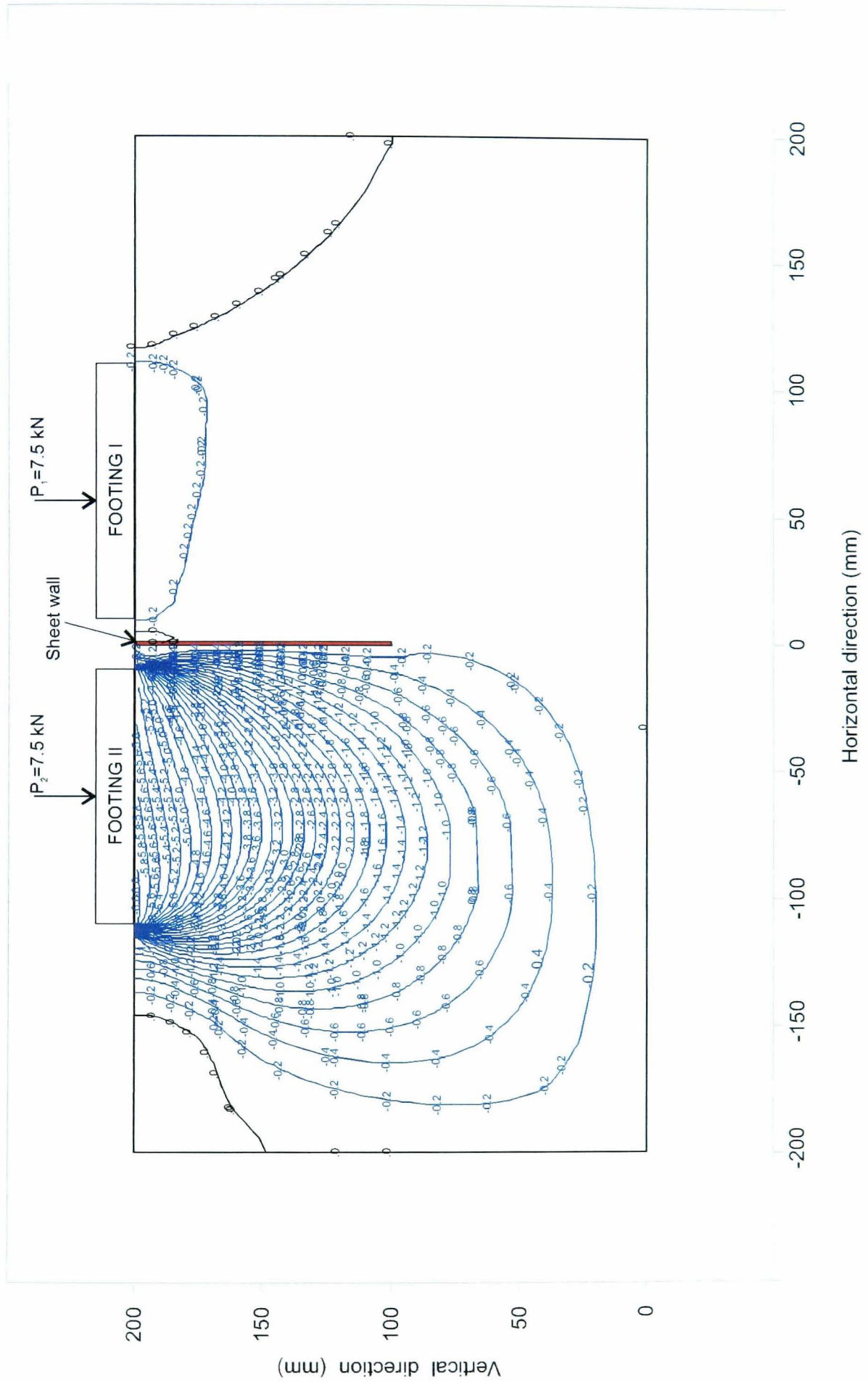
**Figure 6.32:** Vertical displacement contours of due to loading on Footing II with a fixed sheet wall
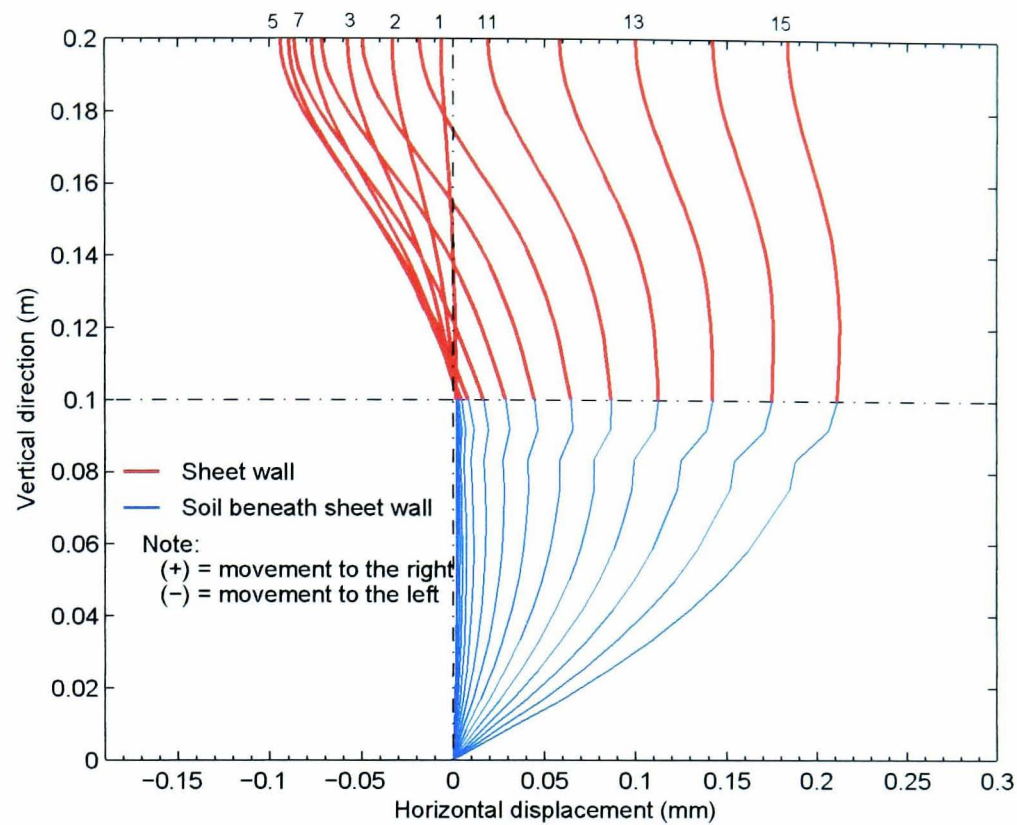
**Figure 6.33:** Horizontal displacement along the centre of sheet wall (vertically restrained) and the underlying soil

the same time, as indicated in Figure 6.34, the shear stresses in the soil on the left side gradually pushed down the sheet wall while the shear stresses in the soil on the right side remained constant. At higher pressures, the wall gradually tilted towards Footing I. The strengths eventually mobilised around the sheet pile wall are illustrated in Figure 6.35. It is evident that the soil strength around the sheet pile wall was highly mobilised. The direction of the soil displacement under the tip of the wall indicates that pressures of Footing II were still distributed to the lower layer of the soil on the right of the wall. This can be examined through the volumetric strain of the soil shown in Figure 6.36. Unlike beneath Footing II, the magnitude of the strain in the lower layer of the soil beneath Footing I was larger than that in the upper layer.
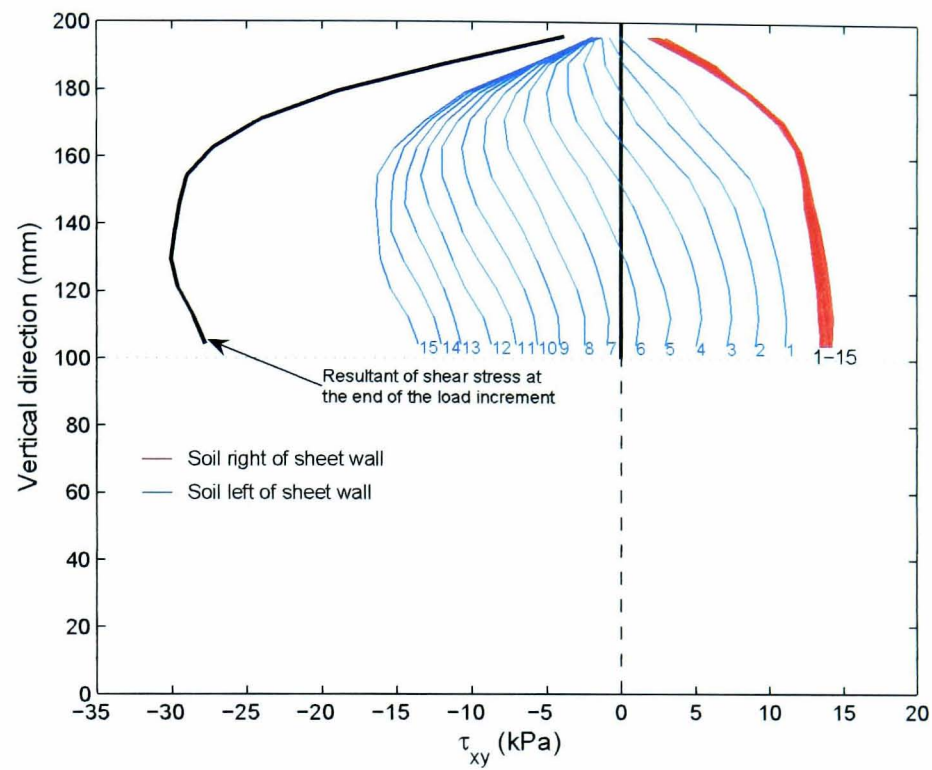
**Figure 6.34:** Progressive shear stresses around fixed sheet wall due to loading increments on Footing II
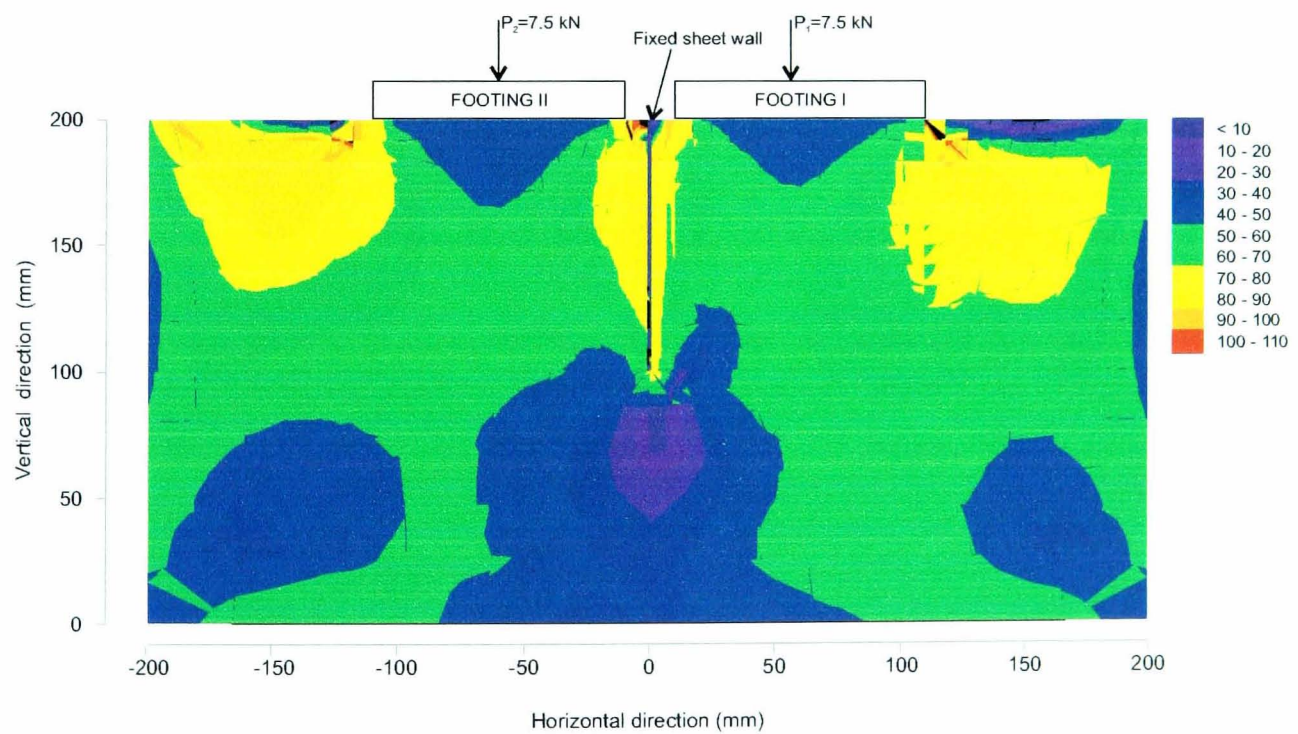


**Figure 6.35:** Strength mobilised due to loading on Footing I and Footing II with a fixed sheet wall
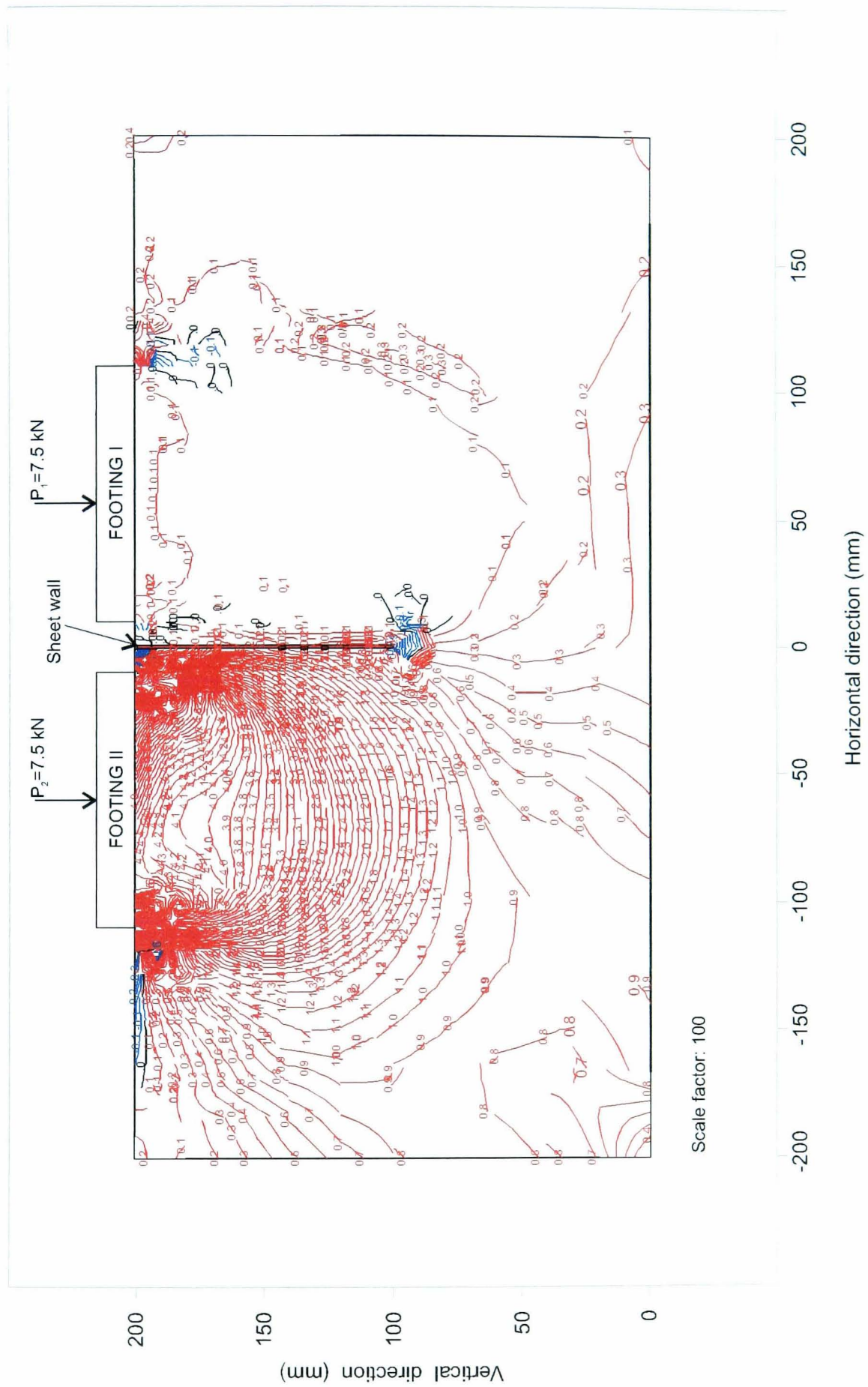
**Figure 6.36:** Volumetric strain contours due to loading on Footing II with a fixed sheet wall

## 6.3 SIMULATION OF PROTOTYPE

In the previous sections, it was shown that the finite element analyses simulated the displacement behaviour resulting from the physical modelling reasonably well. However, it was realised that in the single gravity ($1g$) modelling the stress and strength profiles with depth were not perfectly representative of field conditions. Therefore, further numerical analyses of a typical prototype were undertaken in which ground conditions were more accurately modelled. Typical buildings with 10 m wide raft foundations on Singapore Marine Clay were simulated.

### 6.3.1 Geometry, Boundary Conditions, and Material Properties

Figure 6.37 shows the mesh for the geometry of the prototype ground and two neighbouring buildings (represented by Footing I and Footing II) with a clearance of only 2 metres. The ground depth
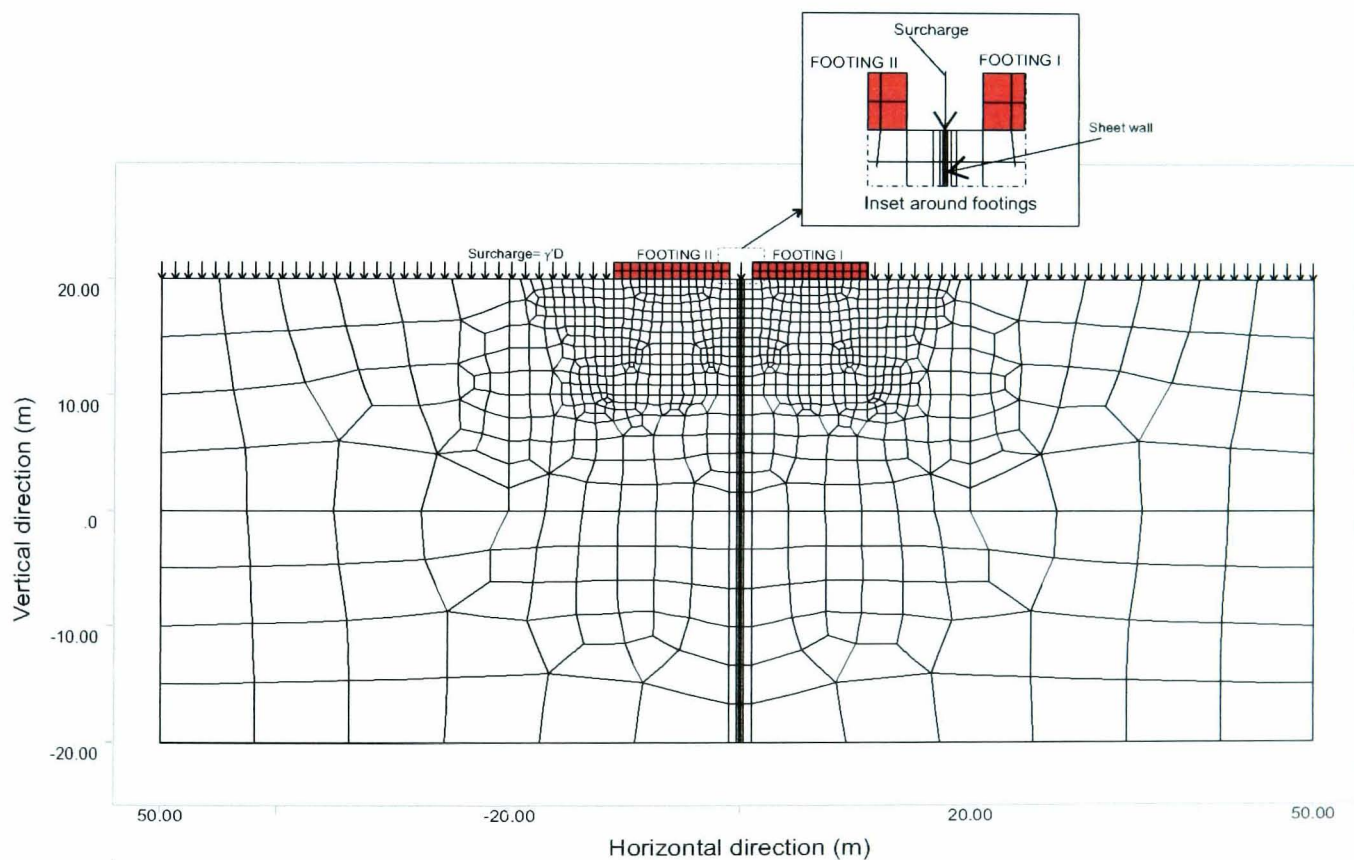


**Figure 6.37:** Geometry and mesh for simulation of prototype

of 40 m was adopted from the general profile of Singapore Marine Clay shown in Figure 6.38 (Cao et al., 2001). The ground was assumed as only one layer of clay, excluding the silty clay and the sand seam layers. A horizontal distance of 100 m was used to avoid the effect of lateral boundary
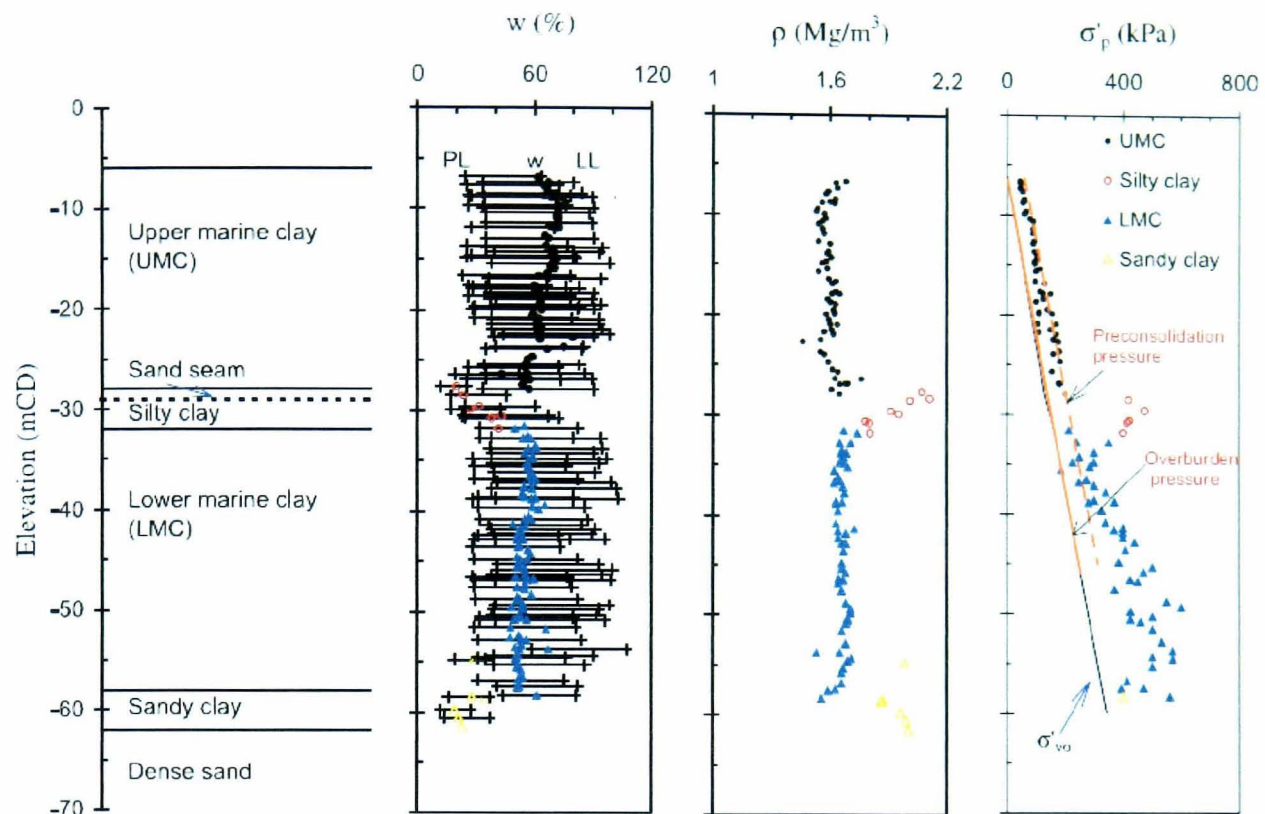
**Figure 6.38:** General soil profile of Singapore Clay (Cao et al., 2001)

confinement. Except for the ground surface, all sides of the soil mass were not allowed to move vertically or horizontally. However, the fixity applied to both right and left sides did not have any effect on the displacement around the footings. This is discussed in Section 6.3.3.1. When the sheet pile wall was assumed to be fixed, only its tip was restrained vertically, while its top was left unrestrained. This was intended to simulate a sheet pile wall supported with intermittent longer piles driven to the depth at which these piles could resist the settlement of the entire sheet pile wall.

Based on Figure 6.38, a soil unit weight of 16 kN/m$^3$ was used in the analyses, producing similar overburden stresses to those shown. These also fell into the range of data published by Hanzawa and Adachi (1983), see Figure 6.39. The undrained strength profile was similar to that used by Simpson (1992) who obtained a suitable preconsolidation pressure. He found that a pressure of 72 kPa was an appropriate maximum past pressure to create a ground with the measured undrained strengths. The OCR profile derived from the preconsolidation pressure and the overburden stresses is illustrated together with that found by Hanzawa and Adachi (1983) in Figure 6.39. The predicted OCRs are consistent with the finding of Tan et al. (2002) that the OCR of Singapore
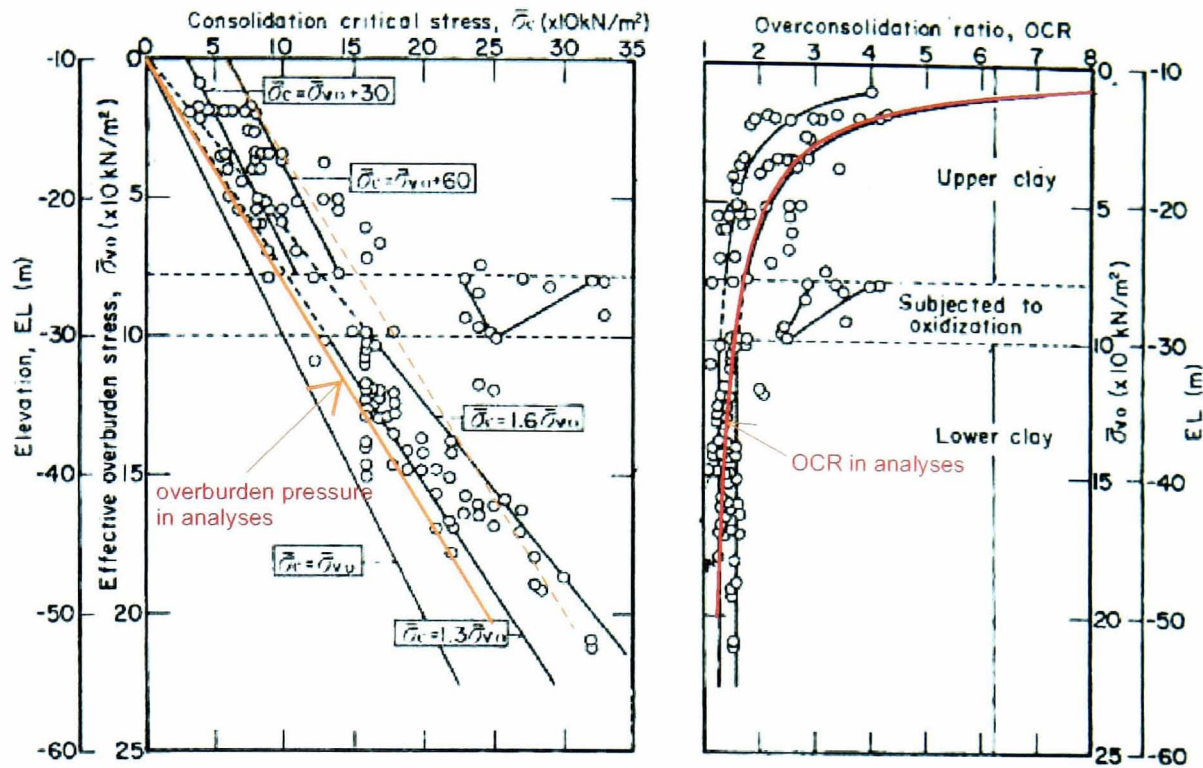
**Figure 6.39:** General soil profile of Singapore Clay (Hanzawa and Adachi, 1983)

Lower Marine Clay ranges between 1.30–1.45. Furthermore, they agree with the statements of Cao et al. (2001) that the top of the Upper Marine Clay has an OCR of 2 to 10 increasing towards the surface, while the OCR of the Lower Marine Clay varies between 1 and 2.

The BRICK parameters input in the analyses were identical to those used by Simpson (1992) for the same clay. The strings used in the previous analyses (see Table 6.2 were therefore applied. The coefficients of $\lambda^*$ and $\kappa^*$ were 0.1 and 0.04 respectively while the values of $\iota$ and $\nu$ were 0.0032 and 0.2. According to BRICK software, the implied critical $\phi'$ for plane strain was $26°$ and $\phi' = 24°$ for triaxial compression. The latter value was in a good agreement with the findings of Tan et al. (2002) that $\phi'$ from triaxial compression tests for the Lower Marine Clay ranged from $22°$ to $25°$. The resulting consolidation behaviour of the BRICK soil was compared to that obtained by Tan et al. (2002) from a triaxial test for remoulded and undisturbed Singapore clay. As shown in Figure 6.40, there is a slight discrepancy in compression behaviour between that predicted by BRICK and the result from the undisturbed soil sample at low stresses. However, when the destructuring of the soil is regarded (see the compression line from the remoulded sample), the prediction matches very well those results, especially at higher stresses.
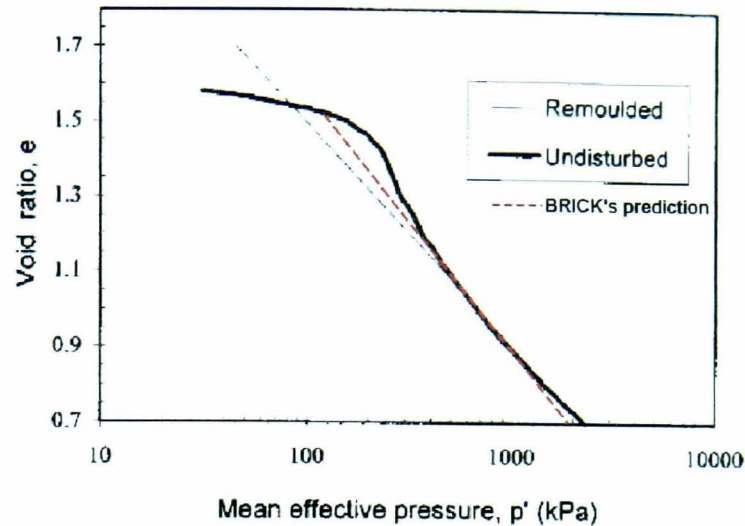
**Figure 6.40:** Compression behaviour of BRICK soil and that observed by Tan et al. (2002)

The footings were assumed semi-rigid as used in the physical modelling. By applying the same elastic modulus of Perspex of $3 \times 10^6$ kPa, the stiffness of the footing was equivalent to that of a footing made of concrete ($E = 2 \times 10^7$ kPa) with a thickness of 800 mm (see Section 3.2.1.1.5).

The selection of the sheet pile type, as mentioned in Section 3.2.1.1.6, was based on a practical consideration. The sheet pile section GSP2 was therefore used in this prototype simulation, with its maximum recommended driving length (British Steel, 1997) of 20 m. Although it was used when studying the effect of some longer sheet pile walls, it was considered unlikely that piles longer than 20 m would provide economic mitigation. For such piles, the issue of driving resistance was not considered. To simulate the bending stiffness of the GSP2 sheet pile with a mesh element thickness of 10 cm, an elastic modulus $E = 2.2 \times 10^8$ kPa was used.

### 6.3.2 Main Procedures of Analysis

As in the model simulations (see Section 6.2.2), the prototype simulations consisted of four stages (Stages 1, 2, 3, and 4) in two parts (Figure 6.41). Additional alternative studies in Stage 4B and Stage 4C were conducted to examine the effects of sheet pile length and stiffness on displacements. The stages in the second part could be independently run, following the three sequential stages in the first part.
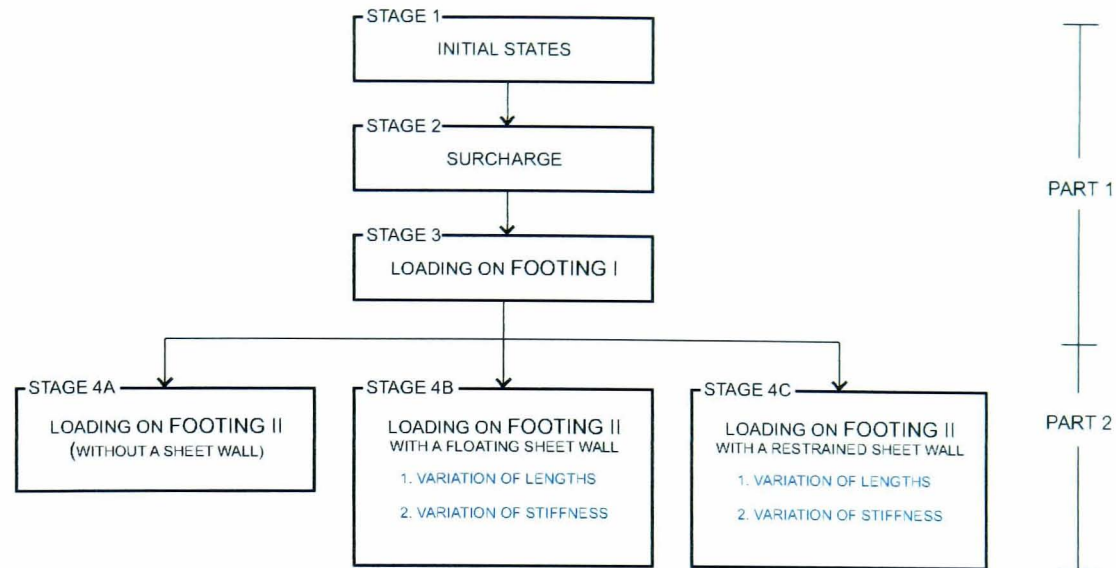
**Figure 6.41:** Stages of finite element analyses implemented in this research

In Stage 1, the ground was initially conditioned to experience a maximum past pressure of 72 kPa by inputting this pressure as one of the BRICK model stress history parameters to suit the ground strength.

In Stage 2, a surcharge of 12.4 kPa was applied along the surface of the ground. This surcharge represented the weight of the ground above the embedment level of the raft foundations. The foundations were assumed to be embedded 2 metres below the ground level, coinciding with the ground water level.

In Stage 3, Footing I, representing the whole raft foundation of the first building, was incrementally loaded at its centre with 2000 kN equivalent to a footing pressure of 200 kPa. The loading was gradually applied in 20 increments.

Stage 4 consisted of three independent studies. The first study analysed the effect of the pressure of Footing II on the ground displacement while maintaining the pressure of Footing I. At this time, no sheet pile wall was present. The same loading magnitude of 2000 kN in 20 increments was also applied at the centre of Footing II. This loading procedure was also performed in the second and the third studies, except that different lengths of floating and fixed sheet pile wall were placed between the neighbouring footings before loading applied to Footing II. In both studies, the effects of variation of sheet pile stiffness were also examined.

### 6.3.3 Results

#### 6.3.3.1 Single Footing

The directions of ground displacements at every node of the mesh, due to the loading of 2000 kN on Footing I, are shown in Figure 6.42. As confirmed by the contours of vertical and horizontal displacements shown in Figure 6.43 and Figure 6.44, it is evident that the displacements were perfectly symmetrical about the centre of Footing I. The displacements faded away before reaching the boundaries of the ground. The horizontal dimension of the mesh was therefore considered adequate for eliminating the lateral boundary effects. This issue was further examined by re-analysing the problem after replacing the fixed restraints by rollers, i.e. both side boundaries were free to move vertically. In another check, Footing II was loaded with the same load magnitude as if this was a mirror of the loading on Footing I. The patterns and the magnitudes of the vertical displacements were identical in the three cases. The vertical displacement profiles beneath the centre of the footing, from the three analyses, are compared in Figure 6.45. The total settlement occurring at the centre of the footing was 1743 mm or 17% of the footing width.
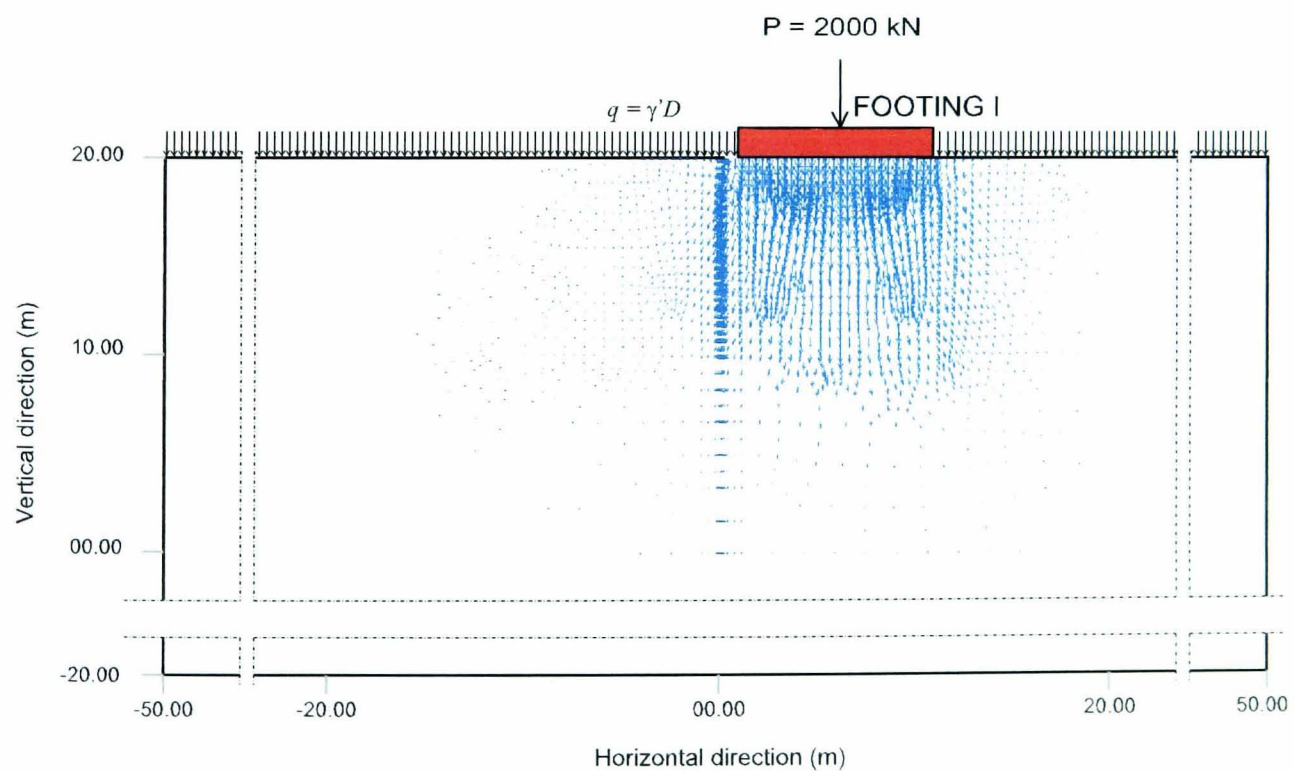


**Figure 6.42:** Vectors of soil displacement due to loading on Footing I
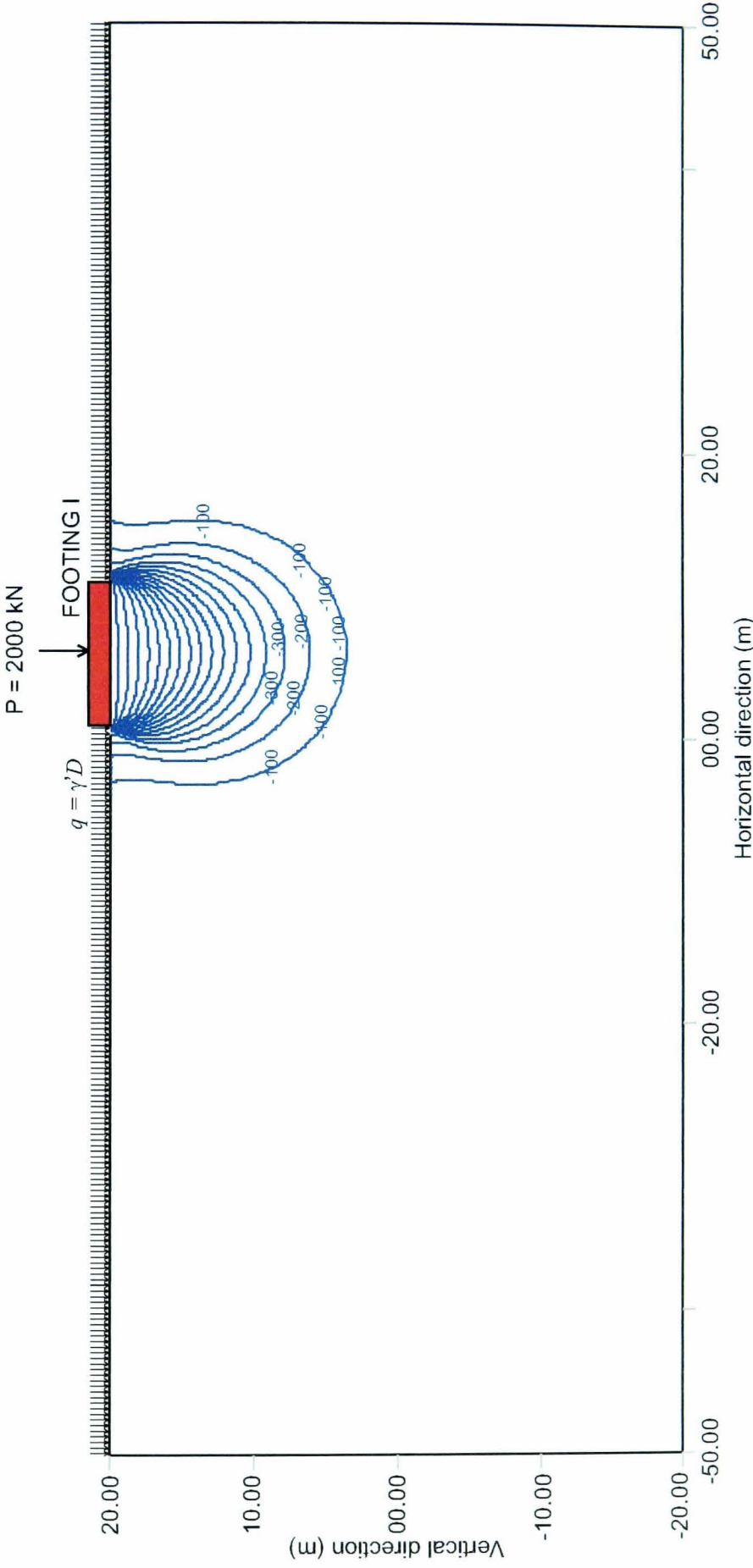
**Figure 6.43:** Contours of vertical displacement due to loading on Footing I
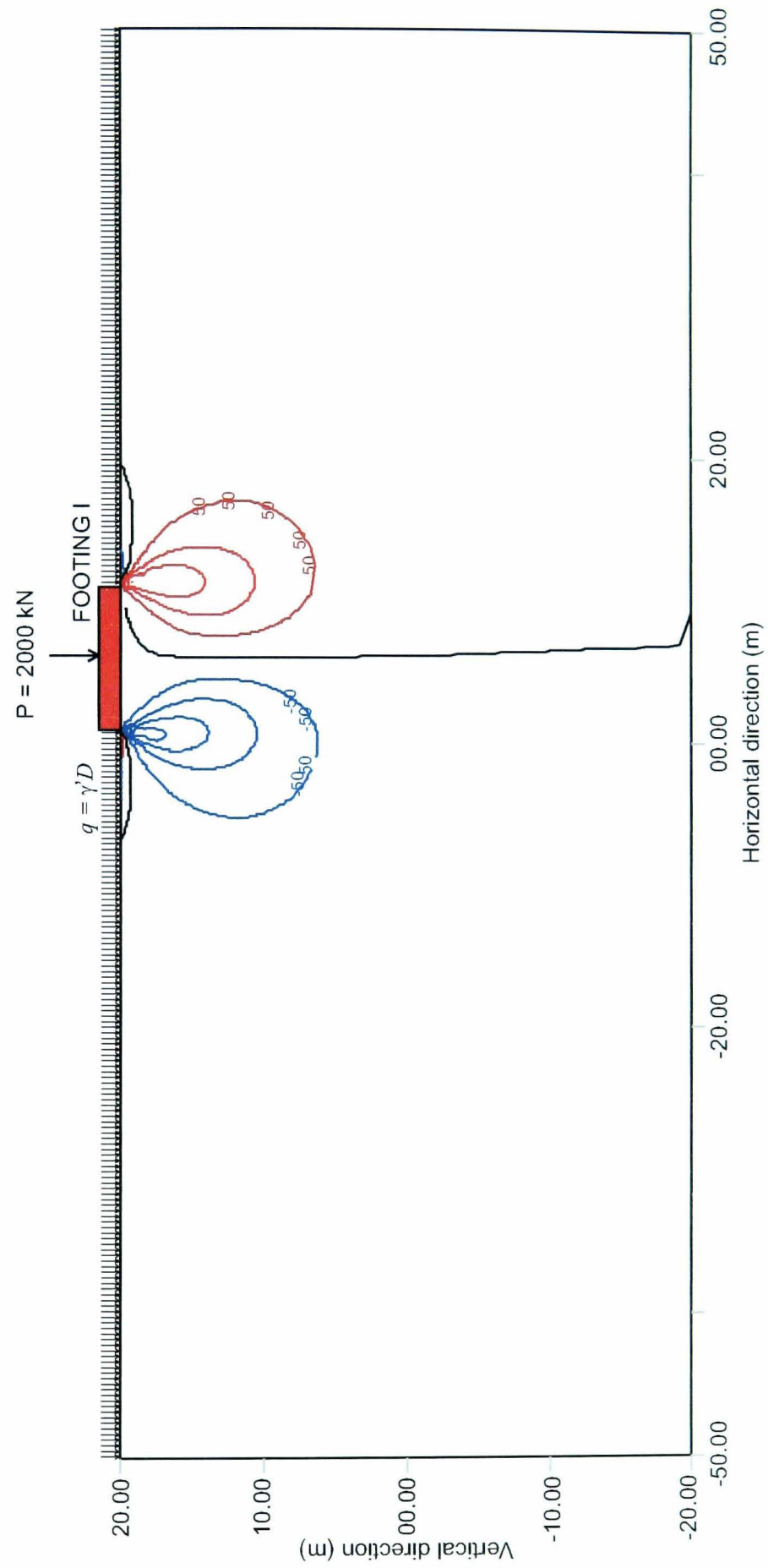
**Figure 6.44:** Contours of horizontal displacement due to loading on Footing I
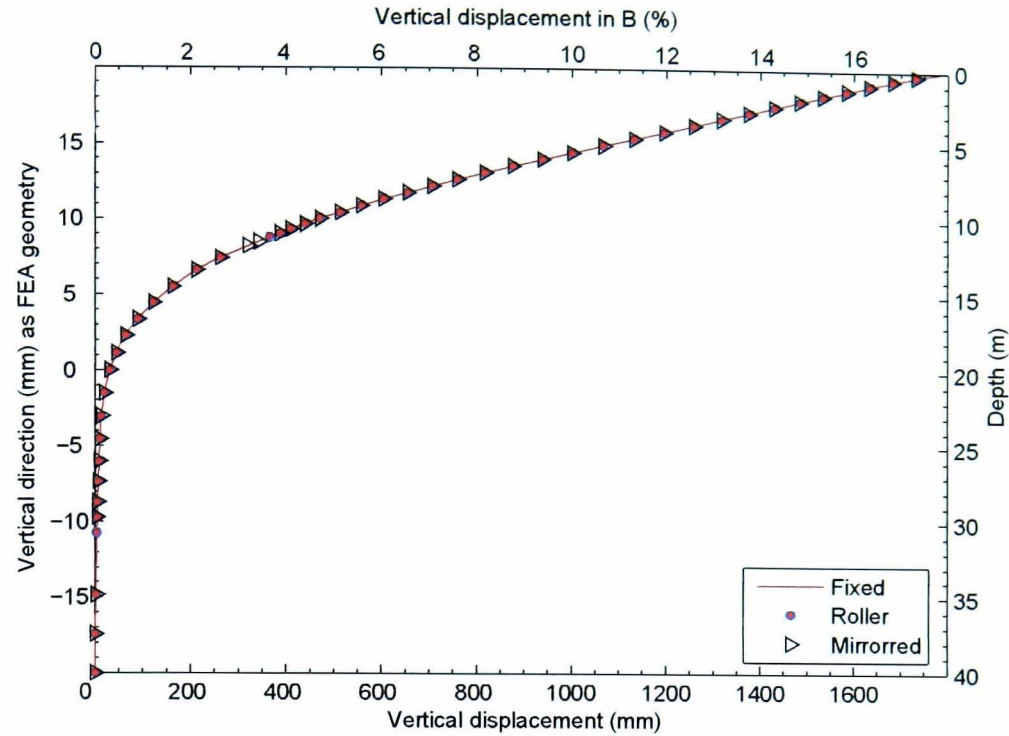
**Figure 6.45:** Vertical displacement profiles beneath the centre of footing, from three different conditions

### 6.3.3.2 Neighbouring Footings

Figure 6.46 presents the directions and the magnitudes of cumulative soil movements with respect to the start of the loading on Footing II. Footing II was incrementally loaded up to 2000 kN while the same loading intensity was being applied on Footing I. The vectors indicate that the loading caused a settlement of Footing I and the underlying soil to move towards the zone below Footing II. The contours of the vertical displacement of the ground are shown in Figure 6.47. Asymmetrical settlements occurred for both footings. At the final pressure of Footing II, Footing I suffered from an additional settlement of 765 mm which was 7.7% of the footing width $B$. The footing tilted towards Footing II with $\delta/l = 1/71$. This is approximately twice the threshold value, $\delta/l = 1/150$, above which a load-bearing wall building could be damaged (Skempton and MacDonald, 1956).

Footing II settled 1550 mm ($0.16B$) or 10% less than Footing I when loaded as an isolated single footing. The footing tilted with $\delta/l \approx 1/35$ away from Footing I. The greater settlement at the left side of the footing resulted from lower resistance of the soil beneath this side. Prior to the initial increment of loading on Footing II, the soil beneath Footing I was being stressed. The stressed soil zone passively resisted the stresses distributed from the pressure of Footing II. The horizontal displacement profiles, at the nodes along the centre line of the ground, resulting from

incremental loading on Footing II are shown in Figure 6.48. The effect of stress interference is clearly seen when the horizontal displacement profiles obtained from an analysis on a single footing are compared in the figure. Here, the term *single footing* signifies that the incremental loading was applied on Footing II while no loading was engaged on Footing I. During the incremental loading
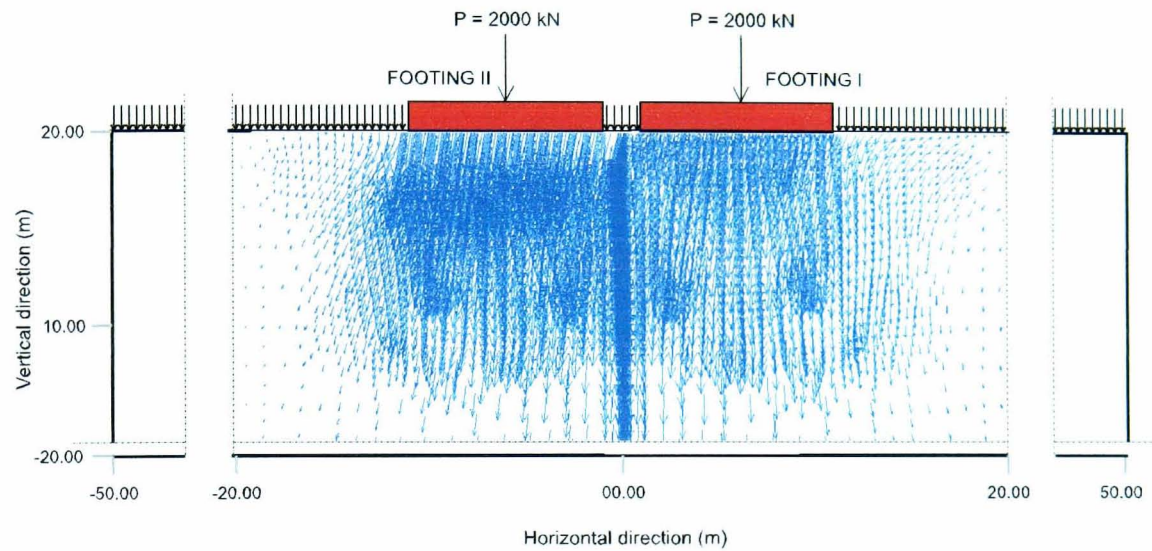
**Figure 6.46:** Displacement vectors due to loading on Footing II
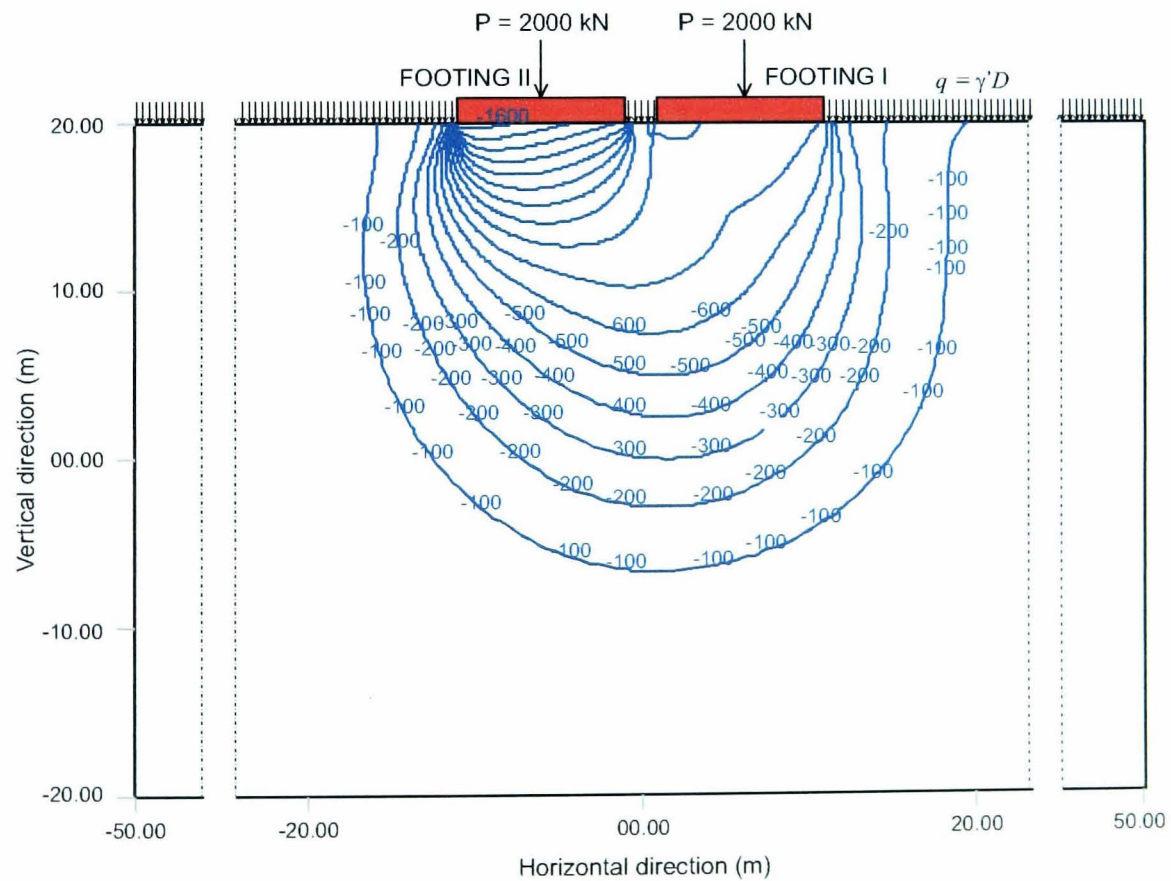
**Figure 6.47:** Contours of vertical displacement due to loading on Footing II

on the single footing, to a depth of about $3B$, the ground was displaced towards Footing I. In contrast, in the neighbouring footing analysis, the ground moved towards Footing II.
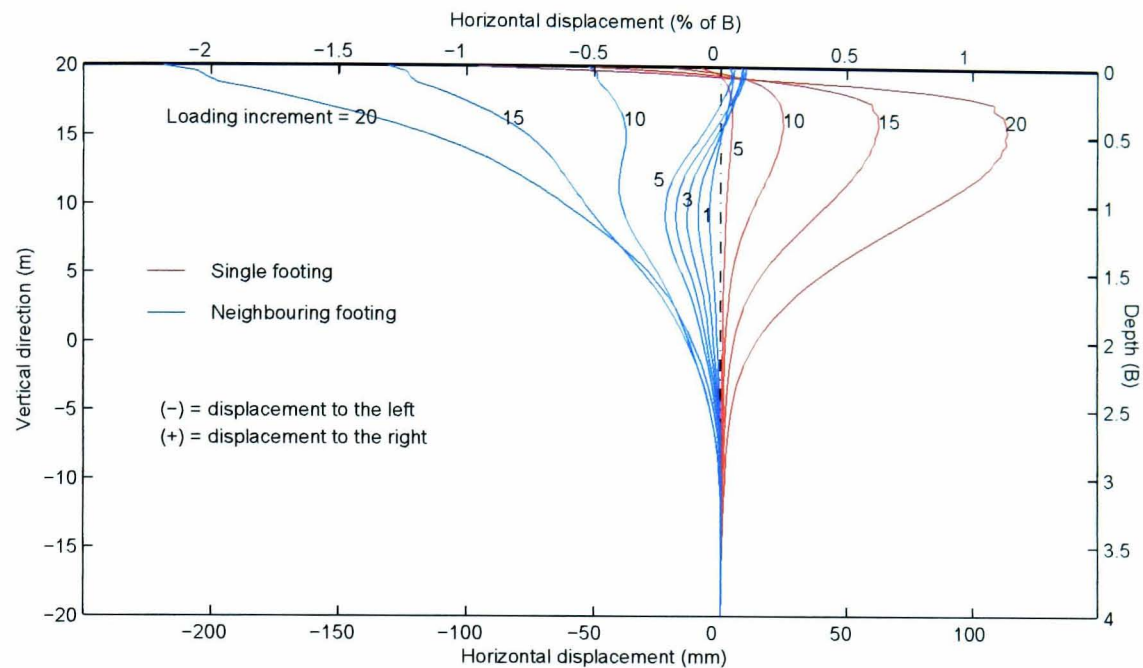


**Figure 6.48:** Horizontal displacement profile at the centre of the spacing between Footing I and Footing II

### 6.3.3.3  *Sheet Pile Wall between Neighbouring Footings*

The lengths used in the finite element analyses for the floating and the vertically restrained sheet pile wall are listed in Table 6.3. Typical contours of vertical displacement, selected from some of

**Table 6.3:** Variation of lengths used in finite element analyses

| Sheet pile | Length (m) | | | | | | | | |
|---|---|---|---|---|---|---|---|---|---|
| Floating | 10.00 | 15.00 | 16.70 | 18.30 | 20.00 | 26.70 | 30.00 | 37.50 | – |
| Vertically restrained | 10.00 | 15.00 | – | – | 20.00 | 26.70 | 30.00 | – | 40.00 |

the analyses, are presented in Figure 6.49 to Figure 6.51 for the footings with the floating sheet pile wall and in Figure 6.52 to Figure 6.54 for the footings with the fixed sheet pile wall. The vertical displacements at the centres of Footing I and Footing II due to loading on Footing II are summarised in Figure 6.55. Significant effects of the length variations of the floating sheet pile wall on the settlement of Footing I were evident after the lengths were extended beyond 10 m or 25% of

the ground thickness $H$. Longer lengths resulted in less settlement of Footing I. The correlation was almost linear with a mitigation rate of $0.0022B$/m with respect to the footing settlement without a sheet pile wall. A similar effect appeared for Footing II when the lengths were extended beyond the middle of the ground thickness. The mitigation rate in this case was $0.0011B$/m, half of that experienced by Footing I.

Different results were found when a fixed sheet pile wall with different lengths was used. With a sheet pile wall 10 m long ($0.25H$), Footing I and Footing II respectively settled by only $0.03B$ and $0.14B$, or 34% and 87% of their settlement when no sheet pile wall was placed. The settlements of Footing I and Footing II were reduced respectively to $0.01B$ and $0.13B$, or 13.5% and 81.3% of their settlement without a pile, after the sheet pile wall was extended to 15 m ($0.375H$). No further mitigation in the settlement was noticed for longer sheet pile walls, even those extending to the full ground thickness.
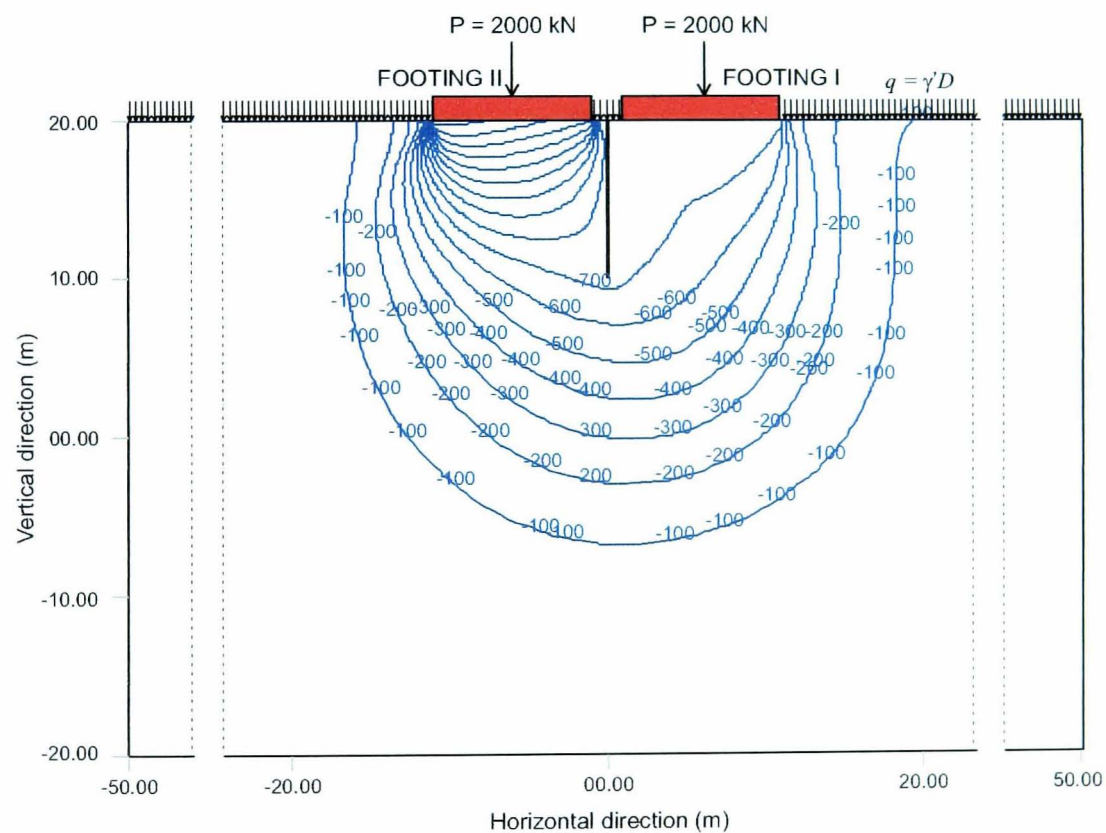


**Figure 6.49:** Contours of vertical displacement due to loading on Footing II with 10-m floating sheet pile wall
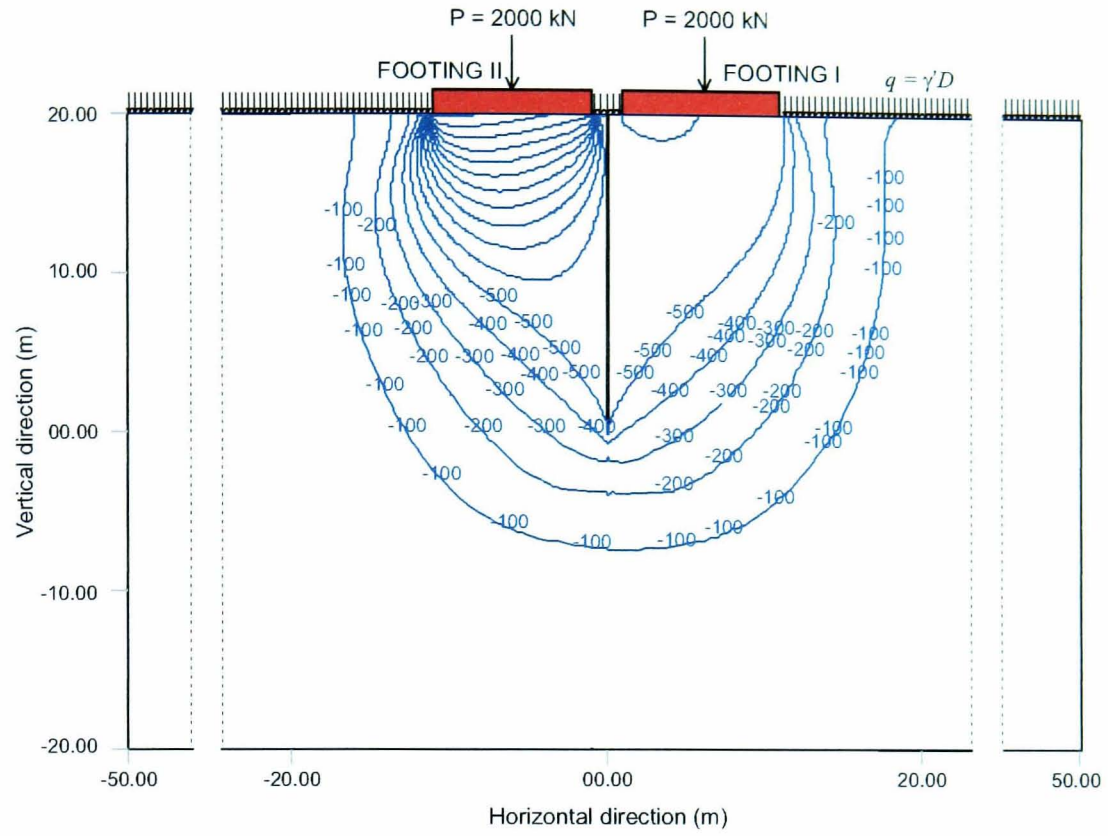
**Figure 6.50:** Contours of vertical displacement due to loading on Footing II with 20-m floating sheet pile wall
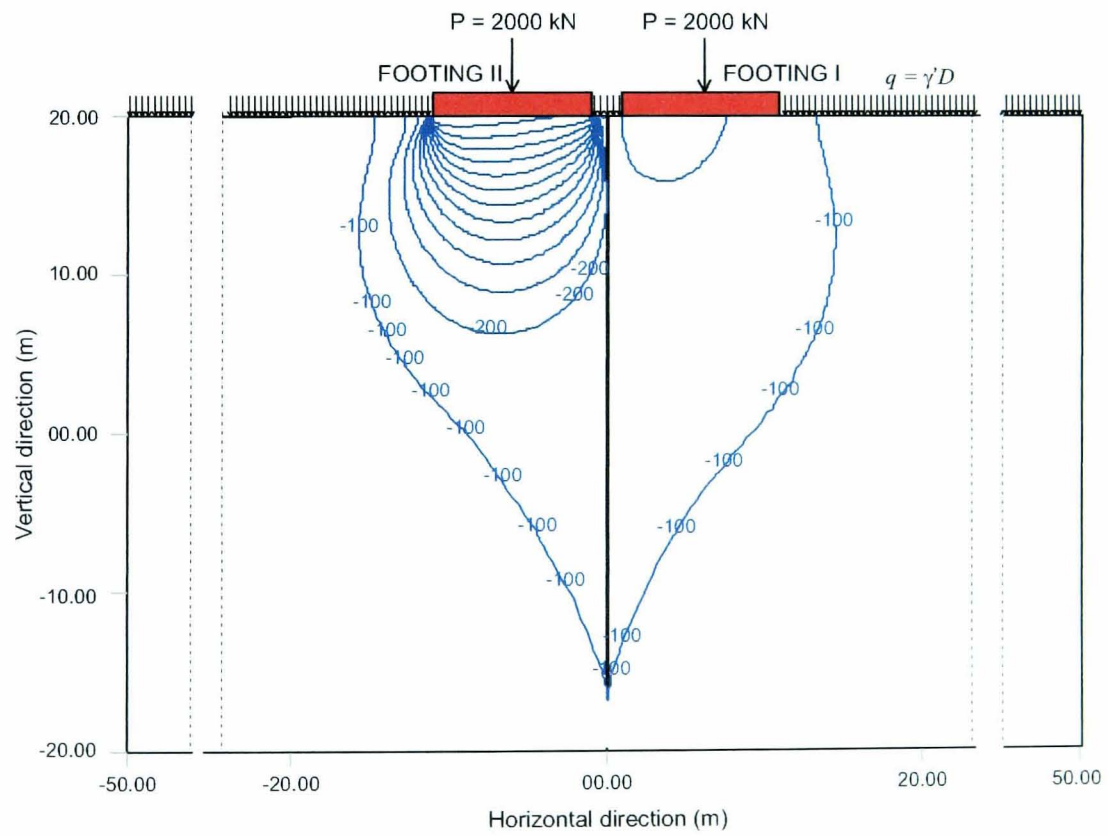


**Figure 6.51:** Contours of vertical displacement due to loading on Footing II with 37.5-m floating sheet pile wall
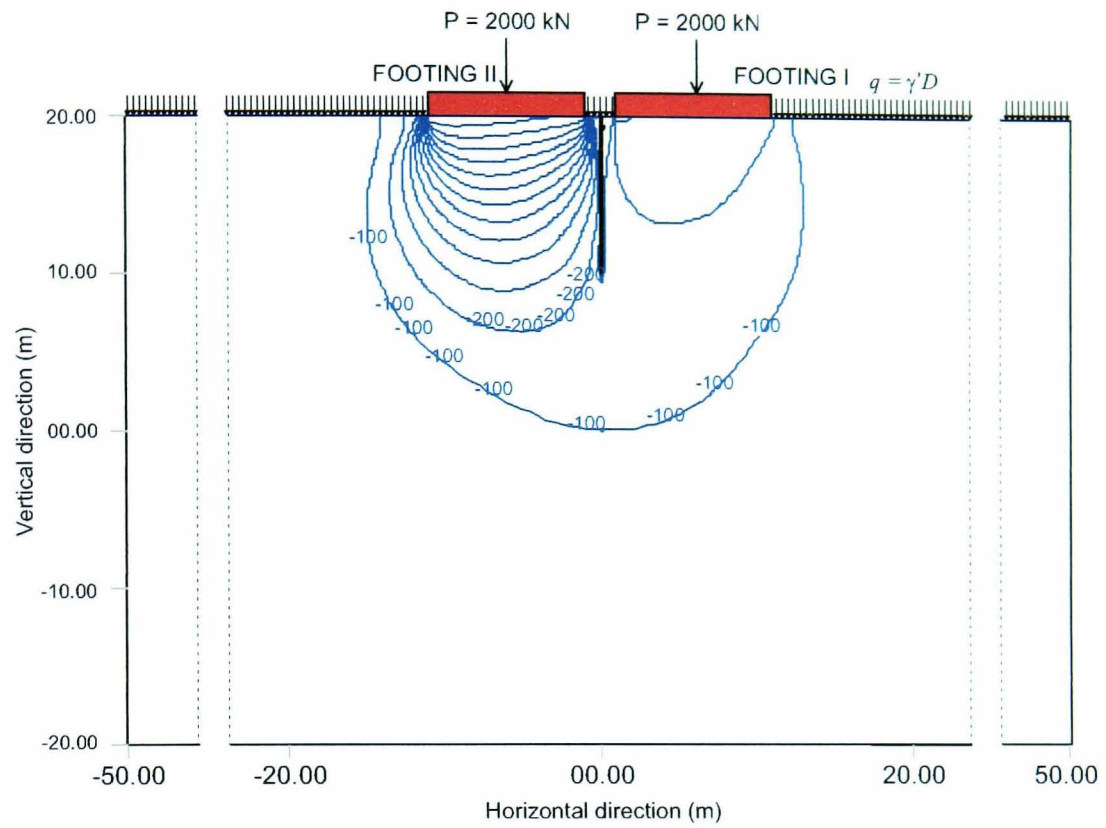
**Figure 6.52:** Contours of vertical displacement due to loading on Footing II with 10-m sheet pile wall vertically restrained
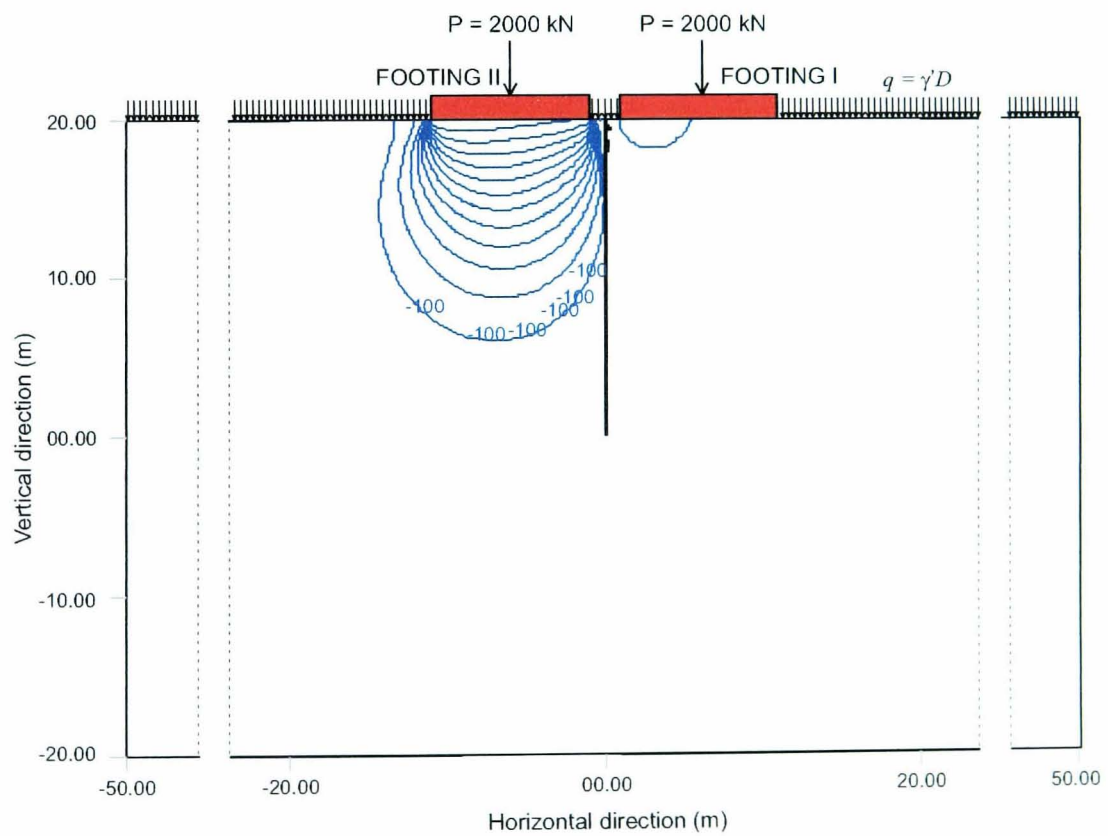
**Figure 6.53:** Contours of vertical displacement due to loading on Footing II with 20-m sheet pile wall vertically restrained
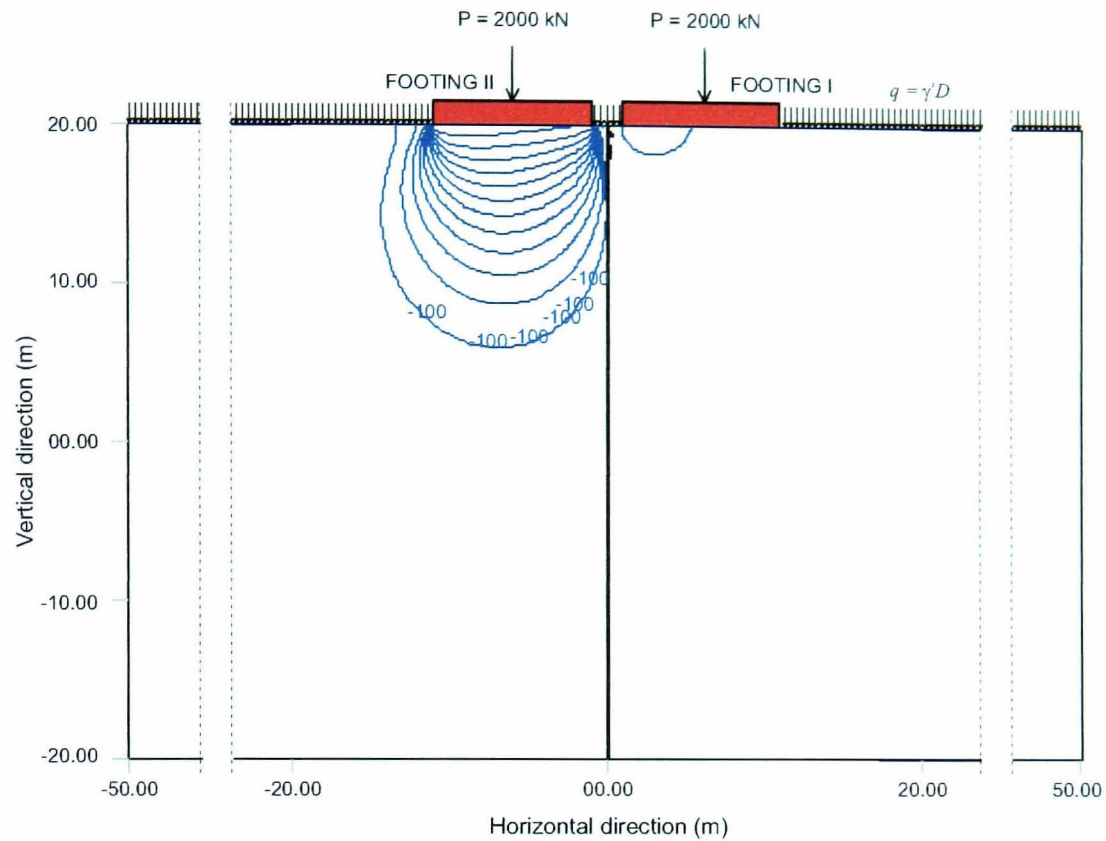
**Figure 6.54:** Contours of vertical displacement due to loading on Footing II with 40-m sheet pile wall vertically restrained
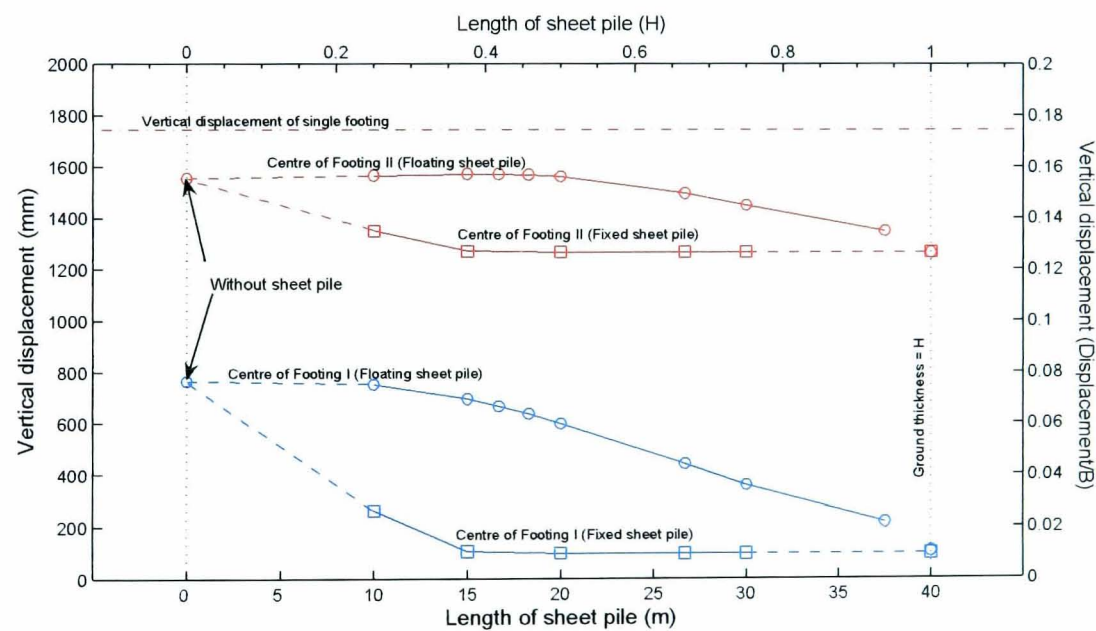


**Figure 6.55:** Effect of sheet pile wall length on vertical displacement at the centres of Footing I and Footing II (due to loading on Footing II)

The characteristics of the settlement mitigation owing to the variations of the pile lengths and fixities were observed through vertical and lateral stresses in the elements located behind the sheet pile wall due to the pressure of Footing II. The elements of interest are shown in Figure 6.56.

The effective vertical and lateral stresses, due to the combination of the pressures of Footing I and Footing II, are depicted in Figure 6.57 and Figure 6.58.  As a benchmark the initial vertical and lateral stresses ($\sigma'_{y0}$ and $\sigma'_{x0}$) at the elements before the application of loading on Footing II are incorporated in the figures.  At this stage, the elements had already been subjected to the stresses distributed from the loading on Footing I.

The degree of the stress interference from the pressure of Footing II and the stress mitigation due to various sheet pile wall lengths can be interpreted from the deviation of the stress profiles from the initial ground stress profile ($\sigma'_{y0}$ or $\sigma'_{x0}$).  Without a sheet pile wall, the contact pressure of 200 kPa at the base of Footing II had significantly increased the effective stresses in the upper elements.  With a floating sheet pile wall, the interference in term of lateral stresses was gradually reduced with increasing sheet pile wall lengths.  This was not the case for the vertical stresses.  A greater stress mitigation by the fixed sheet pile wall 10 m long is also evident in Figures 6.57 and 6.58. Beyond this length, the mitigation seemed independent of the lengths.

The interference effects due to the pressure of Footing II were further examined through the resulting volumetric strains.  The effects of the length variation of the floating sheet pile wall on the volumetric strain are shown in Figures 6.59 to 6.62.   The unmitigated stress interferences beneath the level of the sheet pile wall tip (see Figure 6.57) were clearly seen through the occurring
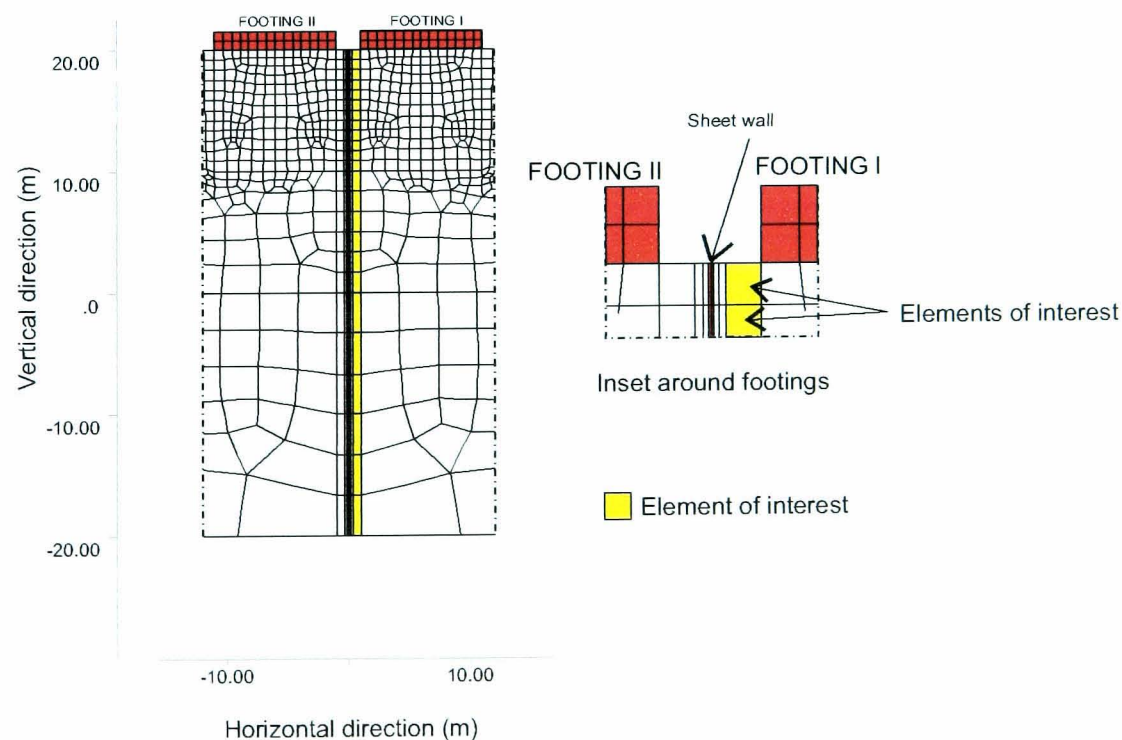


**Figure 6.56:** Elements of interest
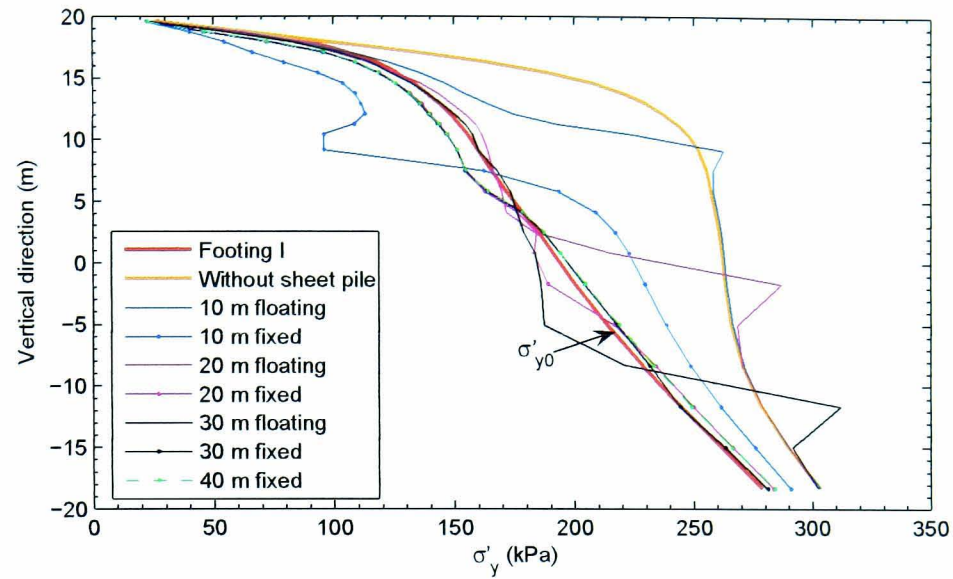
**Figure 6.57:** Vertical stresses at elements of interest (see Figure 6.56) after loading Footing I and Footing II
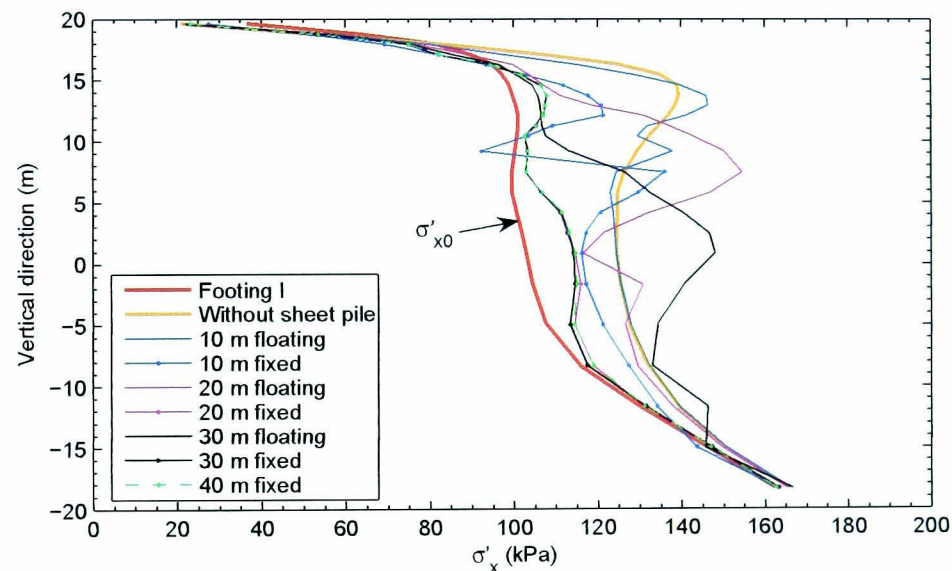


**Figure 6.58:** Lateral stresses at elements of interest (see Figure 6.56)

volumetric strain. The greater lengths shielded a larger area behind the sheet pile wall. In this case, the strain was more concentrated around its tip and in the underlying soil. This phenomenon can be explained through the shearing that took place on the surface of the sheet pile wall. Figure 6.63 illustrates the vertical shearing in the elements right and left of the sheet pile wall over the thickness of the ground. Over the sheet pile wall length, negative magnitudes of the shearing resultants indicate that the soil elements pushed down the pile, while positive values indicate supportive shearing in the interfacing soil elements. The sheet pile wall was always pushed down at the top
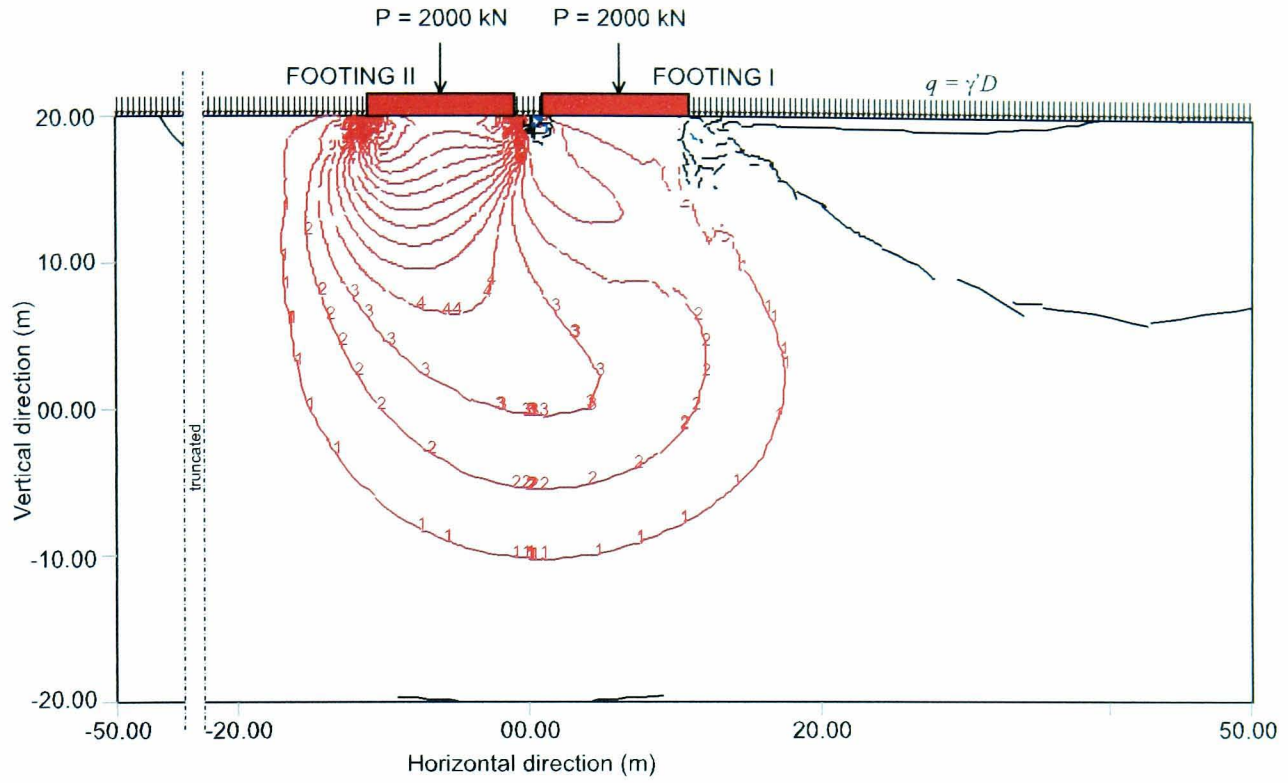
**Figure 6.59:** Contours of volumetric strain due loading on Footing II without sheet pile wall
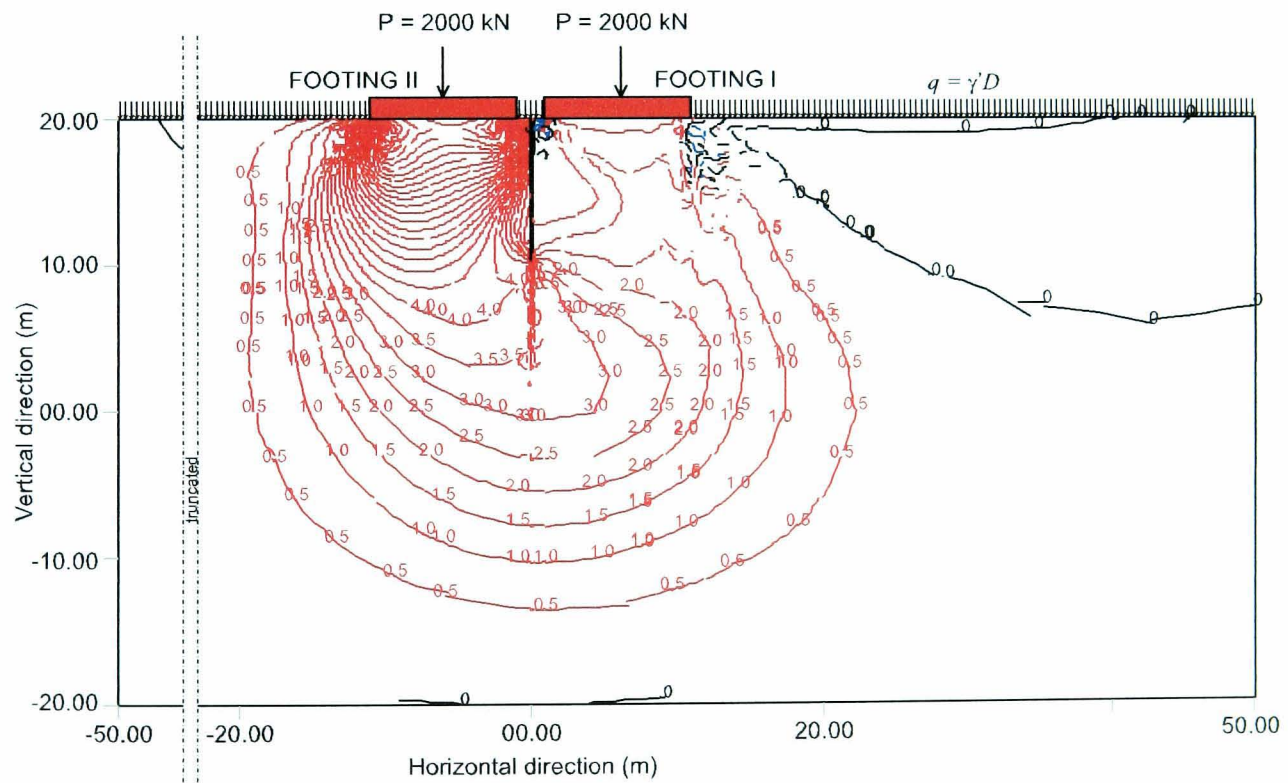


**Figure 6.60:** Contours of volumetric strain due loading on Footing II with 10-m floating sheet pile wall
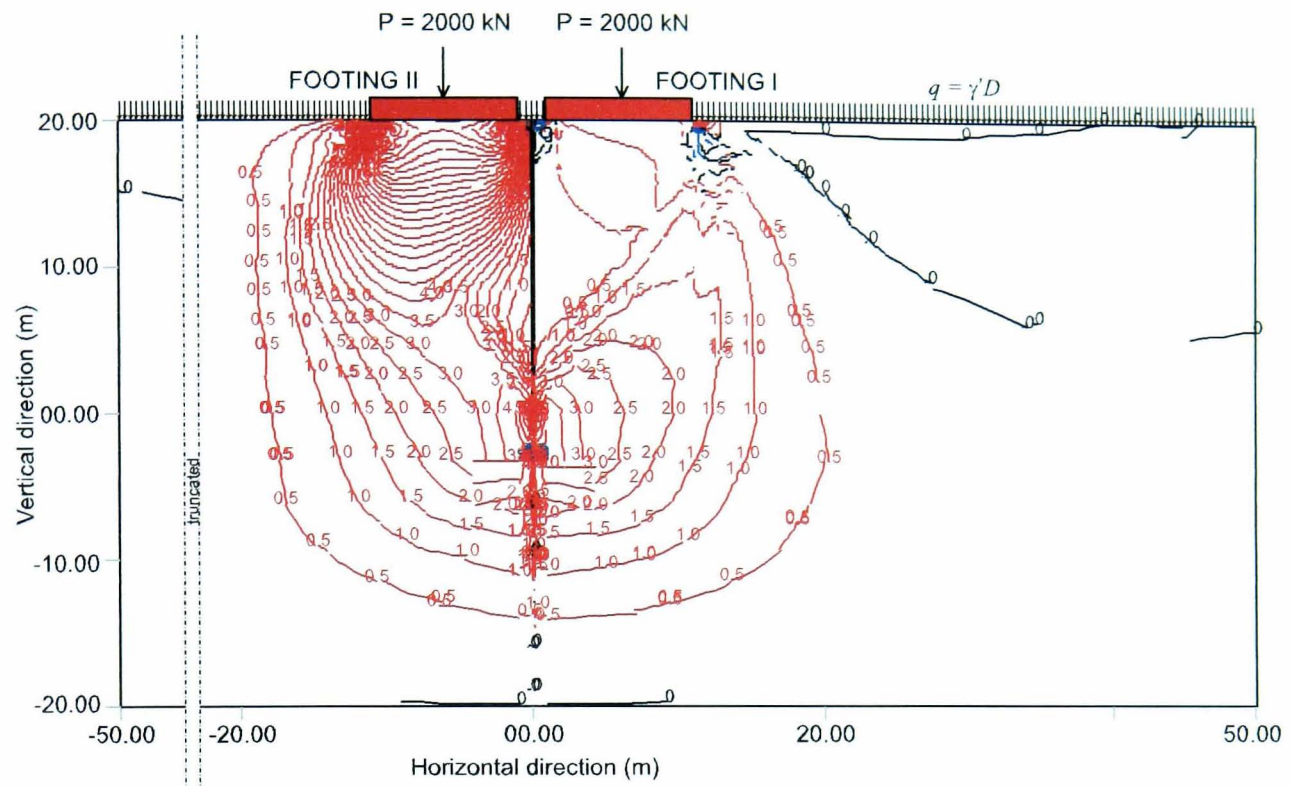
**Figure 6.61:** Contours of volumetric strain due loading on Footing II with 20-m floating sheet pile wall
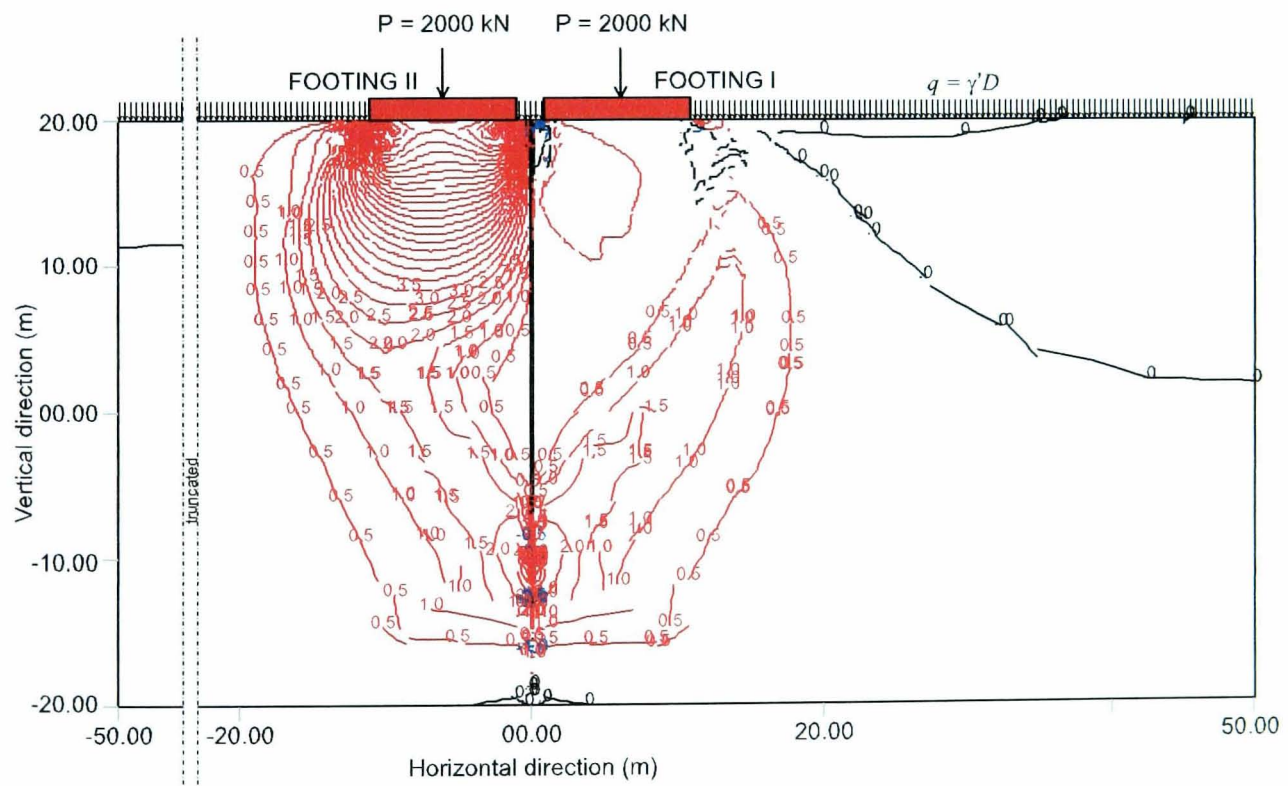


**Figure 6.62:** Contours of volumetric strain due loading on Footing II with 30-m floating sheet pile wall

and supported at the bottom. This phenomenon is similar to that observed in the simulation of the physical modelling (see Section 6.2.3.2.2).
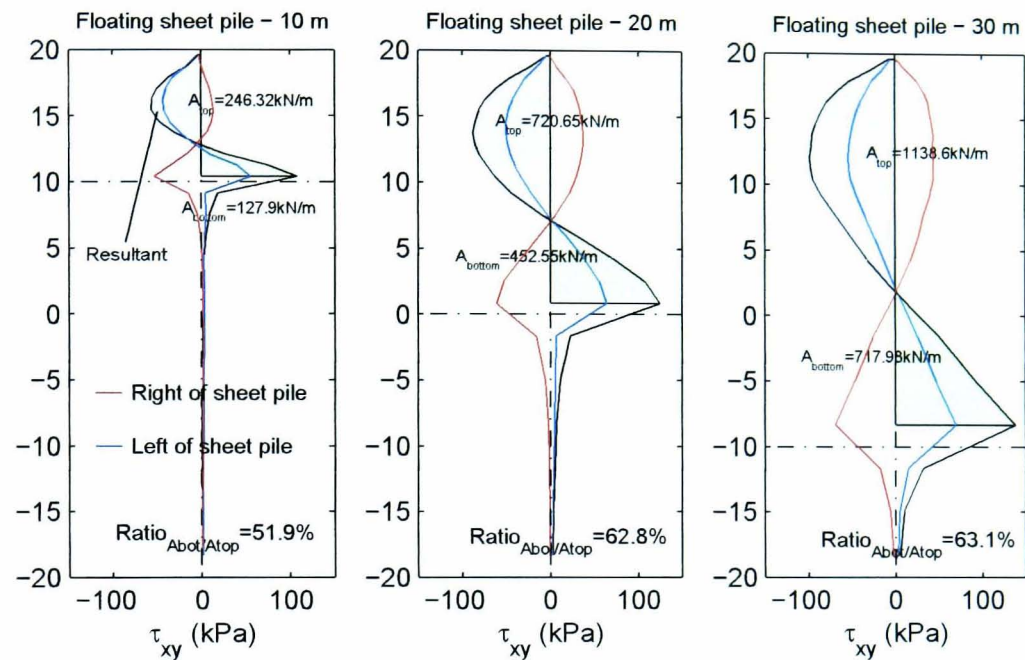


**Figure 6.63:** Typical shearing on the interface of floating sheet pile wall, as observed in the numerical simulation of the physical modelling (see Figure 6.28)

In Figure 6.63, the ratios of less than 100%, for the resultants of the shearing forces on the lower and the upper parts of the wall, show that the sheet pile wall settled with the upper region of the surrounding soil during the loading combination of Footing I and Footing II for a sheet pile wall with a length of 10 m or more. Figure 6.64 shows the strength mobilised in the ground with the sheet pile wall of 10 m, also typical for longer sheet pile walls. While the strength of the soil was highly mobilised in the upper and the lower (around the tip) parts of the sheet pile wall, it always remained lowly mobilised around the central part. This behaviour was also found in the analyses simulating the physical modelling as discussed in Section 6.2.3.2.2 (see Figure 6.30).

The contours of volumetric strain shown in Figures 6.65 to 6.67 were also used to investigate the stress mitigation with different lengths of vertically restrained sheet pile wall. Figure 6.65 reveals that the 10-m sheet pile wall was not long enough to shield the soil beneath Footing I from the stresses distributed from the pressure of Footing II. The figure shows that the soil beneath Footing I beyond the tip level of the sheet pile wall still experienced volumetric strains. Such

FOOTING I     FOOTING II
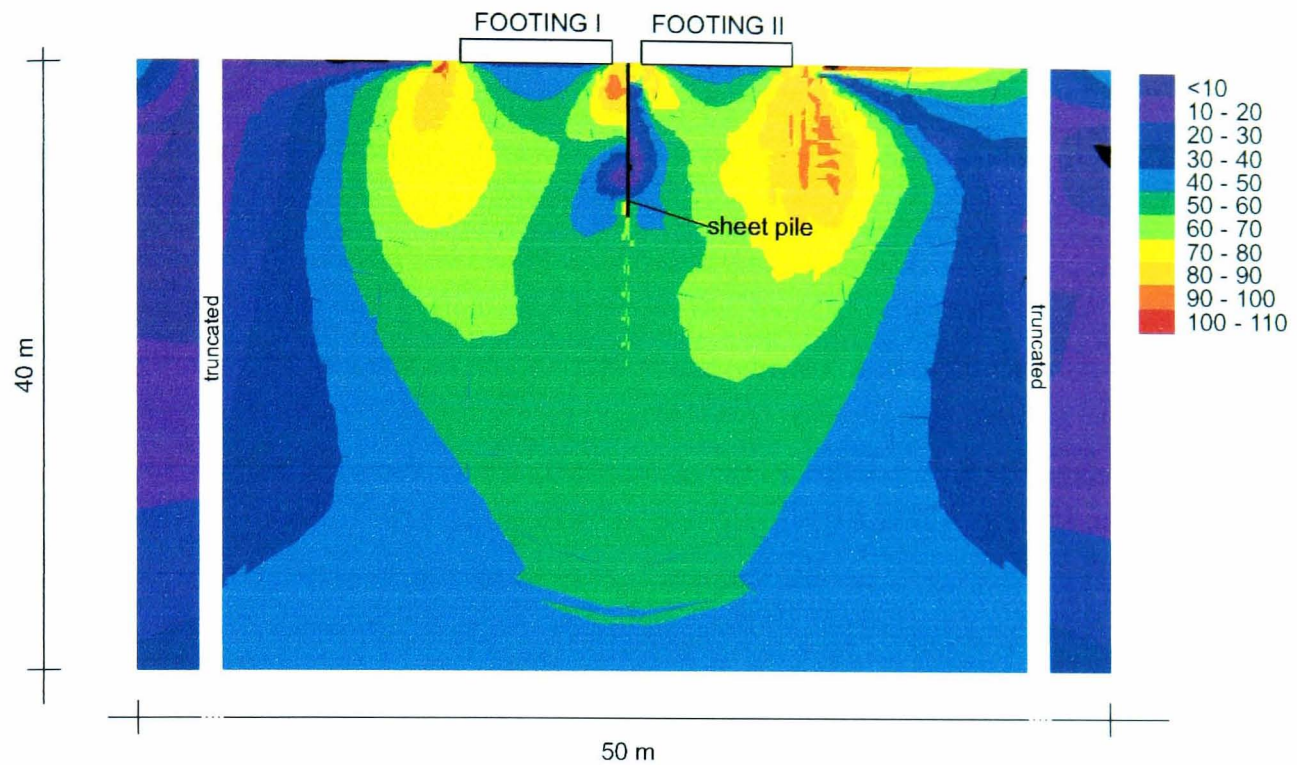


**Figure 6.64:** Strength mobilised with floating sheet pile wall of 10 m

behaviour was no longer apparent after the sheet pile wall was extended to 15 m. As shown in Figure 6.55, further length extension did not alter the vertical displacements of the footings.

Figure 6.68 shows a typical pattern of strength mobilised due to loading on Footing I and on Footing II. It is evident that the strength of the soil near the upper region of the sheet pile wall was highly mobilised. Similar evidence was also found when longer sheet pile walls were used. It also can be seen in Figure 6.69 that higher shear stresses are concentrated in the upper region of the longer sheet pile wall.

The angular distortions $\delta/L$ resulting from varying the lengths of the floating and the fixed (vertically restrained) sheet pile wall, due to loading on Footing II, are shown in Figure 6.70. As mentioned in Section 6.3.3.2, without the sheet pile wall Footing I and Footing II tilted with respectively $\delta/L = 1/71$ and $\delta/L \approx 1/35$. The tilting of Footing II decreased linearly with increasing length of the floating sheet pile wall. It had a constant $\delta/L = 1/71$ after the length was extended to 37.5 m. In contrast, the influence of the length variation was not evident during the use of the fixed sheet pile wall. The tilting remained at $\delta/L = 1/71$ even though the pile length was extended to the full thickness of the ground. Both with the floating and the fixed sheet pile
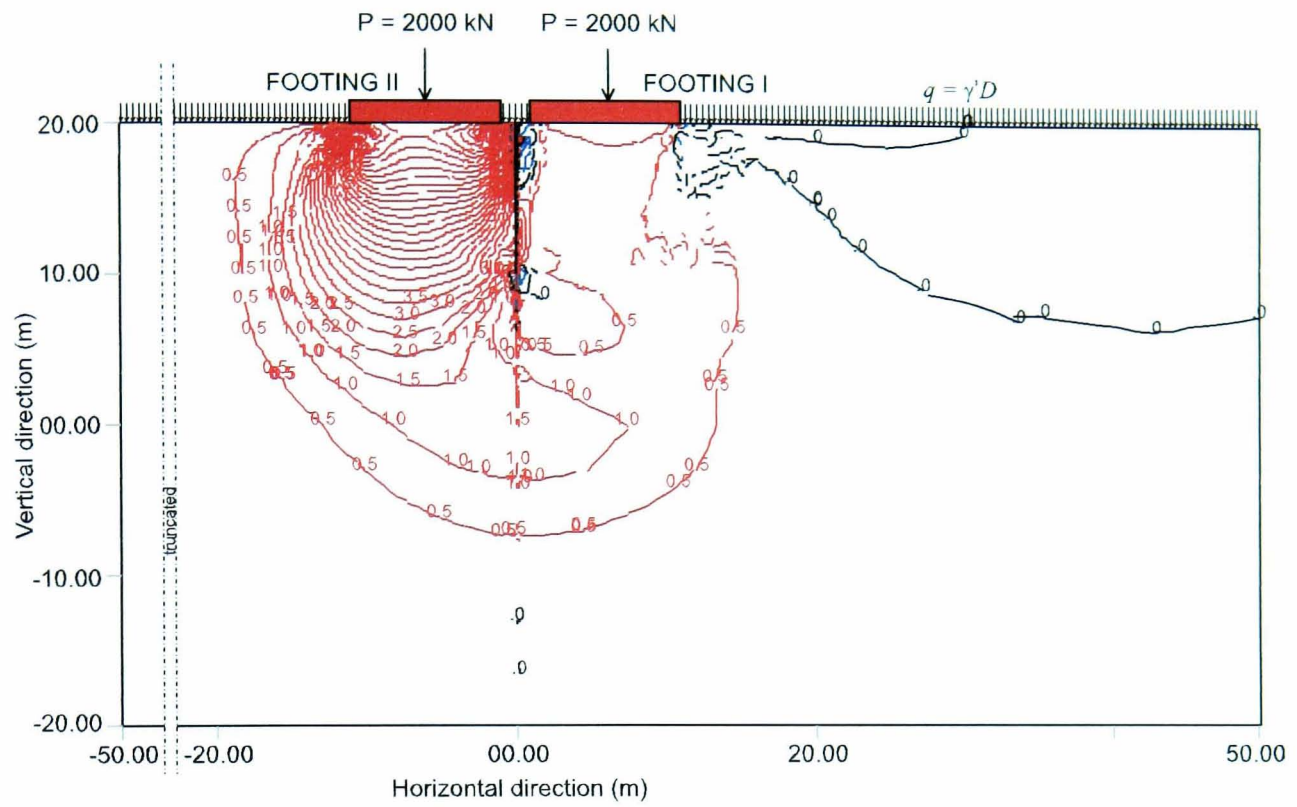
**Figure 6.65:** Contours of volumetric strain due loading on Footing II with 10-m sheet pile wall vertically restrained
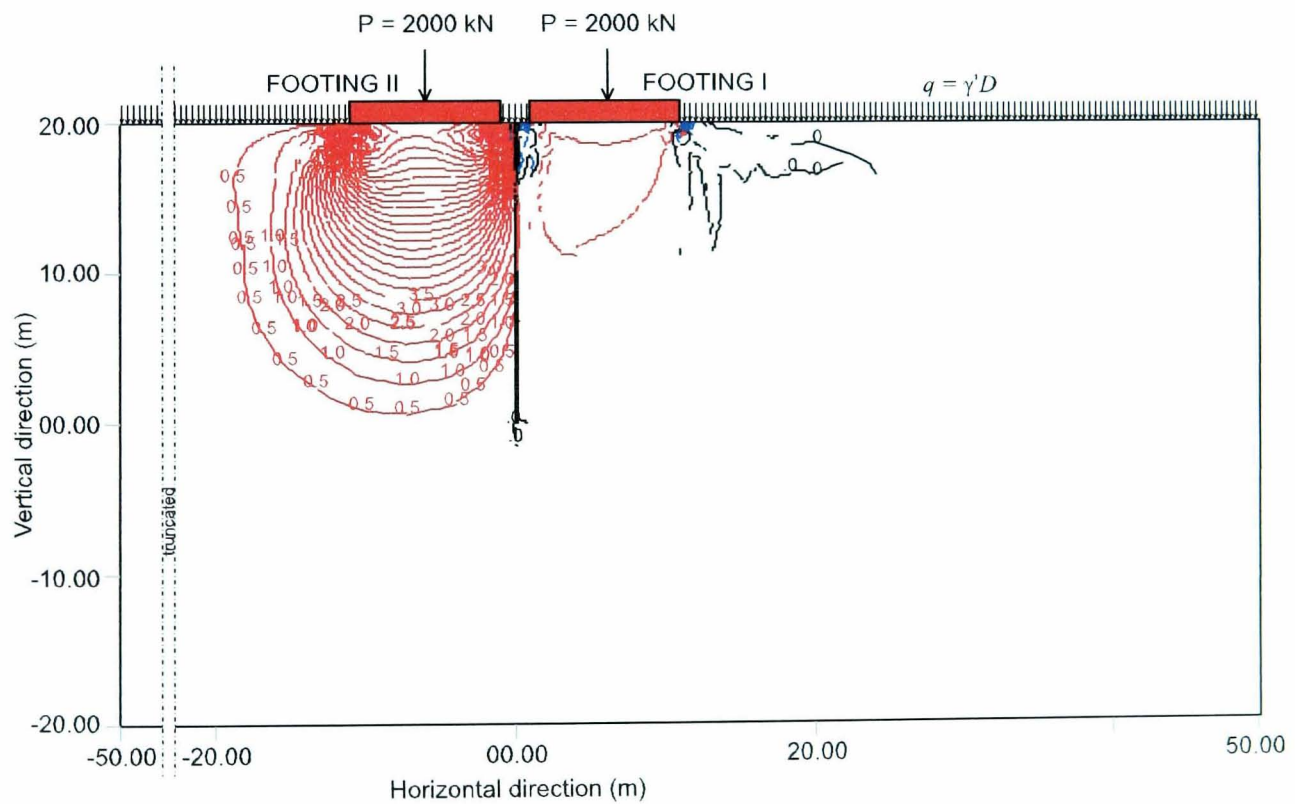


**Figure 6.66:** Contours of volumetric strain due loading on Footing II with 20-m sheet pile wall vertically restrained
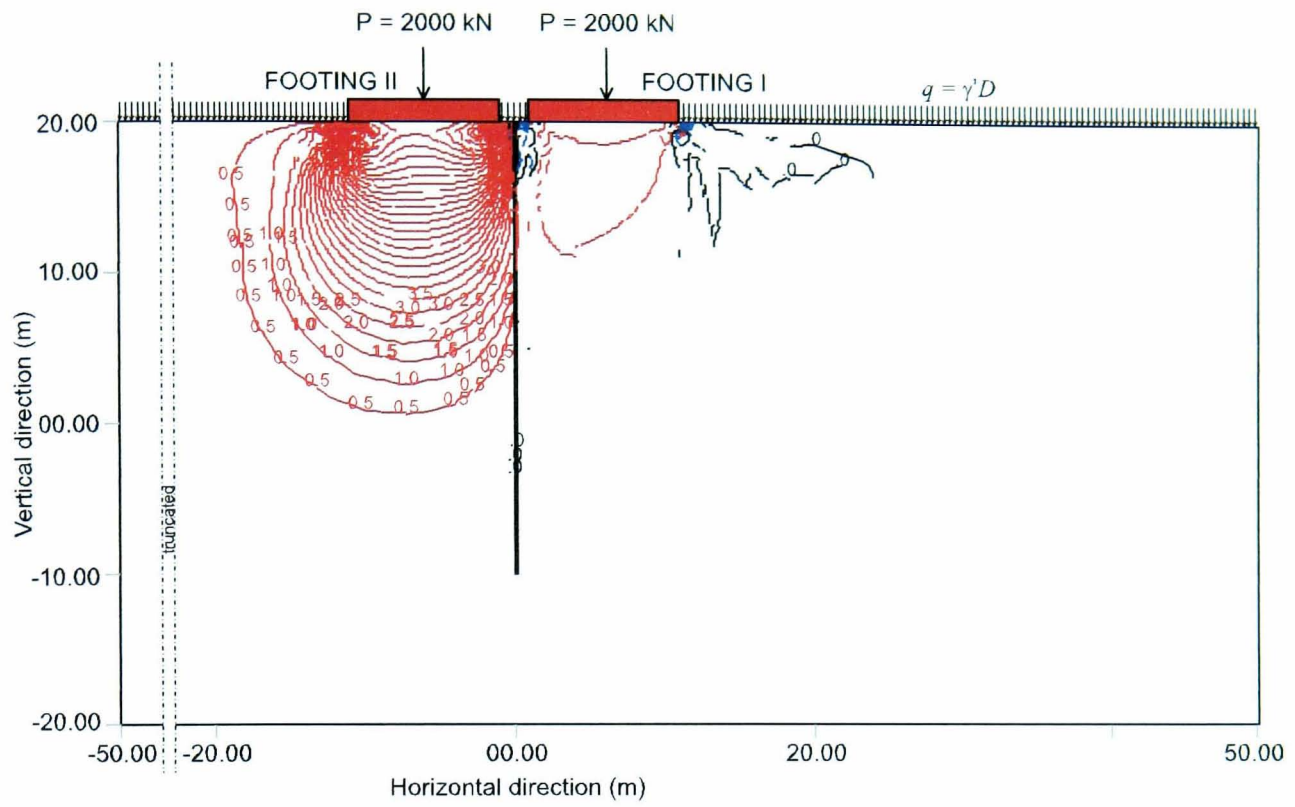
**Figure 6.67:** Contours of volumetric strain due loading on Footing II with 30-m sheet pile wall vertically restrained
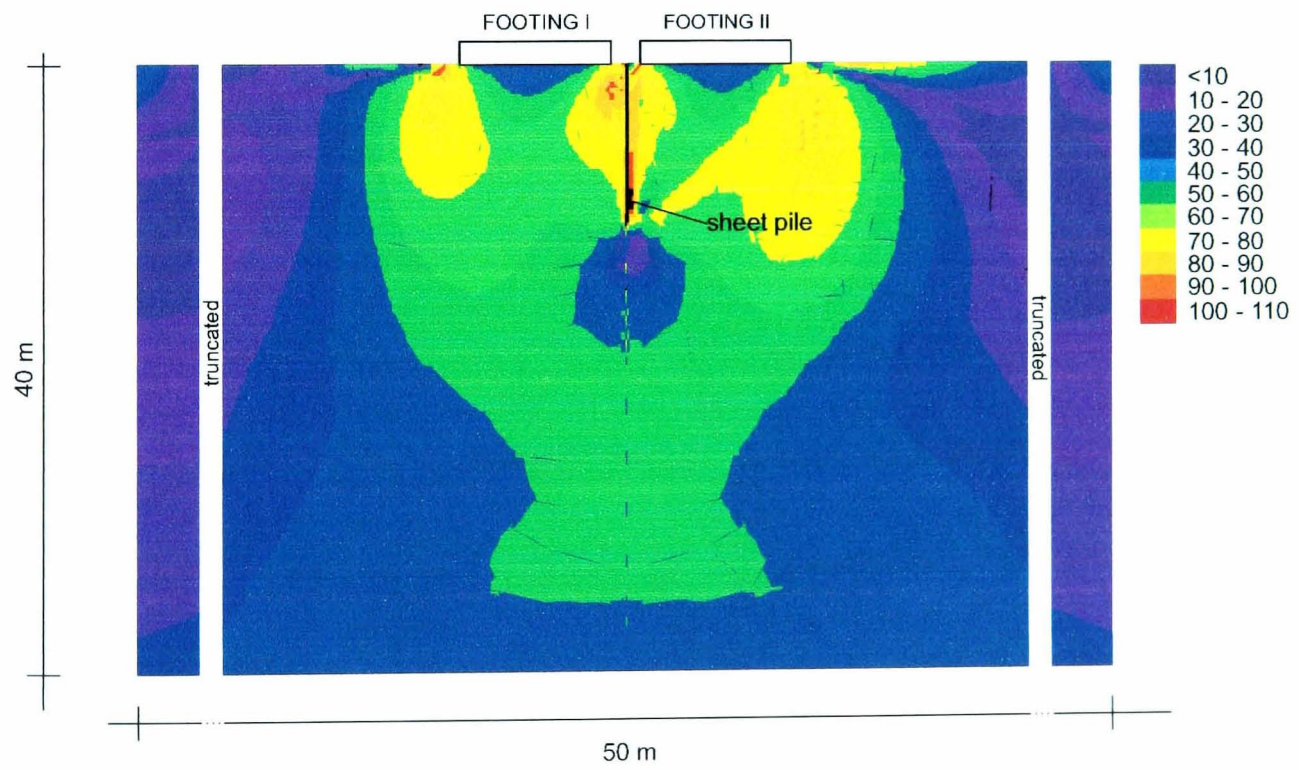


**Figure 6.68:** Strength mobilised with restrained sheet pile wall of 10 m
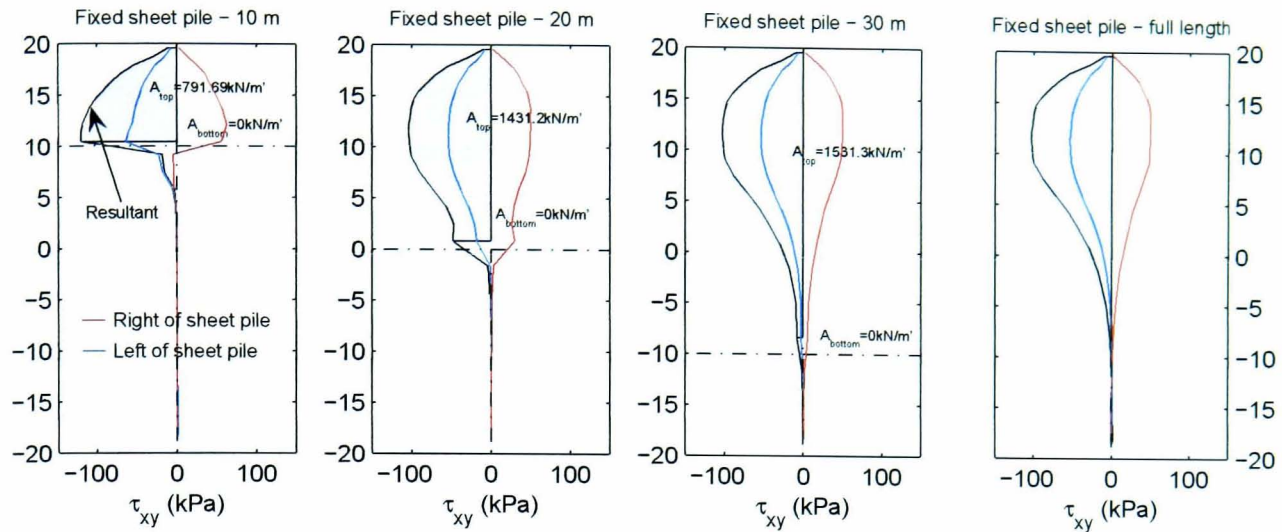
**Figure 6.69:** Shearing on the interface of sheet pile wall

walls, the tilting of Footing II was still above the threshold value of $\delta/L = 1/150$ at which some buildings could be damaged. A decrease of tilting with increasing length of the floating sheet pile wall was also encountered on Footing I. However, the tilting of the footing tended to increase once the length of the sheet pile wall exceeded 15 m. It then started to diminish again after the sheet pile wall occupied 75% of the ground thickness. For the fixed sheet pile wall, additional lengths beyond 15 m did not show further mitigation of tilting. As shown in Figures 6.57 and 6.58 the vertical and
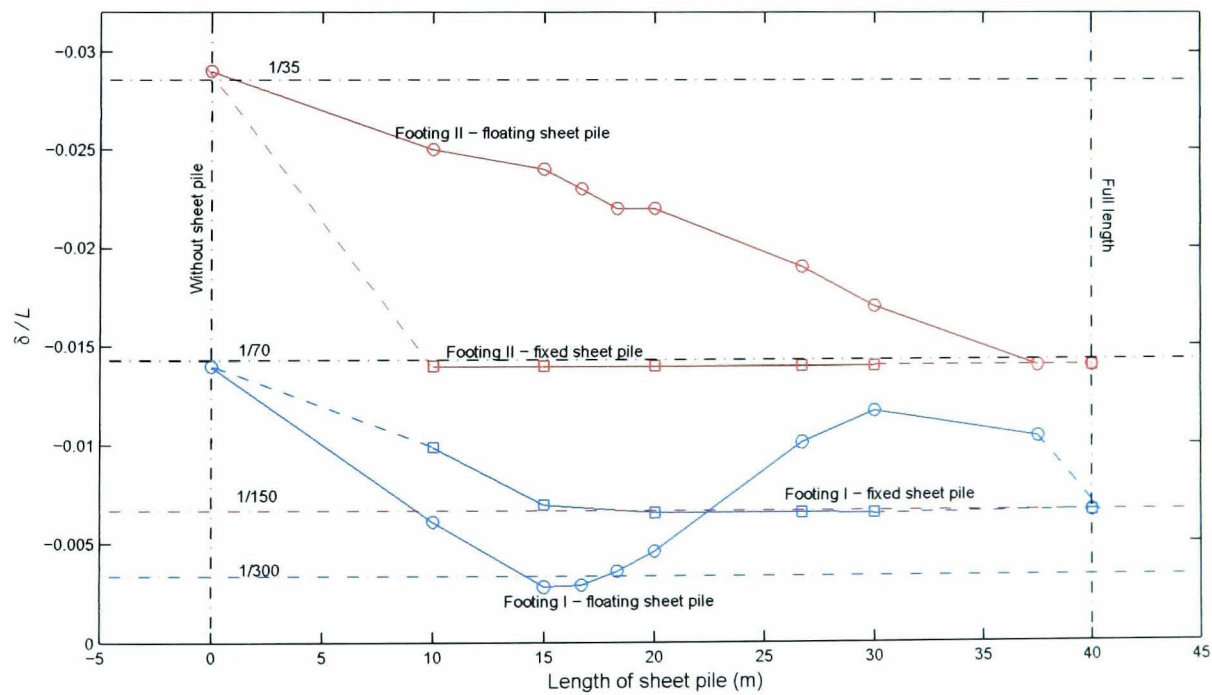


**Figure 6.70:** Effect of sheet pile length on tilting due to loading on Footing II

lateral stress distributions in the elements immediately right of the sheet pile wall had only a very little difference once a fixed sheet pile wall longer than 10 m was used. As shown in Figures 6.65 to 6.67, volumetric strain below Footing I, although as small as 0.5%, was still affected by the pressure of Footing II.

The stress interference was also affected by the flexing of the sheet pile wall. Figure 6.71 illustrates the horizontal displacement at points along the centre of the sheet pile wall. At the
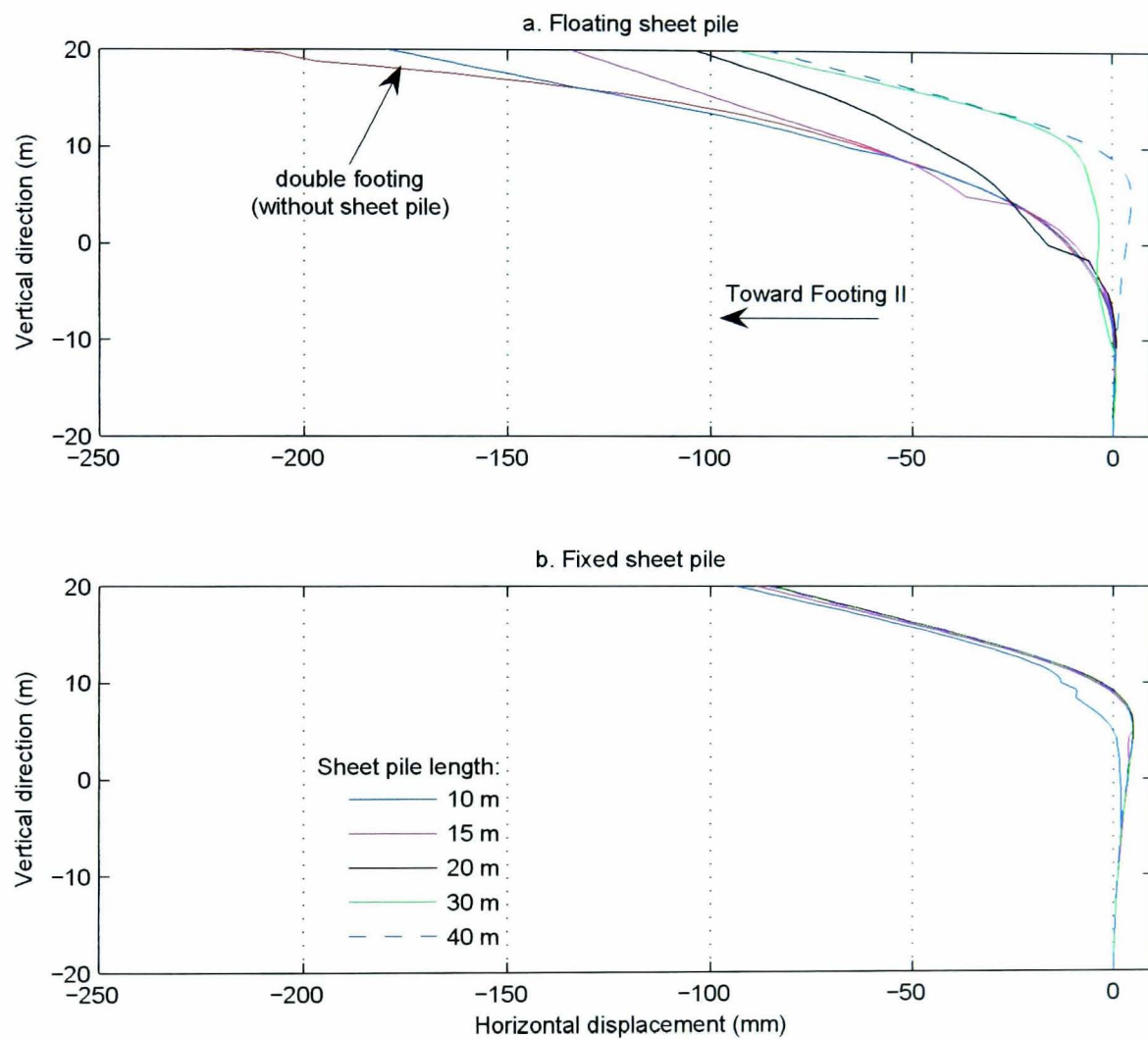


**Figure 6.71:** Horizontal displacements of different lengths of sheet pile wall

final increment of loadings on Footing II, the sheet pile wall was slanted towards Footing II. The inclinations of the floating sheet pile wall were clearly dependent on its the length. A longer sheet pile wall provided resistance to the lateral stresses distributed from the combined pressures of Footing I and Footing II. At a length of 30 m, the sheet pile wall tip seems to provide good

fixity although it was still slightly displaced towards Footing II. The variation of length did not significantly affect the displacement and the inclination of the restrained sheet pile wall.

The effects of the sheet pile flexibility were scrutinised with several further analyses. The pile stiffnesses were varied as factors of that of the sheet pile (GSP2 type) used in the analyses throughout the previous sections, as shown in Table 6.4. The stiffnesses were selected according

**Table 6.4:** Variation of sheet pile stiffness used in finite element analyses

| Type | $I$ (cm$^4$/m) | $EI$ (kN.m$^2$/m) | $EI/EI_{\textbf{GSP2}}$* |
|------|------|------|------|
| **GSP2** | $8.74 \times 10^3$ | $1.835 \times 10^4$ | 1.00 |
| **GSP3** | $1.68 \times 10^4$ | $3.519 \times 10^4$ | 1.92 |
| **GSP4** | $3.87 \times 10^4$ | $8.135 \times 10^4$ | 4.43 |
| **I6** | $1.11 \times 10^5$ | $2.340 \times 10^5$ | 12.75 |
| **Rigid** | $3.97 \times 10^7$ | $8.343 \times 10^7$ | 4,545.50 |

*Ratio of $EI$ to $EI$ of GSP2

to the common sections such as GSP3, GSP4, and I6 (British Steel,1997). In order to investigate the effect of a rigid sheet pile, a very high stiffness was used. The variation of stiffness was implemented using two different sheet pile lengths of 20 m and 26.7 m. In addition, to observe the behaviour of a sheet pile wall with a stiffness magnitude between those of the so-called rigid sheet pile wall and the I6 type, a stiffness $EI = 4.17 \times 10^6 \text{kN.m}^2/\text{m}$ ($EI/EI_{GSP2} = 227.3$) was analysed for the 20 m long floating sheet pile wall. The calculated settlements from these analyses are shown in Figure 6.72. The settlements are presented as ratios of the vertical displacements $\rho$
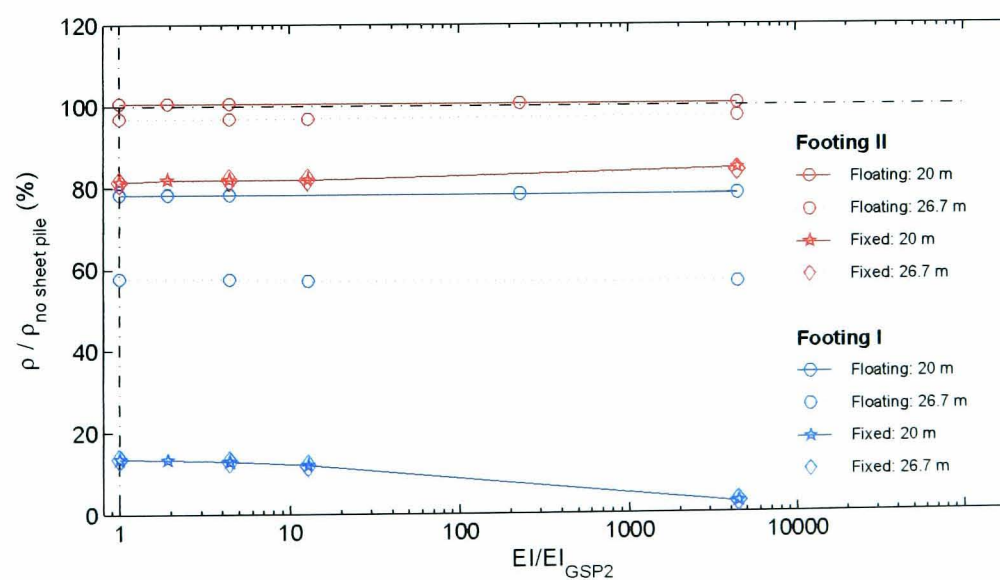


**Figure 6.72:** Effect of sheet pile stiffness on footing settlement

at the centres of Footing I and Footing II to the displacements of each respective footing analysed without a sheet pile wall. The increase of the stiffness did not appear to influence the settlements of the footings with a floating sheet pile wall of the two different lengths, although the displacement pattern of the sheet pile wall was slightly changed (see Figure 6.73 and Figure 6.74). Restraining
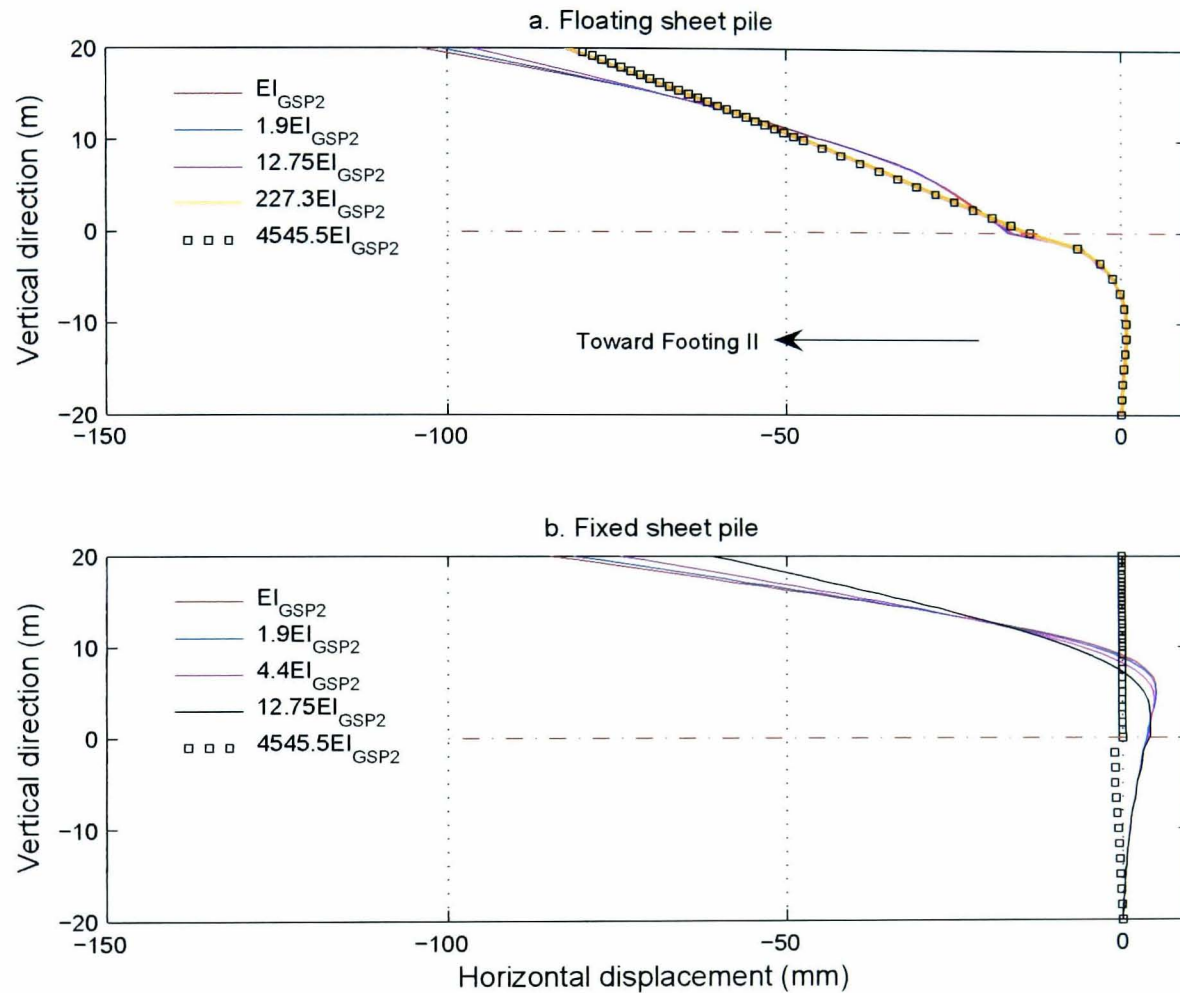


**Figure 6.73:** Effect of stiffness on horizontal displacement of 20-m sheet pile wall

the sheet pile wall showed a slight effect on the settlement of Footing I, especially at the very high stiffness. As shown in the figures, under the combined pressures of Footing I and Footing II the rigid sheet pile wall almost remained in its initial position. However, Figure 6.75 suggests that beneficial effects of increased stiffness were evident for the tilting of both footings.
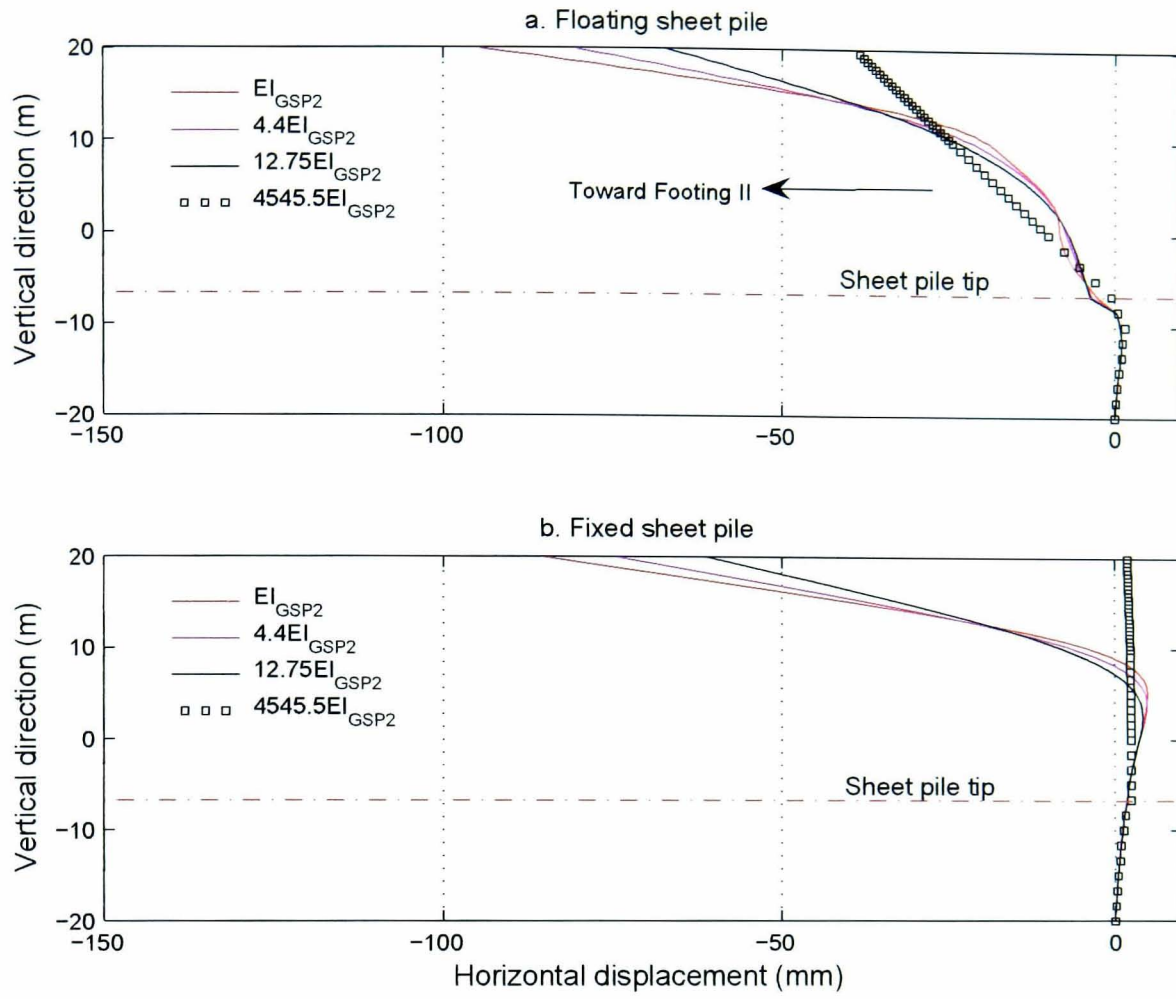
**Figure 6.74:** Effect of stiffness on horizontal displacement of 26.7-m sheet pile wall
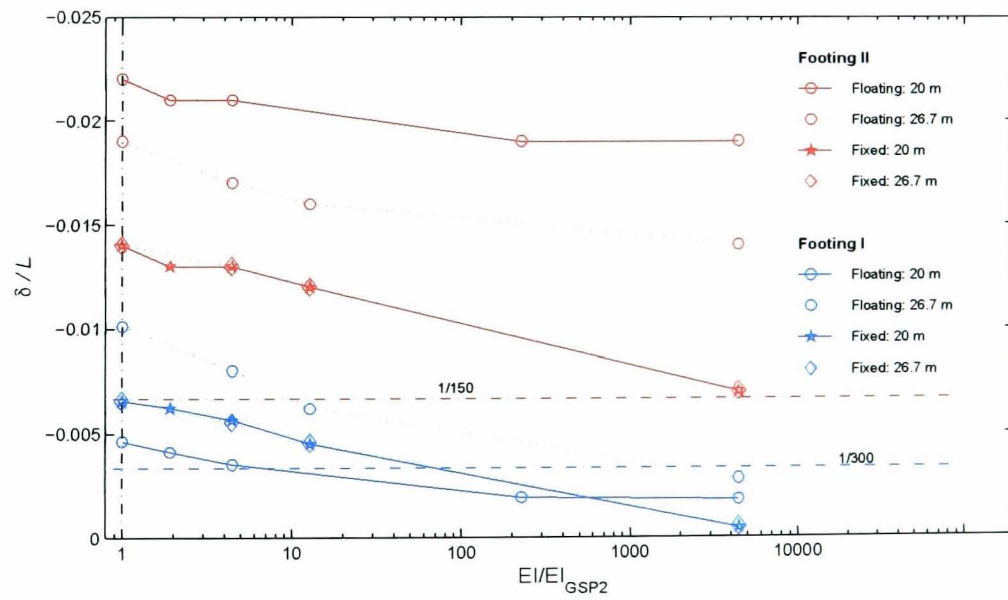


**Figure 6.75:** Effect of sheet pile stiffness on tilting

# Chapter 7

# CONCLUSIONS

## 7.1 Introduction

Field observation shows that buildings with floating-piled raft foundations on deep soft clay deposits will suffer from differential settlement if they are constructed close to each other. To understand the interaction between two closely-constructed buildings, $1g$ small-scale physical modelling (covered in Chapters 3, 4, and 5) with two model footings has been carried out and numerical modelling (Chapter 6) with the finite element method has been performed. A question addressed in this thesis was whether a sheet pile wall inserted between the buildings could mitigate the problem. Building on the success of the finite element method in simulating the physical modelling results, a series of finite element analyses was then performed to simulate a prototype.

## 7.2 Physical Modelling

In the $1g$ laboratory tests, two building foundations were modelled with Perspex plates referred to as "footings" (Section 3.2). The width of each footing was 100 mm representing a 10-m width of the raft foundation of a building. The length of the footings was 150 mm, to suit the length of a rigid chamber (400 mm wide, 150 mm long, and 450 mm high) containing the soil. The tests were designed as plane strain tests. Three types of test were conducted: (1) plain double footing (DF tests), (2) double footing with a floating sheet wall (SP tests), and (3) double footing with a vertically restrained sheet wall (FX tests). Speswhite kaolin was used to simulate the soft ground. The displacements of the model soil were measured using the Particle Image Velocimetry technique with photogrammetric enhancement. The measurements had mean errors of 0.01 mm

(standard deviation = 0.007 mm) in the horizontal direction and 0.0065 mm (standard deviation = 0.005 mm) in the vertical direction (Section 4.4.3).

The key findings from the physical modelling are as follows:

- Soil that experienced loading and unloading during preconsolidation responded more stiffly to future loading than monotonically loaded soil (discussed initially in Section 5.3.1.1).

- The settlement of the second footing (Footing II), when it was loaded adjacent to an existing loaded footing (Footing I), was always smaller than that of Footing I individually loaded (Sections 5.3.2.1, 5.4.4.1, and 5.5.3.1). This behaviour is depicted in Figure 7.1. On average,
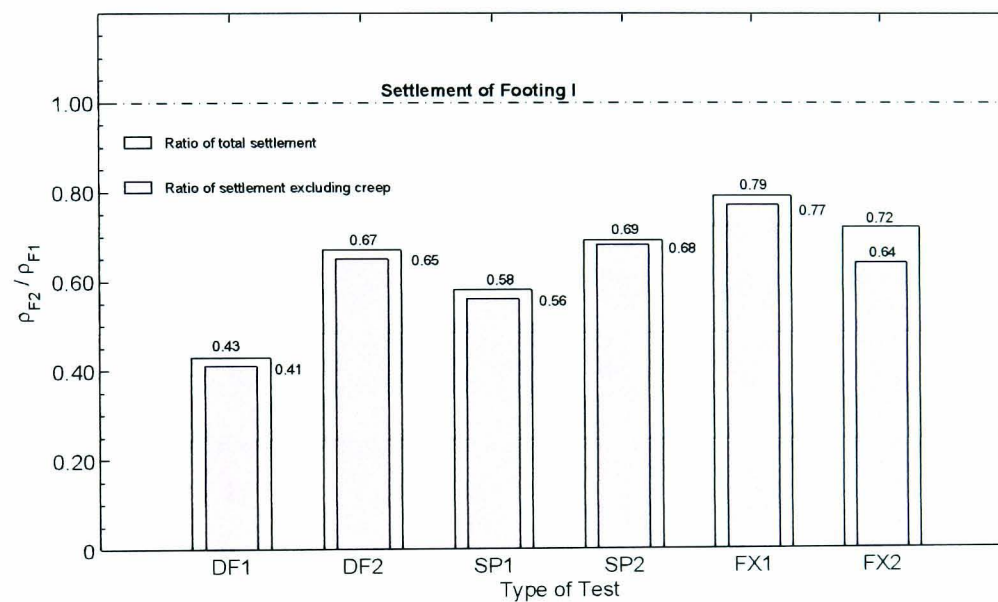


**Figure 7.1:** Ratio of settlement of Footing II due to loading on Footing II to that of Footing I as an individual footing

the settlement of the latterly loaded footing (Footing II) was about 65% of that of Footing I. The settlement ratio became slightly smaller if creep compression was excluded. At the end of all tests the vertical displacement contours were asymmetrical relative to the centre of the soil field, midway between the footings.

- The loading on Footing II induced additional settlement of Footing I. This is illustrated in Figure 7.2 depicting the ratios of the vertical displacements of Footing I to those of Footing II due to the loading on Footing II. The settlement mitigation resulting from a floating sheet wall inserted in the SP tests was not as substantial as that resulting from a vertically restrained wall in the FX tests. Compared with the settlement of Footing I in the DF tests,
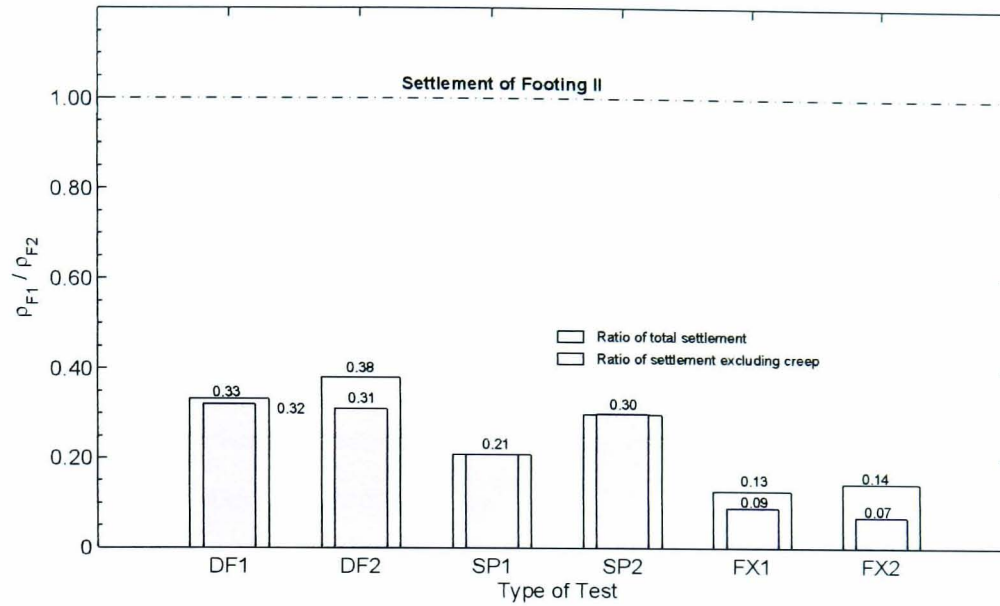
**Figure 7.2:** Ratio of settlement of Footing I to that of Footing II due to loadings on Footing II

excluding creep compression, the settlement of Footing I in the SP tests was only reduced by 9%. In the FX tests, in contrast, the settlement was reduced by 75%.
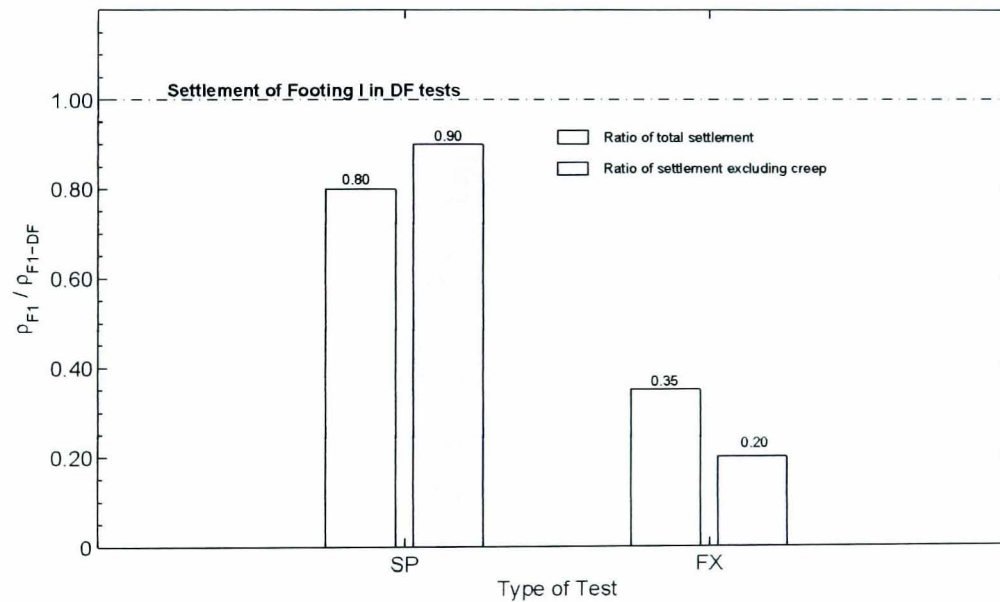


**Figure 7.3:** Ratio of settlement of Footing I in SP and FX tests to that of Footing I in DF tests due to loadings on Footing II

- Due to asymmetrical soil movement relative to the centre of either Footing I or Footing II after loading of Footing II, tilting of both footings was observed (Sections 5.3.2.2, 5.4.4.3, and 5.5.3.3). Significant tilting was found in both SP and DF tests. The tilting was in the form of rigid rotations of the footings and the damage criteria normally recommended for

differential settlement might not be applicable. However, leaving aside the rigidity of the model footings as representative of buildings, the magnitude of $\delta/l$ for both footings in these tests exceeded the limiting values, i.e. $\delta/l \approx 1/300$ (Skempton and MacDonald, 1956) or $\delta/l \approx 1/500$ (Meyerhof, 1956), for buildings to crack and $\delta/l \approx 1/250$ at which, according to Meyerhof (1956), structural damage may occur (Figure 7.4). Overall, the tilting in the SP tests was comparable to that in the DF tests. The vertically restrained sheet wall in the FX tests effectively mitigated the tilting of Footing I. However, the tilting of Footing II seemed to be as large or larger than in other tests.
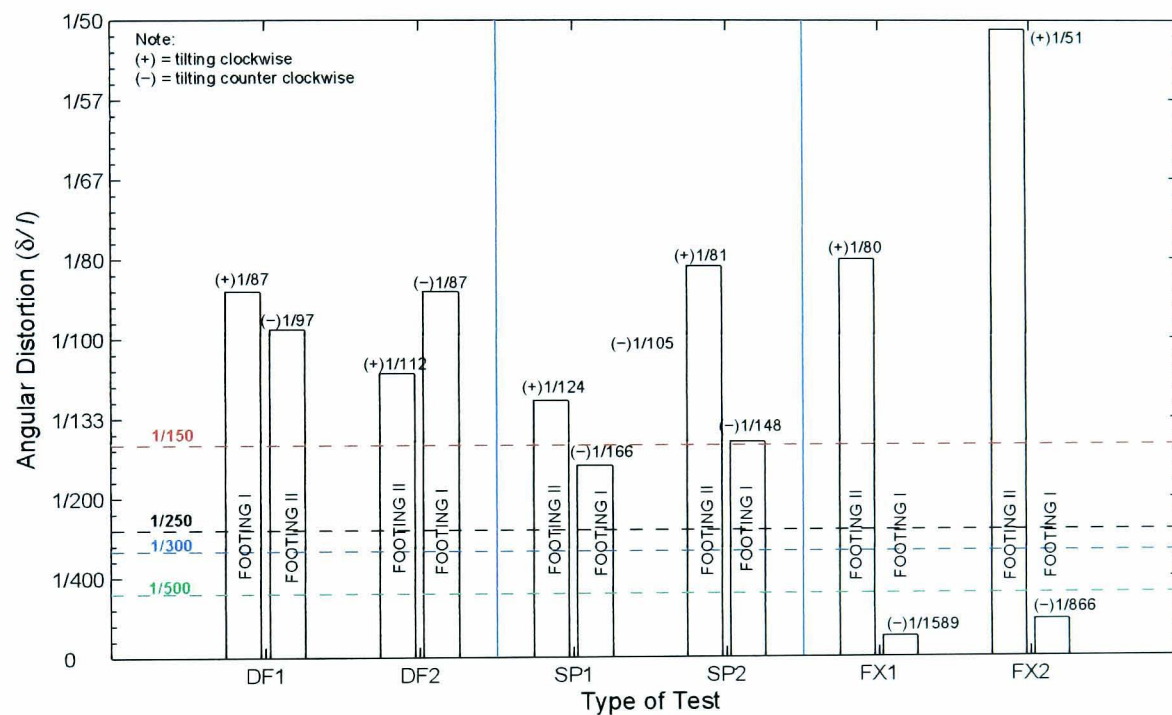


**Figure 7.4:** Tilting of Footing I and Footing II due to loadings on Footing II

### 7.3 NUMERICAL MODELLING

Two series of finite element analyses were conducted. Both employed the program SAFE with BRICK as the constitutive model. The first series was carried out for comparison with the results from the physical modelling. The stages of the analysis therefore mirrored the testing procedures. The second series was performed to simulate field problems regarding two neighbouring buildings founded on Singapore Marine Clay. Similar mitigation of the building interaction, i.e. using a sheet pile wall, was investigated.

### 7.3.1 Simulation of Physical Modelling

As a whole, the behaviour pattern of the displacements of the physical model was successfully reproduced. As observed in the physical models, a stiffer response of the soil beneath Footing II than that beneath Footing I as it was first loaded was evident (Sections 6.2.3.2.1 and 6.2.3.2.2). However, the finite element analyses underestimated the settlements exhibited by Footing II in the physical modelling. This comparison is illustrated in Figure 7.5. The pressure of Footing II led
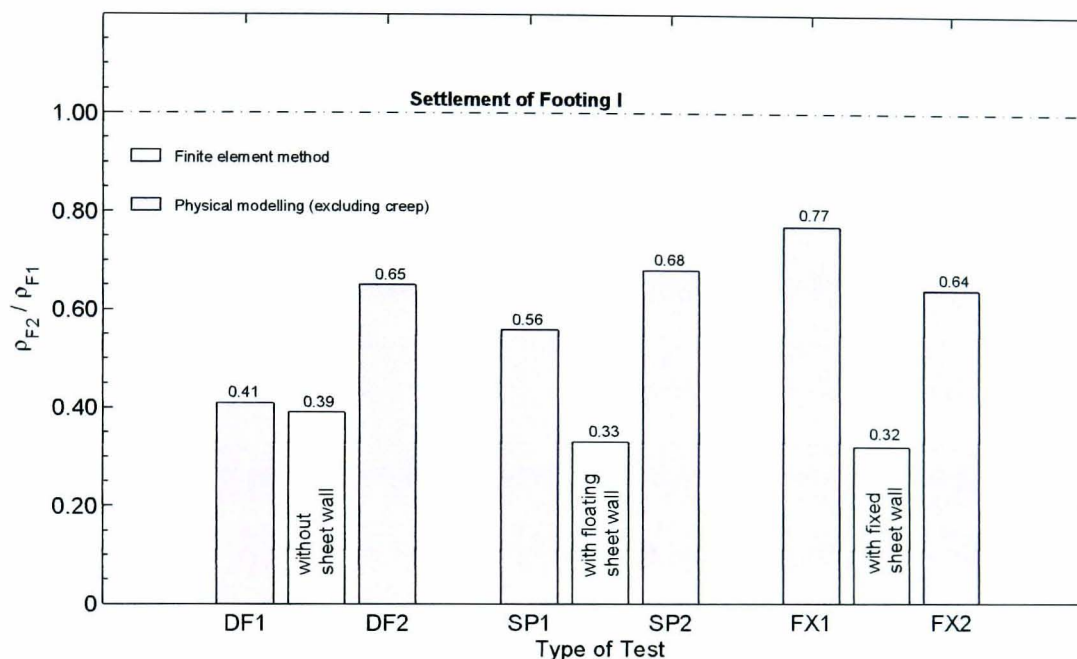


**Figure 7.5:** Ratio of settlement of Footing II due to loading on Footing II to that of Footing I as an individual footing

to some further settlement of Footing I. As shown in Figure 7.6, the settlements analysed for all case studies are comparable to those resulting from the physical modelling. Without a sheet wall, the settlement of Footing I was 32% of that of Footing II. Almost the same settlement ratio was experienced by Footing I in the analysis when a floating sheet wall was included. In contrast, the corresponding settlement ratio resulting from the analysis with a vertically restrained sheet wall was only 0.04, slightly smaller than that obtained from the physical modelling.

Taking a datum at the commencement of loading on Footing I, Footing I and Footing II tilted towards each other (Section 6.2.3.2). This is similar to the trend found by Jao et al. (2002) in their finite element analysis on two closely-spaced footings on compacted kaolin (Section 2.2.2). When the datum is taken at the start of the loading on Footing II, although the trend of mitigation of the tilting of Footing I is similar to that observed in the physical modelling (Figure 7.7), the finite
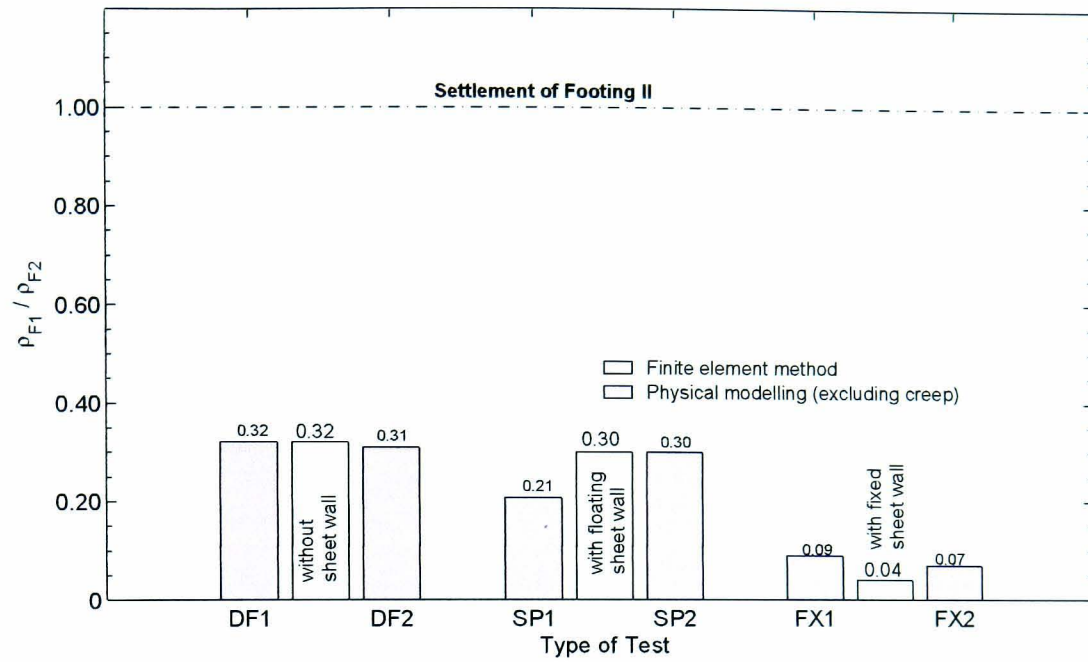
**Figure 7.6:** Ratio of settlement of Footing I to that of Footing II due to loading
on Footing II

element method failed to predict the tilting behaviour of Footing II. Footing II always tilted away

from Footing I, which is the opposite of that encountered in the physical modelling.
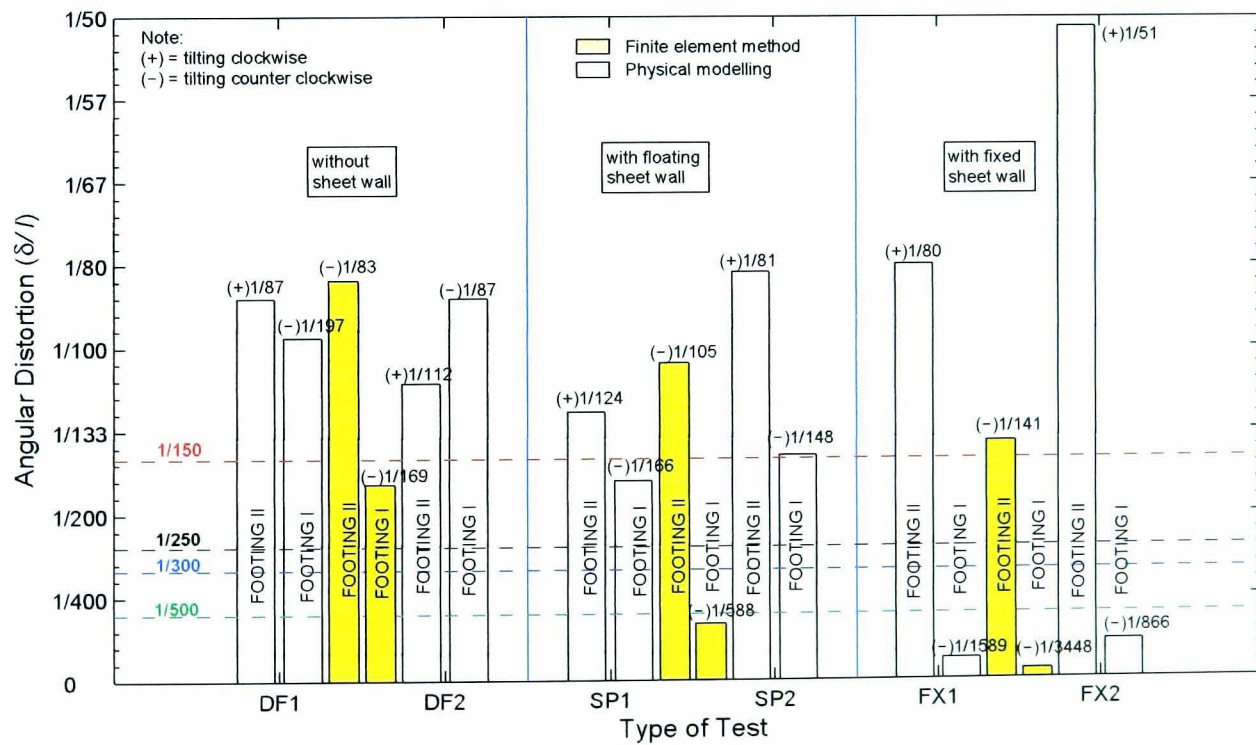


**Figure 7.7:** Tilting of Footing I and Footing II due to loadings on Footing II

### 7.3.2  Simulation of Prototype

In the simulations of field conditions, the effects of the variation of the length and stiffness of a sheet pile wall present between two 10 m wide footings on 40 m deep soft clay were studied. Two different fixity conditions were applied to the sheet pile wall, i.e. floating and fixed (vertically restrained) at the bottom of the wall. The effects were examined in terms of the settlements and the tilts of both footings (Footing I and Footing II) when loaded.

It was evident that, the longer the floating sheet pile wall, the less the settlement of both Footing I and Footing II, due to loading on Footing II (Section 6.3.3.3). The rate of mitigation of the settlement of Footing I, after extending the wall beyond $0.25H$ ($H$ = the ground thickness), was almost linear with a rate of $0.0022B$/m ($B$ = the footing width) relative to the footing settlement without a sheet pile wall. The mitigation rate of the settlement of Footing II was $0.0011B$/m, which was only half of that predicted for Footing I, after the length was extended beyond $0.5H$.

Remarkable settlement mitigation, during loading on Footing II, was found for the fixed sheet pile wall. With a wall length of $0.25H$, Footing I and Footing II respectively settled by only 34% and 87% relative to their settlement without a sheet pile wall. The settlements of Footing I and Footing II (Figure 6.70) were further reduced to respectively 13.5% and 81.3% of their settlement without a pile, when the sheet pile wall was extended to $0.375H$ or $1.5B$, but no further benefit for longer piles.

The stiffness variation of the sheet pile wall, starting with section GSP2 (Table 6.4 and Figure 6.72), did not have a significant effect on the settlement mitigation, except in the case of an unrealistically stiff fixed sheet pile wall.

Without any sheet pile wall, Footing I and Footing II tilted towards each other with $\delta/l = 1/71$ and $\delta/l \approx 1/35$ respectively (Section 6.3.3.2). With a floating sheet pile wall, increasing its length to about $0.38H$ showed a remarkable mitigation of tilting for Footing 1 (Figure 6.70). However, further length increments seemed to lead to more tilting of the footing. The tilting then started diminishing again after the sheet pile wall occupied $0.75H$. Footing II exhibited continuous tilting mitigation as the wall length was increased, the tilting remained above $\delta/l = 1/150$. When the wall was restrained vertically, the tilting mitigation for both footings was no longer improved after the pile extended beyond $0.375H$ and $0.25$ respectively.

Higher stiffness of the floating or the fixed sheet pile wall caused less tilting of both footings (Figure 6.75).

## 7.4 COROLLARY

The presence of a vertically restrained sheet pile wall or, perhaps, some other type of fixed wall, is an effective technique for the mitigation of settlement due to the interaction of closely-constructed buildings. A sufficiently long floating wall could also be effective. However, in deep soft ground, using a long floating sheet pile wall may not be economical. In this case, a shorter vertically restrained sheet pile wall could be a better alternative. In practice, the vertical restraint could be provided with additional long piles, connected to the sheet piles with waling beams. The supporting piles must be extended to a depth at which they can support the sheet pile wall with an acceptable settlement.

## 7.5 RECOMMENDATIONS ON FUTURE RESEARCH

Although this research met its main objectives, a number of extensions and improvements are possible should further research be carried out.

### 7.5.1 Physical Modelling

Unloading and reloading during preconsolidation were caused by the attempts at repositioning (levelling) the consolidation piston in order to avoid uneven friction between the piston and the chamber wall. This changed the settlement behaviour of the soil under footing pressures. This problem might be solved by deepening the piston.

The combination of a raft foundation and piles is commonly used if buildings are constructed on deep soft ground. It is also recommended to perform physical modelling with similar construction, i.e. footings with piles.

In this research, loading on the second footing was applied after it was implemented on the first footing. Physical modelling with simultaneous loading on Footing I and Footing II with a similar mitigation technique is recommended for more complete understanding.

The determination of the end of (primary) consolidation was very important in this research. For example, the end of consolidation around the sheet wall after its installation was estimated

with LVDTs connected to the footing system. However, it would be possible to determine the end of consolidation from the displacements over the areas of interest using PIV, serving as a logging tool. This could be done by logging every image taken by a camera and immediately performing PIV analysis over those areas. Furthermore, in tracing the typical time–settlement curve, it is not necessary to always use the same time interval. Automation would be preferable and would require software development linking image acquisition and PIV subroutines. The end of consolidation could also be determined from pore pressure measured with transducers incorporated in the model.

### 7.5.2  Numerical Modelling

In practice, few buildings are long enough to justify the assumption of plane strain in the soil. In addition, a sheet wall is normally installed in stages, pile by pile. This can only be realistically simulated in a three-dimensional analysis.

Rather than "wishing the sheet pile wall into place" as done in the current analysis, it is recommended to simulate better the sheet pile wall installation, e.g. by vertically displacing the pile an appropriate distance.

In SAFE, no interface element is available. In fact, sliding occurs at the pile–soil interface during the sheet pile wall installation or perhaps between the soil and the footing bases. It is recommended to use appropriate interface elements between these extremely different materials.

It was observed from the physical modelling that the total settlements consisted of the primary consolidation and creep. The finite element analysis with the BRICK constitutive model successfully simulated the settlement but this was after the creep displacement was excluded. This constitutive model does not provide for the modelling of secondary compression. Improvement of BRICK in this respect is therefore desirable.

# REFERENCES

Abdel-Aziz, Y. I. and H. M. Karara (1971). Direct linear transformation from comparator coordinates into object space coordinates in close-range photogrammetry. In *Proceedings of the Symposium on Close-Range Photogrammetry*, Falls Church, VA: American Society of Photogrammetry, pp. 1–18.

Adrian, R. J. (1991). Particle-imaging technique for experimental fluid mechanics. *Annual Reviews in Fluid Mechanics 23*, 261–304.

Akai, K., T. Adachi, and K. Fujimoto (1978). Constitutive equations for geomechanical materials based on elasto-viscoplasticity. In S. Murayama and A. N. Schofield (Eds.), *Constitutive equations of soils: Proceedings of Specialty Session IX, The Ninth International Conference on Soil Mechanics and Foundation Engineering*, Tokyo, Japan, pp. 1–10. Japanese Society of Soil Mechanics and Foundations Engineering: Japanese Society of Soil Mechanics and Foundations Engineering.

Al-Tabbaa (1987). *Permeability and stress-strain response of speswhite kaolin.* PhD Dissertation, University of Cambridge.

Al-Tabbaa, A. and D. M. Wood (1987). Some measurement of the permeability of kaolin. *Géotechnique 37*(4), 499–503.

Al-Tabbaa, A. and D. M. Wood (1989). An experimentally based 'bubble' model for clay. In S. Pietruszczak and G. N. Pande (Eds.), *International Conference of Numerical Models in Geomechanics, NUMOG III*, London, pp. 91–99. Elsevier Applied Science.

Allersma, H. G. B., H. G. Stuit, and P. Holscher (1994). Using image processing in soil mechanics. In *Proceedings of 12th International Conference on Soil Mechanics and Foundation Engineering*, New Delhi, pp. 1341–1344. Balkema.

Anadarajah, A. (2000). Numerical simulation of one-dimensional behaviour of a kaolinite. *Géotechnique 50*(5), 509–519.

Andrawes, K. Z. and R. Butterfield (1973). The measurement of planar displacements of sand grains. *Géotechnique 23*(5), 571–576.

Atkinson, J. H. (1981). *Foundations and slopes*. London: McGraw-Hill Book Company (UK) Limited.

Azizi, F. (2000). *Applied analyses in geotechnics*. London: E & FN Spon.

Bai, X. and P. Smart (1997). Change in microstructure of kaolin in consolidation and undrained shear. *Géotechnique 47*(5), 1009–1017.

Bhaskaran, R. (1974). Strength anisotropy in kaolinite clay. *Géotechnique 24*(4), 674–678.

Bolton, M. D. (1991). Geotechnical stress analysis for bridge abutment design. Contractor Report 270, Transport and Road Research Laboratory.

British Steel (1997). *Piling Handbook* (Seventh ed.). North Lincolnshire, UK: British Steel plc.

Britto, A. M. and M. J. Gunn (1987). *Critical state soil mechanics via finite elements*. West Sussex, England: Ellis Horwood Limited.

Brooker, E. W. and O. H. Ireland (1965). Earth pressures at rest related to stress history. *Canadian Geotechnical Journal 2*(1), 1–15.

Burland, J. B., J. R. Standing, and F. M. Jardine (Eds.) (2001). *Building response to tunnelling. Case studies from the Jubilee Line Extension, London* (First ed.). London: Thomas Telford Publishing.

Burland, J. B. and C. P. Wroth (1974). Settlement of buildings and associated damage. In *Review paper: Session V, Proceedings of the Conference on Settlement of Structures, organized by the British Geotechnical Society*, pp. 611–654.

Canon Inc. (2004). Canon PowerShot Pro1 DIGITAL CAMERA Camera User Guide.

Cao, L. F., M.-F. Chang, C. I. Teh, and Y. M. Na (2001). Back-calculation of consolidation parameters from field measurements at a reclamation site. *Canadian Geotechnical Journal 38*(4), 755–769.

Craig, R. F. (1987). *Soil Mechanics* (Fourth ed.). Wokingham: Van Nostrand Reinhold.

Das, B. M. and S. Larbi-Cherif (1983a). Bearing capacity of two closely-spaced shallow foundations on sand. *Soils and Foundations, Japanese Society of Soil Mechanics and Foundation Engineering 23*(1), 1–7.

Das, B. M. and S. Larbi-Cherif (1983b). Ultimate bearing capacity of closely-spaced strip foundation. *Transportation Research Record, Transportation Research Board* (945), 37–39.

Das, B. M. and E. C. Shin (1996). Laboratory model tests for cyclic load-induced settlement of a strip foundation on a clayey soil. *Geotechnical and Geological Engineering 14*, 25–36.

Davies, E. R. (2005). *Machine Vision: Theory, Algorithms and Practicalities*. Oxford: Morgan Kaufmann.

Desai, C. S. and J. F. Abel (1972). *Introduction to the Finite Element Method: A Numerical Method for Engineering Analysis*. New York: Van Nostrad Reinhold Company.

Dwight, J. B. (1999). *Aluminium Design and Construction*. London: E & FN Spon, an imprint of Routledge.

Eid, M. M. (1978). *Expansion of cylindrical cavities in clay*. Ph. D. thesis, The University of Sheffield, Department of Civil and Structural Engineering.

Elavarasan, R., L. Venkatakrishnan, A. Krothapalli, and L. Lourenco (2000). A PIV study of a supersonic impinging jet. *Journal of Visualization 2*(3/4).

Engineers Edge (2004). Modulus of Elasticity, Average Properties of Structural Materials, Shear Modulus, Poisson's Ratio, Density.
`http://www.engineersedge.com/manufacturing_spec/`.

Forliti, D. J., P. J. Strykowski, and K. Debatin (2000). Bias and precision errors of digital particle image velocimetry. *Experiments in Fluids 28*(5).

Graham, J., G. P. Raymond, and A. Suppiah (1984). Bearing capacity of three closely-spaced footings on sand. *Géotechnique 34*(2), 173–182.

Grant, I. and X. Wang (1995). Directionally-unambiguous, digital particle image velocimetry studies using a image intensifier camera. *Experiments in Fluids 18*(5).

Grant, R., J. T. Christian, and E. H. Vanmarcke (1974). Differential settlement of buildings. *Journal of the geotechnical engineering division 100*(GT9), 973–991.

Guler, M., B. E. Tuncer, and J. B. Peter (1999, April). Measurement of particle movement in granular soils using image analysis. *Journal of Computing in Civil Engineering 13*(2), 116–122.

Hanzawa, H. and K. Adachi (1983). Overconsolidation of alluvial clays. *Soils and Foundations, Japanese Society of Soil Mechanics and Foundation Engineering 23*(4), 106–118.

Haralick, R. M. and L. G. Shapiro (1992). *Computer and Robot Vision, Vol. 1.* Wokingham: Addison-Wesley Pub. Co.

Hart, D. P. (2000). Super-resolution PIV by recursive local-correlation. *Journal of Visualization 3*(2).

Heikkilä, J. (2000a). Camera Calibration Toolbox for Matlab Version 3.0. http://www.ee.oulu.fi/~jth/calibr/.

Heikkilä, J. (2000b). Geometric camera calibration using circular control points. *IEEE Transactions on Pattern Analysis and Machine Intelligence 22*(10), 1066–1077.

Heikkilä, J. and O. Silvén (1997). A four-step camera calibration procedure with implicit image correction. In *CVPR '97: Proceedings of the 1997 Conference on Computer Vision and Pattern Recognition (CVPR '97)*, pp. 1106. IEEE Computer Society.

Hill, D. F., K. V. Sharp, and R. J. Adrian (2000). Stereoscopic particle image velocimetry measurements of the flow around a rushton turbine. *Experiments in Fluids 29*(5).

Hill, R. (1950). *The Mathematical Theory of Plasticity.* London, UK: Oxford: Clarendon Press.

Hird, C. C. and V. J. Moseley (2000). Model study of seepage in smear zones around vertical drains in layered soil. *Géotechnique 50*(1), 89–97.

Houlsby, G. T. and C. P. Wroth (1991). The variation of shear modulus of a clay with pressure and overconsolidation ratio. *Soils and Foundation 31*(3), 138–143.

Hyde, A. F. L. and S. F. Brown (1976). The plastic deformation of a silty clay under creep and repeated loading. *Géotechnique 26*(1), 173–184.

Hyde, A. F. L. and S. J. Ward (1985). A pore pressure and stability model for a silty clay under repeated loading. *Géotechnique 35*(2), 113–125.

Ineos Acrylics UK Ltd. (2001). PERSPEX™for Corporate Imaging, PXTD 261, Eigth Edition. `http://www.bayplastics.co.uk.`

Iskander, M. G., J. Liu, and S. Sadek (2002). Optical measurement of deformation under foundations using a transparent soil model. In R. Phillips, P. J. Guo, and R. Popescu (Eds.), *Physical Modelling in Geotechnics: Proceedings of the International Conference Icpgm '02, 10–12 July,* St. John's, Newfoundland, Canada, pp. 155–159.

Jain, R., R. Kasturi, and B. G. Schunck (1995). *Machine Vision.* Singapore: McGraw-Hill, Inc.

Jaky, J. (1944). The coefficient of earth pressure at rest. *Journal for Society of Hungarian Architects Engineers 78*(22), 355–358.

Jao, M., M. C. Wang, H. C. Chou, and C. J. Lin (2002). Behavior of interacting parallel strip footings. *Electronic Journal of Geotechnical Engineering 7 (Bundle A).* `http://www.ejge.com/2002/Ppr0205/Ppr0205.htm.`

Jovičić, V., M. Coop, and B. Simpson (2006). Interpretation and modelling of deformation characteristics of a stiff north sea clay. *Canadian Geotechnical Journal 43*(4), 341–354.

Kavvadas, M. and A. Amorosi (2000). A constitutive model for structured clay. *Géotechnique 50*(3), 263–273.

Keane, R. D. and R. J. Adrian (1990). Optimization of particle image velocimeters. part i: Double pulsed systems. *Measurement Science and Technology 1*(11), 1202–1215.

Keane, R. D. and R. J. Adrian (1992, July). Theory of cross-correlation analysis of PIV images. *Applied Scientific Research 49*(3), 191–215.

Khing, K. H., B. M. Das, S. C. Yen, V. K. Puri, and E. E. Cook (1992). Interference effect of two closely-spaced shallow strip foundations on geogrid-reinforced sand. *Geotechnical and Geological Engineering 10*(4), 257–271.

Lecuona, A., J. Nogueira, P. A. Rodríguez, and A. Acosta (2004). PIV evaluation algorithms for industrial applications. *Measurement Science and Technology 15*(6), 1027–1038.

Lehane, B. M. and B. Simpson (2000). Modelling glacial till under triaxial conditions using a brick soil model. *Canadian Geotechnical Journal 37*(5), 1078–1088.

Liu, J. and M. Iskander (2004, January). Adaptive cross correlation for imaging displacements in soils. *Journal of Computing in Civil Engineering 18*(1), 46–57.

Maharaj, D. K. (2003). Nonlinear finite element analysis of strip footing on reinforced clay. *Electronic Journal of Geotechnical Engineering 8 (Bundle C)*.
http://www.ejge.com/2003/Ppr0338/Ppr0338.htm.

Maharaj, D. K., D. Chandana, and S. Madhuri (2004). Finite element analysis of strip type shell foundation and its interaction. *Electronic Journal of Geotechnical Engineering 9 (Bundle B)*.
http://www.ejge.com/2004/Ppr0411/Ppr0411.htm.

Mainstone, R. J. (1971). On the stiffness and strengths of infilled frames. *Proceedings of the Institution of Civil Engineers Supplemental Vol. IV, Papers 7360S*, 57–90.

Mainstone, R. J. and G. A. Weeks (1970). The influence of a bounding frame on the racking stiffness and strengths of brick walls. *Proceedings of the 2nd International Brick and Masonry Conference, Building Research Establisment, Watford, England*, 165–171.

Mair, R. J. (1979). *Centrifugal modelling of tunnel construction in soft clay*. PhD Dissertation, University of Cambridge.

Mayne, P. W. and F. H. Kulhawy (1982). $K_0$—OCR relationships in soil. *Journal of the Geotechnical Engineering Division, ASCE 108*(GT6), 851–872.

Meyerhof, G. G. (1951). The ultimate bearing capacity of foundations. *Géotechnique 2*(4), 301–332.

Meyerhof, G. G. (1956). Discussion on 'The allowable settlements of buildings' by A. W. Skempton and D. H. MacDonald. *Proceedings of the Institution of Civil Engineers 5*, 774.

Moseley, V. G. (1998). *Effects of smear during vertical penetration of layered soils*. Ph. D. thesis, The University of Sheffield, Department of Civil and Structural Engineering.

Nunez, I. (1989). *Tension piles in clay*. PhD Dissertation, University of Cambridge.

Obaidat, M. T. and M. F. Attom (1996). Computer vision-based technique to measure displacement in selected soil tests. *Geotechnical Testing Journal 21*(1), 31–37.

Okamoto, K., S. Nishio, T. Saga, and T. Kobayashi (2000). Standard images of particle image velocimetry. *Measurement Science and Technology 11*(6), 685–691.

Osman, A. S., H. C. Yeow, and M. D. Bolton (2004). Estimation of undrained settlement of shallow foundations on london clay. *International Conference on Structural and Foundation Failure, August 2–4*, 443–454.

Ove Arup and Partners (2006). Safe Oasys GEO Suite for Windows Version 18.1. User Manual.

Parry, R. H. G. and V. Nadarajah (1973). Observations on laboratory prepared, lightly overconsolidated specimens of kaolin. *Géotechnique 24*(3), 345–357.

Phillips, R. and A. Valsangkar (1987). An experimental investigation of factors affecting penetration resistance in granular soils in centrifuge modelling. Technical Report CUED/D-SOILS/TR210, Cambridge University, Engineering Department.

Polshin, D. E. and R. A. Tokar (1957). Maximum allowable non-uniform settlement of structures. In *Proceedings of 4th International Conference on Soil Mechanics and Foundation Engineering*, Volume I, London, pp. 402–405. Butterworth's Scientific.

Potts, D. M. (1976). *Behaviour of lined and unlined tunnels in sand.* PhD Dissertation, University of Cambridge.

Potts, D. M. (2003). Numerical analysis: a virtual dream or practical reality? *Géotechnique 53*(6), 535–573.

Potts, D. M., K. Axelsson, L. Grande, H. Schweiger, and M. Long (Eds.) (2001). *Guidelines for the use of advanced numerical analysis.* Heron Quay, London: Thomas Telford Ltd.

Potts, D. M. and Zdravković (2001a). *Finite Element Analysis in Geotechnical Engineering: Theory.* Heron Quay, London: Thomas Telford Ltd.

Potts, D. M. and Zdravković (2001b). *Finite Element Analysis in Geotechnical Engineering: Application.* Heron Quay, London: Thomas Telford Ltd.

Puzrin, A. M. and J. B. Burland (1998). Nonlinear model of small strain behaviour of soils. *Géotechnique 48*(2), 217–233.

Puzrin, A. M. and G. T. Houlsby (2001). Strain-based plasticity models for soils and the brick model as an example of the hyperplasticity approach. *Géotechnique 51*(2), 169–172.

Richard Liew, J. Y. and N. W. Shanmugam (2003). *The Civil Engineering Handbook: Theory and Analysis of Structures.* Boca Raton: CRC Press LLC.

Rossato, G., N. L. Ninis, and R. J. Jardine (1992). Properties of some kaolin-based model clay soils. *Geotechnical Testing Journal, GTJODJ 15*(2), 166–179.

Rouainia, M. and D. M. Wood (2000). A kinematic hardening constitutive model for natural clay with loss of structure. *Géotechnique 50*(2), 154–164.

Saada, A. S., L. Liang, J. L. Figueroa, and C. T. Cope (1999). Bifurcation and shear propagation in sands. *Géotechnique 49*(3), 367–385.

Santiago, J. G., S. T. Wereley, C. D. Meinhart, D. J. Beebe, and R. J. Adrian (1998). A particle image velocimetry system for microfluidics. *Experiments in Fluids 25*(4), 316–319.

Scott, C. R. (1980). *An introduction to Soil Mechanics and Foundation* (Third ed.). Applied Science Publishers.

Sheeran, D. E. and R. J. Krizek (1971). Preparation of homogeneous samples by slurry consolida-tion. *Journal of Materials* 6(2), 356–373.

Simpson, B. (1992). Retaining structures: displacement and design. 32nd rankine lecture. *Géotechnique* 42(4), 541–576.

Skempton, A. W. and D. H. MacDonald (1956). The allowable settlements of buildings. In *Pro-ceedings of the Institution of Civil Engineers, Part III*, Number 5, pp. 727–768.

Slama, C. C. (Ed.) (1980). *Manual of Photogrammetry* (Fourth ed.). 105 N. Virginia Avenue, Falls Church, VA: American Society of Photogrammetry.

Springman, S. (2004). Modelling in geotechnics: Course notes. ETH Zürich, Institute of Geotech-nical Engineering.

Springman, S. M. (1989). *Lateral loading on piles due to simulated embankment construction.* PhD Dissertation, University of Cambridge.

Srisakthivel, S. (2003). *Laboratory measurements of the permeability of clay soils assisted by a self-boring device.* Ph. D. thesis, The University of Sheffield, Department of Civil and Structural Engineering.

Stallebrass, S. E. and R. N. Taylor (1997). The development and evaluation of a constitutive model for the prediction of ground movements in overconsolidated clay. *Géotechnique* 47(2), 235–254.

Stuart, J. G. (1962). Interference between foundations, with special reference to surface footings in sand. *Géotechnique* 12(1), 15–22.

Suzuki, K. and K. Yasuhara (2004). Two case studies of consolidation settlement analysis using constant rate of strain consolidation test. *Soils and Foundations, The Japanese Geotechnical Society* 44(6), 69–81.

Take, W. A. (2003). *The influence of seasonal moisture cycles on clay slopes.* PhD Dissertation, University of Cambridge.

Tan, T., F. Lee, P. Chong, and H. Tanaka (2002). Effect of sampling disturbance on properties of singapore clay. *Journal of Geotechnical and Geoenvironmental Engineering* 128(11), 898–906.

Taylor, R. N., R. J. Grant, S. Robson, and J. Kuwano (1998). An image analysis system for determining plane and 3-d displacements in soil models. In *Proceedings of Centrifuge '98*, Rotterdam, pp. 73–78. Balkema.

Terzaghi, K. (1943). *Theoretical Soil Mechanics*. New York: John Wiley and Sons, Inc.

Timoshenko, S. and S. Woinowsky-Krieger (1959). *Theory of Plates and Shells*. London: McGraw-Hill Book Company.

Tomlinson, M. J. (2001). *Foundation design and construction* (7th ed.). Upper Saddle River, NJ: Prentice Hall.

Tonddast-Navaei, A. and D. B. Sharp (2005). The use of particle image velocimetry in the measurement of sound fields.
`http://acoustics.open.ac.uk/pdf/paper21.pdf`, Retrived February 2005.

Vesić, A. S. (1973). Analysis of ultimate loads of shallow foundation. *Journal of the Soil Mechanics and Foundations Division 99*(1), 45–73.

Wernet, M. P. (2000). Application of dpiv to study both steady state and transient turbomachinery flows. *Optics & Laser Technology 32*(7–8), 497–525.

Westerweel, J. (1997). Fundamentals of digital particle image velocimetry. *Measurement Science and Technology 8*(12), 1379–1392.

Westerweel, J., D. Dabiri, and M. Gharib (1997). The effect of a discrete window offset on the accuracy of cross-correlation analysis of digital piv recordings. *Experiments in Fluids 23*(1), 20–28.

White, D. J. (2002). *An investigation into the behaviour of pressed-in piles*. PhD Dissertation, University of Cambridge.

White, D. J. and M. D. Bolton (2004). Displacement and strain paths during plane-strain model pile installation in sand. *Géotechnique 54*(6), 375–397.

White, D. J. and W. Take (2002). GeoPIV: Particle Image Velocimetry (PIV) software for use in geotechnical testing. Technical Report CUED/D-SOILS/TR322, Cambridge University, Engineering Department.

White, D. J., W. A. Take, and M. D. Bolton (2003). Soil deformation measurement using Particle Image Velocimetry (PIV) and photogrammetry. *Géotechnique 53*(7), 619–631.

Willert, C. E. and M. Gharib (1991). Digital particle image velocimetry. *Experiments in Fluids 10*(4).

Wood, D. M. (1990). *Soil behaviour and critical state soil mechanics*. Cambridge: Cambridge University Press.

Wood, D. M. (2004). *Geotechnical modelling*. Oxfordshire: Spon Press.

Yasuhara, K., K. Hirao, and A. F. L. Hyde (1992). Effects of cyclic loading on undrained strength and compressibility of clay. *Soils and Foundation 32*(1), 100–116.

Yasuhara, K., S. Murakami, N. Toyota, and A. F. L. Hyde (2001). Settlement in fine grained soils under cyclic loading. *Soils and Foundation 41*(6), 25–36.

Yong, K. Y. (1979). *A Laboratory study of the shaft resistance of bored piles*. Ph. D. thesis, The University of Sheffield, Department of Civil and Structural Engineering.

Zienkiewicz, O. C. (1977). *The finite element method* (3rd ed.). London, UK: London: McGraw-Hill.